

## Contrast echocardiography for cardiac quantifications

**Citation for published version (APA):**

Mischi, M. (2004). *Contrast echocardiography for cardiac quantifications*. [Phd Thesis 1 (Research TU/e / Graduation TU/e), Electrical Engineering]. Technische Universiteit Eindhoven. <https://doi.org/10.6100/IR579395>

**DOI:**

[10.6100/IR579395](https://doi.org/10.6100/IR579395)

**Document status and date:**

Published: 01/01/2004

**Document Version:**

Publisher's PDF, also known as Version of Record (includes final page, issue and volume numbers)

**Please check the document version of this publication:**

- A submitted manuscript is the version of the article upon submission and before peer-review. There can be important differences between the submitted version and the official published version of record. People interested in the research are advised to contact the author for the final version of the publication, or visit the DOI to the publisher's website.
- The final author version and the galley proof are versions of the publication after peer review.
- The final published version features the final layout of the paper including the volume, issue and page numbers.

[Link to publication](#)

**General rights**

Copyright and moral rights for the publications made accessible in the public portal are retained by the authors and/or other copyright owners and it is a condition of accessing publications that users recognise and abide by the legal requirements associated with these rights.

- Users may download and print one copy of any publication from the public portal for the purpose of private study or research.
- You may not further distribute the material or use it for any profit-making activity or commercial gain
- You may freely distribute the URL identifying the publication in the public portal.

If the publication is distributed under the terms of Article 25fa of the Dutch Copyright Act, indicated by the "Taverne" license above, please follow below link for the End User Agreement:

[www.tue.nl/taverne](http://www.tue.nl/taverne)

**Take down policy**

If you believe that this document breaches copyright please contact us at:

[openaccess@tue.nl](mailto:openaccess@tue.nl)

providing details and we will investigate your claim.

# **Contrast Echocardiography for Cardiac Quantifications**

PROEFSCHRIFT

ter verkrijging van de graad van doctor aan de Technische  
Universiteit Eindhoven, op gezag van de Rector Magnificus,  
prof.dr. R.A. van Santen, voor een commissie aangewezen door  
het College voor Promoties in het openbaar te verdedigen op  
maandag 4 oktober 2004 om 16.00 uur

door

**Massimo Mishi**

geboren te Rome, Italië

Dit proefschrift is goedgekeurd door de promotoren:

prof.dr. A.A.C.M. Kalker

en

prof.dr. H.H.M. Korsten

This research was supported by the Catharina Hospital Eindhoven, The Netherlands.

©Copyright 2004 Massimo Mischi

All rights reserved. No part of this publication may be reproduced, stored in a retrieval system, or transmitted, in any form or by any means, electronic, mechanical, photocopying, recording or otherwise, without the prior written permission from the copyright owner.

CIP-DATA LIBRARY TECHNISCHE UNIVERSITEIT EINDHOVEN

Mischi, Massimo

Contrast echocardiography for cardiac quantification / by Massimo Mischi. -  
Eindhoven : Technische Universteit Eindhoven, 2004.

Proefschrift. - ISBN 90-386-1613-9

NUR 927

Trefw.: biomedische meettechniek / ultrageluid ; biologie / biomedische  
beeldverwerking / biologische transportverschijnselen / parameterschatting.  
Subject headings: biomedical measurement / biomedical ultrasonics /  
biomedical imaging / biological fluid dynamics / parameter estimation.

*Dedicata ai miei genitori Anna e Mauro*





# Summary

The indicator-dilution-theory for cardiac quantifications has always been limited in practice by the invasiveness of the available techniques. However, the recent introduction of stable ultrasound contrast agents opens new possibilities for indicator dilution measurements. This study describes a new and successful approach to overcome this invasiveness issue.

We show a novel approach for minimally invasive quantification of several cardiac parameters based on the dilution of ultrasound contrast agents. A single peripheral injection of an ultrasound contrast agent bolus can result in the simultaneous assessment of cardiac output, pulmonary blood volume, and left and right ventricular ejection fraction. The bolus passage in different sites of the central circulation is detected by an ultrasound transducer. The detected acoustic (or video) intensities are processed and several indicator dilution curves are measured simultaneously. To this end, we exploit that for low concentrations the relation between contrast concentration and acoustic backscatter is approximately linear.

The Local Density Random Walk Model is used to fit and interpret the indicator dilution curves for cardiac output, pulmonary blood volume, and ejection fraction measurements. Two fitting algorithms based either on a multiple linear regression in the logarithmic domain or on the solution of the moment equations are developed.

The indicator dilution system can be also interpreted as a linear system and, therefore, characterized by an impulse response function. An adaptive Wiener deconvolution filter is implemented for robust dilution system identification. For ejection fraction measurements, the atrial and ventricular indicator dilution curves are measured and processed by the deconvolution filter, resulting in the estimate of the left-ventricle dilution-system impulse response. This curve can be fitted and interpreted by a mono-compartment exponential model for the ejection fraction assessment.

The proposed deconvolution filter is also used for the identification of the dilution system between right ventricle and left atrium. The Local Density Random Walk Model fit of the estimated impulse response allows the pulmonary blood volume assessment.

Both cardiac output and pulmonary blood volume measurements are validated in-vitro with accurate results (correlation coefficients larger than 0.99). The Pulmonary blood volume measurement feasibility is also tested in humans with promising results. The ejection fraction measurement is validated in-vivo. The impulse response

approach allows accurate left ventricle ejection fraction estimates. Comparison with echocardiographic bi-plane measurements shows a correlation coefficient equal to 0.93.

A dedicated image segmentation algorithm for videodensitometry has also been developed for automating the determination of regions of interest. The resulting algorithm has been integrated with the indicator dilution analysis system. The automatic determination of the measurement region results in improved dilution-curve signal-to-noise ratios.

In conclusion, this study proves that quantification of cardiac output, pulmonary blood volume, and left and right ventricular ejection fraction by dilution of ultrasound contrast agents is feasible and accurate. Moreover, the proposed methods are applicable in different contexts (e.g., magnetic resonance imaging) and for different types of measurements, leading to a broad range of applications.

# Samenvatting

Het kwantificeren van hartfunctie parameters met behulp van de indicator-dilutie-theorie werd altijd beperkt doordat de beschikbare technieken invasief van aard waren. De recent op de markt gekomen stabiele contrastvloeistoffen maken het echter mogelijk niet-invasieve metingen met ultrageluid te doen met behulp van de indicator-dilutie-theorie. Dit onderzoek beschrijft een nieuwe en succesvol gebleken aanpak om het probleem van invasiviteit te overwinnen.

Er wordt een nieuwe aanpak beschreven voor het kwantificeren van een aantal hartfunctie parameters, gebaseerd op de verdunning van een toegediende ultrageluid contrastvloeistof waarbij minimale invasiviteit gewaarborgd wordt. Met één enkele perifere injectie van een ultrageluid contrastvloeistof bolus kan gelijktijdig de cardiac output, het pulmonair bloedvolume en de ejectie fractie van het linker en rechter ventrikel gemeten worden. Het passeren van de contrastvloeistof op verschillende plaatsen in de centrale circulatie wordt gedetecteerd met een ultrageluid-transducer. De gedetecteerde geluids- en video-intensiteiten worden zo verwerkt, dat verscheidene indicator-dilutie-curven gelijktijdig kunnen worden gemeten. Er wordt hierbij gebruik gemaakt van het feit dat bij lage concentraties van de contrastvloeistof er –bij benadering– een lineaire relatie bestaat tussen de concentratie van de contrastvloeistof en de akoestische reflectie.

Het Local Density Random Walk Model wordt gebruikt om de indicator-dilutie-curven te fitten en te interpreteren bij het meten van de cardiac output, het pulmonair bloedvolume en de ejectie fractie. Voor het gebruik van het model zijn twee algoritmes ontwikkeld, een gebaseerd op meervoudige lineaire regressie met een logaritmische schaal, de ander op het oplossen van de momenten vergelijkingen.

De indicator-dilutie overdracht kan geïnterpreteerd worden als een lineair systeem en kan daarom gekarakteriseerd worden met een impulsresponsie. Om robuuste identificatie van het dilutie-systeem te verkrijgen is een instelbaar Wiener deconvolutie filter geïmplementeerd. Voor het bepalen van de ejectie fractie worden de atriale en ventriculaire indicator-dilutie-curven gemeten en gedeconvolveerd. Dit resulteert in een schatting van de impulsresponsie van het dilutie-systeem van het linker ventrikel. De geschatte impulsresponsie wordt vervolgens gefit en geïnterpreteerd door middel van een exponentieel mono-compartment model resulterend in een schatting van de ejectie fractie.

Het deconvolutie filter wordt tevens gebruikt ter identificatie van de overdracht tussen het rechter ventrikel en linker atrium. De local density random walk model fit van de geschatte impulsresponsie levert een schatting op van het pulmonair bloedvolume.

Zowel de meting van de cardiac output als die van het pulmonair bloedvolume zijn in vitro gevalideerd waaruit bleek dat de resultaten betrouwbaar zijn (correlatie coëfficiënten groter dan 0,99). De mogelijkheid om het pulmonair bloedvolume in vivo te meten is ook onderzocht en leverde veelbelovende resultaten op. De metingen van de ejection fractie zijn in vivo gevalideerd. De bepaling van de ejection fractie met behulp van de impulsresponsie methode levert een nauwkeurige schatting op van de ejection fractie van het linker ventrikel. De vergelijking van de resultaten met die van de echocardiografische bi-plane metingen geeft een correlatie coëfficiënt van 0,93.

Voor de automatische bepaling van de region of interest is een speciaal beeld segmentatie algoritme voor videodensitometrie ontwikkeld. Het algoritme is geïntegreerd met het indicator-dilutie analyse systeem. De automatische bepaling van de region of interest resulteert in een verbeterde signaal-ruis verhouding van de dilutie-curve.

De conclusie is dat dit onderzoek heeft aangetoond dat nauwkeurige kwantificatie van de cardiac output, het pulmonair bloedvolume en de ejection fractie van het linker en rechter ventrikel door middel van de dilutie van een ultrageluid contrastvloeistof mogelijk is. Bovendien zijn de voorgestelde methoden toepasbaar in verschillende contexten (b.v. magnetic resonance imaging) en voor verschillende typen metingen, wat kan leiden tot een breed gebied van toepassingen.

# Contents

<b>1</b>	<b>Introduction</b>	<b>1</b>
<b>2</b>	<b>Clinical parameters of interest and their measurement</b>	<b>5</b>
2.1	Cardiac output . . . . .	7
2.1.1	Indicator dilution methods . . . . .	8
2.1.2	Angiography . . . . .	15
2.1.3	Magnetic resonance imaging . . . . .	17
2.1.4	Ultrasound flowmeter . . . . .	18
2.1.5	Magnetic flowmeter . . . . .	22
2.1.6	Impedance plethysmography . . . . .	24
2.2	Ejection fraction . . . . .	26
2.3	Pulmonary blood volume . . . . .	30
2.4	Comparative evaluation of the available techniques . . . . .	31
<b>3</b>	<b>Echography and ultrasound contrast agents</b>	<b>35</b>
3.1	Ultrasound principles and echography . . . . .	35
3.1.1	Ultrasound generation and propagation . . . . .	35
3.1.2	Echography principles: A-Mode and M-Mode analysis . . . . .	41
3.1.3	Image reconstruction: B-Mode and 3-D analysis . . . . .	46
3.2	Ultrasound contrast agents . . . . .	49
3.3	Echographic modes for contrast detection . . . . .	62
3.4	Echocardiography . . . . .	65
<b>4</b>	<b>Ultrasound contrast agent dilution curve modelling</b>	<b>69</b>
4.1	Calibration of acoustic and video intensity curves . . . . .	69
4.2	Indicator dilution curve models . . . . .	79
4.2.1	Overview of the indicator dilution models . . . . .	80
4.2.2	The Local Density Random Walk model . . . . .	85
4.2.3	The First Passage Time model . . . . .	89
<b>5</b>	<b>Random walk model fitting and dilution curve interpretation</b>	<b>93</b>
5.1	Least square model fitting . . . . .	93
5.1.1	Linear regression fitting algorithm . . . . .	95

5.1.2	Method of moments . . . . .	101
5.2	Cardiac output measurement . . . . .	105
5.3	Pulmonary blood volume measurement . . . . .	111
5.3.1	Transit and resident time for volume measurements . . . . .	111
5.3.2	Deconvolution and impulse response . . . . .	113
5.3.3	In-vitro and in-vivo volume measurements . . . . .	116
5.4	Ejection fraction measurement . . . . .	126
<b>6</b>	<b>Dilution system identification</b>	<b>129</b>
6.1	Deconvolution techniques . . . . .	129
6.2	Ejection fraction measurement . . . . .	134
6.2.1	Attenuation compensation . . . . .	135
6.2.2	Wiener deconvolution scheme . . . . .	138
6.2.3	In-vivo measurements . . . . .	142
6.3	Pulmonary blood volume measurement . . . . .	144
<b>7</b>	<b>Automatic region of interest detection for real-time applications</b>	<b>149</b>
7.1	The proposed algorithm . . . . .	152
7.2	Results . . . . .	159
<b>8</b>	<b>Conclusion and perspectives</b>	<b>165</b>
<b>A</b>	<b>Multiple linear regression</b>	<b>171</b>
<b>B</b>	<b>Derivation of the LDRW model from a binomial step distribution</b>	<b>173</b>
<b>C</b>	<b>LDRW model and diffusion equation</b>	<b>177</b>
<b>D</b>	<b>LDRW model time integration</b>	<b>181</b>
	<b>Bibliography</b>	<b>185</b>
	<b>List of publications</b>	<b>205</b>
	<b>List of abbreviations</b>	<b>209</b>
	<b>Acknowledgment</b>	<b>211</b>
	<b>Curriculum Vitae</b>	<b>215</b>

## Chapter 1

# Introduction

*Quicquid conaris, quo pervenias cogites (P. Sirius).*

Despite the development of advanced diagnostic techniques, the assessment of clinical parameters such as Cardiac Output (CO), Ejection Fraction (EF), and Pulmonary Blood Volume (PBV) remains a challenge. An accurate measurement of CO and PBV requires the employment of very invasive indicator dilution techniques (dye- or thermo-dilution), which require catheterization. The Left Ventricle (LV) EF can be estimated by use of 2-D or 3-D image segmentation algorithms combined with geometrical modelling, however, the assessment of the Right Ventricle (RV) EF is complicated due to its complex geometry. An extended overview of the most common techniques that are available for quantification of CO, EF, and PBV is presented in chapter 2.

This thesis aims to prove that the combined use of Ultrasound Contrast Agents (UCAs) and indicator dilution principles can result in a method that allows the simultaneous measurement of CO, EF (RV and LV), and PBV. UCAs are micro-bubbles (diameter from  $1\mu\text{m}$  to  $10\mu\text{m}$ ) of an inert gas encapsuled in a bio-compatible shell that are easily detectable by ultrasound investigation (echography). An overview of the principles of echography, as well as a characterization of UCA and an introduction to the echographic modes that are specifically designed for UCA detection is provided in chapter 3.

Some preliminary results are reported in literature on the measurement in-vitro and in animals of flow and CO based on UCA dilution [1–7], as well as on the measurement of EF in dogs using a ventricular UCA bolus injection [8]. However, in this thesis we present a new and minimally invasive approach that integrates several cardiac measurements together. Based on the shell-encapsuled UCA characterization, the relationship between UCA concentration and acoustic (and video) intensity is established for small driving pressure. Exploiting the latest contrast detection modes, an extremely low concentration range is found in which the relation between contrast concentration and measured intensity is well approximated by a linear function. Several procedures were used for the experimental measurements of such calibration curves. They are presented in chapter 4.



Chapter 4 also contains a description of the models that are commonly adopted for indicator dilution applications. They are adopted to overcome the low Signal-to-Noise Ratio (SNR) and contrast recirculation issues, and to provide with an interpretation of the IDC for the assessment of the fluid-dynamic parameters of interest. In particular, two models are selected for the UCA dilution curve interpolation and interpretation. They are the Local Density Random Walk (LDRW) and the First Passage Time (FPT) models. These models (especially the LDRW model), as reported in literature, show the best interpolation of the Indicator Dilution Curve (IDC) [9–14]. Moreover, they are related to the physics of the tracer-dispersion process [15, 16]. In chapter 4, as well as in Appendix B and C, also the LDRW model derivation from the statistical physics is shown. As the presented LDRW model derivations are a structured rearrangement of information already available in literature, a new procedure is proposed for the derivation of the FPT model, which is related to the LDRW model. This thesis shows the very first application of the LDRW and FPT models to UCA dilution methods.

Chapter 5 proposes an UCA IDC method for CO, PBV, and EF measurements. A small UCA bolus is injected in a peripheral vein and detected by an ultrasound scanner in the central circulation. The analysis of the acoustic (or video) intensity of the B-mode output of an ultrasound scanner allows - after calibration - the measurement of several UCA dilution curves. The cardiac parameters of interest are derived from the dilution curve modelling and interpolation. Several cardiac views permit the measurement of different IDCs from different sites. If a trans-esophageal probe is used, the CO can be assessed by the RV IDC analysis (before the bubble loss in the lungs). CO measurements require the use of a trans-esophageal probe because of calibration issues. Placing the probe almost in touch with the posterior cardiac wall permits a reliable establishment of the relation between injected dose and measured signal, which does not depend on the specific characteristics of the patient (gender, fat tissue, rib position, etc.). The LDRW model is fitted to the measured IDC by a dedicated fitting algorithm. The CO is directly derived from the model parameters.

Two alternative fitting algorithms are proposed. They are based on either a multiple linear regression technique in the logarithmic domain or the solution of the LDRW model (or FPT model) moment equations. Both techniques are discussed in chapter 5, as well as the principles of the multi-linear regression are shown in Appendix A. The method of moments requires the analytical solution of the integral and the first two statistical moments of the model. An analytical formula for the calculation of the FPT model moments is reported in literature. However, the same is not available for the LDRW model, so that an analytical calculation of the first two moments is proposed in chapter 5 as well as an analytical solution of the LDRW model time integral is proposed<sup>1</sup> in Appendix D.

---

<sup>1</sup>The LDRW model integral was solved with the fundamental support of prof.dr. Avantaggiati.

---

The CO can be multiplied by the contrast Mean Transit Time (MTT) between any couple of detection sites in the central circulation, resulting in a novel dilution technique for blood volume estimation. The MTT is directly derived from the parameters of the fitted models. For PBV assessments, two IDCs are measured in the RV and the Left Atrium (LA) and the contrast MTT between RV and LA is estimated from the IDC LDRW model fits. Measurements in the RV-outflow tract and in the Pulmonary Artery (PA) are also possible. MTT estimations do not require the employment of a trans-esophageal probe. When a trans-thoracic probe is used, the CO cannot be measured by contrast echocardiography. However, several options are available for a non-invasive assessment of the CO. The difference between MTT and Mean Residence Time (MRT) of the contrast between two detection sites and its relation with volume measurements is also discussed. The use of the MTT is preferred.

CO measurements were validated in-vitro. Two different setups, involving either a centrifugal pump or an artificial ventricle, were used. The correlation coefficient between real and measured flows in a range from 0.5 to 5 L/min is larger than 0.99. Also the volume measurement was validated in-vitro by a specific set-up. Four different volumes from 310ml to 1080ml were measured with flow ranging from 1 to 5 L/min. The correlation coefficient is 0.99 and the standard deviation smaller than 2.7%. PBV measurements were also tested in patients with promising results.

In conclusion of chapter 5, a new technique for the measurement of EF based on the LDRW model fit of LV IDCs is presented. However, the measurements in patients are not accurate. A better solution for EF measurements is proposed in chapter 6.

In general, for a correct EF estimation based on contrast dilution the bolus must be injected into the LV during diastole. Therefore, catheterization is needed and the clinical application of the method is limited by its high invasiveness. A solution for the invasiveness issue is provided by the innovative approach that is proposed in chapter 6, which makes use of an intravenous peripheral injection as used in chapter 5 for CO and PBV measurements. The RV or LV EF is measured by estimation and model fitting of the RV or LV impulse response. In fact, the ventricular dilution system can be approximated by a linear system and its impulse response estimated by a deconvolution technique once the system input and output signals (LA and LV IDC) are known. The estimated impulse response satisfies the hypothesis for a correct EF measurement. The atrial and ventricular IDCs are measured by a trans-thoracic ultrasound transducer and used for the ventricular system identification (impulse response estimation) after compensation for the attenuation effect on the LA IDC. An adaptive Wiener deconvolution scheme is implemented for the impulse response estimation. The choice for a least square approach is due to the low SNR that is shown by UCA IDCs. Eventually, the EF, which in the indicator dilution context is better referred to as Forward Ejection Fraction (FEF), is estimated by the mono-compartment exponential fit of the impulse response.

The EF measurement was validated in-vivo. A group of twenty patients with EF ranging from 10% to 70% and negligible mitral insufficiency was selected. EF dilution estimates were compared to EF measurements by echographic bi-plane method after UCA opacification. The correlation coefficient is 0.93. The Bland-Altman statistical analysis shows an average and a standard deviation equal to 1.6% and 8% respectively [17].

In chapter 6 the same system identification technique is also applied to blood volume measurements. In fact, an impulse response can be estimated between any couple of measurement sites in the central circulation and the MTT of the impulse response, derived from the LDRW fit, multiplied by the CO for the volume assessment. In particular, the PBV is measured by RV and LA IDC measurements. The validation results are very close to those measured by direct LDRW fit of two IDCs as shown in chapter 5.

Chapter 7 presents a dedicated segmentation technique for cardiac contrast quantification. It performs an automatic detection of multiple Regions Of Interest (ROI) for the measurement of multiple video-intensity curves (videodensitometry). The ROI is defined in order to maximize the measurement area and exclude the interference due to moving tissue. It results in improved fits of the measured IDCs with respect to manual ROI delineation.

A consistent part of this thesis has been published in several journal articles and conference proceedings. With reference to the section *List of publications*, part of the introductory sections in chapter 2 and 3 can be found in [PR-1]. In [PR-1], as well as in [JP-4], also some of the calibration issues discussed in chapter 4 are reported. The CO measurement and the multiple linear regression technique in chapter 5 are reported in [JP-4], as well as part of the blood volume measurements in the same chapter are reported in [JP-3], [IC-7], and [IC-8]. The method of moments in chapter 5 is described in [IC-3]. The system identification approach in chapter 6 is reported in [JP-1], [IC-1], and [IC-2]. Finally, the segmentation algorithm that is proposed in chapter 7 is presented in [JP-2].

## Chapter 2

# Clinical parameters of interest and their measurement

*Nunquam inveniatur, si contenti fuerimus inventis (Seneca).*

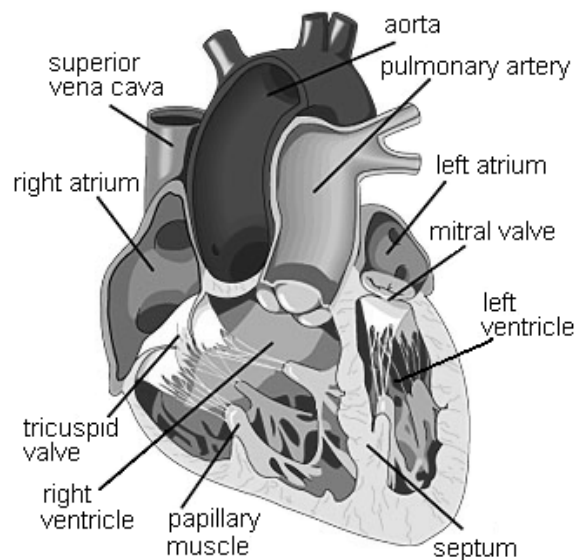


**Figure 2.1:** *Anatomy of the heart.*

The object of this study is the development of non-invasive tools for the measurement of cardiac and cardiovascular parameters. The heart is basically a pump, which makes the blood flow through the circulatory system and carry oxygen to the cells of the human body. It is necessary for the metabolism of the cells and, therefore, for life itself.

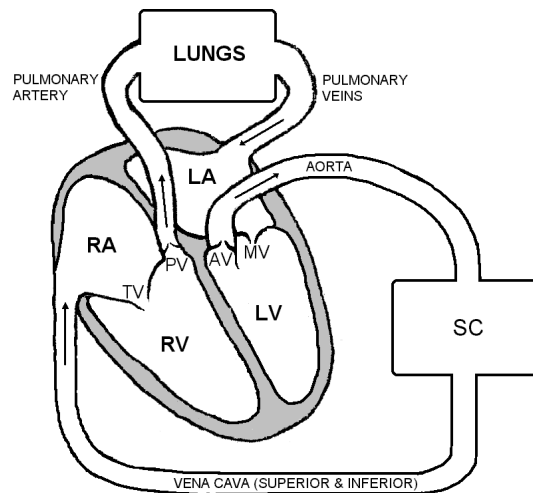


**Figure 2.2:** Scheme of the heart and the circulatory system. It is shown the blood direction through the atria and the ventricles as well as a schematic representation of both the circulation systems, i.e., the Systemic Circulation (SC), which brings oxygen to all the body, and the pulmonary circulation, which passes through the lungs, where the gas exchange takes place (oxygen in, and anhydride carbonic out). The Mitral Valve (MV), the Tricuspid Valve (TV), the Pulmonary Valve (PV), and the Aortic Valve (AV) are shown too.

The heart consists of four chambers (see Fig. (2.1) and Fig. (2.2)): the Left and the Right Atrium (LA and RA in Fig. (2.2)) are filled by blood coming respectively from the pulmonary veins and the vena cava (superior and inferior vena cava), while the other two chambers, the Left and the Right Ventricle (LV and RV in Fig. (2.2)), pump blood into the aorta and the pulmonary artery respectively. The left atrium and ventricle are connected by the Mitral Valve (MV in Fig. (2.2)), while the right atrium and ventricle are connected by the Tricuspid Valve (TV in Fig. (2.2)).

The ventricular cycle is divided in two main phases: diastole and systole. Diastole is the expansion (volume increase and blood filling) of the ventricle while systole is the contraction (volume reduction and blood ejection) of the ventricle. During diastole the mitral (or tricuspid) valve is open and blood flows from the atrium into the ventricle. During systole the valve is closed, and blood is pushed through the Aortic Valve (AV) or Pulmonary Valve (PV) into the aorta (systemic circulation) or the pulmonary artery (pulmonary circulation) respectively. A good closure of the valves prevents from blood leakage (regurgitation due to valve insufficiency) and backward flow.

The overall efficiency of the heart and the circulatory system is usually characterized by few important parameters. They are the Pulse Rate (PR, number of cardiac cycles per minute), the Cardiac Output (CO, blood flow through the aorta out-tract), and the Ejection Fraction (EF, percent volume variation of the ventricles). As the PR is accurately measured by pressure variations or electrical cardiac activity, more complicated is an accurate assessment of CO and EF.

The objective of this study is the development of new minimally-invasive indicator dilution methods for the measurement of CO and EF, which could represent a valid alternative to the invasive indicator dilution techniques and time-consuming geometric imaging techniques that are currently used in the clinical practice. The proposed methods are based on the dilution of specific contrast agents for echocardiography. In addition, based on the same indicator dilution principles, an accurate method for the measurement of Pulmonary Blood Volume (PBV) is proposed. The pulmonary blood volume, which is the blood volume in the pulmonary circulation (see Fig. (2.2)), is currently measured by very invasive techniques. The proposed technique is minimally invasive, so that the measurement of PBV could become a routine practice in outpatients. As a result, also the PBV could be included in the set of important parameters for the assessment of the circulatory system condition.

Since the objective of this study is the assessment of CO, EF, and PBV, the rest of the chapter focuses on the description of the available techniques for the measurement of these parameters. In particular, section 2.1, section 2.2, and section 2.3 describe the measurement techniques for CO, EF, and PBV respectively.

## 2.1 Cardiac output

Several different techniques are clinically used for Cardiac Output (CO) measurements. They are based on different principles with different reproducibility and accuracy [18]. Before considering the main measurement techniques, the CO must be clearly defined.

The blood that is ejected into the aorta carries oxygen to all the cells of the human body (Systemic Circulation, see Fig. (2.2)). Hence, the blood flow that is pumped by the left ventricle into the aorta is the first index of the circulation efficiency. In general, the CO is defined as the volume of blood that is ejected by the left ventricle into the aorta and is expressed in liters per minute. However, the blood flow that is ejected into the aorta is equal to the flow that passes through all the four chambers. This makes the CO measurement simpler, since it can be performed in different locations<sup>1</sup>.

Due to the cyclic contraction-expansion of the ventricles, the CO, as well as the blood pressure, is a periodic function of time. The first harmonic of these functions is

---

<sup>1</sup>If a haemorrhage is not in progress.

the Pulse Rate (PR), which represents the number of ventricular systoles (or diastoles) per minute. Despite the fact that the CO is a periodic function, it is often represented by a single value, which is a measure of the average flow. The CO is related to the ventricular volume variations during a cardiac cycle. If  $V_{ed}$  is the end diastolic volume (maximum volume) and  $V_{es}$  is the end systolic volume (minimum volume), then the Stroke Volume (SV), which is the volume of blood ejected from the ventricle to the artery in one cardiac cycle, equals the difference  $V_{ed} - V_{es}$ . Therefore, the CO can be defined as given in Eq. (2.1)<sup>2</sup>.

$$CO = SV \cdot PR \quad (2.1)$$

The CO for an average size adult (70 kg) at rest is about 5L/min. During severe exercise it can increase to over 30L/min. Miguel Indurain (who won the Tour de France in five successive years) had a resting PR of 28 beats per minute and could increase his cardiac output to 50L/min and his PR to 220 beats per minute. The CO is often divided by the Body Surface Area<sup>3</sup> (BSA) to normalize the value with respect to the size of the subject. In this case, it is referred to as Cardiac Index (CI).

The rest of the section describes the main methods that are commonly employed for the measurement of CO. Since the CO is a flow (even though referred to the heart), it is often referred to as  $\Phi$ , especially in the general theory and the in-vitro modelling context.

### 2.1.1 Indicator dilution methods

Several techniques for the measurement of CO make use of the dilution of an indicator in blood.

**Remark** *In the rest of this thesis, the flow is usually represented by the symbol  $\Phi(t)$ , while the abbreviation CO, which also is a flow (cardiac flow), is only used for cardiac measurements.*

The indicator dilution theory is based on the following concept: if the concentration of an indicator (or tracer) that is uniformly dispersed in an unknown volume  $V$  is determined, and the volume of the indicator (dose) is known, then the unknown volume can be determined too. Since  $\Phi(t) = dV(t)/dt$  ( $\Phi(t)$  and  $V(t)$  are the instantaneous flow and the volume of the carrier respectively) and  $C(t) = dm/dV$  ( $m$

<sup>2</sup>This is true only if we assume that there is no regurgitation (valve insufficiency), otherwise  $SV \neq V_{ed} - V_{es}$ .

<sup>3</sup>There are several formulas to determine the BSA based on the weight and the height of the patient. One of the most common is the Dubois and Dubois formula (1917), which estimates the BSA as  $BSA(cm^2) = 71.84 \cdot weight^{0.425} \cdot height^{0.725}$ , where weight and height are given in kg and cm respectively.

and  $C(t)$  are the mass of the tracer and its concentration at time  $t$  respectively), a differential equation as given in Eq. (2.2) can be derived. The blood flow is usually measured in liters per minute.

$$\Phi(t) = \frac{dV(t)}{dt} = \frac{1}{C(t)} \frac{dm}{dt} \quad (2.2)$$

Two main applications of Eq. (2.2) are used depending on the tracer infusion technique [19–22].

- Continuous tracer infusion, when the tracer is continuously injected into the body during all the measurement process.
- Rapid tracer injection, when the infusion is performed by a fast injection of a small dose (bolus) of tracer.

Both of them, together with their main applications, are explained in this section.

### Indicator dilution techniques that use a continuous tracer infusion

As these techniques use the injection of a large amount of contrast, the adopted contrast must be absolutely inert, harmless, and non-toxic. There are at least two tracers that fulfill these requirements: oxygen, which is used in the *Fick technique* (Fick, 1870), and heat, which is used in the continuous *thermodilution technique* (Fegler, 1954 [23]).

#### *Fick technique*

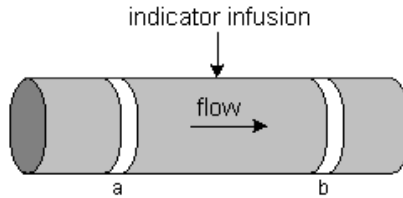


**Figure 2.3:** Scheme of a continuous injection method.

Two sites for the indicator concentration measurement (see Fig. (2.3)) are fixed: the first site  $a$  is located before the injection point while the second one  $b$  is located after it. Thus, assuming constant concentrations of the tracer  $C_a$  and  $C_b$ , steady flow  $\Phi_a = \Phi_b = dV/dt$ , and using Eq. (2.2), Eq. (2.3) can be derived.

$$C_b - C_a = \left( \frac{dm_b}{dt} \right) \left( \frac{dV_b}{dt} \right) - \left( \frac{dm_a}{dt} \right) \left( \frac{dV_a}{dt} \right) = \frac{d(m_b - m_a)}{dt} \Phi \quad (2.3)$$



Since  $d(m_b - m_a)/dt$  represents the tracer injection  $dm/dt$  between the sampling points, Eq. (2.3) can be expressed as given in Eq. (2.4), which is the basic equation of the Fick method.

$$\Phi = \frac{\frac{dm}{dt}}{C_b - C_a} \quad (2.4)$$

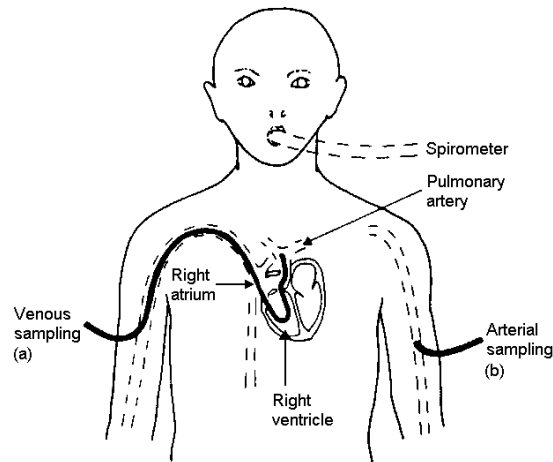


**Figure 2.4:** Fick method set-up.

The “trick” of the method (see Fig. (2.4)) is that the injection is naturally made by the lungs, and  $C_a$  and  $C_b$  are respectively the venous and the arterial concentration of oxygen ( $O_2$ ). Since the concentration of  $O_2$  is different in the different venous returns, the sampling point  $a$  is placed in the pulmonary artery, after the venous blood has been mixed by the right ventricle. The blood samples of the so called “mixed venous blood” are drawn by a catheter inserted through the *jugular vein*<sup>4</sup> (or the *subclavian vein*<sup>5</sup>) across the right atrium and ventricle up to the pulmonary artery. Then the blood samples are analyzed by a *gas analyzer* device for the measurement of the  $O_2$  concentration. The choice for the arterial sampling site is not critical, since the blood from the lung capillaries is well mixed. An arm or a leg artery is usually used.

The measurement of the injected tracer (i.e., the breathed oxygen) is performed by making the patient breath pure oxygen from a *spirometer* [24]. The exhaled  $CO_2$  is absorbed by a soda-lime absorber, so that the oxygen injection rate  $dm/dt$  (or

<sup>4</sup>The jugular vein carries blood from the brain to the superior vena cava and then into the right atrium.

<sup>5</sup>The subclavian vein carries blood from the arm to the superior vena cava and then into the right atrium.

consumption) can be directly measured by the net gas-flow. This method had been considered as the standard technique until the thermodilution replaced it.

#### *Warm (continuous) thermodilution technique*

Like oxygen, heat is non-toxic and naturally cleared. Therefore, it is a perfect indicator to perform a continuous infusion technique. Heat may also be dissipated through the walls of the blood vessels between the injection and the sampling site, therefore, this distance should be as short as possible. Unfortunately, in order to have an adequate mixing this distance should be long. The compromise that is usually adopted consists of the indicator infusion in the RA and its sampling in the PA.

Actually, for continuous infusion, it is not practical to inject heated or cool saline. Therefore, in the continuous infusion, heat is provided by an electric heater (resistor) and the temperature, which determines the concentration of the tracer (heat), is measured by a *thermistor*<sup>6</sup>. Eq. (2.4) can still be applied. The term  $dm/dt$  is given by the heat  $\dot{q}$  (expressed in *Watt*), and the term  $C_b - C_a$  is given by the temperature difference  $T_b - T_a$  (expressed in *Kelvin*) times the specific heat of the blood  $c_b$  (expressed in  $J \cdot kg^{-1} \cdot K^{-1}$ ) times the density of the blood  $\rho_b$  (expressed in  $kg \cdot m^{-3}$ ). In conclusion, the formulation of Eq. (2.4) for the thermodilution technique is given as in Eq. (2.5).

$$\Phi = \frac{\dot{q}}{c_b \rho_b (T_b - T_a)} \quad (2.5)$$

The mass of the tracer is now expressed by the amount of supplied energy (in Joule) and its concentration is given in  $J \cdot m^{-3}$  by the term  $c_b \rho_b T$ . The thermistors are usually placed in a *Wheatstone* configuration [19, 25]. This technique has become very common in the clinical practice and everything is integrated in one single catheter.

The main problem is related to the use of the catheter. This catheter, which is referred to as *Swan-Ganz catheter* from the name of the inventors in 1970 [26], includes not only the circuitry for the thermistor, but also the cable for the heating coil (resistor). Unfortunately, according to several statistical studies [27, 28], the Swan-Ganz catheterization increases the risk of death in ill patients.

The advantage of these continuous methods is the possibility of a continuous monitoring of the CO. However, several techniques based on different applications of Eq. (2.2) make use of a single tracer-bolus injection.

#### **Indicator dilution techniques that use a rapid injection of the tracer**

The field of the rapid injection techniques is really vast and under continuous development [1, 6, 8, 10, 11, 13, 29–32]. This is due to the fact that the constraints about

<sup>6</sup>A thermistor is a semiconductor thermometer, which uses the relation between temperature and material resistivity for the temperature measurement [19, 25].

the nature of the tracer are less strict, since only a bolus of indicator is injected. Invasive techniques, similar to the warm thermodilution, are commonly used, but more advanced developments are leading towards non-invasive applications. After an overview of the basic principles of these methods, the standard techniques that are commonly adopted in the clinical practice are presented.

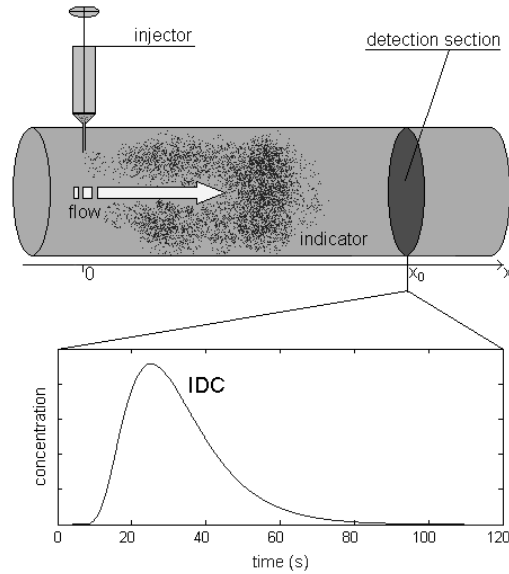


**Figure 2.5:** Measurement of the tracer concentration versus time (IDC) in an infinite tube model. The indicator is injected at distance 0 and detected at distance  $x_0$  from the origin.

Eq. (2.2) is now considered from a different perspective.  $C(t)$  is not constant anymore. In practice, as shown in Fig. (2.5), the indicator is rapidly injected into a fluid dynamic system where a carrier fluid (in our specific case blood) is flowing, and the indicator concentration-time curve  $C(t)$  is measured at the sampling site.  $C(t)$  is referred to as *Indicator Dilution Curve* (IDC). Essential requirement is that the indicator mixes completely with the carrier. The IDC contains all the information to estimate the flow, whose value is derived from Eq. (2.2) by an integration over time as shown in Eq. (2.6). The flow is assumed to be constant, so that  $\Phi$  can be moved out of the integration. The resulting formula, referred to as *Stewart-Hamilton equation* [33,34], gives the measurement of the mean flow  $\Phi$ .

$$\int_0^{\infty} \Phi C(t) dt = \Phi \int_0^{\infty} C(t) dt = \int_0^{\infty} \frac{dm}{dt} dt = m \implies \Phi = \frac{m}{\int_0^{\infty} C(t) dt} \quad (2.6)$$

Eq. (2.6) shows that the injection and subsequent detection of an indicator allows the measurement of flow.

The calculation of the integral in Eq. (2.6) is not trivial. Since the circulatory system is a closed system, there is the problem of the recirculation of the contrast. As a consequence, the tail of the IDC is masked by the rises due to the contrast recirculation (see Fig. (2.6)). In addition, the IDC is often very noisy. Therefore, a model is necessary to fit the IDC and calculate its integral (see section 4.2).

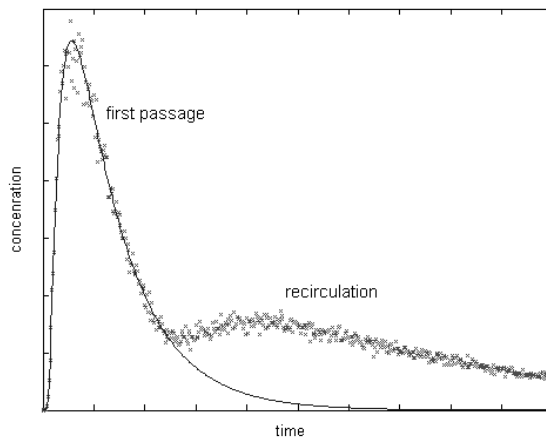


**Figure 2.6:** *The continuous line shows the theoretical IDC (first passage of the indicator) while the dots represent the measured IDC. The second rise due to the recirculation and the noise due to the measurement system are evident.*

All the IDC methods are based on the following assumptions [22, 35], which are also cause of measurement errors.

- The blood flow is constant during the measurement (about one minute).
- There is an instantaneous and uniform mixing of the tracer.
- The injection is so fast to be modelled by a dirac impulse.
- The loss of indicator is either absent or known.

The use of different indicators leads to different sensors and techniques. The most common techniques are the cold thermodilution, the dye dilution, and the lithium dilution [19–21].

### Cold thermodilution

The cold thermodilution was first introduced by Fegler in 1954 [36]. The indicator is either cold *dextrose* or *saline* (blood-isotonic solution). As shown in Fig. (2.7), a Swan-Ganz catheter is inserted via a central vein (usually the internal jugular or subclavian) through the right atrium and ventricle so that its tip lies in the pulmonary artery [26, 27]. It is carried in the right position by the dragging force of the flowing blood thanks to a doughnut-shaped air-filled balloon on the tip of the catheter. The cold solution is injected rapidly through a port of the catheter that ends at a side hole in the right atrium. The cold solution mixes with blood in the right atrium and ventricle before passing into the pulmonary artery, where the temperature decrease is sensed by a thermistor on the side of the catheter. The CO is then calculated from the *temperature-time curve*.

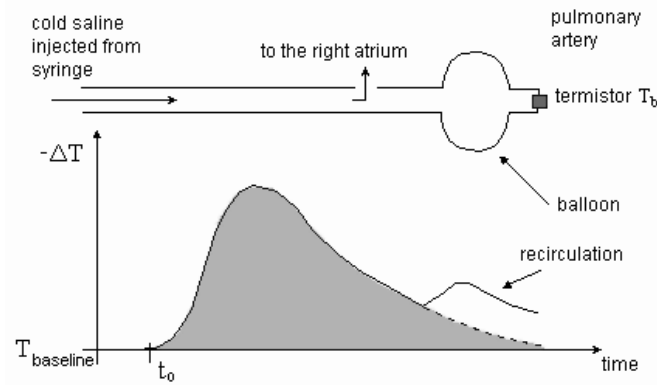


**Figure 2.7:** Swan-Ganz catheter for cold thermodilution. The IDC is measured by the temperature fall.

With the same interpretation of heat and temperature that is used in Eq. (2.5), Eq. (2.6) can be written as in Eq. (2.7), where  $q$  is the total injected heat expressed in Joule and  $\Delta T$  is the temperature fall expressed in Kelvin ( $c_b$  and  $\rho_b$  are the same as in Eq. (2.5)).

$$\Phi = \frac{q}{c_b \rho_b \int_{t_0}^{\infty} -\Delta T(t) dt} \quad (2.7)$$

### Dye dilution

Also a colored dye such as indocyanine green<sup>7</sup>, usually referred to as *cardio-green*, meets all the necessary requirements of a “good” indicator: it is inert, harm-

<sup>7</sup>Also other dye indicators are used, such as Evans Blue (absorption peak at 640nm and 50% loss in 5 days) and Coomassie Blue (absorption peak around 590nm and 50% loss in 15-20 minutes).

less, measurable, and economic. Using the principle of *absorption photometry*, the concentration of cardiogreen, which is usually injected into the pulmonary artery, can be detected by the light absorption peak at the wave-length of 805nm.

In the past, blood samples had to be drawn by a catheter placed in the femoral or brachial artery and analyzed by an external photometry device. Nowadays, the use of optical fibers allows in-situ measurements.

About 50% of the dye is excreted by the kidneys in the first 10 minutes, so that repeated measurements are possible too. Once the system is calibrated, meaning that the peak absorption is related to the concentration  $C(t)$  of the dye, the flow is directly given by Eq. (2.6).

### *Lithium dilution*

Lithium is a fluid that can be injected and detected by a specific sensor [37–40]. The sensor consists of a lithium-selective electrode in a flow-through cell. Two Ag-AgCl electrodes measure the potential across a lithium selective membrane. According to the Nernst equation [19], the electric potential  $E$  (Volt) across a membrane is given as in Eq. (2.8), where  $C_{ext}$  and  $C_{int}$  are the external and the internal (with respect to the membrane) lithium activities, which correspond to the lithium ionic concentrations,  $R$  is the gas constant ( $8.314 J \cdot mol^{-1} \cdot K^{-1}$ ),  $T$  is the absolute temperature (Kelvin),  $F$  is the Faraday constant ( $96485 C \cdot mol^{-1}$ ), and  $n$  is the valence of the ions, which for lithium ions ( $Li^+$ ) is 1.

$$E = \frac{RT \ln(C_{ext})}{nF \ln(C_{int})} \quad (2.8)$$

As a result, the transducer measures a voltage that is logarithmically related to the lithium concentration. The sensor is connected to a three-way tap on the arterial line and a small peristaltic pump draws blood with a flow of 4.5ml/min.

After calibration, the lithium concentration is determined and a lithium IDC generated. The time integral of the measured IDC is used as given in Eq. (2.6) for the CO assessment. Moreover, based on the IDC CO measurement and the establishment of the relation pressure-volume (compliance), a continuous CO monitoring is performed too .

### 2.1.2 Angiography

*Angiography* is an investigation that makes use of either *x-rays* or *radionuclides*. Although a contrast is injected, typical applications do not include the measurement of an IDC. The detection of the contrast allows the application of bi- and tri-dimensional image analysis techniques in order to estimate the EF and the volumes of the cardiac chambers. Thus, the CO can be estimated by Eq. (2.1) once the PR is known.

The use of x-rays or radioactive substances may be a serious contraindication to the use of these methods. In fact, the interaction at the level of cellular nuclei due to x- and  $\gamma$ -radiations does not permit to classify these methods as “inert”, and specific safety precautions are required. In the two following sections both techniques are briefly explained [21, 24, 41, 42].

### Radionuclide techniques

In the radionuclide angiography a small amount of radioisotopes, normally indicated as radiopharmaceuticals, is peripherally injected. The radioactive decay of radioisotopes leads to the emission of  $\alpha$  and  $\beta$  particles as well as  $\gamma$ - and x-radiation. Hence, the detection of the indicator is performed by radioactivity measurements. It is performed by a scintillation camera (Anger 1959), usually referred to as *gamma-camera*. The gamma-camera is a photon counter (minimal photon energy  $\simeq 50\text{keV}$ )<sup>8</sup>. It consists of a scintillator crystal (NaI or NaTI) that covers a matrix of photomultiplier tubes. Only  $\gamma$ - or x-radiation can be detected with detectors that are external to the body. The information detected and recorded by these scanners is analyzed and processed to generate images of the target anatomical structures.

The emission tomography systems are divided in two main groups, depending on the type of radiation emitted by the adopted radiopharmaceutical.

- The *Single Photon Emission Computed Tomography* (SPECT) system makes use of routine single photon gamma emitters such as <sup>99m</sup>Tc, <sup>131</sup>I, <sup>123</sup>I, <sup>67</sup>Ga, and <sup>201</sup>Tl. It is generally designed to collect data from different angles.
- The *Positron Emission Tomography* (PET) system detects annihilation radiation from positron emitters such as <sup>11</sup>C, <sup>13</sup>N, <sup>15</sup>O, <sup>18</sup>F, and <sup>68</sup>Ga. It consists of two or more opposed detectors that permit the detection of the two 511keV gamma photons that are emitted simultaneously in opposite directions by the annihilation process. Therefore, the line that intercept the emission point can be determined.

The most advanced radionuclide technique in order to estimate EF and then CO is the *Multi-Gate* imaging (MUGA, also known as *ventriculogram*), where the gamma-camera takes more images (about 60) triggered by the ECG signal.

The measurement of an IDC is also feasible. In fact, since the images represent the concentration of the radiopharmaceuticals, it is always possible to fix a Region Of

<sup>8</sup>1eV is the energy acquired by an electron ( $1.602 \times 10^{-19}$  C) when inserted in an electrical field of 1 Volt. Hence,  $1\text{eV} = 1.602 \times 10^{-19}$  J. For instance, in case of x-radiation, we can calculate the energy by the formula  $E = \hbar \frac{c}{\lambda}$ , with  $c$  equal to the light speed,  $\lambda$  equal to the radiation wave-length and  $\hbar$  equal to the Planck's constant ( $6.626 \times 10^{-34}$  Js). The average wave-length of the x-radiation is  $10^{-1}$  nm resulting with an energy  $E = \frac{6.626 \cdot 10^{-34} \text{Js} \cdot 3 \cdot 10^8 \text{ms}^{-1}}{10^{-10} \text{m} \cdot 1.602 \cdot 10^{-19} \text{eV}^{-1} \text{J}} = 12.5 \text{keV}$ .

Interest (ROI) and record an IDC based, for instance, on the average video-intensity in the ROI. Therefore, the flow can be estimated by Eq. (2.6).

Since radionuclides cannot be considered as inert, patients in special condition, such as for instance women who are pregnant or breast-feeding, are not allowed to undergo nuclear imaging.

### X-ray techniques

The x-ray angiography is the standard technique to diagnose blood-vessel *stenosis* and *aneurysm*<sup>9</sup>, but it can be also adopted to estimate cardiac volumes and CO.

A standard angiography procedure requires the insertion of a catheter through the femoral artery up to the heart. The injection of a radiopaque is performed through this catheter. A radiopaque is a substance that absorbs x-radiation (e.g., Iodine). As a consequence, the blood mixed with the radiopaque absorbs the x-rays and is detected by the x-ray scanner.

The x-ray scanner is used in *fluoroscopy-mode*<sup>10</sup>, so that a continuous monitoring can be performed. The accuracy of volumes and CO (based on Eq. (2.1)) is improved by the employment of tri-dimensional imaging techniques. The technology that allows a tri-dimensional image reconstruction is the *Computerized Axial Tomography* (CAT). It is based on the Radon transform (Johann Radon, 1917) of multiple x-ray projections [41, 43].

As for radionuclides techniques, since the whole procedure takes about 30 minutes, the *dose*<sup>11</sup> of x-rays absorbed by the patient should be seriously considered.

### 2.1.3 Magnetic resonance imaging

The *Magnetic Resonance Imaging* (MRI) [41, 44] is a tri-dimensional imaging technique used to produce high quality images of the inside of the human body. MRI is based on the principles of *Nuclear Magnetic Resonance* (NMR), a spectroscopic technique that allows the distinction between different biological tissues depending on the hydrogen concentration.

---

<sup>9</sup>Stenosis is an abnormal narrowing of an artery or vein (it can be also referred to the cardiac valves) while aneurysm is an abnormal widening of it.

<sup>10</sup>That means that it makes use of a BI (*Brightness Intensifier*) or, in the near future, of flat panels made by the TFT (Thin-Film Transistors) technology, for real-time imaging.

<sup>11</sup>*Dose* is the energy that is absorbed per unit mass of material invested by x-rays. In the International System it is measured in Gray [Gy],  $1\text{Gy}=1\text{Jkg}^{-1}$ . In case of biological tissues it is measured by the *equivalent dose*, expressed in Sievert [Sv]. The equivalent dose takes into account many factors that determine the biological interaction. The limit dose for common people is 1.7 mSv/year, while the dose given by a fluoroscopy is about  $1\text{cGy} \simeq 1\text{mSv}$  [24].



The patients are introduced inside a tunnel where a constant<sup>12</sup> magnetic field (up to 3 Tesla) is combined with a radiofrequency-alternate one. The radiofrequency magnetic field produces the rotation of the hydrogen dipoles. The subsequent *relaxation* of the dipoles is detected and analyzed to distinguish among different tissues. The system is usually considered to be harmless and shows high contrast images. In general, no indicator is needed since the tissues are already recognized<sup>13</sup>.

The blood flow can be measured either by Eq. (2.1), after estimating the stroke volume, or by the phase-shift measurement of the relaxation signal coming from the blood (the principle is similar to the pulsed Doppler one, see section 2.1.4)

The presence of the tunnel has always represented a problem due to claustrophobic panic attacks, but new developments in the generation of magnetic fields might overcome the problem. New “C-shaped” MRI devices are becoming commercially available.

A disadvantage of MRI is the limited applicability due to the generation of powerful magnetic fields. Any metallic instrument is absolutely forbidden near the MRI scanner, and electronic devices without an appropriate magnetic insulation do not work. As a result, the scanner cannot be used in operating rooms and intensive care units. Furthermore, due to the time required for performing the analysis (mainly due to the preparation of the patient), it does not suit emergency routines. The high costs should be considered too.

#### 2.1.4 Ultrasound flowmeter

The ultrasound flowmeter, referred to as *echo-Doppler* [19, 20, 46], is a non-invasive device for the instantaneous blood flow measurement. It is one of the several *Modes* performed by a typical ultrasound echo-machine (see section 3.1). Actually, it performs only the measurement of the instantaneous blood velocity; for the estimation of the CO, the integral blood velocity, which is the integral of instantaneous blood flow velocities during one cardiac cycle, is measured in the left ventricular outflow tract (other sites can be used) and multiplied times the cross-sectional area and the PR [46]. The cross-sectional area is measured by the ultrasound-scanner in B-Mode (see section 3.1).

The ultrasound flowmeter is based on the principle of the *Doppler effect* (see Fig. (2.8)) and it is commonly used in the clinical practice.

A transmitter ( $T$ ) and a receiver ( $R$ ) are integrated in the same probe. The focus-depth, where the blood velocity is measured, is given by the angle  $\beta$ , which depends on the structure of the transducer and can be varied. The transducer transmits ultrasound pressure-waves with frequency  $f_t$ . If  $c$  is the propagation velocity of ultrasound

<sup>12</sup>Actually it is not constant, there is a gradient that is used for the reconstruction of the image.

<sup>13</sup>However, the perfusion of special contrast agents, such as gadolinium, is also performed [31, 45].

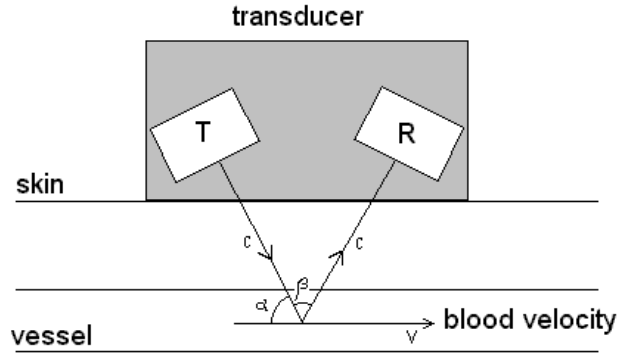


**Figure 2.8:** Scheme of the echo-Doppler principle.

(in water, main component of the human body, it is  $1480\text{ms}^{-1}$ ) and  $v$  is the blood velocity, the blood particles receive the signal with a frequency equal to  $f_t \left(1 - \frac{v \cos \alpha}{c}\right)$  and the receiver  $R$  receives the signal reflected by the blood particles with a frequency  $f_r$  given as in Eq. (2.9).

$$f_r = f_t \left( \frac{c - v \cos \alpha}{c} \right) \left( \frac{c}{c + v \cos(\alpha + \beta)} \right) = f_t \left( \frac{c - v \cos \alpha}{c + v \cos(\alpha + \beta)} \right) \quad (2.9)$$

The frequency shift  $\Delta f = f_t - f_r$ , known as the *Doppler frequency* (frequency of the Doppler signal), is given as in Eq. (2.10).

$$\Delta f = f_t \left( 1 - \frac{c - v \cos \alpha}{c + v \cos(\alpha + \beta)} \right) \simeq v \left( \frac{2f_t}{c} \right) \cos \alpha \quad \text{for small } \beta \text{ and } v \ll c \quad (2.10)$$

Hence, since  $f_t$  and  $c$  are known, the Doppler frequency  $\Delta f$  is linearly related to the blood velocity. For instance, with blood velocity  $v$  of  $1\text{ms}^{-1}$ , the typical  $f_t$  of  $5\text{MHz}$ , and  $\alpha = 45^\circ$ , we obtain  $\Delta f \simeq 5\text{kHz}$ . It is within the human audibility range; that is the reason why the user interface is very often a loud-speaker. An alternative way is to apply the Fast Fourier Transform (FFT) to the Doppler signal for the spectrum estimation.

In the most common implementation of the system,  $\Delta f$  is the frequency of the output signal obtained by multiplication (mixer) of the transmitted and received signals followed by low-pass filtering<sup>14</sup>. The result is the determination of the velocity

<sup>14</sup>Suppose that  $S_t = A_T \cos(2\pi f_t t)$  is the transmitted signal and  $S_r = A_R \cos(2\pi f_r t)$  is the received one. Then the mixer multiplies  $S_t$  times  $S_r$  obtaining  $S_t \cdot S_r = \frac{A_T A_R}{2} [\cos(2\pi (f_t - f_r)t) + \cos(2\pi (f_t + f_r)t)]$ . Finally, by low-pass filtering, the high frequency component  $(f_t + f_r)$  is removed and the remaining part represents the Doppler signal with frequency  $\Delta f = (f_t - f_r)$ .

without any knowledge of the flow direction. However, some methods have been developed and implemented in the ultrasound scanners to distinguish between motion toward and motion away from the transducer<sup>15</sup>.

The described system is the simplest application of the Doppler-effect for blood velocity estimation and it is referred to as continuous wave (CW) or narrow-band Doppler. The main disadvantage of such a technique is the difficulty to distinguish between different moving targets.

This problem is overcome by more advanced systems, referred to as pulsed wave (PW) or wide-band Doppler [46, 48]. The same elements of the transducer are used as transmitter and receiver and a train of bursts is transmitted and received back. As a consequence it is possible to determine the position of the targets depending on the delays of the echoes as in the M- and B-Mode approaches (see section 3.1). To achieve a good spatial resolution, the transmitted pulse duration should be very short. On the other hand, the achievement of a good frequency resolution, which leads to a good velocity resolution, requires the use of long bursts (think of a windowed Fourier transform). The usual compromise is a 5MHz (carrier frequency) burst of  $1\mu\text{s}$  duration (5 cycles).

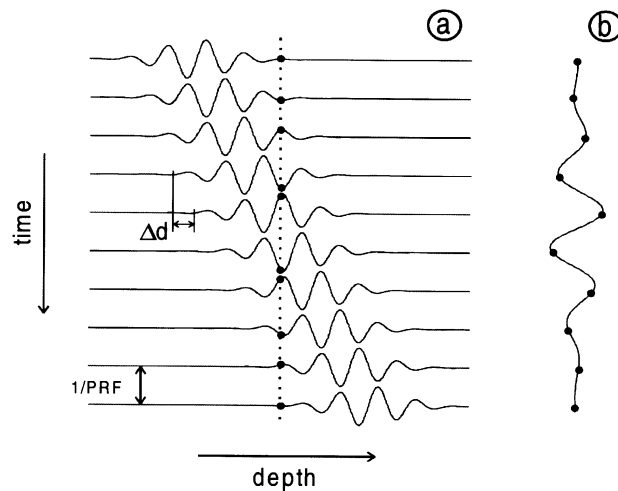


**Figure 2.9:** Pulsed Doppler example. In (a) it is shown the transmitted train of bursts while in (b) it is shown the sampled Doppler signal.

Fig. (2.9) shows the principles of the PW-Doppler assuming  $\alpha = 0$ . In (a) it is shown a train of pulses (bursts) reflected by a particle (blood cell) that is moving

<sup>15</sup>Among the processing methods that have been developed in order to distinguish the velocity direction, commonly used are the Single-Sideband Detection, the Heterodyne Detection, and the Quadrature Phase Detection [47].

away from the transducer (increasing depth) with a velocity equal to  $\Delta d \cdot (\text{PRF})/2$ , where PRF stands for *Pulse Repetition Frequency*. The motion of the particle makes the echo of each pulse relatively delayed by  $\Delta d$ . In (b) it is shown the Doppler signal with frequency  $\Delta f$ , which is sampled with a frequency equal to the PRF, since the transmitting and receiving circuits are synchronized (they are applied to the same crystals). A simple explanation of the relation between the signal of frequency  $f_b$  obtained in (b) and the Doppler signal is the following. The pulse is a spacial wave of length  $\lambda = c/f_t$ , where  $f_t$  is the carrier frequency. If this wave is received with a velocity equal to  $2v$ , then the resulting frequency at the receiver is  $f_b = 2v/\lambda = 2vf_t/c$ , which is the same expression of  $\Delta f$  as given in Eq. (2.10) if  $\alpha = 0$ . This is an interpretation of the discrete system that is described in Fig. (2.9) in the continuous domain<sup>16</sup>. To consider the general case  $\alpha \neq 0$ , it is necessary to project the blood velocity  $\vec{v}$  on the direction of the ultrasound propagation velocity (direction of  $\vec{c}$ ), i.e.,  $v = |\vec{v}| \cos(\alpha)$  (refer to Fig. (2.8) with  $\beta = 0$ ).

A new burst is not transmitted until the reflection from the deepest layer is received back. Hence, the maximum PRF (pulse repetition frequency) equals  $c/2d$  (with  $d$  equal to the distance between the transducer and the deepest layer). The PRF represents also the sampling frequency applied to the Doppler signal, since the whole system has to be synchronized (see Fig. (2.9)). Therefore, the system must satisfy the Nyquist relation  $\text{PRF} > 2 \Delta f$ , which combined with Eq. (2.10) defines the maximum detectable velocity as given in Eq. (2.11), where  $f_t$  is now the carrier frequency within the single pulse.

$$v_{\max} = \text{PRF} \left( \frac{c}{4 f_t \cos \alpha} \right) = \frac{c^2}{8 f_t d \cos \alpha} \quad (2.11)$$

For shorter distance  $d$ , and consequently greater PRF, the maximum detectable velocity is higher. When the blood velocity is higher than  $v_{\max}$ , the aliasing error occurs and the signal interpretation fails. In new machines it is usually implemented a routine to control and handle these errors in order to avoid a wrong diagnosis.

The advantage of this technique is the determination of the blood *velocity profile*. The delay between transmission and reception of a single burst is a direct indication of the distance where it has been reflected. Therefore, if the receiver decomposes the detected echoes into different time-windows (referred to as gates, usually between 6 and 32), each window selects the part of the echoes reflected from a specific depth interval. The received bursts can be processed concurrently in different channels

<sup>16</sup>The same principles can be viewed under a different perspective. Instead of focusing on the Doppler frequency, the *phase shift* ( $\varphi$ ) could be directly considered and evaluated by a *cross-correlation* between the received pulses and the transmitted ones. Once the phase shift is estimated, the blood velocity is given as  $v = \text{PRF} \cdot \frac{\Delta d}{2} = \text{PRF} \cdot \left( \frac{\varphi c}{4\pi f_t} \right)$ , since the distance  $\Delta d/2$  that is covered by the blood particle during the time period between two pulses ( $1/\text{PRF}$ ) is determined by the phase shift ( $\varphi$ ) (Fig. (2.9)).

according to the time-window. The velocity profile is obtained by simply combining the output from each channel. This technique is referred to as *Multi-Gate Pulsed Doppler*.

Both continuous and pulsed Doppler present the problem of the *clutter* noise. It is introduced by the slow motion of the tissues, which add low-frequency components to the Doppler signal. For instance, the slow expansion and contraction of the vessel walls<sup>17</sup>. In order to remove the clutter noise, a high-pass filter is implemented in every system.

Up to now a substantial problem of the method has been neglected. The measured blood velocity depends on the angle  $\alpha$  between the transducer axis and the blood flow. This angle is often unknown or just estimated, therefore, a substantial uncertainty is introduced into the measurement. The only medical application where  $\alpha$  can be approximately estimated is the measurement of a laminar flow in a straight vessel. The angle is estimated from the corresponding image of the longitudinal cross-section of the blood-vessel. However, some methods are being developed to integrate in the system a more accurate and fast estimation of the angle  $\alpha$ . One of them is for instance the modelled evaluation of the axial and lateral components of the velocity [49].

Some devices combine the Doppler-Mode with the B-Mode in order to show the velocity profile with a color mapping scheme applied to the output image (*color flow imaging*). A special scanner, referred to as *duplex scanner*, which combines the technology required by both PW-Doppler and B-Mode analysis is needed.

Nowadays the measurement of CO by ultrasound echo-Doppler is performed also with transesophageal probes (see section 3.4), resulting in measurements whose correlation coefficient with the standard cold thermodilution is about 0.9 [50–59].

**Remark** *The echo-Doppler principle for blood velocity measurements is not only applied by means of ultrasound devices. Laser Doppler equipments are also available, but they can detect only the peripheral blood perfusion [21, 60].*

### 2.1.5 Magnetic flowmeter

The magnetic flowmeter [19, 21] is based on the *Faraday's law of induction* [61]. If a conductor (e.g., a copper wire) of length  $L$  is moving with velocity  $\vec{v}$  perpendicular to a magnetic field of flux density  $\vec{B}$  (Tesla), then the induced *Electro-Motive Force* (EMF) across the ends of the conductor is given as in Eq. (2.12).

$$\text{EMF} = \int_L \vec{v} \times \vec{B} \cdot d\vec{l} = BLv \quad (2.12)$$

<sup>17</sup>The blood vessels are elastic, for this reason they move slightly following the pressure waves produced by the pumping action of the heart. This elasticity, referred to as compliance, introduces a low-pass filter action in the circulatory system, which results in a more continuous blood flow.

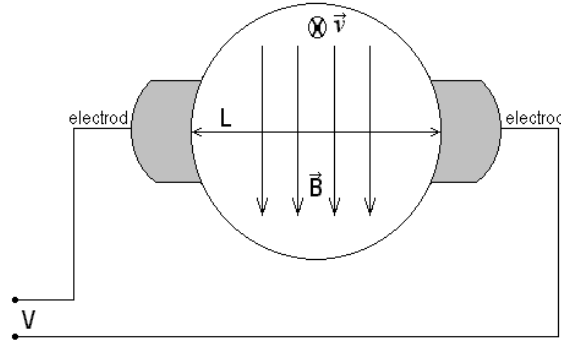


*Figure 2.10: Scheme (section) of a magnetic flowmeter surrounding the walls of a vessel.*

Instead of the conductor (copper wire), the flowmeter depends on the movement of blood, whose conductance is similar to that of saline. The application of the Faraday's law to a magnetic flowmeter is given in Fig. (2.10), where the section of a blood vessel with two applied electrodes is shown. The magnetic field  $\vec{B}$ , the direction of movement of the electrical conductor (blood velocity  $\vec{v}$ ), and the line  $L$  between the electrodes (vessel diameter) are all perpendicular to each other, so that Eq. (2.12) is still valid. There is a linear relation between the induced EMF and the blood velocity. Since  $L$  is known, the relation between blood flow  $\Phi = v\pi L^2/4$  and induced EMF is derived from Eq. (2.12) and given as in Eq. (2.13).

$$\Phi = (\text{EMF}) \cdot \left( \frac{\pi L}{4B} \right) \quad (2.13)$$

If the ends of the conductor are connected to an external circuit, the induced EMF causes a current of intensity  $I$  that can be processed suitably (e.g., by a galvanometer) for the assessment of the flow rate. The resistance of the moving conductor (blood along the line  $L$ ) can be represented by  $R$  to give the terminal voltage  $V_t = (\text{EMF}) - RI$ . Thus, the system has to be calibrated with the estimated  $R$ .

This simple solution, which makes use of a constant magnetic field  $\vec{B}$ , is influenced by several errors, mainly recognized as polarization of the electrodes, random voltage drift (mainly due to the amplifier), and appearance of the harmonic components of the ECG signal, very similar to the harmonic components of the flow. Drift and polarization are solved by the use of an alternate magnetic field, but this introduces a new source of noise. In fact, the alternate magnetic field generates by induction an alternate EMF<sup>18</sup> in the circuit of the electrodes. A common solution to

<sup>18</sup>EMF =  $-\frac{\partial \Phi_m}{\partial t}$ , where  $\Phi_m$  is the magnetic flux concatenated with the circuit.

this problem is the use of a quadrature filter in order to remove the undesired components.

In practice the system has two different applications. The first one makes use of a toroidal structure of the transducer and has to be applied by surgery operation around the blood vessel. The second one makes use of a catheter-tip probe. The probe can be inserted through the femoral artery up to the root of the aorta in order to measure the CO.

In mechanical applications (e.g., in-vitro measurements) the accuracy of the measurement can reach 0.25% [21], but in clinical (in-vivo) applications it is often difficult to obtain correct measurements, since all the perpendicularities as well as the estimation of the vessel diameter are influenced by several errors. Furthermore, using the catheter-tip probe, the transducer has to be perfectly centered in middle of the vessel.

### 2.1.6 Impedance plethysmography

The bio-impedance method has the advantages of providing continuous CO measurement at no risk to the patient [20, 21, 62]. A small current at the frequency of 20kHz to 100kHz is passed through the thorax from a couple of electrodes while another couple of sensing electrodes are used to measure the changes in impedance within the thorax by using a high impedance galvanometer.

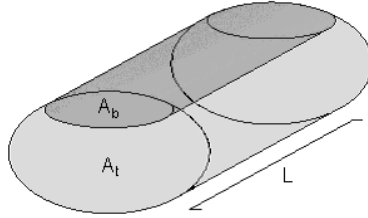


**Figure 2.11:** Cylindrical model for thorax tissue and blood impedance.  $A_t$  and  $A_b$  are the tissue and blood sections while  $L$  is the cylinder length.

A simplified model can be used to describe the thorax as a double cylinder made of tissue and blood, as shown in Fig. (2.11). As a consequence, the total thorax impedance  $Z$  is given by the parallel of the blood and tissue impedances  $Z_b$  and  $Z_t$ . If  $Z$  is differentiated with respect to  $Z_b$ , the resulting differential equation is given as in Eq. (2.14).

$$\frac{dZ}{dZ_b} = \frac{d}{dZ_b} \left( \frac{Z_t Z_b}{Z_t + Z_b} \right) = \left( \frac{Z}{Z_b} \right)^2 \quad (2.14)$$

The biological impedance is in general represented by a complex number (especially the skin impedance), however, the blood impedance is mainly resistive and  $Z_b$  can be represented by a real number. From the model in Fig. (2.11)  $Z_b = \rho_b L A_b^{-1}$ , where  $\rho_b$  is the blood resistivity (usually about  $150 \Omega \cdot cm$ ),  $A_b$  is the cross-section of the blood compartment and  $L$  is the cylinder length. By differentiating the blood volume  $V_b = L \cdot A_b = (\rho_b L^2 / Z_b)$  with respect to  $Z_b$  and substituting  $Z_b$  with  $Z$  as from Eq. (2.14), Eq. (2.15) can be derived.

$$dV_b = d(A_b L) = - \left( \frac{\rho_b L^2}{Z^2} \right) dZ \quad (2.15)$$

Eq. (2.15) relates the blood volume variations to the total impedance variations, so that blood volumes can be measured by means of electrical impedance measurements. The contraction of the ventricles produces a cyclical change in transthoracic impedance of about 0.5%. These changes are exploited by a specific equation, which is referred to as *Kubicek equation* (1966), to assess the SV. Some assumptions are made concerning the relationship between SV and net change in the thorax blood volume. The impedance is assumed to mainly depend on the blood volume in the lungs. Moreover, it is assumed that no blood leaves the lungs during systole. As a consequence, the impedance would continuously decrease during systole. If the time derivative  $\dot{Z}$  of the impedance during systole is estimated, the first order approximation of the total impedance variation  $\Delta Z$  during the ejection time  $\tau_e$  is given as  $\Delta Z = \dot{Z} \tau_e$ . Combining this result with Eq. (2.15), the SV is given as in Eq. (2.16).

$$SV = -\rho_b \frac{\dot{Z} L^2 \tau_e}{Z^2} \quad (2.16)$$

Obviously, since the total impedance is complex, the measured total impedance  $Z$  is the module of the impedance and is a function of the adopted frequency. Eventually, once the SV is known, the CO can be derived by using Eq. (2.1). The accuracy of the method is limited by several factors [20, 63]. First of all, the model in Fig. (2.11) is a significant simplification of the real system. Moreover, the blood impedance depends on several factors, such as the fractional volume concentration of the blood cell as well as their shape and orientation. In addition to that, the effect of the blood flow is still unknown and the measurements are affected by respiratory artifacts too.



## 2.2 Ejection fraction

The measurement of the Ejection Fraction (EF) is a common clinical practice to evaluate the cardiac condition. In particular, it is a measure of the efficiency of the myocardial contraction. If the end-diastolic ( $V_{ed}$ ) and the end-systolic ( $V_{es}$ ) ventricular volumes are measured, the percent EF is defined as given in Eq. (2.17).

$$EF\% = \frac{V_{ed} - V_{es}}{V_{ed}} \cdot 100 \quad (2.17)$$

Possible approaches for the EF measurement is any clinical imaging technique that allows a geometric estimation of  $V_{ed}$  and  $V_{es}$ . They are mainly the MRI, ultrasound imaging, and nuclear imaging (see sections 2.1.2 and 2.1.3) [18, 46, 64–72]. The acquired images are analyzed by manual or automatic segmentation. Due to the complex geometry of the RV, usually only the LV EF can be estimated.

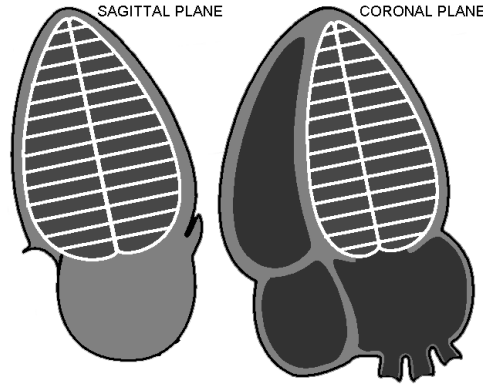


**Figure 2.12:** *The two cross-sectional planes used in the bi-plane method for the estimation of the LV volume. The volume is assumed to be represented by a stack of ellipses. The axes of each ellipses are determined by the lines that are perpendicular to the main axis. If only one plane is used, then the ventricular volume is modelled as a stack of circles and the perpendicular lines represent the circle diameters.*

When an ultrasound scanner is used, a fast method for EF measurements, which is referred to as *Teichholz* technique [73], makes use of the M-mode echocardiography (see section 3.1.2) and quantifies the EF based on the movement of the ventricular endocardium along one line [74]. More accurate estimates are usually derived from a LV bi-dimensional long-axis view, which provides information on a complete ventricular section [18, 46].

The employment of a geometrical model is necessary to transform a bi-dimensional contour into a three-dimensional one (volume). A simple model assumes the ventricle to be represented by a stack of circles along the main axis (long axis) [46,68]. If also the information on a second ventricular section is considered, the volume estimate can be derived from two perpendicular long axis planes (bi-plane method) [46,67,68,70]. This technique defines the ventricle as a stack of ellipses and adds one degree of freedom to the geometrical volume model. The result is an accurate interpolation of the ventricular endocardium [68]. However, none of these techniques, which are based on geometrical models, can detect abnormal shapes due to pathologic conditions (e.g. an aneurysm).

With MRI and advanced tri-dimensional ultrasound imaging, it is possible to measure the real contour for a series of short axes planes (normal to the long axis) [66,69]. As tri-dimensional echocardiography is relatively new, MRI is well established and considered as the gold standard technique for EF and ventricular volume estimates [18,67].

Unfortunately, geometric EF measurements are time consuming. The reliability of automatic border detection algorithms for echo images is sometimes very limited and cardiologists prefer a manual delineation of the cardiac contours. As a consequence, the EF assessment not only slows down dramatically the clinical practice, but also requires the employment of specialized personnel, such as radiologists or cardiologists. Also MRI, despite the better image quality, requires a long procedure both for patient scanning and for data analysis, so that it does not suit emergency routines. Moreover, patients that are claustrophobic or have an implanted pace-maker cannot be scanned.

Geometric EF estimates do not consider blood volume transfers. Some patients present a significant insufficiency of the mitral valve. In this case, the geometric EF is the sum of two undistinguished terms: the Forward EF (FEF), which is due to the blood volume that is ejected into the aorta, and the Regurgitant EF (REF), which is due to the blood volume that is ejected back into the LA due to mitral valve insufficiency<sup>19</sup>. If we refer to the SV as the volume of blood that is ejected from the LV into the aorta per cardiac cycle, then  $FEF = SV/V_{ed}$  and  $REF = (V_{ed} - V_{es} - SV)/V_{ed} = EF - FEF$ . Therefore, only the FEF is a real indicator of the cardiac efficiency and is related to SV and CO.

The FEF assessment can be performed by use of indicator dilution techniques [20,21,35]. A cold saline (thermodilution) or a dye (dye dilution) bolus is injected for the measurement [20,35]. The injected indicator bolus is detected either in the LV or in the aorta out-tract. The measurement is based on the detected indicator concentration and, therefore, is related to blood volume transfers. A mathematical interpretation of the measured IDC allows the FEF assessment [20].

---

<sup>19</sup>The same reasoning also regards aortic valve insufficiency.

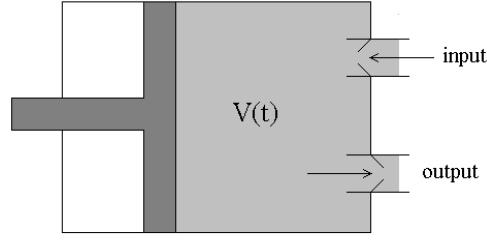


**Figure 2.13:** Mono-compartment cylinder-piston model for LV simulation. An input and an output valve are included and represent the mitral and aortic valve respectively.

A ventricle can be modelled as a mono-compartment system, whose volume changes as a periodic function of time. This can be represented by a cylinder-piston system as shown in Fig. (2.13). The system is filled with an incompressible fluid. Two valves are used for the fluid input and output and are driven by pressure variations. During diastole, the volume increases, the output valve is closed, and the input valve is open for the ventricle filling. During systole, the volume decreases, the input valve is closed, and the output valve is open for the ejection of the ventricular fluid.

If an indicator bolus is rapidly injected within a diastolic phase and the mixing is perfect, then the contrast concentration at the  $n^{\text{th}}$  end-diastolic phase is given by  $C_n$  and equals the indicator mass  $m$  in the ventricle divided by  $V_{ed}$ . During the following systole, part of the contrast mass ( $\Delta m$ ) is ejected out of the cylinder. The concentration  $C_{n+1}$  at the subsequent end-diastole is given as in Eq. (2.18).

$$C_{n+1} = \frac{m - \Delta m}{V_{ed}} = C_n \cdot \left( 1 - \frac{V_{ed} - V_{es}}{V_{ed}} \right) \quad (2.18)$$

Combining Eq. (2.17) and Eq. (2.18), the percent EF can be expressed in terms of  $C_n$  and  $C_{n+1}$  as given in Eq. (2.19).

$$\text{EF} = \left( 1 - \frac{C_{n+1}}{C_n} \right) \cdot 100 \quad (2.19)$$

The sampling timing of  $C_n$  and  $C_{n+1}$  is usually controlled by an electrocardiographic (ECG) trigger, so that the sampling rate is based on the cardiac electrical activity. Moreover, in order ensure that the indicator recirculation (see Fig. (2.6)) does not to influence the measurement, the samples  $C_n$  and  $C_{n+1}$  should be measured before the recirculation time.

The EF estimate in Eq. (2.19) only considers the fluid that is ejected through the output valve (aortic valve in the LV). If the input valve is insufficient, i.e., it

leaks, part of the contrast is ejected back through the input valve (mitral valve in the LV). However, this fraction of contrast comes again into the ventricle during the subsequent diastole and, therefore, does not contribute to  $\Delta m$ . As a consequence, the EF definition in Eq. (2.19) is better referred to as Forward EF (FEF)<sup>20</sup>.

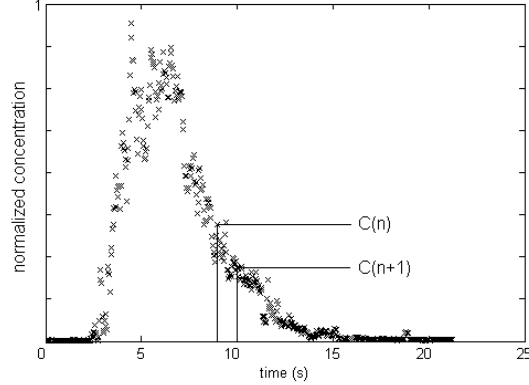


**Figure 2.14:** Example of noisy IDC measured by contrast echocardiography (see section 3.4). An attempt to determine the contrast concentrations  $C(n)$  and  $C(n+1)$  at two subsequent heart beats is shown.

If the SNR of the measured IDC is low (see Fig. (2.14)), the definition of the right samples to estimate  $C_n$  and  $C_{n+1}$  is difficult, resulting in very inaccurate measurements. A better approach makes use of an IDC model interpolation. The LV is well approximated by a simple mono-compartment model, whose impulse response equals an exponential function (see section 4.2.1). If  $C_0$  is the concentration after a sudden indicator injection in the compartment at time  $t = 0$ , then the IDC  $C(t)$  is represented as given in Eq. (2.20), where  $\tau$  is the time constant [8].

$$C(t) = C_0 \cdot e^{-\frac{t}{\tau}} \quad (2.20)$$

The exponential function in Eq. (2.20) can be used to fit the IDC as measured from the model that is shown in Fig. (2.13). The ripple due to the pulsatile flow does not represent a problem because it is averaged over a large number of cycles. Once the exponential model is fitted to the IDC down-slope, the FEF is measured by Eq. (2.19) as given in Eq. (2.21), where  $\Delta t$  is the cardiac period.

$$\text{FEF} = 1 - \frac{C_{n+1}}{C_n} = 1 - \frac{e^{-\frac{(t+\Delta t)}{\tau}}}{e^{-\frac{t}{\tau}}} = 1 - e^{-\frac{\Delta t}{\tau}} \quad (2.21)$$

<sup>20</sup>Again, a similar reasoning may be also applied to aortic valve insufficiency.

Eq. (2.21) is commonly used for IDC FEF measurements. However, it is valid only when the contrast bolus is rapidly injected into the ventricle within a diastolic phase, which is the reason why a correct FEF estimation requires a ventricular injection (Holt method [75]). In fact, the measurement must be performed in the LV (or aorta out-tract) during contrast wash-out with no incoming contrast [8]. Therefore, catheterization is needed and the clinical application of the method is very limited due to the high invasiveness.

An invasiveness reduction is accomplished by use of radio-opaque contrast or radionuclides for x-ray or nuclear angiography (see section 2.1.2), which allow a non-invasive detection of the indicator. In fact, the FEF can be assessed by videodensitometry of cine-loops [76–78]. However, despite a non-invasive contrast detection, contrast injection still needs cardiac catheterization (invasiveness issue) and, as discussed in section 2.1.2, the use of x-rays or radionuclides is not recommended in several cases.

In healthy people the EF is usually bounded between 50% and 85%. However, in heart failure patients the EF can even drop down to 10%. In order to keep a sufficient value of CO, the decrease of EF is compensated by an increase of both  $V_{ed}$  and  $V_{es}$  (dilated ventricle), so that the SV can still guarantee a sufficient CO.

### 2.3 Pulmonary blood volume

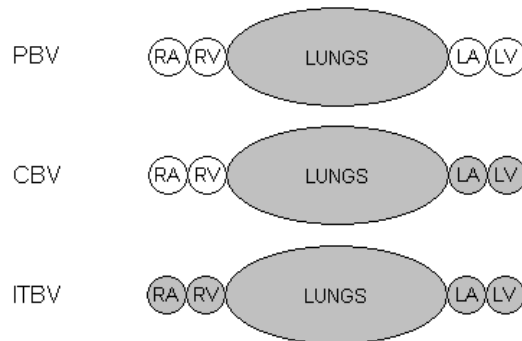


**Figure 2.15:** Scheme of the common blood volume measurements: Pulmonary Blood Volume (PBV), Central Blood Volume (CBV), and Intra-Thoracic Blood Volume (ITBV). The volumes of the compartments that are included in the measurement are filled with gray color.

Blood volume measurements provide valuable information on the circulatory system functionality. In particular, the Pulmonary Blood Volume (PBV, blood volume between the pulmonary artery and the LA), the Central Blood Volume (CBV, blood volume between the pulmonary artery and the LV) and the Intra-Thoracic Blood Volume (ITBV, blood volume between the RA and the LV) are important parameters in anaesthesiology, intensive care, and cardiology to evaluate the cardiac preload and the symmetry of the cardiac efficiency. For instance, LV EF and SV are closely related to PBV and CBV [79, 80]. A scheme of the typical blood volume measurements is shown in Fig. (2.15). In order to make the volumes independent on the size of the subject, they are usually normalized (indexed) as already explained for the CI (section 2.1). PBV measurements are based on trans-pulmonary indicator dilution techniques, which make use of an injection and subsequent detection of an indicator bolus.

Nowadays, trans-pulmonary indicator dilution techniques are very invasive due to the need for a double catheterization [79–84]. In fact, a catheter for thermodilution (or dye dilution) must be inserted through the femoral artery up to the aorta, where the IDC is measured. Moreover, since the indicator must be injected into a central vein, the insertion of a second catheter is necessary to reach the injection site. The Mean Transit Time (MTT) that the indicator takes to cover the distance between the injection site (central vein) and the detection site (aorta out-tract) is multiplied times the CO as given in Eq. (2.22) for the measurement of the blood volume ( $V$ ) between injection and detection site.

$$V = \text{MTT} \cdot \text{CO} \quad (2.22)$$

The measured  $V$  is the PBV plus the average volume of the four cardiac chambers, i.e., the ITBV. Common applications make use of a Pulmonary Artery Catheter (PAC) in order to inject the contrast in the pulmonary artery and measure the CBV [27]. The measurement of the MTT between the first and the second passage of the indicator allows the assessment of the Total Circulating Blood Volume (TCBV).

An alternative technique, whose application is non-invasive, is the impedance plethysmography (see section 2.1.6). In fact, the application of Eq. (2.15) allows the determination of the blood volume variations in the thorax. However, it only allows the measurement of differential values rather than absolute values.

## 2.4 Comparative evaluation of the available techniques

The presented techniques for CO, EF, and blood volumes measurements are compared. Nowadays, what is considered the gold standard technique for CO measurements is the thermodilution, especially the cold one, which also allows a simultaneous RV EF estimate. Still very common in the clinical practice is the dye-dilution method, especially after the introduction of optical fibers. The Fick method procedure is more

complicated, since it requires the use of both a spirometer and a gas analyzer. This is the reason why the thermodilution and the dye-dilution methods are preferred. Also the use of lithium dilution is spreading due to the less invasive approach. The uncertainty of the measure is similar in all the indicator dilution techniques and it can be considered bounded in a range of  $\pm 0.5 \text{ Lmin}^{-1}$  ( $\simeq \pm 10\%$  of an average CO of  $5 \text{ Lmin}^{-1}$  [35, 50]). The indicator dilution methods can be easily performed in the operating room during surgery and in the intensive care unit. The main disadvantage is the use of catheterization, which brings several risks and complications [27, 28].

The echo-Doppler technique does not imply catheterization and represents, together with the magnetic flowmeter and some lithium systems, the only solution to obtain an direct instantaneous measurement. A disadvantage of the echo-Doppler approach could be a limited accuracy, which derives from the uncertainty about the velocity direction. Furthermore, it provides only velocity measurements. For the CO estimation the cross sectional area of the vessel (the aorta for instance) must be also determined, resulting in further measurement errors. However, as reported in section 2.1.4, TEE Doppler measurements of CO correlates well with thermodilution.

Although we have mentioned the magnetic flowmeter, its medical application for CO measurements is limited because of the combination of low accuracy (difficulties in the probe positioning) and invasiveness.

The angiographic techniques are well established, but mainly focused on the diagnosis of stenosis and aneurysms of the blood vessels (especially the *coronary arteries*<sup>21</sup>). Usually the CO is indirectly measured by Eq. (2.1). Furthermore, infusion of radionuclides is not applicable to patients under surgery or intensive care as well as to patient in special conditions (e.g., pregnant or breast feeding women).

The MRI technique is non-invasive and extremely accurate. The disadvantage is mainly represented by the high cost of the equipment and its limited applicability in emergency routines due to the tunnel-shape, the amplitude of the generated magnetic fields, and the long time required for performing the analysis.

Rather than CO measurements, CAT and especially MRI can perform accurate tri-dimensional measurements of LV EF. However, they are geometrical measurements that cannot take into account any valve insufficiency. For an assessment of the FEF, the employment of indicator dilution techniques is necessary. The assessment of RV EF is better performed by PAC, since the RV geometry is rather complex and difficult to model. Radionuclides are also used for EF assessments based on IDC measurements. In general, the agreement between EF estimates made by different techniques shows large variances [18, 67, 68, 70, 71], so that the follow up of cardiopath patients must make use of the same technique.

---

<sup>21</sup>The study of the coronary artery conditions by use of a tracer is often referred to as *myocardium perfusion* (MP). According to the latest developments in the MP analysis, the measurement can also be performed by use of ultrasound contrast agents. This technique is referred to as *replenishment curve* [85, 86] (see section 3.3).

The same measurements as by radiography, nuclear imaging, and MRI, can be also performed by ultrasound *tri-dimensional echocardiography*. It is still in an early stage, but it shows already promising results (see section 3.1.3). The disadvantage, like for all the tri-dimensional techniques, is that the data processing is slow and has to be executed off-line. Moreover, the quality (contrast, signal to noise ratio, etc.) of echographic images is lower with respect to other 3-D imaging techniques (especially MRI).

The plethysmography, which is based on bio-impedance measurements, despite the non-invasive assessment of SV, does not show sufficient accuracy and for accurate measurements of CO it is replaced by classic indicator dilution techniques. This technique also allows the ITBV estimate, however, for an accurate measurement a double catheterization is preferred.

As from this overview of the techniques that are commonly employed for cardiac measurements, there is no unique approach for the simultaneous measurement of CO, LV EF, RV EF, and blood volumes (ITBV, CBV, and PBV). Different techniques must be used, which make the measurement a complex and slow procedure. Moreover, accurate measurements of CO and especially blood volumes require catheterization, resulting in very invasive applications. Also the measurement of FEF requires catheterization, as well as the assessment of RV EF, whose geometrical assessment is rather complex.

In this context, we propose a novel approach which makes use of ultrasound contrast agents. It permits the simultaneous measurement of CO, LV EF, RV EF, and blood volumes (ITBV, CBV, and PBV) by use of an ultrasound scanner and a single peripheral injection of a small contrast agent bolus. A single minimally-invasive measurement can replace the application of two time-consuming imaging techniques (LV and RV EF measurements by MRI or echography) and a very invasive indicator dilution technique (tras-pulmonary thermodilution or dye-dilution for CO and CBV measurements). The measurements are based on the hemodynamics, therefore, they are directly related to the cardiac efficiency without use of any geometrical model or assumption.

The same principles can be applied to all the contrast imaging techniques (radionuclides, gadolinium, and iodine respectively for nuclear, magnetic, and x-ray imaging). However, ultrasound contrast agents are inert (the contrast is basically made of air bubbles, see section 3.2), resulting in a safe and easy measurement procedure, which is suitable for operating-room and emergency routines where ultrasound scanners are widely employed. In addition, since the analysis is performed by use of an ultrasound scanner, the IDC measurement can be integrated with all the information already available by standard ultrasound investigations (see section 3.1), resulting in a complete and objective evaluation of the cardiac conditions, which can be easily made in outpatients.





## Chapter 3

# Echography and ultrasound contrast agents

*Tardi ingenii est rivulos consecrari, fontes rerum non videre (Cicero).*

After the introductory overview of the cardiac parameters to measure, in this chapter we focus on the technology that we intend to use for our measurements. At first, the basics of the ultrasound technology for clinical echography are explained (section 3.1), then the characteristics and use of ultrasound contrast agents are described (section 3.2) together with the specific techniques and modes for their detection (section 3.3). In conclusion of the chapter, the clinical use of ultrasound echography in cardiology is presented (section 3.4).

### 3.1 Ultrasound principles and echography

In this section the basics of ultrasound generation and propagation (section 3.1.1), the principles of echography (section 3.1.2), and their extension to 2-D and 3-D imaging (section 3.1.3) are presented.

#### 3.1.1 Ultrasound generation and propagation

Ultrasounds are elastic waves like the sound that we can hear by our ear. The only difference is the frequency  $f$  ( $f = \omega/2\pi$ , where  $\omega$  is the angular velocity in radians per second), which is higher than the audibility threshold (20kHz). Assuming a non-viscous medium, ultrasound waves are longitudinal and described by the *wave equation* as given in Eq. (3.1), where  $v$  is the propagation velocity,  $z$  is the propagation axis, and  $A$  is the amplitude, i.e., the displacement of the medium particles with respect to the equilibrium position [87, 88].

$$\frac{\partial^2 A}{\partial z^2} = \frac{1}{v^2} \frac{\partial^2 A}{\partial t^2} \quad (3.1)$$

A solution of Eq. (3.1) is given as in Eq. (3.2), where  $i = \sqrt{-1}$ ,  $A_0$  is the maximum displacement, and  $k$  is the *wave number*, which is equal to  $2\pi\lambda^{-1}$  ( $\lambda$  is the wave length and is equal to  $2\pi v\omega^{-1}$ ).

$$A(t, z) = A_0 e^{ik(vt-z)} \quad (3.2)$$

Usually the real part of the wave equation solution  $\text{Re}[A] = A_0 \cos(k(vt - z))$  is used for the wave representation.

The ultrasound propagation velocity  $v$  is  $343\text{ms}^{-1}$  in air and  $1480\text{ms}^{-1}$  in water at  $20^\circ\text{C}$ <sup>1</sup>. It is equal to  $\sqrt{B\rho^{-1}}$ , where  $\rho$  is the density of the medium ( $\text{kg} \cdot \text{m}^{-3}$ ) and  $B$  is the *bulk modulus*, which is measured in Pascal ( $1\text{Pa} = 1\text{kg} \cdot \text{m}^{-1} \cdot \text{s}^{-2}$ ) and is the measure of the stiffness of the material<sup>2</sup>. The energy carried by the acoustic wave is defined by its intensity  $I$ , which represents the power across an unitary surface ( $\text{Watt} \cdot \text{m}^{-2}$ ). It is given as in Eq. (3.3), where  $Z$  is acoustic impedance, which for a planar wave equals  $P/\dot{A} = \rho v$  ( $P$  is the ultrasound pressure and  $\dot{A}$  the oscillation velocity) [61, 87].

$$I = \frac{1}{2} Z (2\pi f A)^2 \quad (3.3)$$

The physical principle of echography is the reflection of the ultrasound waves at the discontinuities of a material (*medium*). The discontinuity is described in terms of acoustic impedance<sup>3</sup>  $Z$ . In Table (3.4), sound velocity and acoustic impedance for several biological tissues are listed [42].

Biological Material	Sound Velocity	Acoustic Impedance
Air	$343 \text{ ms}^{-1}$	394.35 Rayls
Blood	1580	1.67 MRayls
Bone	$2240 \pm 8\%$	$3.89 \pm 8\%$
Brain	$1470 \pm 4\%$	1.52
Fat	1450	1.38
Kidney	1560	1.62
Liver	1550	1.64
Muscle	1580	1.70
Soft Tissue (average)	1540	1.63

(3.4)

<sup>1</sup>The velocity of the sound in the soft biological tissues is about 1540m/s. It is similar to the velocity in water, since soft biological tissues are made by 80% of water.

<sup>2</sup>The bulk modulus is the reciprocal of the compressibility, and can be expressed as  $B = \Delta P \cdot (\Delta V/V)^{-1}$ , where  $\Delta V$  is the decrease of volume,  $V$  is the original volume, and  $\Delta P$  is the applied pressure variation. It can be also proven that  $B = \gamma P$  for a gas in adiabatic condition (i.e.,  $PV^\gamma = \text{constant}$ ), where  $\gamma$  is the adiabatic polytropic exponent and  $P$  is the static pressure [61, 89].

<sup>3</sup>The acoustic impedance is usually expressed in *Rayls*:  $1\text{Rayl} = 1\text{kg} \cdot \text{m}^{-2} \cdot \text{s}^{-1} = 1\text{N} \cdot \text{s} \cdot \text{m}^{-3}$ . For water  $Z = 1.49\text{MRayls}$ .

In the simplest case, when the incidence angle is equal to zero, the amplitude  $A_r$  of the reflected wave and the amplitude  $A_t$  of the transmitted wave (see Fig. (3.5)) are related to the amplitude  $A_i$  of the incident<sup>4</sup> wave as given in Eq. (3.5) [47,87,91].

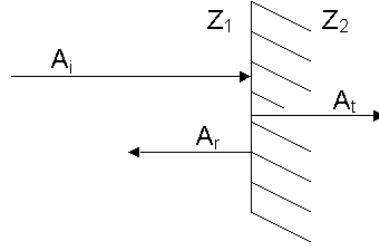


**Figure 3.1:** Reflection and transmission of the acoustic wave across a discontinuity.

$$\begin{aligned}\frac{A_r}{A_i} &= \left( \frac{Z_2 - Z_1}{Z_2 + Z_1} \right) \\ \frac{A_t}{A_i} &= \left( \frac{2Z_2}{Z_2 + Z_1} \right)\end{aligned}\quad (3.5)$$

Across a discontinuity the wave frequency remains the same. Therefore, an expression for reflection and transmission in terms of the intensity  $I$  can be derived combining Eq. (3.3) and Eq. (3.5) as given in Eq. (3.6).

$$\begin{aligned}\frac{I_r}{I_i} &= \left( \frac{A_r}{A_i} \right)^2 = \left( \frac{Z_2 - Z_1}{Z_2 + Z_1} \right)^2 \\ \frac{I_t}{I_i} &= \frac{Z_1}{Z_2} \left( \frac{A_t}{A_i} \right)^2 = \frac{Z_1}{Z_2} \left( \frac{2Z_2}{Z_2 + Z_1} \right)^2 = \frac{4Z_1 Z_2}{(Z_2 + Z_1)^2}\end{aligned}\quad (3.6)$$

<sup>4</sup>In general, when the incidence angle is not equal to zero, Eq. (3.5) is given as follows:

$$\begin{aligned}A_r &= A_i \left( \frac{Z_2 \cos \alpha_i - Z_1 \cos \alpha_r}{Z_2 \cos \alpha_i + Z_1 \cos \alpha_r} \right) \\ A_t &= A_i \left( \frac{2Z_2 \cos \alpha_i}{Z_2 \cos \alpha_i + Z_1 \cos \alpha_r} \right)\end{aligned}$$

where  $\alpha_i$  and  $\alpha_r$  are the incidence and refraction angles respectively [49,90]. This result is obtained by imposing the continuity of the displacement amplitude and the pressure amplitude ( $P = 2\pi fAZ$ ) across the interface as given below [91].

$$\begin{aligned}A_i \cos \alpha_i + A_r \cos \alpha_i &= A_t \cos \alpha_r \\ A_i Z_1 - A_r Z_1 &= A_t Z_2\end{aligned}$$

The amplitude  $P$  of the pressure wave is given as  $P = \sqrt{2ZI}$  (i.e.,  $P = 2\pi fAZ$ ) [47, 87, 91], therefore, Eq. (3.5) does not change if the displacement amplitudes  $A_i$ ,  $A_r$ , and  $A_t$  are replaced by the respective pressure amplitudes<sup>5</sup>. Consequence of the *energy conservation principle* is that  $I_i = I_r + I_t$ .

In general the biological materials inside the body have similar composition, hence the reflections are very limited. Special cases are the lungs, which contain air, and the bones. For instance, when the ultrasound beam reaches the lungs coming from a soft tissue (e.g., muscle),  $\frac{I_r}{I_i} = 0.9990$  and  $\frac{I_t}{I_i} = 0.0010$ . More than 99.9% of the incident energy is reflected.

An important aspect for a complete characterization of sound propagation is the acoustic attenuation. The intensity of the sound wave decays with an exponential law as given in Eq. (3.7), where  $I_0$  is the initial intensity,  $z$  is the covered distance, and  $a$  is the absorption coefficient in Neper per cm [42, 47, 92]<sup>6</sup>.

$$I = I_0 e^{-2az} \quad (3.7)$$

The coefficient  $a$  depends on the material as well as on the frequency of the ultrasound wave. It increases as the frequency increases. The relation between  $a$  and the frequency for soft tissues is nearly linear<sup>7</sup> and  $a$  represented in  $cm^{-1} \cdot MHz^{-1}$ . Values of  $a$  for different biological tissues are listed in Table (3.8) [47, 92].

TISSUE	$a_{dB} [dB \cdot cm^{-1} \cdot MHz^{-1}]$
brain	0.53
heart	0.66
kidney	0.79
liver	0.43
muscle	0.55
blood	0.18
fat	0.6
skull	20

(3.8)

<sup>5</sup>Notice that the amplitude of the molecules displacement  $A$  is  $\pi/2$  delayed with respect to the pressure wave  $P$  [91]. In fact,  $P = B(\partial A/\partial z)$  and  $P = Z\dot{A}$ , where  $z$  is the sound-propagation axis,  $B$  the bulk modulus, and  $Z$  is the acoustic impedance ( $Z = \rho v$ ) [61].

<sup>6</sup>Since the intensity is related to the squared value of the pressure amplitude, for pressure Eq. (3.7) becomes  $P = P_0 e^{-az}$ .

<sup>7</sup>Actually, the absorption coefficient for soft tissues is a linear function of  $f^b$ , where  $b$  is slightly larger than 1 ( $b \simeq 1.15$ ) and  $f \in [0.1MHz, 50MHz]$  [87]. This nearly linear relation, which is in general valid for soft tissues, is not valid for contrast agents, which show a more complex behavior.

Very often the attenuation  $a$  is measured in  $dB \cdot cm^{-1} \cdot MHz^{-1}$ , as a consequence Eq. (3.7) is given as in Eq. (3.9) [92]<sup>8</sup>.

$$I = I_0 e^{-0.23 a_{dB} x f} \quad (3.9)$$

The ultrasound generator is referred to as transducer. It is made of *piezoelectric crystals*, which can be natural (e.g., quartz) or synthetic (e.g., Lead-Zirconate-Titanate, Poly-Vinylidene-Di-Fluoride, Lead-Magnesium-Niobate, and Barium Lead Titanate or Zirconate), and are placed on the tip of a probe. The crystals are the vibrating material that converts electrical energy into acoustic energy and vice versa. Each crystal makes an approximately linear conversion between mechanical pressure and electrical voltage. The input voltage amplitude usually ranges from 10 to 400 Volts, depending on the output ultrasound intensity that is required.

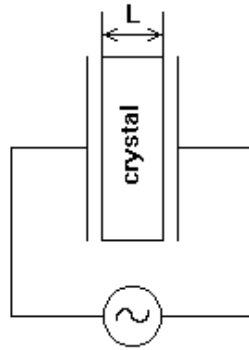


**Figure 3.2:** Crystal excited by an alternate voltage. The vibration of the crystal goes along the axis that is perpendicular to the electrode plaques (thickness-mode vibration).

The resonance frequency and the size of the crystal are related as given in Eq. (3.10) [20, 42, 47], with  $v_{crystal}$  equal to the propagation velocity of sound in the crystal (about  $4000ms^{-1}$ ) and  $L$  equal to the distance between the crystal surfaces, i.e., between the electrodes<sup>9</sup> (see Fig. (3.2)).

$$f_{res} = \frac{v_{crystal}}{2L} \quad (3.10)$$

<sup>8</sup>It is common to find  $a$  expressed in  $dB$ , i.e.,  $a_{dB} = 20 \log_{10}(P/P_0)$ . As a consequence  $P = P_0 10^{-\frac{a_{dB} f z}{20}} = P_0 e^{-\ln(10) \frac{a_{dB} f z}{20}} = P_0 e^{-0.115 a_{dB} f z}$ . The conversion is then  $a = \frac{\ln 10}{20} a_{dB} = 0.115 \cdot a_{dB}$ .

<sup>9</sup>Formula (3.10) derives from the fact that the resonance is given by the coupling of the electrical input and the acoustic waves within the crystal, which have to cover the distance  $2L$  (reflection from the opposite surface, see Fig. (3.2)) at the same frequency of the electrical input. Therefore, for a typical resonance frequency of 5MHz, the crystal width must be  $L = 4 \cdot 10^{-4}m$ .

The acoustic adaptation between crystals and skin tissue in order to transmit the maximum bandwidth with the minimum loss [20, 47] is made by a *matching layer* designed with a thickness of  $\lambda/4$  ( $\lambda$  is the length of the acoustic wave in the layer at the resonance frequency  $f_{res}$  of the transducer) and an acoustic impedance between those of the crystal ( $Z_{crystal}$ ) and the external medium (the acoustic impedance  $Z_{skin}$  of the human skin)<sup>10</sup>. Without matching layers, there would be a direct interface between transducer ( $Z_{crystal} \simeq 30\text{MRayls}$  for a Lead-Zirconate-Titanate crystal [47]) and skin ( $Z_{skin} \simeq 1,63\text{MRayls}$ , see Table (3.4)), with a consequent reflection, as derived by Eq. (3.6), of 80% of the energy. The ideal acoustic impedance of the matching layer can be determined by several different methods.

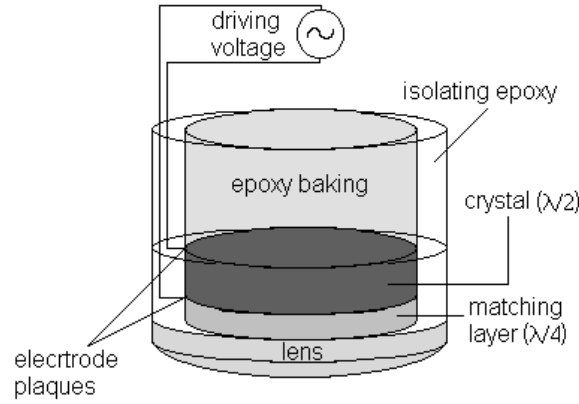


**Figure 3.3:** Scheme of an ultrasound transducer.

For a given frequency (narrow-band) and optimized matching-layer thickness (equal to  $\lambda/4$ ) the transmission coefficient equals 1 if  $Z_{match}$  is equal to  $\sqrt{Z_{crystal}Z_{skin}}$  [90]<sup>11</sup>. In general the transmission should be maximized for a wide bandwidth, and

<sup>10</sup>Such layers are basically made by aluminium powder in an epoxy resin: the higher is the concentration of aluminium the higher is the acoustic impedance. However, new generations of transducers aim to avoid the matching layer. They are made by polyvinylidene fluoride PVF<sub>2</sub> with an acoustic impedance close to that of tissues [47].

<sup>11</sup>For a fixed frequency and a quarter-wave matching layer  $L = \lambda/4$ , the intensity transmission coefficient is given as follows,

$$\frac{I_t}{I_0} = \frac{4Z_1Z_2}{Z^2 \left(1 + \frac{Z_1Z_2}{Z^2}\right)^2}$$

where  $Z_1$ ,  $Z$ , and  $Z_2$  are the acoustic impedance of the first medium, the matching layer, and the second medium respectively. It is evident that for  $Z = \sqrt{Z_1Z_2}$  the transmission coefficient is unitary.

therefore the complexity of the matching-layer design increases. Using the *Krimholts Leedom Matthaei model* (KLM model 1970 [93]) an ideal acoustic impedance of the matching layer is found to be equal to  $\sqrt[3]{Z_{crystal}Z_{skin}^2}$  [94]. Other formulae such as  $Z_{match} = \log^{-1}((\log(Z_{crystal}) + \log(Z_{skin}))/2)$  are also adopted [47], and the use of more layers is considered too.

The transducer can be used in continuous or pulsed Mode. In the pulsed Mode it is necessary to have a short pulse and then to stop the crystal vibrations as soon as the electric signal is turned off. To obtain this result the internal surface of the crystals is covered by a thick damping layer (epoxy). Fig. (3.3) shows the structure of a mono-crystal transducer [87, 95].

**Remark** *The acoustic intensity that is generated by an ultrasound transducer that produces a typical (high) pressure peak of 1MPa is  $33W \cdot cm^{-2}$ . It is interesting to compare it to the pain-threshold for the human ear (frequency equal to 1kHz), which is only 30Pa and  $10^{-4}W \cdot cm^{-2}$  [61]. There are limitations imposed for each analysis by the United States Department of Health and Human Services and the Center for Devices and Radiological Health (CDRH) of the Food and Drug Administration (FDA). They have been estimated according to studies developed by the American Institute of Ultrasound in Medicine (AIUM), and the latest thresholds were delivered in 1997 [96]. For the most of the tests the threshold is defined by an intensity (spatial-peak and pulse-average)  $I_{SPPA}$  equal to  $190Wcm^{-2}$  and Mechanical Index<sup>12</sup> (MI) equal to 1.9, meaning that the pressure amplitude is about 3MPa (for the MI assume a frequency of about 3MHz). A pressure of 10MPa ( $I = 3300W \cdot cm^{-2}$ ) could even induce cavitation in mammals [92].*

### 3.1.2 Echography principles: A-Mode and M-Mode analysis

Echography, as the name suggests, is based on the analysis of the echoes: if a pulse (usually five ultrasonic cycles) is transmitted inside the body and the resulting echoes (reflections) received back, then it is possible to derive the position of the intercepted discontinuities that generated the echoes. In fact, since the propagation velocity of ultrasonic waves through biological tissues is known (see section 3.1.1), the delays of the received echoes can be interpreted in terms of distance. The distance  $d$  between the transducer and the discontinuity is given as in Eq. (3.11), where  $v$  is the

<sup>12</sup>It is defined [96] as the peak rarefactional (therefore negative) pressure (expressed in MPa) when a uniform material is scanned, divided by the square root of the center frequency of the pulse expressed in MHz (usually between 2.5 and 5 MHz). The material is assumed to have an attenuation  $a_{dB}$  of  $0.3dB \cdot cm^{-1} \cdot MHz^{-1}$  ( $a \simeq 0.035cm^{-1} \cdot MHz^{-1}$ ). It is the standard attenuation used to give an estimation of the in situ value of the acoustic pressure (or intensity). This estimated value is referred to as *derated*.



ultrasound velocity in tissue and  $T$  is the time interval between the transmission and the reception of the pulse. An example is given in Fig. (3.4).

$$d = \frac{vT}{2} \quad (3.11)$$

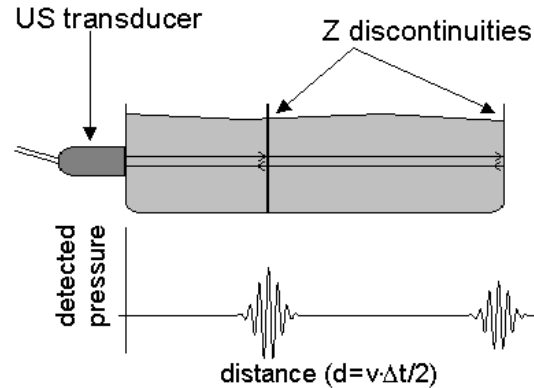


**Figure 3.4:** Distance estimation by means of echography. The discontinuity is represented by a plastic layer inserted in a water-filled basin. Notice that the border of the basin represents a discontinuity too, and that the resulting echo is more attenuated due to the longer path.

This is the basic *Mode* of an ultrasound scanner, and it is referred to as *A-Mode* (“A” stands for “Amplitude”). A pulse is transmitted and received back in order to reconstruct the discontinuities along a line. The received signal is demodulated in order to suppress the frequency (usually between 2.5MHz and 5MHz for clinical applications) of the ultrasound pulse. This operation is typically implemented by a mixer and a low-pass filter. Before demodulation the signal is referred to as RF (*Radio Frequency*) signal while after demodulation it is referred to as *A-line* (Amplitude line). The A-line that is obtained after demodulation represents the amplitude of the ultrasound echoes as a function of the ultrasound depth, i.e., the profile of the acoustic impedance discontinuities.

**Remark** According to Eq. (3.7), the received energy reduces exponentially as a function of the distance. In order to compensate this effect, the ultrasound scanner applies a logarithmic non-linearity (function of the time delay of the received reflection) to the received signal, which is referred to as *Time Gain Compensation* [47]. The RF signal is already compensated.

A very important characteristic of the system is the resolution. Two different resolutions can be distinguished: the axial resolution and the lateral resolution [49, 87].

The axial resolution is the ability to distinguish two different discontinuities along the direction of propagation of the ultrasound beam. It depends on the time-length of the ultrasonic pulse. In fact, as from Eq. (3.11), the system can distinguish two discontinuities at the minimum distance of  $vT/2$ , with  $T$  equal to the time length of the pulse<sup>13</sup>.

More complicated is the determination of the lateral resolution. It is a measure of the narrowness of the ultrasound beam. The aim of an ultrasound system is to receive information (i.e., reflections) coming from the  $z$  axis without spreading the beam along the  $X$  and  $Y$  axis (refer to Fig. (3.5), where the beam is spread with an angle equal to  $\theta_0$ ). This allows resolving the  $XY$  plane with higher accuracy when the transducer is moved (translated) to reconstruct either 2D- or 3D-images (section 3.1.3).

The surface of a transducer can be assumed to consist of point-sources transmitting spherical waves. Thus, to calculate the acoustic field, according to the *Huygens' principle* [61, 91], all the point-source contributions should be summed to each other. This results in two effects, which, in case of a flat circular transducer of radius  $r$  (see Fig. (3.5)), are modelled as follows [20, 42, 49, 87, 90, 97].

1. The pressure of the sound-wave along the  $z$  axis goes through a series of maxima and minima in the near field (*Fresnel zone*), it reaches a wide maximum at the focal distance  $d = r^2/\lambda$ , which represents the transition distance to the far field (*Fraunhofer zone*), and then it slowly decreases. The mathematical formulation is given as in Eq. (3.12), where  $P_z$  is the maximum pressure wave amplitude along the  $z$  axis and  $P_0$  is the reference pressure on the crystal surface.

$$\frac{P_z}{P_0} = 2 \left| \sin \left( \frac{\pi}{\lambda} \sqrt{r^2 + z^2} - z \right) \right| \quad (3.12)$$

2. There is a beam pattern of the pressure that is a function of the angle  $\theta$  respect to the  $z$  axis. In the near field it can be solved only numerically, but in the far field the Fraunhofer approximation (plane waves) allows describing<sup>14</sup> the

<sup>13</sup>Common values are 5 cycles at 5MHz, resulting with a resolution distance  $d \approx 0.8mm$ .

<sup>14</sup>In the far field the formulation of the beam pattern, i.e., the distribution of the pressure (amplitude) of the sound wave, is given as follows:

$$P(\theta) \propto \frac{2J_1 \left( \frac{2\pi r}{\lambda} \sin(\theta) \right)}{\frac{2\pi r}{\lambda} \sin(\theta)}$$

where  $J_1$  is the Bessel function of the first order [49, 87, 90, 98].

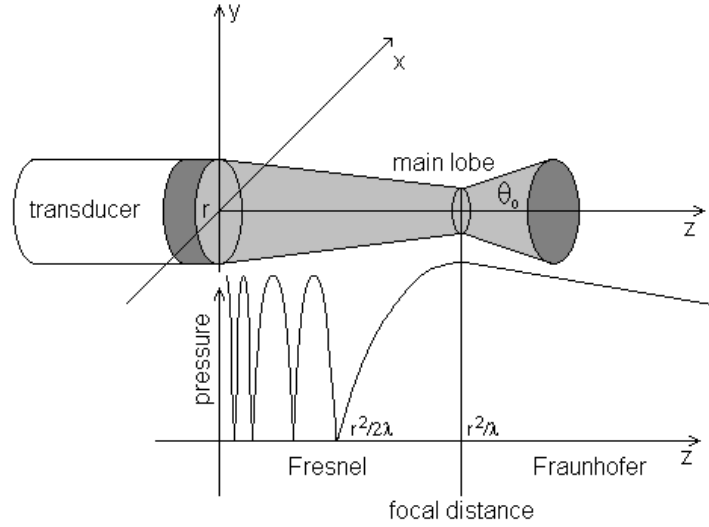


**Figure 3.5:** Model of the acoustic field of a circular transducer. Notice the peak pressure along the  $Z$ -axis at distance  $z = r^2/\lambda$  (focal distance, transition between the Fresnel and the Fraunhofer field) and the last pressure minimum (zero) at distance  $z = r^2/2\lambda$ . The beam section diameter at the focal distance is half of the transducer diameter [47].

pressure as a function of  $\theta$ . Hence, it is possible to derive a parameter to measure the spread of the main lobe. It is the angle  $\theta_0$  where the main lobe is constricted (i.e., the first null of the main lobe). Its formulation is given as in Eq. (3.13).

$$\theta_0 = \arcsin\left(\frac{0.61\lambda}{r}\right) \quad (3.13)$$

Two points covered by the main lobe cannot be distinguished, therefore,  $\theta_0$  describes the angular lateral resolution of the system, which decreases as the distance of the discontinuities from the transducer increases.

The best compromise to avoid both the Fresnel fluctuations and the decrease of resolution in the far field is to have the  $Z$  discontinuity at the focal distance  $d = r^2/\lambda$ , which is also the distance where the main lobe is self focused. In fact, the analysis of the near-field beam shows that for distance  $r^2/\lambda$  from the transducer the width of the main lobe is reduced to its minimum value, which is half of the transducer width (see Fig. (3.5)).

A reduction of the lateral resolution is also determined by the side lobes of the transducer. In fact, apart from the main lobe, there are lateral lobes whose intensity is normally 60dB to 100dB lower than that of the main lobe [47, 87]. As a consequence, not only the reflections from the main lobe, but also those from the side lobes are detected. These noise components, especially evident in B-Mode analysis (see section 3.1.3), are referred to as *side lobe artifacts*.

Although the beam pattern depends on the shape of the transducer, in every transducer the lateral resolution is proportional to both frequency of the ultrasound beam and size of the crystal (see Eq. (3.13)).

Acoustic lenses are often used to improve the lateral resolution. They are placed on the tip of the transducer. Acoustic lenses are designed like the optical ones, according to the *Snell Law* and the *Equal Acoustic Path Rule*<sup>15</sup>.

In conclusion, to reconstruct the information on one line the following steps are performed.

- A pulse (few cycles at the resonance frequency of the transducer) is transmitted along one line.
- All the echoes coming from that line are detected (in practice, the echoes from all the directions that are covered by the main and the side beam lobes are detected).
- The time-gain compensation is applied (the resulting signal is the RF signal).
- The RF-line is demodulated to obtain the amplitude depth information (A-line, see Fig. (3.4)).

As by means of the A-Mode echography it is possible to detect the discontinuities along one line, the same procedure can be repeated continuously by generating multiple pulses in sequence. This technique is referred to as *M-Mode* analysis (“M” stands for “Motion”), and it plots a function of time that describes the motion of the discontinuities along one direction<sup>16</sup>. While the A-Mode analysis is mainly used in ophthalmology and encephalology, the M-Mode analysis is mainly used to detect moving parts, such as the cardiac chambers and valves.

<sup>15</sup>The acoustic path is given by  $\sum \frac{d_i}{v_i}$ , where  $d_i$  is the distance covered in the material with propagation speed  $v_i$ . The Snell Law in acoustics is formulated as follows:

$$\sin(\alpha_{inc}) \cdot v_2 = \sin(\alpha_{refr}) \cdot v_1$$

where  $v_1$  and  $v_2$  are the propagation speed in the first and in the second material and  $\alpha_{inc}$  and  $\alpha_{refr}$  are the incidence and refraction angles respectively [47, 91].

<sup>16</sup>As for the echo-Doppler (see section 2.1.4), it is important to take care of the pulse repetition frequency (PRF). From the Nyquist theorem, the PRF must be at least twice as high as the frequency components of the tissue movements. However, in the velocity range of biological tissues, the PRF does not represent a limitation.

### 3.1.3 Image reconstruction: B-Mode and 3-D analysis

The same principles that are used to reconstruct the distribution of the acoustic impedance discontinuities along one line (A-line) can be used to obtain the discontinuity distribution on one plane [20, 99]. In fact, a plane can be spanned by translating the transducer in one direction and taking measurements for a series of lines. The voltage of the multiple A-lines (dynamic range) is mapped into gray-level (usually 256 gray levels coded by 8 bits) by using a logarithmic compression, or, more in general, a non-linear compression. The result is a bi-dimensional image that represents a slice of the body. The bi-dimensional application of echography is referred to as *B-Mode*, where “B” stands for “Brightness”. The first simple B-Mode implementation was based on the mechanical translation of the transducer, but more advanced developments followed very rapidly.

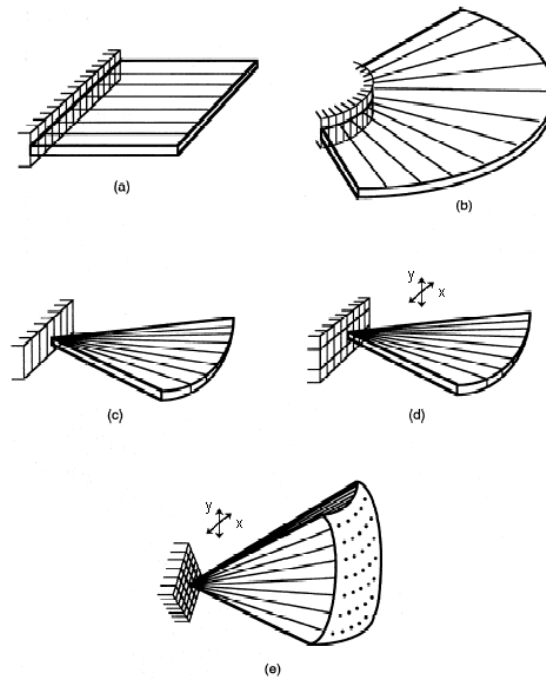


**Figure 3.6:** Structures of the array transducers commercially available. In (a) it is shown a linear sequential array, in (b) a curvilinear array, in (c) a linear phased array, in (d) a 1.5-D array, which is phased along the X axis and focused along the Y axis, and finally in (e) it is shown a 2-D phased array for tri-dimensional imaging.

Apart from the mechanical solutions, the latest technologies are based on electronic array processing. It is implemented in the array transducers and allows the focalization and steering of the ultrasound beam to different directions (*beam steering*). Each crystal can be activated separately with a specific delay. By choosing the appropriate delays it is possible either to focus the ultrasound beam (like an optical lens) or change (steer) its orientation to span a wide angle. The crystals are “phased” along one direction. A complete description of the array beam-forming configurations that are commercially available is given below (see Fig. (3.6)).

- Linear sequential arrays (*a* in Fig. (3.6)): they usually have 512 elements and a sub-aperture of 128 elements is selected to operate at a given time. The scanning lines are perpendicular to the face of the transducer. The acoustic beam is focused, but not steered. The advantage is the higher resolution with respect to a steered beam, while the disadvantage is that the field view is limited to the width of the transducer, which consequently must be large.
- Curvilinear arrays (*b* in Fig. (3.6)): they operate in the same manner as the linear sequential arrays, but the field view opens with an angle depending on the convex shape.
- Linear phased arrays (*c* in Fig. (3.6)): they usually have 128 elements and they use the beam steering technology. The main advantage consist of a field view that is much wider than the transducer width. As a result, these transducers are ideal for cardiac transthoracic imaging, where the transducer must scan through a small window between the ribs (see also Fig. (3.13)).
- 1.5-D arrays (*d* in Fig. (3.6)): 1.5-Dimensional means that the array is bi-dimensional, but the second dimension (elevation plane) contains only few elements (3 to 9), which are used to improve the resolution along the second dimension (elevation focus).
- 2-D phased arrays (*e* in Fig. (3.6)): this is the last step towards tri-dimensional imaging. A bi-dimensional array allows to steer the beam in two directions, leading to the reconstruction of a tri-dimensional view. However, if a typical array of 128 elements is considered, a complete 2-D array would require 16384 channels, which are impossible to handle (consider, for instance, how the probe cable would look like). The solution, nowadays, is represented by the sparse matrix technology. A  $50 \times 50$  element design can be reduced to about 500 channels.

Recent applications of electronic array controls also involve the implementation of specific filters to improve the detection of second harmonic reflections [100]. This allows a better detection of ultrasound contrast agents (see section 3.3).

Tri-dimensional echography represents the latest development of the echographic technology and different implementations are available. It is a step similar to the passage from A-Mode to B-Mode echography. Once two dimensions are solved, it is sufficient to repeat the measurement along the third dimension to obtain a 3-D view. Apart from the 3-D beam steering, which is controlled electronically, mechanical solutions are also available. The most common are shown in Fig. (3.7).

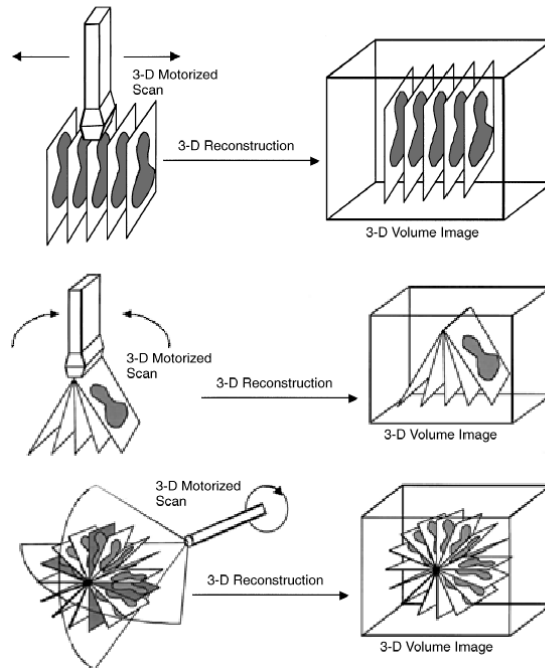


**Figure 3.7:** Mechanical solutions for 3-D echo-scanning.

The computation required by an electronic 3-D ultrasound scanner is heavy and real time processing is barely realized. For instance, a modern 3-D scanner such as the Philips Sonos 7500, allows an “almost real time” 3-D processing, so that one volume is reconstructed each four cardiac cycles. Faster solutions are represented by mechanical rotational 3-D transducers, which allow real time applications [101].

3-D Echography, as well as MRI or CAT, can be used to measure the volumes of the cardiac chambers and to estimate EF, SV, and CO. It is reported a correlation coefficient greater than 0.8 between the EF measurements made by CAT and by 3D echography [102], a correlation coefficient equal to 0.99 between 3-D echography and radionuclide angiography [103], and a correlation coefficient around 0.95 between the volume estimation made by 3-D echography and MRI [69,71,72]. How-

ever, despite the high correlation coefficients, bias and standard deviations are in general very large [67].

Apart from the image formation, another critical issue, especially for 3-D images, is the off-line detection of the cardiac structures for the automatic analysis and interpretation of the acquired data. As discussed in section 2.2, the volume measurements require the endocardiac-wall detection, which is often difficult to automate and needs manual intervention of expertises.

## 3.2 Ultrasound contrast agents

Ultrasound Contrast Agents (UCA) are made of a solution of micro-bubbles (diameter from  $1\mu\text{m}$  to  $10\mu\text{m}$ ). They are smaller than red blood cells (diameter from  $6\mu\text{m}$  to  $8\mu\text{m}$ ) and, therefore, suitable for intravenous injection. As for all tracers, ultrasound contrast agents have to be inert and non-toxic. Commercial agents can be distinguished in three generations [104]. The first generation includes the early air micro-bubbles that were not stabilized by a shell, such as Echovist® (Schering, Berlin, Germany), which was approved in Europe in the early 90's. Second generation agents were introduced in the mid 90's and included the first encapsulated air bubbles, such as Albunex® (Molecular Biosystems, San Diego, CA, USA) and Levovist® (Schering), whose shell was made of albumin and galactose respectively.

The latest third generation micro-bubbles for ultrasound detection are composed of air,  $SF_6$ ,  $C_3F_8$ , or other perfluorocarbons encapsulated in a phospholipid, albumin, or polymer shell [105–108]. The optimized use of a shell creates a strain that opposes to the Laplace pressure and stabilizes bubbles against dissolution<sup>17</sup>. Third-generation agents are SonoVue® (Bracco, Milan, Italy), Optison® (Amersham General Electric), Definity® (Du Pont Pharmaceuticals, USA), Quantison® (Quadrant Andaris, Nottingham, UK), Sonazoid® (Nycomed, Roskilde, Denmark), AI-700® (Acusphere, Watertown, MA, USA), EchoGen® (Sonus Pharmaceuticals, Bothell, WA, USA), Imavist® (Alliance Pharmaceuticals, Village Main, South Africa), Bisphere (Point Biomedical, San Carlos, CA, USA) and Sonavist® (Schering). Once injected into blood, the effect of the bubbles (see Fig. (3.8)) is a significant increase of the ultrasonic energy backscatter, which at first analysis could be simply explained by the reflection across the blood-air acoustic-impedance discontinuity.

Due to the natural oscillations (contraction-expansion) of the bubbles when invested by a pressure input, the interaction between contrast agents and ultrasound is a nonlinear process, which adds several harmonics to the backscattered ultrasound.

---

<sup>17</sup>According to the Laplace law, the pressure inside a gas sphere, referred to as Laplace pressure, equals  $2\sigma/R$ , where  $\sigma$  and  $R$  are the surface tension ( $N \cdot m^{-1}$ ) and the sphere radius respectively [109]. The high internal pressure due to small radius is held by the strain that is provided by the shell.



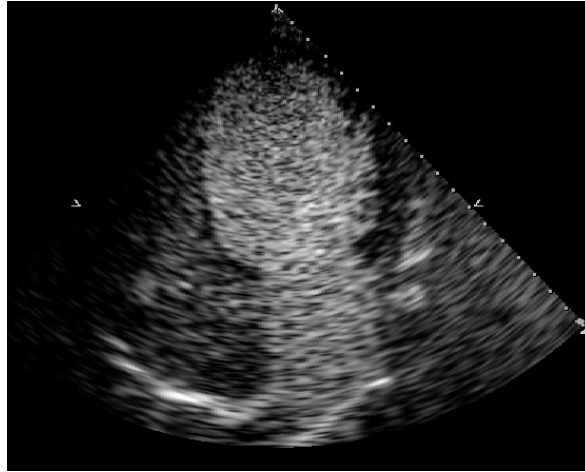


**Figure 3.8:** TTE using SonoVue® contrast agent. The contrast is recognizable in the left side of the heart.

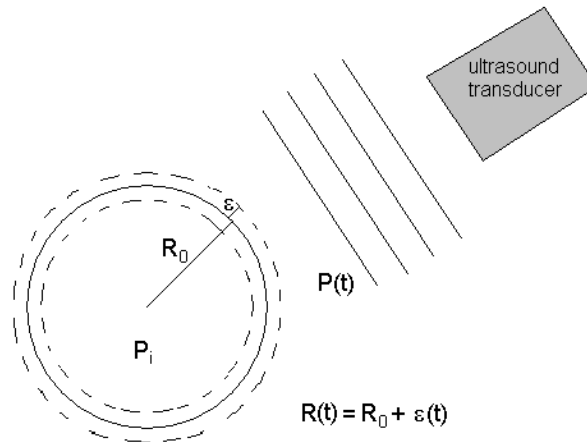


**Figure 3.9:** Schematic drawing of an oscillating bubble in an ultrasound pressure field.

The oscillations of a single bubble are commonly characterized by the model developed by Rayleigh and Plesset to describe the motion of vibrating spheres [109, 110]. The bubble is represented as a sphere of radius  $R$  and its motion is considered spherically symmetric as shown in Fig. (3.9). Therefore, bubble oscillations are described by radius variations. The surrounding fluid is assumed to be Newtonian (incompressible with constant viscosity).

The equation that is commonly used to describe the relation between velocity and pressure in a fluid-dynamic system is the *Navier-Stokes equation* [111]. If the steady external forces (e.g., the gravitational force) are not considered, the Navier-Stokes equation can be written as given in Eq. (3.14), where  $\rho$  and  $\mu_f$  are the density and the viscosity of the fluid respectively [112].

$$\rho \left( \frac{\partial v}{\partial t} + \nabla \frac{v^2}{2} \right) + \nabla \times \nabla \times v - \mu_f \nabla^2 v = -\nabla P \quad (3.14)$$

When the fluid (Newtonian fluid) vorticity is negligible, the velocity field is irrotational ( $\nabla \times v = 0$ ) and the viscosity term  $\mu_f \nabla^2 v$  in Eq. (3.14) disappears [111]. Moreover, we can define a potential  $\Psi$  so that  $v = \nabla \Psi$ . As a result, Eq. (3.14) is simplified as given in Eq. (3.15) [109].

$$\rho \nabla \left( \frac{\partial \Psi}{\partial t} + \frac{v^2}{2} + P \right) = 0 \quad (3.15)$$

Due to the radial symmetry hypothesis, the fluid velocity field has a radial symmetry and can be described as a function  $v(r, t)$  of the radial distance  $r$  from the bubble center and the time  $t$ . As a direct consequence,  $v(R, t) = \dot{R}$ , where  $R$  is the bubble radius. Moreover,  $\Psi = 0$  for  $r \rightarrow \infty$ . Another condition concerns the pressure field for  $r \rightarrow \infty$ , which is defined as  $P_\infty$  and equals the sum of two contributes: the hydrostatic pressure  $P_0$  and the ultrasound driving pressure  $P(t)$ . Using these conditions, the integration of Eq. (3.15) over  $r$  allows defining the relation between the pressure field  $P(r, t)$  and the bubble radius  $R(t)$ , which for  $r = R$  is given as in Eq. (3.16).

$$P(R) - P_\infty = \rho R \ddot{R} + \frac{3}{2} \rho \dot{R}^2 \quad (3.16)$$

$P(R)$  can be related to the internal pressure  $P_i$  of the gas bubble as given in Eq. (3.17), where  $P_v$  is the vapor pressure and  $\sigma$  is the *surface tension coefficient* ( $N \cdot m^{-1}$ ) [110].

$$P(R) = P_i - \frac{2\sigma}{R} + P_v \quad (3.17)$$

$R_0$  is the bubble radius at the equilibrium condition. Since the gas expansion and contraction can be considered isothermal and adiabatic respectively, the whole process is described by a polytropic transformation<sup>18</sup>, whose exponent<sup>19</sup>  $k$  ranges from 1 (isothermal) to  $\gamma$  (adiabatic). The value of  $\gamma$  for a noble gas (e.g., Argon and Xenon)

<sup>18</sup>A polytropic transformation is characterized by a constant value of the product  $P(V - b)^k$ , where  $b$  is the Van der Waals volume, i.e., the volume of the gas molecules [89].

<sup>19</sup>It can be calculated as  $\frac{c_k - c_p}{c_k - c_v}$ , where  $c_k$  is the molar heat of the transformation,  $c_p$  is the molar heat for constant pressure, and  $c_v$  is the molar heat for constant volume [91].

is  $5/3$ . Therefore, assuming the gas to obey a polytropic law for real gas with constant polytropic exponent  $k$ ,  $P_i$  is given as in Eq. (3.18), where  $h$  is the Van der Waals radius<sup>20</sup> [113].

$$P_i = \left( P_0 + P_v + \frac{2\sigma}{R_0} \right) \left( \frac{R_0^3 - h^3}{R^3 - h^3} \right)^k \quad (3.18)$$

For a driving pressure that does not cause bubble collapse ( $MI < 0.3$ ),  $R \gg h$  and the Van der Waals radius may be neglected (ideal-gas rather than real-gas assumption). As a result, Eq. (3.18) is simplified as given in Eq. (3.19).

$$P_i = \left( P_0 + P_v + \frac{2\sigma}{R_0} \right) \left( \frac{R_0}{R} \right)^{3k} \quad (3.19)$$

Combining Eq. (3.18) and Eq. (3.17) with Eq. (3.16), we obtain Eq. (3.20), which describes the non-linear motion of an ideal bubble and is referred to as *Rayleigh-Plesset equation* [109, 110].

$$\rho R \ddot{R} + \frac{3}{2} \rho \dot{R}^2 = \left( \frac{2\sigma}{R_0} + P_0 - P_v \right) \left[ \left( \frac{R_0}{R} \right)^{3k} - 1 \right] - P(t) \quad (3.20)$$

A modified expression of the Rayleigh-Plesset equation also adds to the second member of Eq. (3.20) the term  $4\mu_f \dot{R} R^{-1}$ , which defines the pressure drop that is caused by the viscous damping of the bubble-fluid system and is related to the fluid viscosity  $\mu_f$  (see [109] pp. 189-190 and [114] pp. 68-70). The resulting equation is given as in Eq. (3.21). It is referred to as the *modified Rayleigh-Plesset equation*, which is the result of the work of Noltingk, Neppiras, and Poritsky [115, 116].

$$\rho R \ddot{R} + \frac{3}{2} \rho \dot{R}^2 = \left( \frac{2\sigma}{R_0} + P_0 - P_v \right) \left[ \left( \frac{R_0}{R} \right)^{3k} - 1 \right] + \frac{4\mu_f \dot{R}}{R} - P(t) \quad (3.21)$$

As already mentioned, modern contrast agents (second and third generation) are made of encapsulated bubbles, therefore, the shell properties must be included in the bubble motion equation. Starting from the Rayleigh-Plesset equation, several authors have made modifications and added different terms according to different shell characterizations. The major contributions were proposed by de Jong (1993) [110], Church (1995) [117, 118] (see also [114] pp. 106-108), Frinking-de Jong (1998) [104], and Hoff (2000) [114, 119, 120].

Also other models have been derived to remove some of the assumptions of the Rayleigh-Plesset equation. They are based on the Herring (1941) and Gilmore (1952) equations [121, 122], which consider the enthalpy energy and a compressible medium

<sup>20</sup>The radius of a sphere that has the same volume of all the gas molecules in the bubble.

(non Newtonian) in order to give a better prediction of cavitation and large oscillations [109, 123, 124]. Based on these equations, Flynn (1975) developed a model that also included the thermal effects inside the bubble [125]. Still based on the Herring equation, the Trilling (1952) and the Keller-Kolodner (1952) models were derived [114]. The Trilling model was then extended to a population of bubbles by Chin and Burns (1997) [126], while the Keller-Kolodner model was first modified by Keller-Miksis (1980) [127] to introduce the driving pressure field and then modified by Prosperetti (1988) [128]. Another model - still based on a modified Herring equation - was also introduced by Morgan and Hallen (2000) [129].

A complete overview of all the proposed bubble dynamics models is beyond the purpose of this study. The agent that we used for the validation the indicator dilution methods that are proposed in this study is SonoVue®. This agent is well described by the model proposed by de Jong in 1993 [130], therefore, we focus on this model [110].

With respect to Eq. (3.21), the model does not consider only the damping due to the fluid viscosity  $\mu_f$ , but also other contributes related to re-radiation and heat conduction, together with the contributes to pressure due to the shell-properties. The pressure that is related to the presence of a shell is mainly caused by the shell viscous damping and elasticity. After collecting all these terms together, the resulting equation is given as in Eq. (3.22).

$$\rho R \ddot{R} + \frac{3}{2} \rho \dot{R}^2 = \left( \frac{2\sigma}{R_0} + P_0 - P_v \right) \left[ \left( \frac{R_0}{R} \right)^{3k} - 1 \right] - S_p \left( \frac{1}{R_0} - \frac{1}{R} \right) +$$

$$-2\pi f \delta_t \rho R \dot{R} - P(t) \quad (3.22)$$

The pressure due to the shell elasticity is defined by the shell elasticity parameter  $S_p$ , which is derived from the application of the Hooke law<sup>21</sup> under hypothesis of homogeneous, thin, and perfectly elastic shell (see [131], pp. 152-155, equation 5.10). The first order approximation of the Hooke law for a thin shell is given as in Eq. (3.23) [110], where  $E$  is the *Young modulus*,  $\nu$  is the *Poisson ratio*, and  $T_s$  is the shell thickness (the thin shell hypothesis allows the approximation  $T_s \ll R$ ) [131].

$$R - R_0 = (\Delta P) R_0^2 \left( \frac{1 - \nu}{2ET_s} \right) \quad (3.23)$$

Therefore, due to the shell elasticity (stiffness), there is a restoring force that, after a further approximation for small radius variations, corresponds to the pressure

<sup>21</sup>According to the Hook law,  $F = -k \Delta R$ , where  $F$  is the applied force,  $k$  is the elasticity constant, and  $\Delta R$  is the radius variation.

difference  $\Delta P = S_p(R^{-1} - R_0^{-1})$  as given in Eq. (3.22). As a result,  $S_p$  is measured in  $N \cdot m^{-1}$  and given as in Eq. (3.24) [110].

$$S_p = \frac{ET_s}{(1 - \nu)} \quad (3.24)$$

In this model the shell thickness is assumed to be constant during oscillations<sup>22</sup>.

$\delta_t$  in Eq. (3.22) is the total damping factor<sup>23</sup> and is the sum of four terms as given in Eq. (3.25).

$$\delta_t = \delta_{rad} + \delta_{vis} + \delta_{th} + \delta_f \quad (3.25)$$

$\delta_{rad}$  represents the re-radiation damping<sup>24</sup>,  $\delta_{vis}$  the fluid viscosity damping (already included in Eq. (3.21), see also [109], pp. 189-190),  $\delta_{th}$  the damping due to thermal losses, and  $\delta_f$  the damping due to the shell friction<sup>25</sup>. The expression for the four dimensionless terms, usually considered at the natural frequency  $f_n$  (a derivation of  $f_n$  for a linearized system is given in Eq. (3.28)) [109], is given below, where  $\mu_s$  is the shell viscosity,  $v$  is the ultrasound velocity in the medium, and the expression for  $B(f, R)$  was derived by Anderson and Medwin<sup>26</sup> [132–134].

<sup>22</sup>Other models, such as the Hoff model, assume a constant shell volume and, therefore, the shell thickness becomes a function of the bubble radius  $R$ .

<sup>23</sup>In a linear system of the second order, such as a mass-spring damped system, the damping factor (non-dimensional) is defined as the inverse of the quality factor and equals  $b/2\pi f_n m$ , where  $b$  is the damping coefficient,  $f_n$  is the natural frequency of the system, and  $m$  is the mass. For high quality factors, the resonance frequency is close to the natural frequency (without damping) of the system and the oscillations have a large amplitude.

<sup>24</sup>Similar to a plane wave (see Eq. (3.2)), a spherical wave generated by a bubble can be expressed as  $P(r) = P(R_0)(R_0/r)e^{ik(vt-r)}$ , where  $P(r)$  is the pressure at distance  $r$  from the origin,  $P(R_0)$  is the pressure at the bubble surface, and  $vk = \omega$  [109]. The linear Navier-Stokes equation for irrotational flow at the bubble surface is given as  $\rho(dv/dt) = \rho\ddot{e} = -\nabla P$ . After inserting the spherical pressure  $P(r)$ , the Navier-Stokes equation at the bubble surface becomes  $\rho\ddot{e} = -[\partial P(r)/\partial r]_{R_0} = (P(R_0)/R_0)(1 + ikR_0)$ . As a result, the pressure amplitude at the bubble surface for  $kR_0 \ll 1$  is given as below.

$$P(R_0) = \rho R_0 \frac{1 - ikR_0}{1 + (kR_0)^2} i\omega\dot{e} \cong \omega\rho R_0\dot{e}(kR_0 + i)$$

The force at the bubble surface equals  $-4\pi R_0^2 P(R_0) = -4\pi R_0^3 \omega\rho\dot{e}(kR_0 + i)$ . Therefore, the acoustic impedance is given as  $Z_{rad} = 4\pi R_0^3 \omega\rho(kR_0 + i) = (\text{Re}[Z_{rad}] + i\omega m)$ , where  $m = 4\pi\rho R_0^3$  is the effective mass of the oscillating bubble and  $\text{Re}[Z_{rad}] = 4\pi R_0^4 \rho k\omega$  is the radiation resistance or damping  $b$ . Since the damping factor  $\delta$  is equal to  $b/m\omega$ , it follows that  $\delta = kR_0 = (2\pi/\lambda)R_0 = (2\pi f_n/v)R_0$ .

<sup>25</sup>The derivation of  $\delta_f$  for a fully linearized thin shell model is reported in [114], pp. 76-78.

<sup>26</sup>The same expression for  $B(f, R)$  as derived in [132] (pp. 296-299), which is referred to as  $d/b$  and given below, can be also found in [109] (equation 3.186), where it is referred to as  $d_{th}$ .

$$B(\omega, R_0) = (3\gamma - 1) \left[ \frac{\frac{R_0}{I_D} \left( \sinh\left(\frac{R_0}{I_D}\right) + \sin\left(\frac{R_0}{I_D}\right) \right) - 2 \left( \cosh\left(\frac{R_0}{I_D}\right) - \cos\left(\frac{R_0}{I_D}\right) \right)}{\frac{R_0^2}{I_D^2} \left( \cosh\left(\frac{R_0}{I_D}\right) - \cos\left(\frac{R_0}{I_D}\right) \right) + \frac{R_0}{I_D} (3\gamma - 1) \left( \sinh\left(\frac{R_0}{I_D}\right) - \sin\left(\frac{R_0}{I_D}\right) \right)} \right]$$

$$I_D(\omega) = \sqrt{\frac{K_g}{4\pi f} \rho_g C_p}$$

$$\begin{aligned}\delta_{rad} &= \frac{2\pi f_n}{v} R_0 \\ \delta_{vis} &= \frac{2\mu_f}{\pi f_n \rho R_0^2} \\ \delta_{th} &= B(f, R_0) \frac{f_n^2}{f^2} \\ \delta_f &= \frac{6\mu_s T_s}{\pi f_n \rho R_0^3}\end{aligned}$$

All the damping factors are function of the frequency  $f$  and the bubble radius  $R_0$ . For instance, as from the term  $f_n^2/f^2$ , the thermal damping is only effective for intermediate frequencies (near the natural frequency  $f_n$ ). In fact, for high frequencies the process is adiabatic (no heat transfer due to the short period of the oscillations) and the polytropic exponent  $k$  equals  $\gamma$ , while for low frequencies the process is isothermal (the oscillations are sufficiently slow to allow the heat transfer to keep the bubble temperature constant) and the polytropic exponent  $k$  equals 1. Instead, for intermediate frequencies, like for instance around the natural frequency  $f_n$ , the temperature oscillates in the bubble and causes pressure variations that are out of phase with respect to the driving pressure.

The bubble dynamic model is used to study and predict the response of the bubble system to a pressure input (driving pressure). The major interest is the definition of a frequency range that maximizes the bubble oscillations and, therefore, the backscattered ultrasound signal. In order to derive the frequency response of the bubble, the system is analyzed for small oscillations and a Taylor first order approximation of Eq. (3.22) is considered. The resulting system is a typical second order linear system (like a damped mass-spring system, see [114], page 109) as given in Eq. (3.26), where  $\epsilon$  represents the small radius oscillation  $R - R_0$  for a driving pressure  $P(t)$  (see Fig. (3.9)).

$$\begin{aligned}m\ddot{\epsilon} + b\dot{\epsilon} + s\epsilon &= -4\pi R_0^2 P(t) \\ m &= 4\pi\rho R_0^3 \\ b &= 2\pi f m \delta_t \\ s &= 4\pi R_0 \left[ 3k \left( P_0 - P_v + \frac{2\sigma}{R_0} \right) - \frac{2\sigma}{R_0} + p_v + \frac{2S_p}{R_0} \right]\end{aligned}\tag{3.26}$$

---

$I_D$  is referred to as thermal diffusion length and is a function of the gas thermal conductivity  $K_g$ , the gas thermal capacity at constant pressure  $C_p$ , and the gas density  $\rho_g$  (see also [114]). This representation for the thermal damping was initially introduced by Devin (1959) and later developed by Eller (1970) and Prosperetti (1977).

The frequency response  $|\epsilon(f)|/|P(f)|$  of the system is given as in Eq. (3.27) [109, 114].

$$\frac{|\epsilon(f)|}{|P(f)|} = \frac{1}{R_0 \rho \sqrt{(f_n^2 - f^2)^2 + (f f_n \delta_t)^2}} \quad (3.27)$$

$f_n$  is the natural frequency of the bubble without damping and is given as in Eq. (3.28).

$$f_n = \frac{1}{2\pi} \sqrt{\frac{s}{m}} = \frac{1}{2\pi \sqrt{\rho} R_0} \sqrt{3k \left( P_0 - P_v + \frac{2\sigma}{R_0} \right) - \frac{2\sigma}{R_0} + P_v + \frac{2S_p}{R_0}} \quad (3.28)$$

Based on Eq. (3.27) and Eq. (3.28), the peak frequency response (resonance frequency) of the damped bubble is given as in Eq. (3.29).

$$f_0 = f_n \sqrt{1 - \left( \frac{\delta_t}{2} \right)^2} \quad (3.29)$$

As a consequence, the maximum oscillation, when for instance the viscous damping is included, is generated for a driving frequency  $f_0$  given as in Eq. (3.30) (see [109], pp. 305-306).

$$f_0 = \frac{1}{2\pi \sqrt{\rho} R_0} \sqrt{3k \left( P_0 - P_v + \frac{2\sigma}{R_0} \right) - \frac{2\sigma}{R_0} + P_v + \frac{2S_p}{R_0} - \frac{4\mu_f^2}{\rho R_0^2}} \quad (3.30)$$

As already mentioned, the de Jong model, as well as all the models in literature, are based on a series of assumptions that are not realistic. In particular, in a real clinical application there is a large number of bubbles that may interact with each other with multiple thermal and radiation energy exchanges. The interaction forces are not considered in the presented model. Moreover, as recently observed by de Jong and Versluis using an ultra-fast camera, the assumption of spherical symmetry of the bubble oscillations is not realistic [135, 136]. Bubbles oscillate using several different geometrical modes, so that more sophisticated models are needed. Also a large variability of the maximum bubble expansion for same driving pressures and same bubble original diameters is recognizable. This phenomenon is complex to explain and might be the result of different elastic properties of the bubble shell [137]. In this case, the elasticity parameter  $S_p$  could be substituted with a statistical distribution.

However, especially for small pressure (low MI) and low concentrations (negligible interaction between bubbles), the available models can already predict with sufficient accuracy the interaction between ultrasound and bubbles and are widely adopted for contrast quantification [30, 98, 104, 130, 138–141]. In particular, contrast

quantification involves the estimation of the agent *echogenecity*<sup>27</sup>, which is commonly determined by the measurement of the ultrasound backscatter.

The ultrasound backscatter is defined by the *backscatter coefficient*  $\beta$ , which is the *scattering cross-section* ( $\text{cm}^2$ ) per unit volume ( $\text{cm}^3$ ) and per scattering angle (sr). The scattering cross-section of a bubble is the ratio between the power scattered in all directions and the incident acoustic intensity. The scattered power equals the energy that is dissipated because of the radiation damping. In general, if the damping coefficient equals  $b$ , then the force  $F$  that is necessary to compensate for it equals  $\dot{\epsilon}b$ . For  $\epsilon(t) = \epsilon_0 \cos(2\pi ft)$ , the average power  $W$  (energy per cycle) that is dissipated is given as in Eq. (3.31), where  $T = 1/f$ .

$$W = \frac{1}{T} \int_0^T (F \cdot \dot{\epsilon}(t)) dt = \frac{1}{T} \int_0^T (\dot{\epsilon}(t)b \cdot \dot{\epsilon}(t)) dt = \frac{1}{2} 4\pi^2 f^2 \epsilon_0^2 b \quad (3.31)$$

The re-radiation average power is given as in Eq. (3.31) for radiation damping coefficient  $b_{rad} = \delta_{rad} m \omega = 4\pi \rho R_0^4 \omega^2 / \nu$ . Combining Eq. (3.31) with Eq. (3.27), the scattering cross-section  $\Sigma$  for a single bubble, which is defined as the ratio between average scattered power and ultrasound intensity, is a function of the radius  $R$  of the bubble and the ultrasound frequency  $f$  as given in Eq. (3.32), where  $W$  is the average scattered power,  $I_0$  is the amplitude of the incident intensity ( $I_0 = P_0^2 / 2Z$ ),  $Z = \text{Re}[Z_{rad}] = 8\pi^2 f R_0^4 \rho k$ , and  $f_n$  is the natural frequency of the bubble [109, 110, 114, 120, 130, 142].

$$\Sigma(R_0, f) = \frac{W}{I_0} = \frac{\frac{1}{2} 4\pi^2 f^2 \epsilon_0^2 b}{\frac{P_0^2}{2Z}} = \frac{4\pi R_0^2}{\left[ \left( \frac{f_n(R_0)}{f} \right)^2 - 1 \right]^2 + \delta_t(R_0, f)} \quad (3.32)$$

The term  $\delta_t(R_0, f)$  summarizes all the damping factors. Since the adopted model represents a second order system, the scattering cross-section shows a resonance frequency where the system gives the strongest response in terms of scattered power. For  $f \gg f_n \implies \Sigma(R_0, f) \simeq 4\pi R_0^2$ , which is the physical cross-section, i.e., the bubble surface [130, 139]. The resonance frequency is inversely proportional to the radius  $R_0$  of the bubbles at the equilibrium. Therefore, the total scattering cross-section  $\Sigma_{tot}(f)$  depends on the normalized radius distribution  $n(R)$  of the bubbles as given in Eq. (3.33) [143, 144].

$$\Sigma_{tot}(f) = \int_{R_{min}}^{R_{max}} n(R) \Sigma(R, f) dR \quad (3.33)$$

<sup>27</sup>Echogenecity is the ability of the agent to generate echoes when interacting with ultrasound waves.



$n(R)$  is a characteristic of the specific contrast. Assuming an isotropic scattering and a low concentration of bubbles, the backscatter coefficient  $\beta$  (expressed in  $\text{cm}^{-1} \cdot \text{sr}^{-1}$ ) is given as in Eq. (3.34), where  $\rho_n$  is the number of bubbles per unit volume (concentration) [143].

$$\beta(f) = \frac{\rho_n \Sigma_{\text{tot}}(f)}{4\pi} \quad (3.34)$$

Therefore, the backscatter coefficient is a linear function of the UCA concentration [6, 30, 98, 140, 143–145] and the backscattered acoustic intensity  $I$  that is measured by the transducer can be approximated as in Eq. (3.35), where  $I_0$  is the acoustic intensity insonating the contrast,  $dV = dz \cdot dA$  is the volume of insonated contrast, and  $z$  is the distance between  $dV$  and the transducer<sup>28</sup>.

$$I = \frac{dV}{z^2} \beta(f) I_0 = \frac{dV}{z^2} \frac{\rho_n \Sigma_{\text{tot}}(f)}{4\pi} I_0 \quad (3.35)$$

Possible experimental solutions for the estimation of  $\beta(f)$  are based on the measurement of the ratio between the acoustic intensity coming from the contrast and from an acoustic mirror (100% reflecting layer) when contrast is absent [98, 104, 110]. The result of the measurement is the ratio  $I/I_0$  for different frequencies, which, after taking into account the geometry of the system, allows the estimation of the spectrum  $\beta(f)$ . When  $\beta(f)$  is averaged over the frequency spectrum of the ultrasound transducer it is referred to as *Integrated Backscatter Index* (IBI) [146].

The interaction between ultrasound and UCA is not only described by the backscatter coefficient, but also by the attenuation coefficient, which represents the loss of acoustic pressure in Neper per cm. It occurs along the distance that the ultrasound beam covers through the contrast solution, and it is related to the three main factors that are listed below.

- Micro-bubble decay ( $a_d$ ) due to both chemical decay (dissolution) and dispersion through the capillaries.
- Diffusion or scattering of the acoustic energy in multiple directions ( $a_s$ ).
- Viscous and thermal damping of the ultrasound waves ( $a_\delta$ ) as in Eq. (3.25).

It is assumed that the total increase of attenuation  $\Delta a$  is given as in Eq. (3.36), where  $a_d$  is proportional to the chemical constituents of the contrast while  $(a_s + a_\delta)$  is proportional to the concentration of the contrast.

$$\Delta a = a_d + a_s + a_\delta \quad (3.36)$$

---

<sup>28</sup>An homogeneous scattering with a spherical symmetry of the backscattered pressure is assumed (see [134] pp. 357-361).

The attenuation that is expressed by the term  $a_s + a_\delta$  is referred to as *extinction*. It is possible to define an extinction cross section  $\Sigma_e$  as the sum of the backscatter cross section  $\Sigma$  (see Eq. (3.32)) and the absorption cross section  $\Sigma_a$ . Similarly to Eq. (3.32), the absorption cross section is defined as the ratio between the loss of power and the incident intensity  $W_{loss}/I$ . Power can be always expressed as a linear function of the damping coefficient  $b$  as given in Eq. (3.31). Since  $b = 2\pi\delta m f_n$  by definition, the ratio between the loss of power caused by a specific damping and the acoustic scattering  $W_{loss}/W$  equals the ratio between the respective damping factors. This concept can be formulated as given in Eq. (3.37) (see [114] pp. 25-28 and [132] pp. 302-304).

$$\Sigma_a = \left( \frac{\delta_{vis} + \delta_{th} + \delta_f}{\delta_{rad}} \right) \Sigma \quad (3.37)$$

Since  $\Sigma_e = \Sigma_a + \Sigma$ ,  $\Sigma_e$  is also given as in Eq. (3.38).

$$\Sigma_e = \left( \frac{\delta_t}{\delta_{rad}} \right) \Sigma \quad (3.38)$$

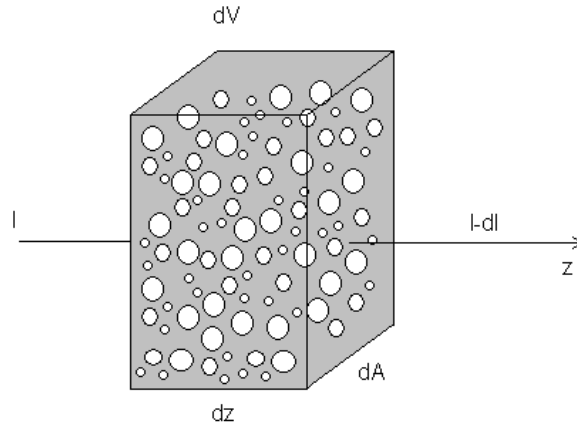


**Figure 3.10:** Schematic passage of an ultrasound beam of intensity  $I$  through a volume sample  $dV$  of bubbles. The volume length is  $dz$  while the cross-section area is  $dA$ . The intensity loss through the sample equals  $dI$ .

The extinction coefficient  $a_e = a_s + a_\delta$  can be derived from the extinction cross section. In fact, from the definition of extinction cross section, the differential loss of power  $dW_{loss}$  can be written as given in Eq. (3.39), where  $dV = dA \cdot dz$  is a volume

sample as shown in Fig. (3.10). The total extinction cross-section  $\Sigma_{e_{\text{tot}}}$  is derived from  $\Sigma_e$  as given in Eq. (3.33) for the scattering cross-section  $\Sigma_{\text{tot}}$ .

$$dW_{\text{loss}} = I \left( \rho_n \int_{R_{\text{min}}}^{R_{\text{max}}} n(R) \Sigma_e dR \right) dV = I \rho_n \Sigma_{e_{\text{tot}}} dAdz \quad (3.39)$$

Therefore, the loss of intensity  $dI$  is given as in the differential Eq. (3.40), whose integral is given as in Eq. (3.41).

$$dI = I \left( \rho_n \int_{R_{\text{min}}}^{R_{\text{max}}} n(R) \Sigma_e dR \right) dz \quad (3.40)$$

$$I(z) = I_0 e^{-\rho_n \Sigma_{e_{\text{tot}}} z} \quad (3.41)$$

As a consequence, the extinction coefficient  $a_e$  is given as in Eq. (3.42), where the factor 2 in the exponent derives from the fact that the attenuation coefficient is defined in terms of pressure loss, which is related to the intensity by a quadratic function ( $P = \sqrt{2ZI}$ ).

$$a_e = \frac{\rho_n}{2} \Sigma_{e_{\text{tot}}} = \frac{\rho_n}{2} \int_{R_{\text{min}}}^{R_{\text{max}}} n(R) \Sigma_e dR \quad (3.42)$$

For shell encapsulated bubbles the first term  $a_d$  in Eq. (3.36) can be neglected if the measurement is executed in a short time (i.e., few minutes). As a result, the attenuation is linearly proportional to the concentration of the contrast  $\rho_n$ , as also shown in Eq. (3.34) for the backscatter coefficient  $\beta$  [5, 98, 110, 143, 144, 147]. If only the extinction is considered,  $a_e$  in Eq. (3.42) corresponds to the attenuation coefficient  $a$  introduced in Eq. (3.7).

Because of the linear relation between total attenuation and contrast concentration, some authors have considered the opportunity of measuring the attenuation-time curve rather than the backscatter-time curve for the estimation of fluid-dynamic parameters (see section 4.1) [5].

The same set up that is used for backscatter measurements can be also employed for attenuation measurements [98]. A clear description can be also found in [114] (pp. 89-94).

According to Eq. (3.7), the received echo intensity can be rewritten as given in Eq. (3.43), where  $\beta$  is the backscatter coefficient in the examined organ (without contrast),  $a$  is the attenuation coefficient of tissue,  $z_0$  is the depth of the organ that

is opacified, and  $\Delta z$  is the depth of the insonated volume sample  $dV$  within the opacified organ.

$$I = \frac{dV}{z^2} \beta e^{-4a(z_0 + \Delta z)} I_0 \quad (3.43)$$

The return distance that is covered by ultrasound (after reflection) is taken into account by the factor 4 at the exponent (instead of 2). Assuming  $\Delta\beta$  to be the increase of backscatter proportional to the concentration of the contrast, combining Eq. (3.36) with Eq. (3.43), the intensity  $I$  that is received from distance  $z_0 + \Delta z$  is given as in Eq. (3.44).

$$I = \frac{dV}{z^2} (\beta + \Delta\beta) I_0 e^{-4a(z_0 + \Delta z) - 4\Delta a \Delta z} \quad (3.44)$$

This is the model that is usually adopted to interpret the backscattered intensity. In fact, both  $\Delta\beta$  and  $\Delta a$  are linearly proportional to the contrast concentration. A good measure of the efficacy of contrast agents in terms of ultrasound detection, which considers both backscattering and attenuation, is represented by the *Scattering-To-Attenuation Ratio* (STAR)  $\frac{\Sigma_{\text{tot}}}{\Sigma_{\text{e tot}}} = \frac{\delta_{rad}}{\delta_r} = \frac{2\pi \Delta\beta}{\Delta a_e}$  [104, 143, 144].

**Remark** *Cost is a potential issue for ultrasound contrast agents. At an approximate cost of \$100 per dose, ultrasound contrast agents currently cost about as much as the ultrasound imaging examination itself. However, the amount of contrast in one vial is sufficient for many indicator dilution inspections (up to 100), so that a single clinical inspection becomes economically inexpensive.*

The contrast adopted for the present study is SonoVue® (previously known as BR1, trademark of Bracco Diagnostic, Milan). Its clinical use in the Netherlands was allowed in the beginning of 2002<sup>29</sup>. SonoVue® is a sulfurhexafluoride bubble encapsulated in a mono-layer phospholipidic shell. The diameter varies from 0.7  $\mu\text{m}$  to 10  $\mu\text{m}$ , with an average value equal to 2.5  $\mu\text{m}$  [130, 141, 148, 149].  $SF_6$  is a large molecule (molecular weight equal to 146) with low solubility in water (Ostwald solubility<sup>30</sup> equal to 0.0054). As a consequence, the molecule diffusion is low and the contrast very stable. In addition, the presence of a shell creates a strain that compensates the Laplace pressure and stabilizes bubbles against dissolution. For instance, the video-intensity decay due to bubble dissolution is 0.2dB/min [150, 151], which is not significant within an IDC measurement procedure that lasts for about 1 minute. However, once the SonoVue® solution is reconstructed, it should be used within six to eight hours. The SonoVue® solution is isotonic and its viscosity  $\mu_f$  is similar to that of blood [149].

<sup>29</sup>Since the middle of 2004 the clinical use of SonoVue® has been temporary restricted to non-echocardiographic applications by the European Agency for the Evaluation of Medicinal Products (EMA) due to some allergic reactions in heart failure patients.

<sup>30</sup>Volume of gas dissolved per unit volume of solvent.

The echogenicity of SonoVue® was studied using fundamental harmonic echography with a frequency range from 1MHz to 7MHz, representative of the clinical use [130]. The results prove that the larger the bubbles the higher the backscattered power, and the lower the resonance frequency  $f_0$ . As a result, the bubble count is a poor indicator of the echogenicity of SonoVue®. Much better is the volume measurement, which is highly related with the amount of larger bubbles. As a consequence, the best contrast response (large oscillations) to a driving alternate pressure is obtained for a frequency of about 3MHz, which is the resonance frequency of the largest bubbles [130].

This echogenicity study for SonoVue® was performed by fitting (least square fit) the backscatter cross-section model in Eq. (3.32) to experimental measurements. It was also concluded [130] that the constant thickness assumption of the de Jong model shows a better interpolation of the experimental measurements with respect to the constant shell volume assumption of other models such as, for instance, the Hoff model [114].

Micro-bubbles are not only used as contrast agents for echographic inspections. An important application field regards the delivery of drugs and genes [152]. Bubbles are loaded with either a drug or a gene. A targeting ligand in the bubble shell makes the injected bubbles settle and attach to specific sites [153]. Once the bubble is located in the right site, i.e., where the drug is intended to be delivered, a high MI ultrasound beam makes the bubbles collapse and release the drug. This technique allows both targeting the delivery and increasing the drug uptake. It is considered as a real asset for gene and radionuclide therapies [154].

### 3.3 Echographic modes for contrast detection

Specific imaging methods have been developed in order to preferentially detect the echoes from the agent while suppressing those from other structures, such as tissue. Tissue structures are basically linear (i.e., described by linear equations) while the contrast micro-bubbles, as from Eq. (3.22), are non-linear. Therefore, all the methods for contrast detection exploit the bubble non-linear behavior. Applications are mainly in echo-Doppler and B-Mode analysis. Our interest concerns the second application.

The non-linear behavior of the bubbles is mainly evident for driving pressures above 50kPa [139]. Above this threshold, the backscatter cross-section  $\Sigma$  differs from the physical value of  $2\pi R_0^2$  according to Eq. (3.32). However, to avoid the bubble destruction the driving pressure should be smaller than 800kPa [155]. Therefore, the MI (mechanical index), which is the standard indicator of the exposure of bubbles to ultrasound, should be bounded between 0.02 and 0.35 (for a central frequency of 5MHz).

The nonlinear echoes produced by ultrasound contrast agents presents an opportunity to distinguish the echoes due to contrast from those due to tissue [107, 108, 139, 156–158]. These methods, referred to as *harmonic imaging*, are now widely available in ultrasound scanners. The objective of these harmonic imaging techniques is to maximize the Contrast-to-Tissue Ratio (CTR) [159–161]. In *Harmonic Mode*, the system transmits at one frequency (resonance frequency of the transducer), but is tuned to receive echoes preferentially at a different frequency. Therefore, the frequency transfer function of the transducer must be broad band.

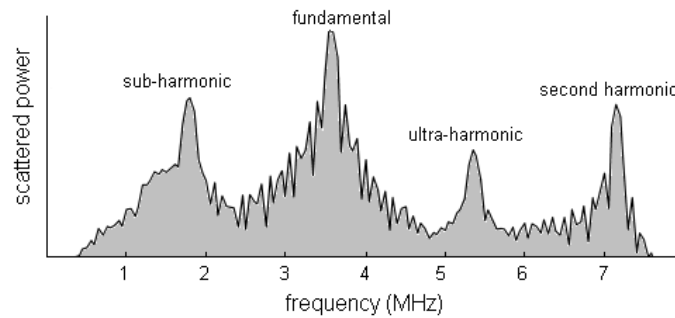


**Figure 3.11:** Frequency response spectrum of SonoVue® following excitation in fundamental harmonic.

As shown in Fig. (3.11), the frequencies that are commonly used for contrast detection are distinguished in sub-harmonic (about half of the fundamental harmonic), ultra-harmonic (between the fundamental and the second harmonic), second harmonic, and higher harmonics [107, 108, 162, 163]. For these frequencies, the signal due to contrast shows larger amplitudes with respect to that due to tissue. In fact, due to the linear response, tissue echoes contain approximately the same frequency components as the pressure waves that are generated by the transducer (fundamental harmonic). Fig. (3.11) shows the frequency spectrum of the power backscatter of SonoVue® [107].

The implementation of filters in order to detect specific frequencies is not the only solution to enhance the bubble detection pulses. Alternative techniques involve the modulation of the amplitude and the phase of the transmitted ultrasound. They are referred to as *power modulation imaging* and *phase modulation imaging* respectively (see Fig. (3.12)). The most common phase modulation technique is referred to as *pulse inversion*. Two pulses  $p_1(t)$  and  $p_2(t) = -p_1(t)$  are transmitted in sequence into tissue. The sum of the received echoes results in the cancellation of the echoes from linear structures (i.e., tissues). Instead, the echoes from non-linear reflectors (i.e., from the bubbles) do not cancel, resulting in a selective detection of the contrast agents that is especially evident in the even harmonics.

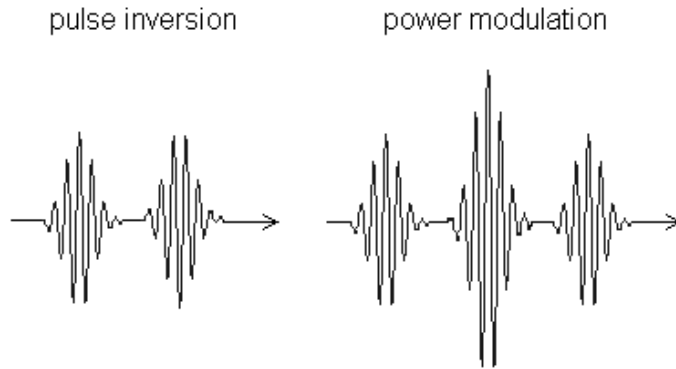


**Figure 3.12:** Examples of phase modulation (*pulse inversion*) and power modulation pulse sequences.

The implementation of an amplitude modulation (*power modulation*) allows detecting the bubble non-linear response in fundamental harmonic. This technique is economically more convenient, since it does not require the employment of expensive broad-band transducers. Although the best response in terms of high harmonics is obtained for middle MI, usually modulation imaging techniques are used together with low MI ( $MI \leq 0.3$ ) to avoid bubble disruption. Typical implementations use the transmission of three adjacent ultrasound pulses  $p(t)$ . The amplitude of the central pulse is twice as that of the side pulses. The receiver sums the reflections of the side pulses and subtracts the reflection of the central pulse. Due to the bubble non-linear response,  $2h(p) \neq h(2p)$ , where  $h(\cdot)$  represents the bubble response to the pressure pulses. Therefore, this technique allows detecting the non-linear response of bubbles while deleting the linear response of tissue structures. Several implementations also combine Power Modulation and Pulse Inversion (PMPI) with a number of different pulse sequence schemes.

The non-linear oscillations of bubbles can be also excited by use of particular pulses, different from the typical Gaussian pulses at fixed frequency. For instance, the use of chirp pulses<sup>31</sup> results in enhanced bubble responses and, therefore, it could be used for contrast detection imaging [164].

<sup>31</sup>A pulse is referred to as a chirp pulse of the order  $n$ , if and only if, its instantaneous frequency  $f(t)$  increases and/or decreases linearly within the pulse, and the first time derivative of the instantaneous frequency is a step function with the number of time intervals (where it is constant) equal to  $n$ .

Despite the use of a low MI, the bubble destruction rate is sometimes significant. A reduction of this effect can be obtained by use of Intermittent Harmonic Imaging (IHI) [156, 157]. An image is reconstructed every  $n$  cardiac cycles ( $n \geq 1$ ) in triggered mode<sup>32</sup>, so that the number of pressure pulses is reduced.

The use of high MI ( $MI > 1$ ) produces a high-rate bubble disruption [139, 155, 165]. Some techniques use the bubble disruption as a contrast imaging technique [166, 167]. Two pulses are transmitted in fast sequence. The first one is reflected and destroys the bubble. After the bubble destruction, the second pulse is not reflected. By taking the difference of the reflections from the two pulses it is easy to distinguish bubbles from tissue, unless the fast motion of tissue is confused with the bubble destruction (clutter noise). More sophisticated implementations of the same concepts are possible and are referred to as release-burst imaging [107, 158, 167].

The destruction of micro-bubbles followed by a low MI detection phase is also used as a specific technique for the measurement of the myocardial flow. After perfusion, the contrast in the myocardium is destroyed by a high MI ultrasound burst. The following *replenishment curve* is detected by recording the acoustic or video intensity-versus-time curves in defined regions of interest in the myocardium. The interpolation of these curves by a specific model<sup>33</sup> allows the quantification of the myocardial flow [85, 86].

The improved sensitivity of the ultrasound system for contrast detection has also an advantage in terms of resolution. The ultrasound frequency must be limited due to the attenuation, which increases together with the frequency (see Eq. (3.9)). Improved detection modes allow increasing the ultrasound frequency, resulting in higher axial and lateral resolution of the system (see section 3.1.2 and Eq. (3.13)).

### 3.4 Echocardiography

The focus of this section is on classical B-Mode echography, which shows a “slice” of the body. The object of this study is the human heart. When echography is applied to the heart it is referred to as *echocardiography*.

Until the mid 80’s only the *transthoracic echocardiography* (TTE) was used for cardiac investigations. The name derives from the fact that the ultrasound transducer is positioned on the chest (thorax) of the patient. From that position, several windows can be found between the ribs in order to obtain different views (slices) of the heart

<sup>32</sup>The scanner is triggered with the electrocardiogram, i.e., the scanner timing is controlled by the cardiac electrical activity.

<sup>33</sup>The time-concentration curve  $C(t)$  during replenishment is modelled by the following exponential curve

$$C(t) = A \left( 1 - e^{-\beta t} \right),$$

where  $A$  and  $\beta$  are the model parameters and  $t$  is the time. The flow is then proportional to  $A\beta$ .



[46]. Fig. (3.13) shows the TTE windows together with the apical views, which are used in this study.

Nowadays, also another technique is available [168]. Thanks to the latest technology, the ultrasound transducer could be miniaturized in order to be introduced through the mouth into the esophagus or the stomach (see Fig. (3.14)). It is placed on the tip of a catheter and its orientation can be controlled by an external hold, which is referred to as proximal housing.

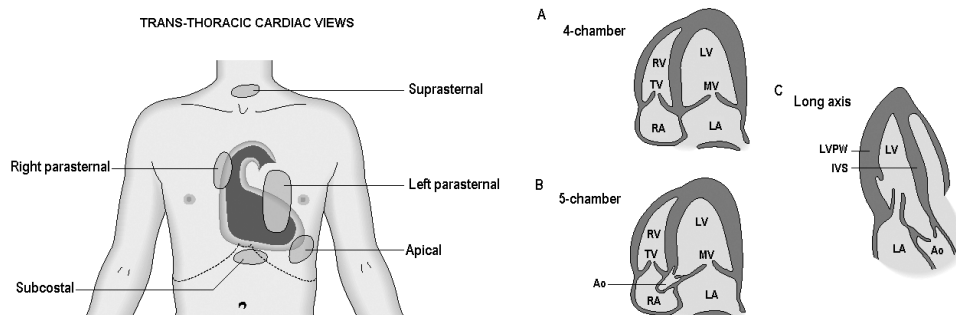


**Figure 3.13:** Trans-thoracic windows for echocardiography. On the right the apical views are shown. The four chamber view (A) is particularly interesting. It allows the simultaneous insonation of the four chambers, and, therefore, it is widely adopted in this study.

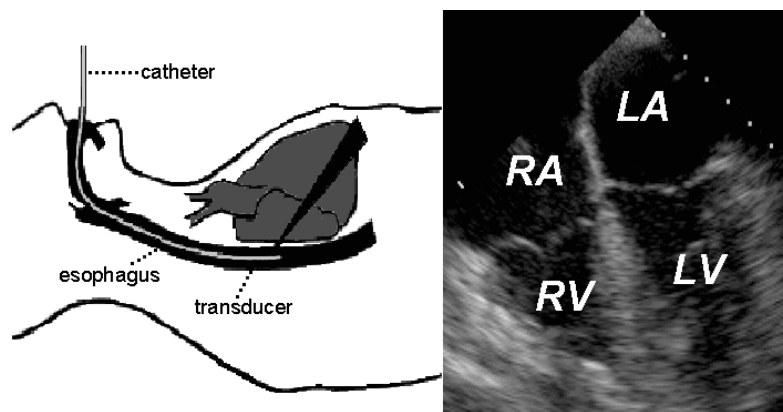


**Figure 3.14:** Transesophageal echocardiography. Example of a four-chamber view.

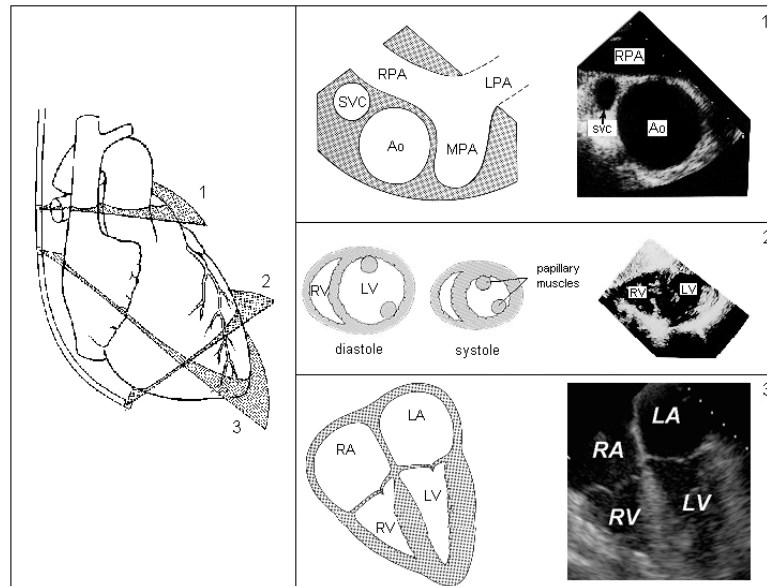


**Figure 3.15:** Three examples of TEE views. View 1 shows the aorta (Ao), the superior vena cava (SVC), and the pulmonary artery (PA), as seen from the upper esophagus. View 2 shows the section of both ventricles at the mid-papillary muscle level cross-section, as seen from the stomach. View 3 shows the four-chamber view, as seen from the mid-part of the esophagus.

Since the heart is analyzed from the esophagus, this technique is known as *trans-esophageal echocardiography* (TEE) and has a big advantage over the classical TTE. In fact, using TTE the ultrasound beam has to pass through the ribs and the lungs, resulting in lower quality images. Furthermore, added difficulties arise from the female breast and the fat tissue when dealing with obese patients. Instead, the esophagus is directly behind the heart, separated only by a thin layer of tissue. That is the reason why the TEE produces higher Signal-to-Noise Ratio (SNR) images, which are also suitable for contrast detection [169]. On the other hand, a disadvantage is that the method is unpleasant for the patient, since the transducer has to be inserted through the mouth. However, for applications during surgery or in intensive care unit, there are no disadvantages and TEE is becoming widely used in the clinical practice.

Fig. (3.15) shows some of the TEE views. The third view in Fig. (3.15) allows to observe simultaneously all the four cardiac chambers (it is referred to as *four-chamber view*). As for the TTE investigation, it is an interesting view and allows the simultaneous measurement of echo-contrast dilution curves from all the cardiac chambers.



## Chapter 4

# Ultrasound contrast agent dilution curve modelling

*Carpe viam, et suspectum perface munus (Virgilius).*

The interaction between ultrasound and UCA allows detecting the passage of the contrast in any site of the circulatory system. If a Region of Interest (ROI) is fixed and the signal due to the contrast passage recorded versus time, an acoustic (or video) intensity curve can be derived. The first section of this chapter (section 4.1) regards the calibration process and all the issues concerning the relation between contrast concentration and detected signals. The ultimate goal is the derivation of an IDC. Once an IDC is derived, the following sections provide with an overview of the models that are employed for the IDC interpretation (section 4.2) and a detailed derivation of two specific models: the Local Density Random Walk model (LDRW model, section 4.2.3) and the First Passage Time model (FPT model, section 4.2.2). The LDRW model is used in the rest of this study for the interpolation of measured UCA IDCs while the FPT model is compared to the LDRW model in the next chapter to explain some interesting concepts regarding volume measurements.

### 4.1 Calibration of acoustic and video intensity curves

In the previous chapter (section 3.2) the interaction between UCA and acoustic intensity is characterized for a small driving pressure (low MI) and contrast concentrations. The bubble is approximated by a linear second order mechanical system and a frequency response is derived (Eq. (3.26)). Within the reported representation, the relationship between contrast concentration and acoustic backscatter coefficient is linear (Eq. (3.34)). Among the assumptions that are made for the UCA characterization, very important is that regarding the interaction forces between neighbor bubbles, which are neglected. This assumption is realistic only for low contrast concentrations. As a consequence, our study focuses on a low UCA concentration range

using a low MI ( $MI \leq 0.3$ ). With this hypothesis, not only the backscatter coefficient, but also the attenuation coefficient is linearly related to the contrast concentration (Eq. (3.41) and Eq. (3.42)).

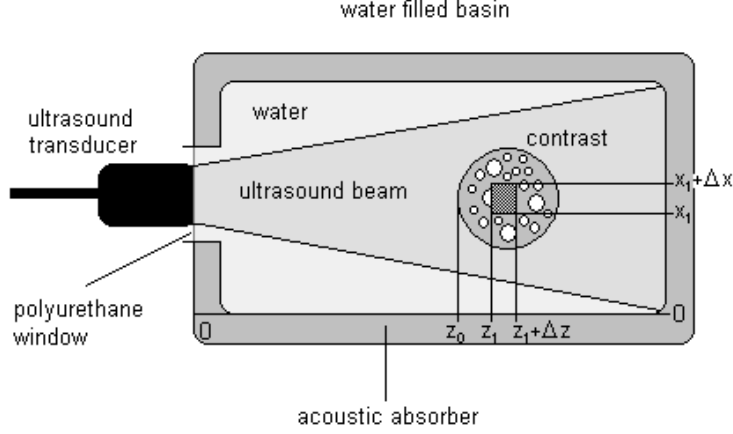


**Figure 4.1:** Measurement set-up for acoustic intensity calibration.

In this study, the measurements of acoustic and video intensity for the IDC measurement are performed in a ROI. Therefore, the equations derived in section 3.2 must be averaged over a bi-dimensional ROI. Using Eq. (3.44), the measurement at distance  $z$  is replaced by the measurement of the average intensity  $I_{av}$  over a rectangular ROI of size  $\Delta z \times \Delta x$ , which is shown in Fig. (4.1). With reference to Fig. (4.1), neglecting the attenuation of the medium  $a$  and the geometric intensity decay  $z^{-2}$ , which can be compensated by the ultrasound scanner [134, 140, 145], Eq. (3.44) becomes as given in Eq. (4.1).

$$\begin{aligned}
 I_{av} &= \frac{1}{\Delta z \Delta x} \int_{z_1}^{z_1 + \Delta z} \int_{x_1}^{x_1 + \Delta x} (\beta + \Delta\beta) I_0 e^{-4(\Delta a)z} dz dx = \\
 &= \frac{I_0(\beta + \Delta\beta)e^{-4(\Delta a)(z_1 - z_0)}}{4\Delta z \Delta a} (1 - e^{-4\Delta z \Delta a})
 \end{aligned} \tag{4.1}$$

In the low concentration range and for  $\Delta z$  sufficiently small, the product  $\Delta a \cdot \Delta z$  is very small. As a consequence, a first order approximation of Eq. (4.1) is applicable and the result is given as in Eq. (4.2).

$$I_{av} = I_0 (\beta + \Delta\beta) e^{-4(\Delta a)(z_1 - z_0)} \tag{4.2}$$

This first order approximation is adopted to model the attenuation in the present study.

A specific experiment was made in order to test the linearity of the relation between backscattered acoustic intensity and contrast concentration. A Sonos 5500 ultrasound scanner (Philips Medical Systems) was used to generate B-mode videos. The scanner was set in Tissue Contrast Enhancement mode at 25 Frames Per Second (FPS) and the MI fixed to 0.1. Series of three adjacent ultrasound pulses of four cycles at 1.9MHz are transmitted. The amplitude of the central pulse is twice that of the side pulses. The receiver sums the reflections of the side pulses and subtracts the reflection of the central pulse. This technique, which is a specific implementation of the power modulation mode (see section 3.3), allows the enhancement of the bubble non-linear response and the cancellation of the tissue linear response.

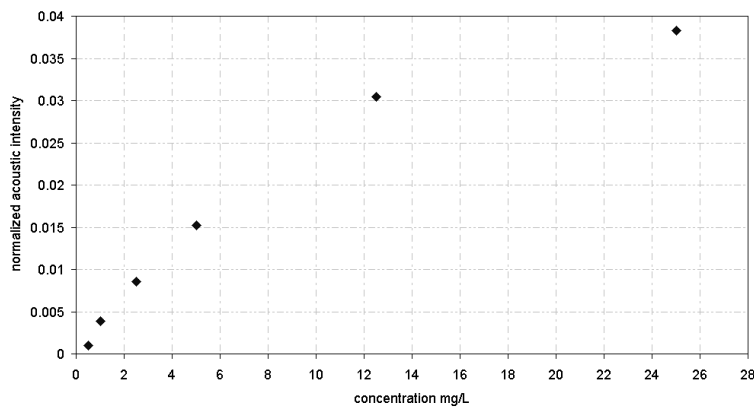


*Figure 4.2: Acoustic intensity calibration curve for the power modulation mode using a Sonos 5500 ultrasound scanner. The backscattered acoustic intensity is measured by software Q-Lab for SonoVue® concentrations going from 0.5mg/L to 25mg/L.*

The adopted contrast for UCA IDC measurements was SonoVue® which is delivered in a septum-sealed vial containing 25mg of lyophilized product in SF<sub>6</sub> gas. The suspension of gas micro-bubbles is reconstructed before use by introducing 5ml of saline (0.9% NaCl solution) through the vial septum, followed by 30 seconds of hand shaking. After that, the product is ready for further dilutions. Different dilutions of SonoVue® in 100ml of saline (concentrations varying from 0.5mg/L to 25mg/L) were prepared in small rubber bags and submerged in a water-filled basin for a good acoustic impedance matching as shown in Fig. (4.1). The basin water was degassed to avoid the formation of scattering bubbles. The ultrasound transducer was separated from water by a thin polyurethane window in the basin wall. The basin was

entirely covered by an acoustic absorber layer made of sponges to avoid reverberation noise. The distance between the transducer and the contrast bag was fixed and equal to 8cm. The acoustic intensity was measured by software Q-Lab® (Philips) for acoustic quantification.

Fig. (4.2) shows the detected acoustic intensity using the described harmonic setting. Above 12.5mg/L the attenuation effect becomes evident. Below this threshold, the correlation coefficient between concentration and acoustic intensity is 0.99 and the relation is well approximated by a linear function. Therefore, the contrast concentration is linearly related to the measured acoustic intensity for low concentrations ( $\leq 12.5\text{mg/L}$ ). For equal transmitted intensity, the use of specific contrast modes allows reducing the injected dose of contrast with a consequent improvement of the linear relation between contrast concentration and backscattered acoustic intensity.

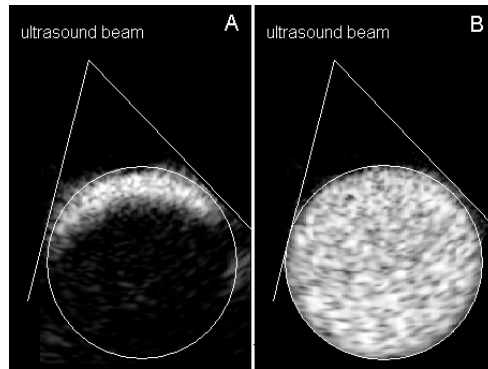


**Figure 4.3:** In figure A, a 250mg/L SonoVue® dilution results in a half moon shape (shadowing effect) of the detected backscattered intensity (power-modulation scanner setting) due to attenuation. In figure B, the detection of a 12.5mg/L SonoVue® dilution is shown.

For very concentrated dilutions, the first layer of contrast that is intercepted by the ultrasound beam attenuates a large fraction of the incoming energy and produces a strong *shadow effect* to the rest of the contrast, which remains undetected [5, 170]. Typical evidence of the shadowing is the resulting *half moon* shape of the detected contrast dilution. An example for a 250mg/L concentration of SonoVue® is shown in Fig. (4.3) (the scanner setting is the same as for the power modulation calibration in Fig. (4.2)). Due to this effect, some authors have shaped the ROI as a half (or quarter) moon in order to minimize the influence of shadowing on contrast quantification [171]. The employment of different ROIs, from circular to a moon quarter, have been also considered.

Several ultrasound scanners do not provide with any access to the RF signal or permit any B-mode acoustic intensity quantification. However, also the B-mode

video output, which is available in every scanner, can be a suitable signal for contrast quantification. The resulting technique is referred to as videodensitometry and consists in the measurement of the average gray level that the contrast passage produces in the video output of the ultrasound scanner. Despite the linear relation between acoustic intensity and contrast concentration, for the videodensitometric IDC measurement also the relationship between gray levels and acoustic intensity must be established.

The ultrasound transducer performs a linear conversion between ultrasound pressure and electrical voltage (see section 3.1.1). After demodulation, the voltage is quantized into gray-levels by means of a non-linear function, which is usually implemented as a logarithmic-like compression [145, 172]. In addition, the gamma compensation<sup>1</sup> and the effects of the machine setting (gain and time-gain compensation) should also be considered. For low contrast concentrations and a well adjusted time-gain compensation  $T(z)$ , the attenuation effect can be neglected [145]. Moreover, in modern scanners, the gamma compensation can be always set as linear. If  $G(z)$  is the gray level for depth  $z$ ,  $G_0$  is the gain, and  $L(\cdot)$  is the non linear compression function, then the backscattered intensity that is given in Eq. (3.35) for a volume  $dV$  at distance  $z$  from the transducer is transformed into gray levels as given in Eq. (4.3).

$$G(r) = G_0 L \left( \sqrt{\frac{(dV)T(z)e^{-4(\Delta a)z}}{z^2} (\beta + \Delta\beta) I_0} \right) \approx G_0 L \left( \sqrt{(dV)(\beta + \Delta\beta) I_0} \right) \quad (4.3)$$

The squared root is due to the fact that the gray levels are quantized from the voltage signal, which is linearly related to the ultrasound pressure. The contrast concentration is assumed to be homogeneous and the resulting attenuation  $\Delta a$  is considered as constant. Eq. (4.3) does not depend on the distance  $z$ , so that the average value over an extended ROI is also given by the same equation.

If  $L(\cdot)$  performs a logarithmic compression, the transformation in Eq. (4.3) can be modelled as given in Eq. (4.4), where  $a_0$ ,  $a_1$ , and  $a_2$  are the parameters of the model, and  $G(\rho_n)$  is the mean gray-level as a function of the UCA concentration  $\rho_n$ .

$$G(\rho_n) = a_0 \log(a_1 \rho_n + a_2) \quad (4.4)$$

The term  $(a_1 \rho_n + a_2)$  represents the linear relation between backscattered intensity and UCA concentration as given by the term  $(dV)(\Delta\beta + \beta)I_0$  in Eq. (4.3).  $\Delta\beta$  is a linear function of the contrast concentration, so that  $(dV)\Delta\beta I_0 = a_1 \rho_n$ , where  $\rho_n$  is the contrast concentration in the volume sample  $dV$  at distance  $z$  from the transducer.

---

<sup>1</sup>Since monitors introduce a nonlinear relation between luminance ( $l$ ) and input voltage ( $v$ ), which is referred to as *gamma* and can be expressed as  $l = v^\gamma$  (typically  $\gamma = 2.2$ ), usually a compensation for this effect is implemented (*gamma compensation*).



The coefficient  $a_2$  is equal to  $(dV)\beta I_0$  and  $a_0$  represents three factors: the squared relation between voltage and ultrasound intensity, the gain  $G_0$ , and the unknown basis of the logarithmic compression<sup>2</sup>.

The model in Eq. (4.4) is used to fit the experimental calibration data. The measurements shown in Fig. (4.2) were converted by software Q-Lab® into digital video files (AVI-DivX format<sup>3</sup>) as shown in Fig. (4.4). The measured video intensities were interpolated by the model in Eq. (4.4) using a Levenberg-Marquardt fitting algorithm (see section 5.1). The resulting calibration fit, which is shown in Fig. (4.5), is very accurate with a determination coefficient ( $\rho^2$ , correlation coefficient squared) equal to 0.997.

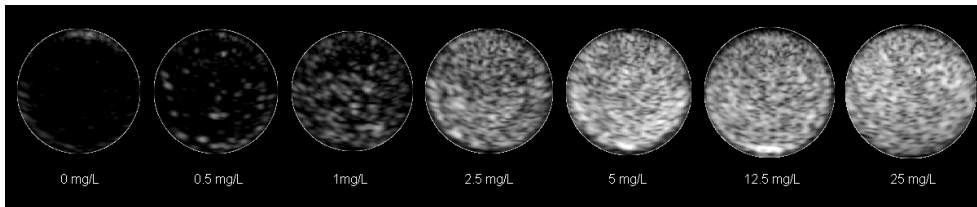


**Figure 4.4:** Video B-mode output for different SonoVue® concentrations going from 0 to 25 mg/L. The scanner (Philips Sonos 5500) was set in power modulation at 1.9MHz with MI = 0.1. Gain and time gain compensation were fixed to 90 and 80 respectively.

An alternative set-up for fundamental harmonic (transmission and reception are tuned to the same frequency) measurements was also tested for video calibration. 100ml rubber bags were filled with different dilutions of SonoVue® in saline. The external TTE ultrasound transducer was replaced by a TEE ultrasound transducer, which was submerged into water to improve the acoustic impedance matching. The B-mode video output of the ultrasound scanner was interfaced to a personal computer by a National Instrument frame grabber (1407 PCI) and analyzed for all the different dilutions. The mean gray-level measurements were fitted by the model in Eq. (4.4). The scanner was set in fundamental harmonic at 5MHz and the MI was set to 0.3.

The model was tested with two different scanners to verify the machine independency of the model. Fig. (4.6) shows the results as measured with a Philips Sonos 4500 and Sonos 5500 ultrasound scanner. The determination coefficient  $\rho^2$  between the experimental data and the fitted model is 0.99 and 0.98 respectively. Sometimes, due to the presence of air bubbles, it was difficult to establish the background mean gray-level and, therefore, the correct measurements for very low UCA concentrations. Since the logarithmic fitting is very sensitive to low-concentration

<sup>2</sup>For an unknown logarithmic basis  $x$ ,  $\lg_x(c) = \frac{1}{\log(x)} \cdot \log(c)$ .

<sup>3</sup>Official site: <http://www.divx.com/>

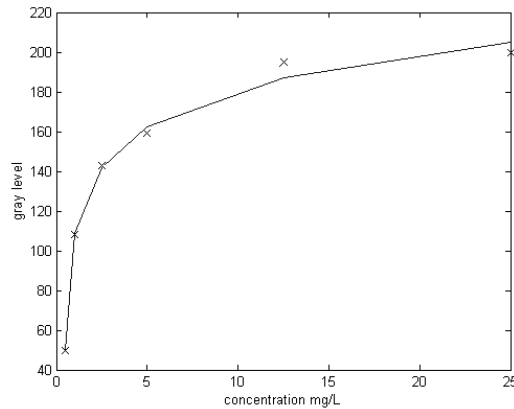


**Figure 4.5:** The same measurements as shown in Fig. (4.2) after conversion (by software *Q-Lab*) into digital AVI video as shown in Fig. (4.4). The model fit shows a determination coefficient equal to 0.997.

data, the application of the non-linear calibration in Eq. (4.4) for IDC measurements is rather complicated.

Instead, it is interesting to notice that for low concentrations of SonoVue® (below 5mg/L), the relation between UCA concentration and mean gray-level can be approximated by a linear function  $G(\rho_n) = a_0 + a_1\rho_n$  with  $\rho^2 \geq 0.95$ . The use of a linear calibration, already introduced for early agents such as Albunex [1], is also supported by previous studies on the response of SonoVue® to Doppler signals [173].

The increased detection efficiency of harmonic modes, such the adopted power modulation mode, makes the saturation due to video logarithmic compression already significant for low concentrations (2.5mg/L). However, this high contrast sensitivity can be exploited with a further reduction of the injected dose, so that the resulting attenuation effects are totally negligible (see Fig. (4.2)). In general, harmonic mode contrast detection is better employed for acoustic measurements, which show a wide linear-calibration range.

A problem related to the proposed calibration procedure, which we like to refer to as *static calibration*, is the destruction of the bubbles, which is evident even for very low MI (MI = 0.1). The main issue is probably represented by the number frames per second, which with the adopted scanner could not be decreased<sup>4</sup> below 25Hz. As a result, the bubbles intercepted by the plane of the ultrasound beam were rapidly destroyed, and it was difficult to establish the correct value for the backscattered intensity.

<sup>4</sup>The scanner uses automatically the maximum frequency (frames per second) for a given depth.

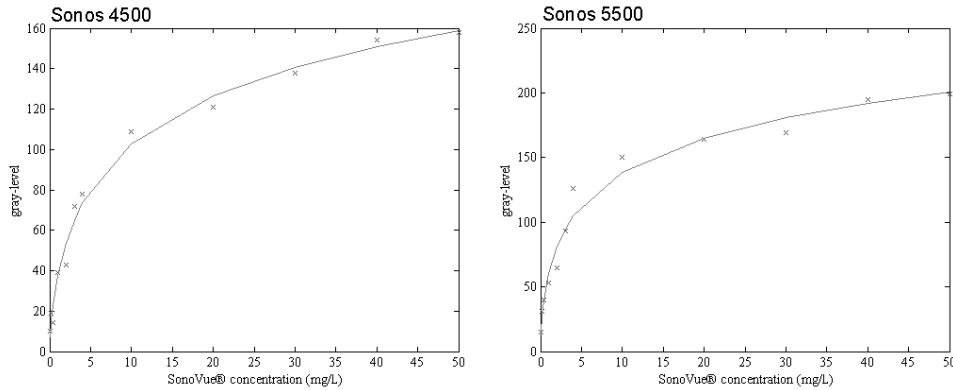


**Figure 4.6:** The left graph shows the calibration fit for a Sonos 4500 scanner in fundamental harmonic. The machine setting was  $MI = 0.3$ ,  $FPS = 25$ , burst carrier frequency = 5MHz, gain = 44, time gain = 50. The estimated parameters of the fitted model are  $a_0 = 83.1$ ,  $a_1 = 1.6$ , and  $a_2 = 1.2$ . The determination coefficient is 0.99.

The right graph shows the calibration fit for a Sonos 5500 scanner in fundamental harmonic. The machine setting was  $MI = 0.3$ ,  $FPS = 25$ , burst carrier frequency = 5MHz, gain = 44, time gain = 50. The estimated parameters of the fitted model are  $a_0 = 90.5$ ,  $a_1 = 3.2$ , and  $a_2 = 1.4$ . The determination coefficient is 0.98.

In opposition to this static calibration, a *dynamic calibration* procedure has been designed and implemented. Since the long insonification of the same bubbles leads to their destruction, the basic principle of a dynamic calibration is to perform the gray level measurements on moving bubbles, so that the insonified bubbles are different in time. A gray level intensity curve is measured after injection of a small bolus of SonoVue® into a hydro-dynamic circuit as shown in Fig. (4.7). The unknown concentration is determined by using a second calibrated indicator dilution system in parallel. In particular, the SonoVue® bolus is injected together with a lithium bolus and the lithium IDC is detected simultaneously with the ultrasound gray level curve by a calibrated Lidco® system (Lidco Ltd, Cambridge, UK) for lithium CO measurements (see the lithium dilution method in section 2.1.1) [37, 39, 40].

The flow in the circuit is generated by a centrifugal pump and accurately measured by an electromagnetic flowmeter (a calibrated Medtronic 550 bio-console centrifugal pump, see also section 2.1.5). Therefore, the lithium dilution curve can be adjusted (multiplied by a coefficient) in order satisfy Eq. (2.6) for the SonoVue®

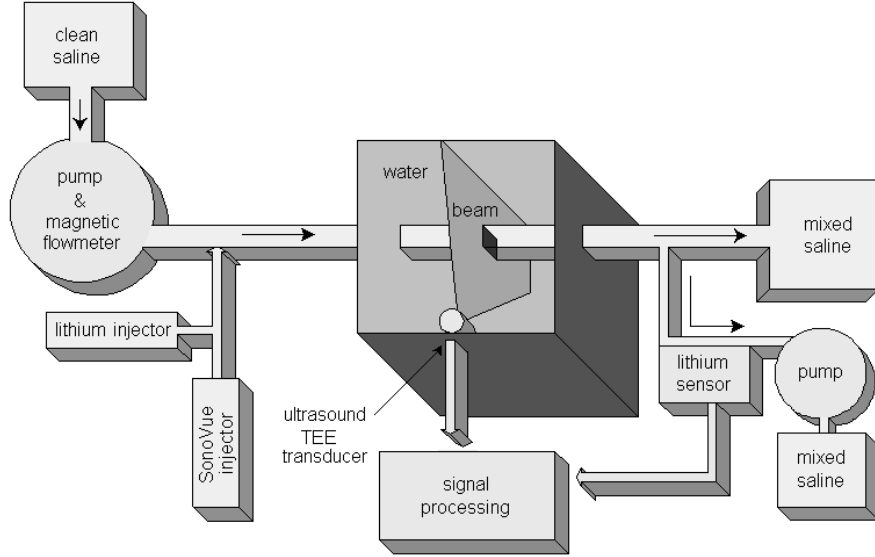


**Figure 4.7:** Scheme of the dynamic calibration set-up. A centrifugal pump generates the flow into a tube where a SonoVue® and a lithium bolus are simultaneously injected. The SonoVue® bolus is detected in a water-filled basin by a submerged TEE transducer while the lithium bolus is detected by a Lidco system.

injected dose. Following this procedure, the lithium curve is transformed into a real SonoVue® IDC, based on the real contrast concentration  $\rho_n(t)$ . Once the reference curve  $\rho_n(t)$  is determined, it is transformed by the non-linear model in Eq. (4.4) and fitted to the echographic videodensitometric curve  $G(t)$ . A Levenberg-Marquardt fitting algorithm is used. The result is the vector  $[a_0, a_1, a_2]$  that minimizes the squared error  $\varepsilon^2$  that is given as in Eq. (4.5), where  $t_1$  is any time before the contrast injection and  $t_2$  is any time after the contrast clearance.

$$\varepsilon^2 = \int_{t_1}^{t_2} (G(t) - a_0 \log(a_1 \rho_n(t) + a_2))^2 dt \quad (4.5)$$

However, this calibration procedure, which allows solving the bubble destruction problem of the static calibration, shows a different problem. In fact, the lithium IDC is measured after the passage of lithium through a sampling tube that leads to the sensor. The flow in the tube is generated by a peristaltic pump and is only 4ml/min. As a consequence, the diffusion process in the sampling tube influences the shape of the lithium IDC. Especially when the primary flow generated by the centrifugal pump is high, the difference between the lithium and the echographic

curves is significant, resulting in an unreliable calibration. Obviously, this additional diffusion has no influence on the lithium system performance, which is focused on flow measurements (real time CO measurements) and uses only the integral of the IDC as given in Eq. (2.6).

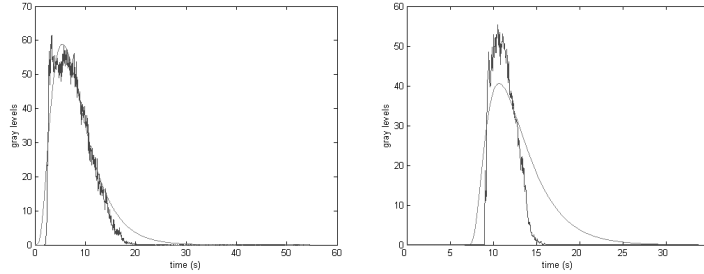


**Figure 4.8:** Two fits of  $G(t)$  by the log-transformed lithium IDC for flow equal to 0.9L/min (left) and 2.2L/min (right).

Fig. (4.8) shows the result of the fitting procedure for two IDCs with flow equal to 0.9L/min and 2.3L/min respectively. The lithium IDC, i.e., the reference curve  $\rho_n(t)$ , is interpolated by the LDRW model (see section 4.2.2) before the calibration fitting. For higher primary flows, as evident from the duration time of the curve,  $\rho_n(t)$  is very diffused and the fit of  $G(t)$  is erroneous. Fig. (4.9) shows the calibration curve (gray level versus UCA concentration) as measured from the low flow curve in Fig. (4.8). The scanner adopted for these measurement was a Sonos 4500 with a TEE probe in fundamental harmonic. MI, gain, and time-gain compensation were set to 0.2, 90, and 60 respectively. The injected doses of SonoVue® and lithium were 2.5mg and 1ml respectively.

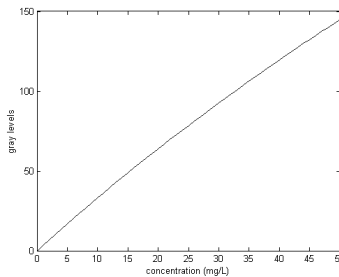


**Figure 4.9:** Resulting calibration curve of a Sonos 4500 ultrasound scanner based on the fit of the left IDC in Fig. (4.8).

In conclusion of this section, several techniques are proposed to determine the relation between UCA concentration, acoustic intensity, and displayed gray levels. Interesting issues arise when performing the measurements, however, for low contrast concentrations, the relation between contrast concentration and both acoustic and video intensity can be approximated by a linear function. While the acoustic intensity is independent on the ultrasound scanner settings, the same is not applicable to the video intensity (gray levels), which require the definition and use of a fixed and calibrated setting.

## 4.2 Indicator dilution curve models

In chapter 2 the use of indicator dilution methods is shown as an effective approach for the measurement of EF, CO, and blood volumes. All measurements that are based on the dilution of an indicator bolus are based on the analysis of the IDC. Depending on the adopted technique, the IDC is affected by several noise components, which make the analysis complex and the resulting cardiac quantifications unreliable.

A noise source that is common to all the techniques is the recirculation of the contrast, which causes the IDC down-slope to be covered by the rises due to the recirculation (see Fig. (2.6)). Thus, it is necessary to adopt a model in order to fit the first part of the curve and “guess” the lower part of the tail. The use of a model plays also the function of a filter to suppress the rest of the noise components introduced by the measurement system.

In particular, the noise sources for echographic IDC measurements are the bad mixing of the contrast, the acoustic reverberation, the speckle, the backscatter oscillations due to pressure variations [174, 175], the bubble disruption due to ultrasound pressure (especially with high MI) [176], and the patient-movement and blood-acceleration artifacts, resulting in very noisy IDCs.

The acoustic reverberation is usually caused by multiple reflection paths of ultrasounds, which are interpreted as reflections coming straight from the ultrasound main-lobe beam (also the presence of side lobes may contribute to reverberation noise, which in this case, as discussed in section 3.1.2, is referred to as side lobe artifacts). The speckle noise is due to the small scatterers that are dispersed in the ultrasound field. As already clear from Eq. (3.29), hydrostatic pressure  $P_0$  variations influence the bubble resonance frequency and, therefore, the backscattered intensity for a given driving pressure [174]. Very interesting are the artifacts due to blood acceleration, which produce an enhancement of the response of several harmonic-mode contrast-detection techniques, which exploit the bubble non-linear behavior (see section 3.3). More in detail, the enhancement is produced by the frequency shift  $\Delta f$  that is caused by the Doppler-effect (see section 2.1.4) due to blood velocity accelerations.

An accurate characterization and filtering of all the noise components is very complex, therefore, the employment of an IDC model is necessary for the signal interpolation and interpretation. Several models have been used for the IDC fitting. They are usually distinguished in two main groups as given below [10, 14].

- The compartmental models.
- The statistical (distributed) models.

The first group represents the dilution process as a cascade of mixing chambers [10, 14, 15, 30]. Each chamber is a linear system that is represented by an impulse response. The second group describes the dilution process by means of statistical distributions. Since the input is usually modelled as an impulse, also the statistical distribution can be interpreted as the impulse response of a linear system. Therefore, in practice, it does not make sense to distinguish into two groups and the focus should turn to the function that describes the impulse response of the system.

In the following two sections an overview of the main indicator dilution models and a detailed derivation of the Local Density Random Walk (LDRW) model and the First Passage Time (FPT) model is given. The last two models are reported by several authors as to give the best IDC fit in terms of mean square error [9–16]. Moreover, they are related to the physics of the dispersion process, being solution of the *diffusion equation* (see Appendix 3) [16]. For this reason, these two models are employed in this study for the interpretation of ultrasound contrast agent IDCs.

#### 4.2.1 Overview of the indicator dilution models

The first IDC fitting model was developed by Hamilton [8, 13, 32]. He noticed that the IDC is mainly composed by a sharp rise followed by a slower descent, which resembles an exponential function. Thus, he modelled the descent by an exponential decay with time-constant  $\tau$  as given in Eq. (4.6), where  $C(t)$  is the IDC (i.e., the concentration-time curve) and  $t_0$  is the injection time.

$$C(t) = C(t_0) e^{-\frac{t-t_0}{\tau}} \quad (4.6)$$

This model, which represents the impulse response of a mono-compartment model, also allows estimating the EF without ECG triggering<sup>5</sup> (see Eq. (2.20) in section 2.2). The estimation of the parameters of the model is very simple, since a ln-transformation (ln stands for Neper logarithmic) of  $C(t)$  allows the use of a linear regression (see Appendix A). However, a disadvantage is represented by the fact that the fitting is performed along a short segment of the IDC down-slope before the rise given by the recirculation of the contrast (see Fig. (4.10)), resulting in a less accurate “guess” of

<sup>5</sup>Only an estimate of the cardiac period is necessary.

the remaining part of the curve and higher noise dependency [9]. Another disadvantage of this model is the overestimation of the integral of  $C(t)$ , which is used to measure the carrier flow, especially evident for noisy IDCs [9, 29, 177].

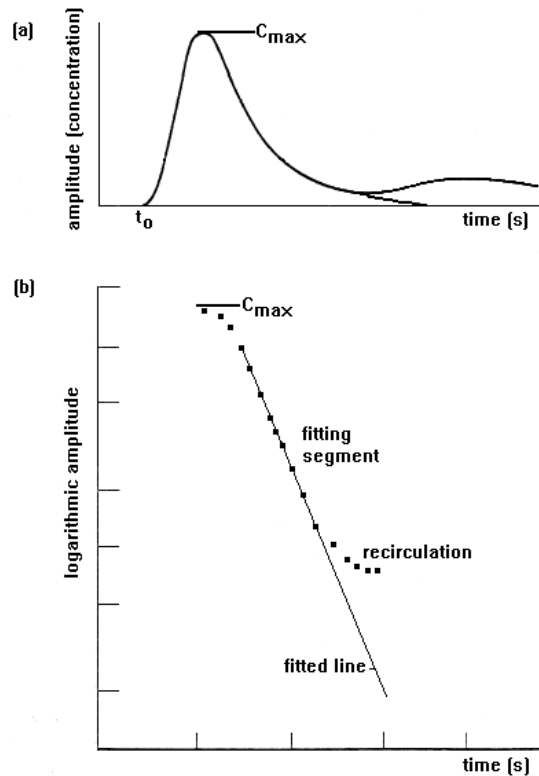


**Figure 4.10:** In (a) the IDC (i.e.,  $C(t)$ ) with recirculation is shown. In (b) the logarithmic plot of the IDC as well as the short segment that is suitable for the exponential fitting are shown.

As already mentioned, Eq. (4.6) can be interpreted either as an exponential distribution or as the impulse response of a mono-compartment model. Assuming to have a chamber (compartment) of volume  $V$  with only one input and one output where a fluid is flowing, if the chamber is not elastic and the fluid incompressible, then the input and output flow  $\Phi$  is the same. For the *mass conservation principle* (see Appendix C), the variation of tracer mass in the chamber (i.e.,  $VdC(t)$ ) equals the mass of tracer that leaves the chamber (i.e.,  $C(t)dV$ ). Therefore, since  $C(t)dV = C(t)\Phi dt$ , the system can be described by a differential equation as given in Eq. (4.7).

$$VdC(t) = -C(t)\Phi dt \quad (4.7)$$



Eq. (4.7) can be written as given in Eq. (4.8) and solved in the Laplace domain as given in Eq. (4.9), where  $C_0$  represents the initial condition at time  $t_0$ .

$$\frac{V}{\Phi} \frac{dC(t)}{dt} + C(t) = 0 \quad (4.8)$$

$$\frac{C(s)}{C_0} = \frac{1}{s + \frac{\Phi}{V}} \quad (4.9)$$

If a tracer-bolus is rapidly injected in the chamber at time  $t_0$  and the mixing is perfect<sup>6</sup>, then  $C_0 = m/V$  (with  $m$  equal to the injected mass of tracer). The result of the anti-transformation of Eq. (4.9) in the time domain is given as in Eq. (4.6), with  $\tau = V/\Phi$  and  $C(t_0) = C_0 = m/V$ .

$(m/V)u_0(t - t_0)$  represents the input impulse<sup>7</sup>, while  $h(t) = e^{-\frac{t-t_0}{\tau}}$  represents the impulse response of the mono-compartment system. Without any loss of generality, we assume  $t_0 = 0$ .

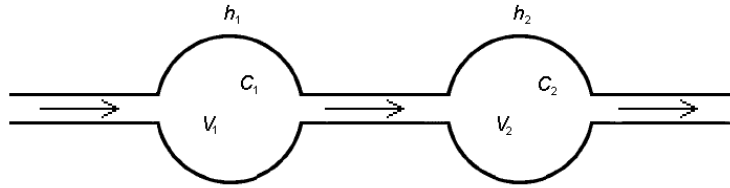


**Figure 4.11:** Scheme of a two-compartment model.  $V_i$  and  $C_i$  ( $i = 1, 2$ ) represent the compartment volume and concentration respectively.  $h_i(t)$  is the impulse response of each compartment.

A model that is often adopted in the IDC theory is the *two-compartment model*, which is obtained by adding a second equation (representing the second compartment) to Eq. (4.8). It is related to the cardiac functionality, which is based on two double-compartment pumps. The resulting differential system is given in Eq. (4.10), where  $C_1(t)$  and  $C_2(t)$  are the contrast concentrations in the two chambers of volume  $V_1$  and  $V_2$  respectively (see Fig. (4.11)).

$$\begin{cases} \frac{V_1}{\Phi} \frac{dC_1(t)}{dt} + C_1(t) = 0 \\ \frac{V_2}{\Phi} \frac{dC_2(t)}{dt} + C_2(t) - C_1(t) = 0 \end{cases} \quad (4.10)$$

<sup>6</sup>For all the compartmental models it is assumed to have a good mixing of the indicator in each chamber.

<sup>7</sup> $u_0(t - t_0)$  defines the dirac impulse centered at time  $t_0$ .

A solution of system (4.10), assuming the injection time equal to zero, gives  $C_1(t)$  and  $C_2(t)$  as in Eq. (4.11), where  $\tau_1 = V_1/\Phi$  and  $\tau_2 = V_2/\Phi$ .

$$\begin{aligned} C_1(t) &= \frac{m}{V_1} e^{-\frac{t}{\tau_1}} \\ C_2(t) &= \frac{m}{V_1 - V_2} \left( e^{-\frac{t}{\tau_1}} - e^{-\frac{t}{\tau_2}} \right) \end{aligned} \quad (4.11)$$

To make the model more general, it is possible to consider only a fraction of the first compartment out-flow as the in-flow of the second compartment (the rest of the flow is lost). As a consequence, different flows (e.g.,  $\Phi_1$  and  $\Phi_2$ ,  $\Phi_1 \geq \Phi_2$ ) can be used to model the output vessels of the compartments [10]. However, the only difference with respect to Eq. (4.11) concerns the coefficient in front of the exponentials that represent  $C_2$ . The new coefficient equals  $m/(V_1 - V_2\Phi_2/\Phi_1)$ .

More interesting is the IDC in a cascade of  $n$  equal chambers. The  $n^{\text{th}}$  equation of the system is given as in Eq. (4.12).

$$\frac{V}{\Phi} \frac{dC_n(t)}{dt} + C_n(t) - C_{n-1}(t) = 0 \quad (4.12)$$

For each chamber ( $n \geq 2$ ) the initial condition is  $C(0) = 0$ . Thus, in the Laplace domain the iterative equation (4.12) is given as in (4.13).

$$C_{n-1}(s) = \frac{\frac{1}{\tau}}{s + \frac{1}{\tau}} C_n(s) \quad \text{with } \tau = \frac{V}{\Phi} \quad (4.13)$$

If the input to the first chamber ( $n = 1$ ) is an impulse (Dirac function) of area  $m/V$  at time  $t_0 = 0$  (i.e.,  $(m/V)u_0(t)$ ), then, for  $n \geq 2$ ,  $C_n(s)$  can be expressed as given in Eq. (4.14) (Laplace domain) and Eq. (4.15) (time domain).

$$C_n(s) = \frac{m}{V} \left( \frac{\frac{1}{\tau}}{s + \frac{1}{\tau}} \right)^{n-1} \quad (4.14)$$

$$C_n(t) = \frac{m t^{n-2} e^{-\frac{t}{\tau}}}{V \tau^{n-1} (n-2)!} \quad (4.15)$$

Eq. (4.15) also represents a  $\chi^2$ -distribution with  $2n$  degrees of freedom. Therefore, the  $n$ -compartment model (with equal volume of the chambers) is basically a distribution with three independent parameters, like the standard distributed models.

If the volumes of the chambers are different, a different model, which is basically a multi-exponential model, is obtained. It is the summation of a number of exponential functions equal to the number of compartments. The number of degrees of freedom increases as well as the complexity of the fitting algorithm. Developing such models is an effort that does not lead to better results in terms of representation and interpolation of a real dilution system (see [16], p. 251).

Rather than focusing only on the impulse response, also the system response to different inputs can be considered and the input function integrated in the model. A common approach replaces the standard Dirac input with a rectangular input [30]. A valid alternative for modelling the input function is represented by a Gaussian function. In [178], for instance, a Gaussian input is convoluted with a mono-compartment exponential model in order to fit the measured IDC.

The impulse response of the compartment could be also chosen according to different criteria. The *Local Density Random Walk* (LDRW) and the *First Passage Time* (FPT) models are based on the assumption of random walk of the tracer particles (see next sections). They are the models that we have employed to fit and interpret the echo-contrast dilution curves, especially for flow and volume measurements. In particular, we focus on the LDRW model since it gives a better fit for very skew curves [9–11, 14]) and a better IDC interpretation for volume measurements (see section 5.3).

Other distributions that are commonly adopted to fit the IDC are the *lognormal distribution* and the *gamma-variate distribution* [29, 30, 179, 180]. Even without a real physical explanation, they fit the IDC giving very good results in terms of mean square error and correlation coefficient. The formulation of the lognormal and the gamma-variate model, as typically used for the IDC fitting, is given as in Eq. (4.16) and Eq. (4.17) respectively.

$$C(t) = \begin{cases} 0 & t \leq 0 \\ \frac{A}{\sqrt{2\pi}\sigma t} e^{-\frac{(\ln(t)-\mu)^2}{2\sigma^2}} & t > 0 \end{cases} \quad (4.16)$$

$$C(t) = \begin{cases} 0 & t \leq 0 \\ At^\alpha e^{-t\beta} & t > 0 \end{cases} \quad (4.17)$$

The parameter A is the scale factor of the model. The integrals of Eq. (4.16) and Eq. (4.17), which can be used for flow measurements, equal A and  $A\beta^{-(1+\alpha)}\Gamma(1+\alpha)$  respectively<sup>8</sup>. In the lognormal distribution,  $\sigma$  is related to the skewness of the curve while  $\mu$  is related to the peak-concentration time.

**Remark** Notice that any such statistical model has to obey the mass conservation law as given in Eq. (4.18), where  $m$  is the injected mass (dose).

$$\int_0^{\infty} C(t) dt = \frac{m}{\Phi} \quad (4.18)$$

In general, the use of distributed models, such as the gamma-variate and the log-normal distribution, leads to a more precise interpolation of the IDC [9, 30]. For

---

<sup>8</sup>  $\Gamma(\alpha) = \int_0^{\infty} t^{(\alpha-1)} e^{-t} dt.$

instance, for very symmetric curves the two-compartment model does not give an accurate fitting of the IDC [10, 13, 14]. This is not a surprise, since modelling the human circulatory system by a number of compartments is not a reliable assumption and does not provide any physical information on the diffusion process. Moreover, the lognormal model fits better than the gamma distribution the rising part of the distribution, especially for skewed IDCs [12]. In conclusion, the lognormal model seems to fit the IDC better than any other model except the LDRW model, which has been shown to fit closely to the lognormal model (the LDRW model makes an accurate interpolation of the lognormal model [12]), and provides with a physical interpretation of the model parameters (see next section).

The presented IDC-modelling theory is mainly founded on studies that were developed for thermo-, dye-, and lithium-dilution techniques. However, also echo-contrast IDCs have been fitted with compartmental (usually one- or two-compartment models), gamma-variate, and lognormal models combined with the ultrasound attenuation model that is given as in Eq. (3.44) [30, 181].

Except for the exponential model, the IDC fitting is usually executed by means of nonlinear regression techniques, such as *Levenberg-Marquardt* or *Gauss-Newton* algorithms (see section 5.1) [178, 182]. Also some geometric techniques have been developed. They give an estimate of the area below the curve in order to measure the CO. The inflection triangle technique, for instance, is a technique that has been applied to all the distributions [12, 13, 180]. The area is estimated on the base of the triangle that is tangent to the two inflections (second derivative equal to zero) of the IDC.

### 4.2.2 The Local Density Random Walk model

The Local Density Random Walk (LDRW) model is a mono-dimensional characterization of the dilution process (see Fig. (4.12)). It describes the injection of an indicator into a straight infinitely-long tube where a fluid (carrier) flows with constant velocity  $u$ . This model was introduced by Sheppard and Savage in 1951 [15, 183]. The assumptions are a fast injection (modelled as a Dirac impulse) and a Brownian motion<sup>9</sup> of the indicator, whose particles interact by pure elastic collisions. Without any loss of generality, we consider the injection time  $t_0$  and the injection position  $x(t_0)$  equal to zero. If we focus on the discrete motion of a single particle, its position  $X(nT)$  at time  $nT$  can be described by the stochastic process given in Eq. (4.19),

---

<sup>9</sup>Brownian motion, better referred to as arithmetic Brownian motion, is the name given to the irregular movement of pollen grains suspended in water. The phenomenon was observed by the Scottish botanist Robert Brown in 1827, but only in 1905 a quantitative analysis was developed by Albert Einstein on the basis of the principles of kinetic-molecular theory of heat. According to this theory, particles microscopically visible suspended in a liquid will perform irregular thermal movements called Brownian molecular motion.

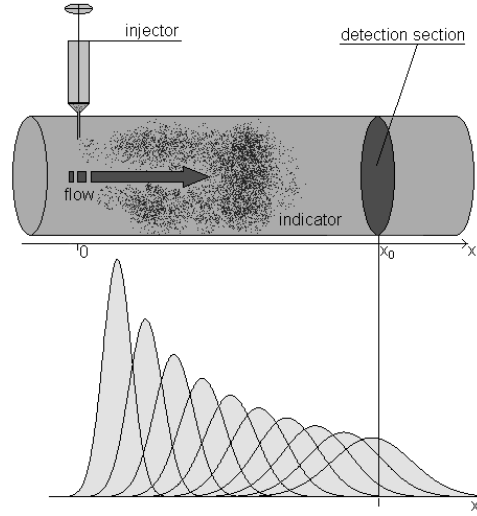


**Figure 4.12:** LDRW experimental model. The lower curves represent the probability distribution function of the tracer for increasing time.

where  $S$  is a random variable that represents the distance covered by the particle in the time interval  $T$  (single step).

$$X(nT) = \sum_{i=1}^n S(iT) \quad (4.19)$$

No assumptions are made on the probability density function of the random variable  $S$  (a specific derivation of the LDRW model for a Binomial step distribution is given in Appendix B). As a consequence of the Brownian motion hypothesis, each step  $S(iT)$  is independent from the previous ones and  $X(nT)$  is a *Markov* process<sup>10</sup> [184]. Therefore, for increasing  $n$  (or decreasing  $T$ ) the *Central Limit Theorem* (CLT, see Appendix B) [185] is applicable to the process  $X(nT)$ . If  $\mu$  and  $\sigma$  are the mean and the standard deviation of  $S$  respectively, then the probability density function of the random variable  $X$  at time  $nT$  is described by the process  $W(x, nT)$  as given in Eq. (4.20).

$$W(x, nT) = \frac{1}{\sqrt{2\pi n\sigma^2}} e^{-\frac{(x-n\mu)^2}{2n\sigma^2}} \quad (4.20)$$

<sup>10</sup>A Markov process is a stochastic process where the past has no influence on the future, if its present is specified. In mathematical terms,

$$P\{x(t_n) \leq x_n | x(t), t \leq t_{n-1}\} = P\{x(t_n) \leq x_n | x(t_{n-1})\},$$

where  $P\{\cdot\}$  represents the probability function.

In terms of continuous time  $t = nT$  (with  $T$  infinitely small), Eq. (4.20) can be expressed by the Wiener process [186] as given in Eq. (4.21), where  $\alpha = \sigma^2/T$  and  $u = \mu/T$ .

$$W(x, t) = \frac{1}{\sqrt{2\pi t\alpha}} e^{-\frac{(x-tu)^2}{2t\alpha}} \quad (4.21)$$

The concentration of the indicator  $C(x, t)$  is determined by  $(m/A)W(x, t)$ , where  $m$  is the mass of injected indicator and  $A$  is the section of the tube. Thus, as shown in Fig. (4.12),  $C(x, t)$  is described by a normal distribution that moves along the tube with the same velocity as the carrier (mean equal to  $tu$ ) and spreads with a variance that is a linear function of time (variance equal to  $t\sigma^2$ ). If we consider  $\alpha = 2D$  ( $D$  diffusion coefficient),  $C(x, t)$  is a solution of the mono-dimensional diffusion with drift equation, which is given as in Eq. (4.22) with boundary conditions given as in Eq. (4.23) and Eq. (4.24) [16].

$$\frac{\partial C(x, t)}{\partial t} = D \frac{\partial^2 C(x, t)}{\partial x^2} - u \frac{\partial C(x, t)}{\partial x} \quad (4.22)$$

$$C(x, 0) = \frac{m}{A} u_0(x) \quad (4.23)$$

$$\int_0^{\infty} C(x, t) dx = \frac{m}{A} \quad (4.24)$$

The conditions stated in Eq. (4.23) and Eq. (4.24) express the fast injection hypothesis and the mass conservation law respectively. Eq. (4.22) represents the link between the statistical and the physical interpretation of the dilution process. A more extensive discussion on the diffusion equation and the links with the LDRW model is given in Appendix C.

The derivation of a model for the IDC interpretation requires to focus on a fixed section of the tube (detection section) where the concentration of the indicator is evaluated versus time (see Fig. 4.12). The distance between the injection point and the detection section is determined by  $x = x_0 = u\mu$ . Therefore,  $\mu$  is the *Mean Transit Time* (MTT) of the indicator from the injection to the detection site. Wise and Bogaard [9, 11, 12] formalized the concentration time curve evaluated at distance  $x_0$  as given in Eq. (4.25), where  $\Phi = uA$  is the flow of the carrier and  $\lambda = \mu u^2/2D = \mu\Phi^2/2DA^2$  is a parameter related to the skewness of the curve.

$$C(t) = \frac{m}{\mu\Phi} e^{\lambda} \sqrt{\frac{\lambda\mu}{2\pi t}} e^{-\frac{\lambda}{2}\left(\frac{t}{\mu} + \frac{\mu}{t}\right)} \quad (4.25)$$

The maximum of  $C(t)$  is reached for  $t = \mu(2\lambda)^{-1}(\sqrt{1+4\lambda^2} - 1) > \mu$ . Notice that  $\max[C(t)]$  is given when  $t = \mu$  only for  $\lambda \rightarrow \infty$ . It can be explained by the

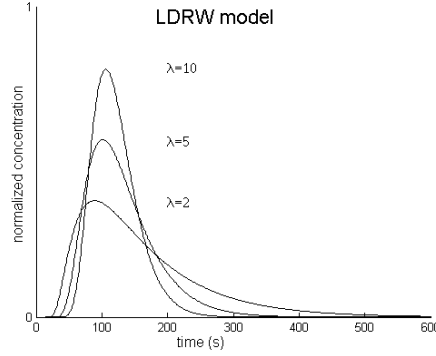


**Figure 4.13:** LDRW model for  $\lambda$  equal to 2, 5, and 10.  $\mu$  is fixed and equal to 100s.

physics of the dilution process. If we consider  $L = x_0$  as the characteristic length of the LDRW model, it follows that  $2\lambda$  equals the *Peclet number*, which is defined as  $uL/D$  and is the hydrodynamic parameter used to quantify the ratio between convection and diffusion in a dilution process [11,187]. The limit  $\lambda \rightarrow \infty$  can be interpreted as an infinitely small contribution of the diffusion in comparison to the convection. As a consequence, all the particles reach the detection section at the same time  $\mu = x_0/u$ . Already for  $\lambda > 10$ , as shown in Fig. (4.13), the curve is almost symmetric, while for  $\lambda < 2$  the curve is very skew.

The parameter  $\lambda$  (and therefore also the Peclet number divided by two) can be also viewed as the ratio between the *diffusive time*  $\tau_D$  (defined as  $\tau_D = x_0^2/(2D)$ )<sup>11</sup> and the *convective time*  $x_0/u = \mu$  [11].

In conclusion, it is evident that the LDRW model is related to the physical interpretation of a dilution as described by classic hydrodynamics. Some important properties of  $C(t)$  are listed below and are used for the assessment of flow and volume in the next chapter.

$$\int_0^{\infty} C(t) dt = \frac{m}{\Phi} \quad (4.26)$$

$$\frac{\int_0^{\infty} tC(t) dt}{\int_0^{\infty} C(t) dt} = \mu \left( 1 + \frac{1}{\lambda} \right) \quad (4.27)$$

<sup>11</sup>The diffusive time  $\tau_D$  can be interpreted as the time taken by the standard deviation  $\sqrt{2Dt}$ , which describes the pure diffusion process as given in Eq. (4.21) for  $u = 0$ , to reach the distance  $x_0$ .

The flow  $\Phi$  can be directly calculated by Eq. (4.26) once the injected dose  $m$  is known. Eq. (4.27) is the first moment of the LDRW model and it is referred to as *Mean Residence Time* (MRT) of the indicator between the injection and detection sites [11]. A discussion on the MRT interpretation and the difference between MRT and MTT is postponed to the next chapter. An analytical derivation of the solution of the integrals in Eq. (4.26) and Eq. (4.27) is proposed in section 5.1.2 and Appendix D.

### 4.2.3 The First Passage Time model

Like the LDRW model and with reference to Fig. (4.12), also the First Passage Time (FTP) model represents the IDC as the result of the passage of an injected contrast bolus (fast injection described by a Dirac function), which flows in a fluid-dynamic system (an infinitely-long tube), through a detection section.

The only difference with respect to the LDRW model concerns the bubble passage through the detection site. The FPT model hypothesis allows only a single passage of the bubbles while the LDRW model hypothesis includes multiple passages. It is like if an absorber layer captured the bubbles right after the detection site. Therefore, the FPT model is derived from the LDRW model when only the first passage through the detection site is considered and its formulation is given as in Eq. (4.28) [9–11], where the meaning of the symbols is the same as for Eq. (4.25).

$$C(t) = \frac{m}{\Phi} e^{\lambda} \sqrt{\frac{\lambda \mu}{2\pi t^3}} e^{-\frac{\lambda}{2} \left( \frac{t}{\mu} + \frac{\mu}{t} \right)} \quad (4.28)$$

Fig. (4.14) shows three different FPT curves for different values of  $\lambda$ . In the UCA dilution context, a practical hypothesis might be a compromise between the FPT and the LDRW model. In fact, despite the use of a small MI, part of the bubbles is still destroyed while passing through the ultrasound pressure beam.

The derivation of the FPT model is rather complicated. However, it can be simplified by exploiting the LDRW model definition. The probability  $p(x, t)$  that a bubble moves from a distance  $d = 0$  to  $d = x$  in time  $t$  is described by the unbiased (diffusion without drift) LDRW model as given in Eq. (4.29), where  $D$  is the diffusion constant.

$$p(x, t) = \frac{1}{\sqrt{4\pi Dt}} e^{-\frac{x^2}{4Dt}} \quad (4.29)$$

If the bubble reaches the distance  $x$  for the first time at time  $t - \tau$  ( $\tau \in [0, t]$ ), the probability of finding the particle at distance  $x$  at time  $t$  can be divided into two contributions:  $l(x, t - \tau)$  and  $p(0, \tau)$ .  $l(x, t - \tau)$  is the probability of a first passage in  $x$  at time  $t - \tau$  and  $p(0, \tau)$  is the probability of a subsequent passage in  $x$  at time  $\tau$  after the first passage. Thus,  $p(x, t)$  is given by a convolution operation as in Eq. (4.30).



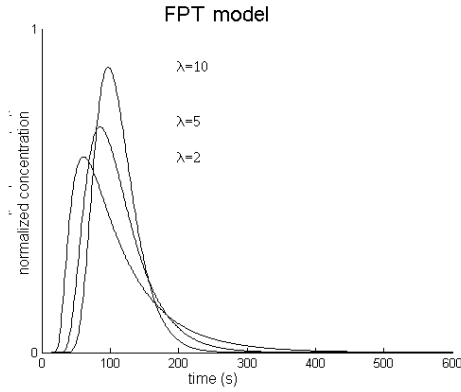


**Figure 4.14:** FPT model for  $\lambda$  equal to 2, 5, and 10.  $\mu$  is fixed and equal to 100 s.

$$p(x, t) = \int_0^t l(x, t - \tau) p(0, \tau) d\tau \quad (4.30)$$

In the Laplace domain Eq. (4.30) can be expressed as given in Eq. (4.31).

$$P(x, s) = L(x, s) \cdot P(0, s) \quad (4.31)$$

As a consequence,  $L(x, s)$  is given as in Eq. (4.32).

$$L(x, s) = \frac{P(x, s)}{P(0, s)} \quad (4.32)$$

$p(x, t)$  is expressed in the Laplace domain as given in Eq. (4.33).

$$P(x, s) = \frac{1}{\sqrt{4\pi Ds}} e^{-\sqrt{\frac{x^2 s}{D}}} \quad (4.33)$$

Therefore,  $L(x, s)$  is given as in Eq. (4.34).

$$L(x, s) = e^{-\sqrt{\frac{x^2 s}{D}}} \quad (4.34)$$

The FPT process is the anti-transformation in the time domain of  $L(x, s)$ , which is given as in Eq. (4.35).

$$l(x, t) = \frac{x}{\sqrt{4\pi Dt^3}} e^{-\frac{x^2}{4Dt}} \quad (4.35)$$

$l(x, t)$  represents the probability density function that the bubble reaches the distance  $x$  for the first time at time  $t$ .

The same procedure is applicable in case of drifting diffusion.  $p(x, t)$  is now defined as given in Eq. (4.36), where  $u$  is the carrier fluid velocity.

$$p(x, t) = \frac{1}{\sqrt{4\pi Dt}} e^{-\frac{(x-ut)^2}{4Dt}} \quad (4.36)$$

If the detection distance is fixed to  $x = x_0 = u\mu$ , and  $D/u^2 = K^2$ , Eq. (4.36) can be rewritten as given in Eq. (4.37).

$$p(\mu, t) = \frac{1}{u\sqrt{4\pi K^2 t}} e^{-\frac{(\mu-t)^2}{4K^2 t}} \quad (4.37)$$

The model is valid for  $u > 0$ . For  $u = 0$  the diffusion without drift model must be used. As for the diffusion without drift case, Eq. (4.37) is substituted into Eq. (4.30), which is now expressed as given in Eq. (4.38).

$$p(\mu, t) = \int_0^t l(\mu, t - \tau) p(0, \tau) d\tau \quad (4.38)$$

Once again, Eq. (4.38) can be solved in the Laplace domain. The resulting  $L(\mu, s)$  represents the FPT model in the Laplace domain when drift is included.  $L(\mu, s)$  is expressed as given in Eq. (4.39).

$$L(\mu, s) = e^{-\frac{\mu(1-\sqrt{1-4sK^2})}{2K^2}} \quad (4.39)$$

Taking the inverse Laplace transform, Eq. (4.39) is expressed in the time domain as given in Eq. (4.40).

$$l(\mu, t) = \frac{\mu}{\sqrt{4\pi K^2 t^3}} e^{-\frac{(\mu-t)^2}{4K^2 t}} \quad (4.40)$$

$l(\mu, t)$  represents the FPT model with drift in the time domain. Since  $L(\mu, 0) = 1$ , the integral of  $l(\mu, t)$  in the interval  $(0, \infty)$  equals 1 and  $l(\mu, t)$  may be considered

as a statistical distribution. With the substitution  $\lambda = (u^2\mu)/(2D)$ , it follows that  $K^2 = \mu/2\lambda$  and Eq. (4.40) is expressed as given in Eq. (4.28), which is the FPT model definition as reported by Bogaard, Reth, and Wise [9–11]. The first moment of the model, as proven by Sheppard [15], is equal to  $\mu$ .

## Chapter 5

# Random walk model fitting and dilution curve interpretation

*Non scholae sed vitae discimus (Seneca).*

Based on the models that describe the interaction between ultrasound and contrast agents, and using a random walk interpretation of the dilution curve, the measurement of the cardiac parameters of interest is presented in this chapter. The first issue is the interpolation and interpretation of the calibrated IDC by the adopted models. In particular, we are interested in the LDRW model fitting. Therefore, after a brief introduction to the most common fitting techniques (section 5.1), two techniques that are specifically designed for the LDRW model fitting are proposed. The first technique is based on a multiple linear regression and allows overcoming the contrast recirculation issue (section 5.1.1) while the second one is based on the moment equations and could be affected by contrast recirculation (section 5.1.2). The same techniques can be also applied to the FPT model interpolation. Eventually, the fitted model is used to interpret the IDC for flow (section 5.2), volume (section 5.3), and EF (section 5.4) measurements. Experimental and clinical results are provided.

### 5.1 Least square model fitting

The first solution to fit the IDC by a nonlinear model (LDRW) appears to be a nonlinear interpolation. The goal is to minimize the *square error* as given in Eq.(5.1), where  $y_i$  are the samples of the original signal,  $f(x_i, \underline{\theta})$  are the samples of the model to fit ( $\underline{\theta}$  is the vector of parameters to optimize), and  $n$  is the number of samples that represents the signal.

$$\varepsilon(\underline{\theta}) = \sum_{i=1}^n (y_i - f(x_i, \underline{\theta}))^2 \quad (5.1)$$

The interpolation techniques that minimize the square error are referred to as *Least Square Estimation* (LSE) algorithms. There are many algorithms developed to

fit a nonlinear model. However, the most of them are iterative ones<sup>1</sup> [188], whose common problem is the convergence-time. Any iterative fitting algorithm needs the determination of an initial value for the vector  $\underline{\theta}$ . After this value has been chosen, the iterations can start. The error  $\varepsilon(\underline{\theta})$  is approximated by *Taylor expansion* around the initial value and its minimum gives the value of  $\underline{\theta}$  for the following step. For a second order approximation we have that  $\underline{\theta}_{i+1} = \underline{\theta}_i - [H(\varepsilon(\underline{\theta}_i))]^{-1} \left[ \frac{\partial \varepsilon(\underline{\theta}_i)}{\partial \underline{\theta}} \right]$ , where  $i$  is the iteration step number and  $H$  is the Hessian matrix<sup>2</sup> [188]. The term  $[H(\varepsilon(\underline{\theta}_i))]^{-1} \left[ \frac{\partial \varepsilon(\underline{\theta}_i)}{\partial \underline{\theta}} \right]$  is referred to as *Newton Step*.

In the implemented algorithms the Hessian matrix is usually approximated<sup>3</sup>, since its evaluation at each iteration would result in a very slow process. If  $[J(\underline{\theta})]$  is the Jacobian matrix<sup>4</sup> of  $(y - f(x, \underline{\theta}))$ , it follows that  $\left[ \frac{\partial \varepsilon(\underline{\theta})}{\partial \underline{\theta}} \right] = 2[J(\underline{\theta})]^t [y - f(x, \underline{\theta})]$  and  $[H(\varepsilon(\underline{\theta}))] = 2\left([J(\underline{\theta})]^t [J(\underline{\theta})] + [A(\underline{\theta})]\right)$ , where the matrix  $[A(\underline{\theta})]$  is related to the Hessian matrix. The difference between the most common methods stands in the approximation of  $[A(\underline{\theta})]$ . In fact,  $[A(\underline{\theta})]$  is usually approximated as  $\lambda [I]$ , where  $\lambda$  is an integer and  $[I]$  is an identity matrix, whose dimension equals the length of the vector  $\underline{\theta}$ . In the *Gauss-Newton* algorithm  $\lambda$  is equal to 0, in the *Levenberg-Marquardt* algorithm  $\lambda$  can be any finite value different from 0, and in the *Steepest Descent* algorithms  $\lambda \rightarrow \infty$  [188, 189]. Since the value of  $\lambda$  can be adjusted, the Levenberg-

<sup>1</sup>An alternative non-iterative algorithm can be the *method of moments*, where a set of equations is derived by equating the statistical moments of the model to the moments as calculated by the experimental data. The number of equations and then of moments that are used must be equal to the number of parameters to optimize. Unfortunately, this powerful method, which is proposed in section 5.1.2, could encounter some problems due to the recirculation of the indicator. In fact, the moments might be not properly estimated from the experimental data.

<sup>2</sup>The Hessian matrix of  $\varepsilon(\underline{\theta})$  for  $\underline{\theta}$  constituted by  $p$  elements (parameters) is defined as follows:

$$H(\varepsilon(\underline{\theta})) = \begin{bmatrix} \frac{\partial^2 \varepsilon(\underline{\theta})}{\partial \theta_1 \partial \theta_1} & \dots & \frac{\partial^2 \varepsilon(\underline{\theta})}{\partial \theta_1 \partial \theta_p} \\ \vdots & \ddots & \vdots \\ \frac{\partial^2 \varepsilon(\underline{\theta})}{\partial \theta_p \partial \theta_1} & \dots & \frac{\partial^2 \varepsilon(\underline{\theta})}{\partial \theta_p \partial \theta_p} \end{bmatrix}$$

<sup>3</sup>To achieve a more accurate approximation of the Hessian matrix there are special algorithms, which are referred to as *Large-Scale methods*.

<sup>4</sup>The Jacobian matrix  $J(\underline{\theta})$  of  $(y - f(x, \underline{\theta}))$ , for  $\underline{\theta}$  constituted by  $p$  elements (parameters), and  $x$  and  $y$  sampled by  $n$  samples, is obviously equal to the Jacobian of  $f(x, \underline{\theta})$ , and defined as follows:

$$J(\underline{\theta}) = \begin{bmatrix} \frac{\partial f(x_1, \underline{\theta})}{\partial \theta_1} & \dots & \frac{\partial f(x_1, \underline{\theta})}{\partial \theta_p} \\ \vdots & \vdots & \vdots \\ \frac{\partial f(x_n, \underline{\theta})}{\partial \theta_1} & \dots & \frac{\partial f(x_n, \underline{\theta})}{\partial \theta_p} \end{bmatrix}$$

Marquardt algorithm gives a better approximation of the Hessian matrix. Therefore, although it is slower, it suits better high-residual problems.

Usually the IDC is very noisy, leading to large residuals and long convergence time of the iterative algorithms. The convergence time is strongly related to the initial values of the parameters to optimize. Therefore, the initial “guess” of the vector  $\underline{\theta}$  should be as close as possible to the optimum  $\underline{\theta}$ . With the LDRW model this can be done by the inflection triangle technique (see the end of section 4.2) or by a logarithmic transformation of the measured IDC followed by a *multiple linear regression* limited to a small part of the IDC [13, 182].

The solution that we propose in the next section is a linear-regression algorithm that makes possible to avoid the following nonlinear regression, since the result is already optimum in the LSE sense. The advantage of a linear regression over a nonlinear one stands in the reliability of the fit, which does not need to be initialized with a preliminary estimation of the model parameters. A nonlinear regression can either show very high convergence-time, or converge into local minima of  $\varepsilon(\underline{\theta})$  (wrong fitting), or even fail the approximation (no convergence and no fit).

As an alternative to the LSE approach, we also propose in section 5.1.2 a technique that is based on the derivation of the moment equations for the LDRW model.

### 5.1.1 Linear regression fitting algorithm

A new automatic fitting algorithm that is based on multiple linear regression is proposed. No assumptions are needed on the input IDC and the injection time. The calibrated intensity signal  $C(t)$ , which contains the IDC, is processed in two main phases.

In the first phase  $C(t)$  is filtered by a low-pass FIR filter (Finite Impulse Response filter, whose impulse response is defined by  $h(t)$ ) to remove the high frequency noise introduced by the measurement system. Then the filtered signal  $G(t) = h(t) * C(t)$  is used to determine the position of the IDC within the signal  $C(t)$ . The time coordinate  $t_{\max}$  of the maximum of  $G(t)$  is determined, and based on this value the time interval for performing the multiple linear regression is established. This regression time interval is defined for  $t \in [t_{\text{start}}, t_{\text{end}}]$ , with  $G(t_{\text{start}}) = 0.1G(t_{\max})$  along the rising edge of  $G(t)$  and  $G(t_{\text{end}}) = 0.3G(t_{\max})$  along the descending edge of  $G(t)$ , which is the recirculation appearance time [13], i.e., the time when the contrast reappears into the ROI after a first passage through all the circulatory system.

The initial part of  $C(t)$  contains only background noise from the measurement system while the IDC is absent. Furthermore, especially when  $\mu$  is large, the first part of the IDC shows a low SNR (smaller than -50dB). As a consequence, it is impossible to determine the injection time  $t_0$  by a simple analysis of either  $G(t)$  or  $C(t)$ . The definition of  $t_{\text{start}}$  ensures that  $t_{\text{start}} > t_0$  and therefore that the regression interval does not include the low-SNR initial part of the IDC.

Before starting the linear fitting, the baseline of  $C(t)$  is estimated and subtracted. It is estimated as the mean of  $C(t)$  calculated in an early time interval with  $t < t_0$ .

Once the interval  $[t_{\text{start}}, t_{\text{end}}]$  is defined and the baseline adjusted, in the second phase of the fitting process  $C(t)$  and the LDRW model are ln-transformed to obtain a linear model and to apply the multiple linear regression. The resulting linear model is given as in Eq. (5.2).

$$\begin{aligned} \ln(C(x_1)) + \frac{1}{2} \ln(x_1) &= P_1 - P_2 x_1 - P_3 x_2 & (5.2) \\ x_1 &= t - \widehat{t}_0 \\ x_2 &= \frac{1}{t - \widehat{t}_0} \\ P_1 &= \lambda + \ln\left(\frac{m}{\mu\Phi}\right) + \frac{1}{2} \ln\left(\frac{\lambda\mu}{2\pi}\right) \\ P_2 &= \frac{\lambda}{2\mu} \\ P_3 &= \frac{\lambda\mu}{2} \end{aligned}$$

$P_1$ ,  $P_2$ , and  $P_3$  are the parameters to be optimized,  $x_1$  and  $x_2$  are the variables of the linearized model, and  $\widehat{t}_0$  is the estimate of  $t_0$ . The least square estimation of the parameters  $P_1$ ,  $P_2$ , and  $P_3$  is solved by Eq. (5.3) [190], which gives the optimum estimation  $\underline{P}^{\text{opt}} = [P_1^{\text{opt}} \ P_2^{\text{opt}} \ P_3^{\text{opt}}]$ . The matrix  $[X]$  and the vector  $\underline{Y}$  are defined as shown in Eq. (5.4), where  $x_{i1}$  and  $x_{i2}$  ( $i \in [1..n]$ ) are the  $n$  samples of  $x_1 = t - \widehat{t}_0$  and  $x_2 = (t - \widehat{t}_0)^{-1}$  in the regression interval.

$$\underline{P}^{\text{opt}} = ([X]^t [X])^{-1} [X]^t \underline{Y} = \begin{bmatrix} P_1^{\text{opt}} \\ P_2^{\text{opt}} \\ P_3^{\text{opt}} \end{bmatrix} \quad (5.3)$$

$$\begin{aligned} [X] &= \begin{bmatrix} 1 & x_{11} & x_{12} \\ 1 & x_{21} & x_{22} \\ \vdots & \vdots & \vdots \\ 1 & x_{n1} & x_{n2} \end{bmatrix} & (5.4) \\ \underline{Y} &= \begin{bmatrix} \ln(C(x_{11})) + \frac{1}{2} \ln(x_{11}) \\ \ln(C(x_{21})) + \frac{1}{2} \ln(x_{21}) \\ \vdots \\ \ln(C(x_{n1})) + \frac{1}{2} \ln(x_{n1}) \end{bmatrix} \end{aligned}$$

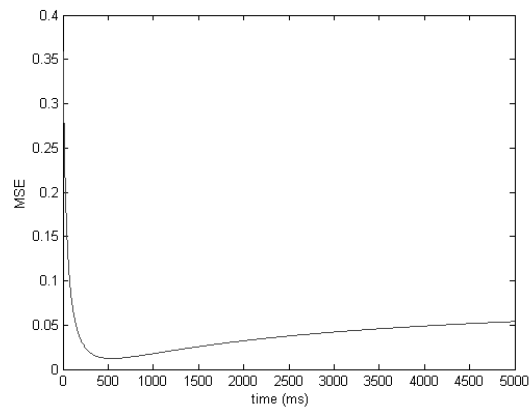


**Figure 5.1:** MSE of the fitting in the regression interval as function of  $t_{start} - \hat{t}_0$ .

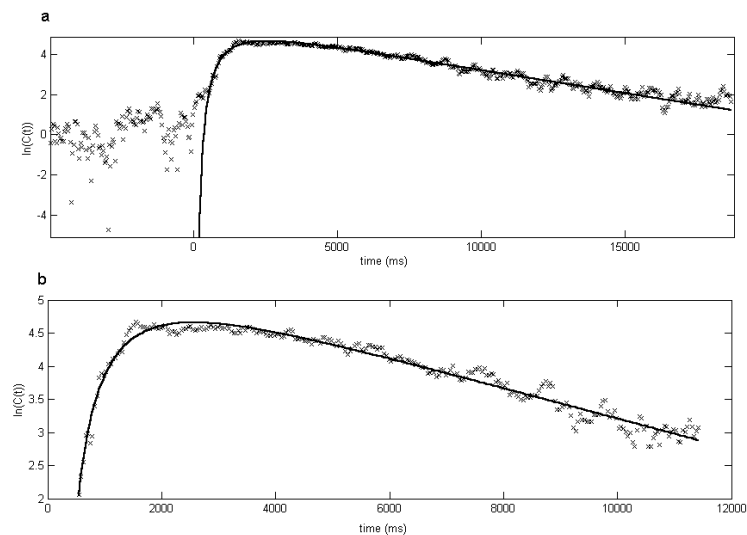


**Figure 5.2:** Linear fitting of  $\ln(C(t))$ . Fig. (a) shows the fitting in the complete time domain with  $t_0 = 0$ . Note that  $C(t)$  does not go to  $-\infty$  when  $t \rightarrow 0$  because of the noise.  $\text{Re}[\ln(C(t))]$  is plotted for negative values of  $C(t)$ . Fig. (b) shows the time interval where the multiple linear regression is performed.



However,  $t_0$  is not determined yet. Since by definition  $t_{\text{start}} > t_0$ , the optimum  $t_0$  can be estimated by applying Eq. (5.3) and Eq. (5.4) recursively for decreasing values of  $\hat{t}_0$  starting from  $\hat{t}_0 = t_{\text{start}}$  until the LSE of the fit is found. This technique is based on the characteristic relation between the *Mean Square Error* (MSE) of the fit and  $\hat{t}_0$  ( $\hat{t}_0 \leq t_{\text{start}}$ ). In fact, the relation shows a monotonic behavior and an global minimum for  $\hat{t}_0 = t_0$  (see Fig. (5.1)). In order to decrease the time-complexity the recursive search is performed by two sub-searches with resolution of 40ms (as the CCIR system, standard European format) and 1ms respectively. Therefore, the final time resolution is 1ms.

Curves of 2000 samples are fitted in less than 1s using a Matlab® (The Mathworks) implementation with an AMD 750MHz processor and 128MBytes RAM.

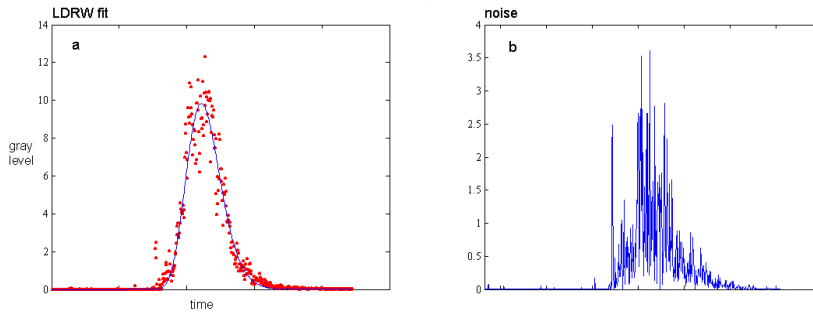


**Figure 5.3:** A measured IDC with fitted LDRW model (a) and the absolute value of the difference between the model and the experimental data (b). The noise amplitude is clearly modulated by the signal amplitude.

When  $C(t)$  is simulated by Eq. (4.25), the curve fit is very accurate. When  $C(t)$  is measured experimentally, the importance of defining  $t_{\text{start}}$  large enough to exclude from the linear fitting the initial part of the IDC emerges. In fact, due to the noise, limit  $t \rightarrow t_0$  of  $\ln(C(t))$  does not go to  $-\infty$  as expected. Therefore, when the regression interval is close to  $t_0$ , the parameter  $P_3$ , which is factor of the hyperbole  $1/(t - t_0)$ , is not properly estimated. Fig. (5.2) shows  $\ln(C(t))$  in the complete time domain (a) and in the selected regression interval (b). It is evident how the linear regression is not performed on the low-SNR time interval.

The performance of the fitting algorithm was evaluated by adding noise to the theoretical LDRW curve  $C_i(t)$ . The experimental measurements show a modulated white noise, whose amplitude is linearly related to the amplitude of  $C(t)$  with determination coefficient  $\rho^2 > 0.7$  (see Fig. 5.3). Therefore, artificial white noise  $N(t)$  was generated by a random sequence of numbers whose variance (*var*) was a linear function of  $C_i^2(t)$ , i.e.,  $\text{var}[N(t)] = kC_i^2(t)$ , so that  $k$  can be interpreted as  $(\text{SNR})^{-1}$ .

The low-power background noise was neglected. The fitting of  $C_N(t) = C_t(t) + N(t)$  was performed for  $k \in [0..1/16]$  (SNR from  $\infty$  to 12dB). Lower SNRs have never been encountered in the experimentation.

The evaluation of the fitting is mainly aimed to study the relationship between parameter estimates and noise levels. This relation is especially evident regarding the estimation of the integral of  $C_t(t)$  when noise is added. The area below the LDRW model is equal to  $m/\Phi$  (see Eq. (4.26)), which, as from the Stewart-Hamilton equation (see Eq. (2.6)) and the LDRW model definition, is the only parameter involved in the flow measurement. Once the vector  $\underline{P}^{\text{opt}}$  of Eq. (5.2) and Eq. (5.3) is estimated on the curve  $C_N(t)$ , the IDC estimated area is given as in Eq. (5.5).

$$\left[ \frac{m}{\Phi} \right]_e = \sqrt{\frac{\pi}{P_2^{\text{opt}}}} e^{\left( P_1^{\text{opt}} - 2\sqrt{P_2^{\text{opt}} P_3^{\text{opt}}} \right)} \quad (5.5)$$

The estimated area  $[m/\Phi]_e$  of the LDRW fit of  $C_N(t)$  was compared to the area  $m/\Phi$  below  $C_t(t)$ . The results, averaged over 1000 different noise sequences, show a negative bias of  $([m/\Phi]_e - m/\Phi)$  that increases for increasing noise (i.e., increasing  $k$ ). No significant differences were appreciated for different  $\lambda$  ( $\lambda \in [1..10]$ ). Different  $\mu$  and  $m/\Phi$  also led to the same results. Therefore, the results obtained for different  $\lambda$  were averaged as shown in Fig. (5.4) and interpolated by linear regression ( $\rho^2 > 0.9990$ ). The resulting linear relation between  $(\text{bias}/[m/\Phi]_e)$  and  $k$  is given as in Eq. (5.6).

$$\frac{\text{bias}}{[m/\Phi]_e} \cong 0.5255 \cdot k \quad (5.6)$$

The bias described in Eq. (5.6) can be explained as an effect of the logarithmic transformation of  $C_N(t)$  before the linear fitting, which changes the error metrics. In fact, the ln-transformation compresses the positive noise more than the negative one. As a consequence, the fitted curve is lower than the original  $C_t(t)$ , resulting in a reduced area below the curve (see Fig. (5.5)).

Based on Eq. (5.6), a compensation of this effect is implemented in the fitting algorithm.  $k$  is determined as the variance of the difference between the LDRW fit and  $C(t)$  - estimated where the LDRW fit is larger than 95% of its peak - divided by the squared value of the LDRW-fit peak. When the fitting includes the compensation algorithm, no bias is found in the estimation of the integral of  $C(t)$ . Fig. (5.5) gives an example of compensation in case of high power noise ( $k = 1/16$ ).

The variance of  $([m/\Phi]_e - m/\Phi)$  is not affected by the compensation algorithm. It is a linear function of  $k(m/\Phi)^2$ . The angular coefficient for  $\lambda \in [1..10]$  is estimated to be equal to 0.0049 with  $\rho^2 = 0.98$ . Therefore, in the worst considered case ( $k = 1/16$ ) the standard deviation of  $([m/\Phi]_e - m/\Phi)$  is equal to 1.75% of  $m/\Phi$ .

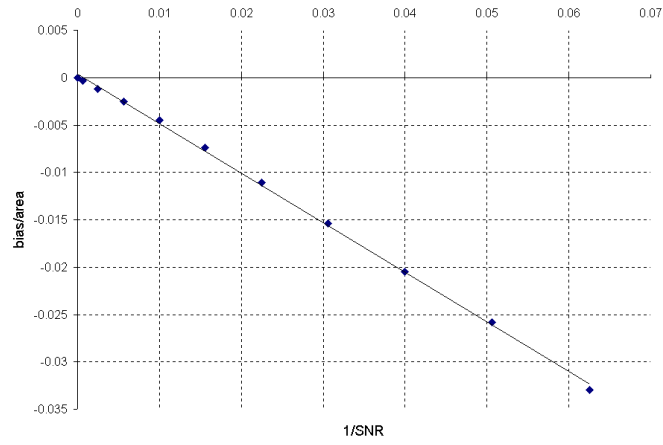


**Figure 5.4:** Increase of the negative bias (normalized to the estimated area  $[m/\Phi]_e$ ) as function of  $k$ , i.e.,  $(SNR)^{-1}$ .

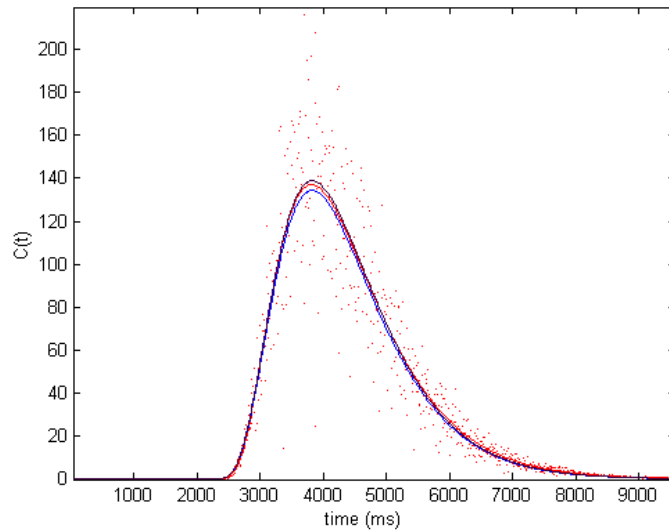


**Figure 5.5:** Simulation of the fitting. The dots and the upper curve represent the LDRW model ( $\lambda = 5$ ) with and without added noise ( $k = 1/16$ ) respectively. The mid and the lowest curve are the LDRW fit of the noise-added curve with and without area compensation.

No bias was recognized in the estimation of  $\lambda$  and  $\mu$ , therefore, the MTT and MRT (end of section 4.2.2) estimates, which are given as in Eq. (5.7) and Eq. (5.8), are unbiased also for small SNR.

$$\text{MTT} = \mu = \sqrt{\frac{P_2}{P_3}} \quad (5.7)$$

$$\text{MRT} = \mu \left(1 + \frac{1}{\lambda}\right) = 2\sqrt{P_2 P_3} \quad (5.8)$$

The same algorithm can be easily adopted for the FPT model fitting (see Eq. (4.28)). In this case, the model linearization in Eq. (5.2) becomes as given in Eq. (5.9).

$$\ln(C(x_1)) + 3 \ln(x_1) = P_1 - P_2 x_1 - P_3 x_2 \quad (5.9)$$

$$x_1 = t - \widehat{t}_0$$

$$x_2 = \frac{1}{t - \widehat{t}_0}$$

$$P_1 = \lambda + \ln\left(\frac{m}{\Phi}\right) + \frac{1}{2} \ln\left(\frac{\lambda\mu}{2\pi}\right)$$

$$P_2 = \frac{\lambda}{2\mu}$$

$$P_3 = \frac{\lambda\mu}{2}$$

### 5.1.2 Method of moments

An alternative LDRW-model fitting algorithm also is proposed. It is based on the calculation of the first two moments ( $M_1$  and  $M_2$ ) and the integral ( $M_0$ ) of the model in order to obtain a system of three independent equations and three unknowns (the model parameters). The  $n^{\text{th}}$  moment  $M_n$  ( $n \geq 1$ ) of  $C(t)$  is defined as given in Eq. (5.10).

$$M_n = \frac{\int_0^{\infty} t^n C(t) dt}{\int_0^{\infty} C(t) dt} \quad (5.10)$$

While a clear recursive relation for the analytical expression of the moments of the FPT model is derived in literature (see [15], page 253), the same is not available for the LDRW model. Therefore, we propose our own derivation of the moments  $M_0$ ,  $M_1$ , and  $M_2$  of the LDRW model.

The LDRW model  $C(t)$  can be expressed (see section 4.2.2) as given in Eq. (5.11), where  $A$  is the area under the curve,  $\mu$  is the MTT, and  $K^2 = 2D/v^2 = \mu/\lambda$  ( $D$  is the diffusion constant of the fluid-dynamic system).

$$C(t) = \frac{A}{\sqrt{2\pi K^2 t}} e^{-\frac{(\mu-t)^2}{2K^2 t}} \quad (5.11)$$

We define the functions  $m_n$  as given in Eq. (5.12), so that the zero moment of  $C(t)$  is  $M_0 = m_{-1/2}$ , the first moment is  $M_1 = m_{1/2}/m_{-1/2}$ , and the second moment is  $M_2 = m_{3/2}/m_{-1/2}$ .

$$m_n = \int_0^\infty \frac{t^n A}{\sqrt{2\pi K^2}} e^{-\frac{(\mu-t)^2}{2K^2 t}} dt = \frac{Ae^{\frac{\mu}{K^2}}}{\sqrt{2\pi K^2}} \int_0^\infty t^n e^{-\frac{\mu}{2K^2} \left(\frac{\mu}{t} + \frac{t}{\mu}\right)} dt \quad (5.12)$$

With the substitution  $t/\mu = y$ , Eq. (5.12) becomes as given in Eq. (5.13), where  $\beta = \mu/2K^2$ .

$$m_n = \frac{Ae^{\frac{\mu}{K^2}}}{\sqrt{2\pi K^2}} \mu^{n+1} \int_0^\infty y^n e^{-\beta \left(y + \frac{1}{y}\right)} dy \quad (5.13)$$

In order to simplify the calculations, we focus on the term  $m_n^*$ , which is defined as in Eq. (5.14).

$$m_n^* = m_n \frac{\sqrt{2\pi K^2}}{Ae^{\frac{\mu}{K^2}}} \frac{1}{\mu^{n+1}} = \int_0^\infty t^n e^{-\beta \left(t + \frac{1}{t}\right)} dt \quad (5.14)$$

**Theorem 5.1**  $m_n^* = \frac{n}{\beta} m_{n-1}^* + m_{n-2}^*$

*Proof.*

$$m_n^* = \int_0^\infty t^n e^{-\beta \left(t + \frac{1}{t}\right)} dt = - \int_0^\infty \left( t^n e^{-\frac{\beta}{t}} \right) d \left( \frac{e^{-t\beta}}{\beta} \right)$$

Integrating per parts we obtain the following.

$$\begin{aligned} m_n^* &= \left[ -\frac{t^n}{\beta} e^{-\left(\frac{\beta}{t} + t\beta\right)} \right]_0^\infty + \int_0^\infty \left( \frac{e^{-t\beta}}{\beta} \right) d \left( t^n e^{-\frac{\beta}{t}} \right) = \\ &= 0 + \int_0^\infty \left( \frac{n}{\beta} t^{n-1} + t^{n-2} \right) e^{-\beta \left(t + \frac{1}{t}\right)} dt = \frac{n}{\beta} m_{n-1}^* + m_{n-2}^* \end{aligned}$$

□

**Theorem 5.2**  $m_n^* = m_{-(n+2)}^*$

*Proof.*

$$m_n^* = \int_0^{\infty} t^n e^{-\beta(t+\frac{1}{t})} dt$$

With the substitution  $t = 1/y$ ,  $dt = -dy/y^2$  and  $m_n^* = -\int_{\infty}^0 y^{-(n+2)} e^{-\beta(y+\frac{1}{y})} dy = m_{-(n+2)}^*$ .  $\square$

**Corollary 5.2.1**  $m_{-3/2}^* = m_{-1/2}^*$

*Proof.* Directly from Theorem 5.2.  $\square$

From Theorems 5.1 and 5.2, Corollary 5.2.1, Eq. (5.14), and the fact that  $m_{-1/2} = A$  (for the analytical solution of the integral  $m_{-1/2}$  see Appendix D) we can derive  $m_{-1/2}^*$ ,  $m_{1/2}^*$ , and  $m_{3/2}^*$  as given in Eq. (5.15), Eq. (5.16), and Eq. (5.17) respectively.

$$m_{-1/2}^* = m_{-1/2} \sqrt{\frac{2\pi K^2}{A^2 \mu}} e^{-\frac{\mu}{K^2}} = \sqrt{\frac{2\pi K^2}{\mu}} e^{-\frac{\mu}{K^2}} \quad (5.15)$$

$$m_{1/2}^* = \frac{1}{2\beta} m_{-1/2}^* + m_{-3/2}^* = \left( \frac{1}{2\beta} + 1 \right) m_{-1/2}^* \quad (5.16)$$

$$m_{3/2}^* = \frac{3}{2\beta} m_{1/2}^* + m_{-1/2}^* = \left[ \frac{3}{2\beta} \left( \frac{1}{2\beta} + 1 \right) + 1 \right] m_{-1/2}^* \quad (5.17)$$

Therefore, using Eq. (5.14), Eq. (5.16), Eq. (5.17), and the relations  $\beta = \mu/2K^2$  and  $K^2 = \mu/\lambda$ , we can calculate the first and the second moment  $M_1$  and  $M_2$  of the LDRW model as given in Eq. (5.18) and Eq. (5.19) respectively.

$$M_1 = \frac{m_{1/2}}{m_{-1/2}} = \mu \frac{m_{1/2}^*}{m_{-1/2}^*} = \mu \left( 1 + \frac{1}{2\beta} \right) = \mu \left( 1 + \frac{1}{\lambda} \right) \quad (5.18)$$

$$M_2 = \frac{m_{3/2}}{m_{-1/2}} = \mu^2 \frac{m_{3/2}^*}{m_{-1/2}^*} = \mu^2 \left[ \frac{3}{2\beta} \left( \frac{1}{2\beta} + 1 \right) + 1 \right] = \left( \frac{\mu}{\lambda} \right)^2 (\lambda^2 + 3\lambda + 3) \quad (5.19)$$

**Remark** Notice that  $M_1$  can be expressed as  $M_1 = \mu + (2D/v^2)$ , which makes evident the fact that the first moment is given by the average time  $\mu$  that the particle takes to go from the injection to the detection site plus a term that is directly correlated to the diffusion constant  $D$  of the system.

The calculation of the moments can be used in order to fit the IDC by the LDRW model. If we refer to the expression for the LDRW model  $C(t)$  as given in Eq. (4.25), then the fitting consists of the estimation of the parameters  $A = m/\Phi$  ( $m$  injected dose mass),  $\mu$ , and  $\lambda$ . The parameter  $A$  is given by the integral of the curve  $C(t)$  in the interval  $(0, \infty)$ , which is given by  $M_0 \triangleq m_{-1/2} = A$  (see Appendix D). The parameters  $\mu$  and  $\lambda$  are calculated by solving the system of two equations in two unknowns ( $\mu$  and  $\lambda$ ) as given in Eq. (5.18) and Eq. (5.19). The solution of the system leads to two quadratic equations whose solutions express  $\mu$  and  $\lambda$  as function of  $M_1$  and  $M_2$ .

The equations for  $\mu$  and  $\lambda$  are given as in Eq. (5.20) and Eq. (5.21) respectively.

$$\mu^2 - 3M_1\mu + (3M_1^2 - M_2) = 0 \quad (5.20)$$

$$\lambda^2 (M_2 - M_1^2) + \lambda (2M_2 - 3M_1^2) + (M_2 - 3M_1^2) = 0 \quad (5.21)$$

The solution of Eq. (5.20) and Eq. (5.21) are given in Eq. (5.22) and Eq. (5.23). The negative roots of the quadratic equations are selected for the solution.

$$\mu = \frac{1}{2} \left( 3M_1 - \sqrt{4M_2 - 3M_1^2} \right) \quad (5.22)$$

$$\lambda = \frac{3M_1^2 + M_1\sqrt{4M_2 - 3M_1^2} - 2M_2}{2(M_2 - M_1^2)} \quad (5.23)$$

An iterative algorithm – as already for the linear regression in section 5.1.1 – is implemented to determine the IDC starting time that minimizes the MSE of the fit.

The same fitting method can be used for the FPT model fit. In this case, the moments  $M_0$ ,  $M_1$ , and  $M_2$  are equal to  $m/\Phi$ ,  $\mu$ , and  $\mu^2(1 + 1/\lambda)$  respectively [15]. As a consequence,  $\mu = M_1$  and  $\lambda = M_1^2/(M_2 - M_1^2)$ .

As for the linear regression method, this algorithm was tested with experimental curves that were recorded by means of the in-vitro set-up that is described in section 5.2 for flow measurements. A 0.5ml SonoVue® contrast agent bolus (2.5mg) was injected and the IDC measured by a Sonos 5500 ultrasound scanner (Philips Medical Systems) in a range of flows going from 0.5L/min to 5L/min.

The LDRW model was fitted to 80 IDCs by means of both the linear regression and the moment algorithm. The average determination coefficient  $\rho^2$  equaled 0.957 and 0.950 respectively (variance equal to  $1.210^{-3}$  and  $10^{-3}$ ). The methods were also compared in-vivo by means of 20 injections in humans. The result was an average

$\rho^2$  equal to 0.926 and 0.924 for the linear regression and the moment method fits respectively (variance equal to  $3.510^{-3}$  with both techniques).

In conclusion, the linear regression LDRW fits are slightly more accurate. For in-vivo measurements, where the contrast recirculation can be evident, the moment method cannot provide an accurate estimate of the moments based on the measured IDC, resulting in less accurate fits. In opposite, the linear regression fitting performs the LSE optimization in an IDC interval where the recirculation is not present. For the rest of this study, due to the robustness to recirculation, the interpolation and interpretation of the IDC is performed by the linear regression fitting.

## 5.2 Cardiac output measurement

The flow measurement requires the video or acoustic intensity curves to be transformed into IDC (contrast concentration curves) and fitted by the LDRW model. As from Eq. (5.5), the flow  $\Phi$  is directly provided by the fitted model once the injected dose  $m$  is known. Since  $m/\Phi$  is the time integral of the LDRW model, the same measurement of  $\Phi$  is obtained by the application of Eq. (2.6) (Stewart Hamilton equation). As discussed in section 2.1, we refer to flow with either the symbol  $\Phi$  or the abbreviation CO, depending on the context. Therefore,  $\Phi = \text{CO}$ , and we use  $\Phi$  or CO referring to in-vitro or in-vivo flow respectively. In fact, in this study, in-vivo measurements aim to assess the cardiac flow, which is referred to as CO.

As reported in section 4.1, we inject a small contrast bolus so that the relation between the measured signal and the contrast concentration is in an approximately-linear range. Referring to Eq. (4.4), the linear calibration for video intensity is given as  $G(t) = a_1 C(t) + a_0$ .  $a_0$  becomes equal to zero after the fitting algorithm adjusts the baseline to the zero level. Proven to be in the linear calibration range,  $a_1$  can be easily derived from the LDRW model fit of one of the measured curves and integrated into the injected dose  $m$  (see Eq. (4.25)). In fact, based on the fit and known the real flow  $\Phi$ , the value for  $m$  can be derived from Eq. (5.5) and used to fit and interpret the rest of the measured curves. The value of  $m$  can be interpreted as the “video dose” (average video intensity times volume unit or voxel) corresponding to the injected contrast bolus. The same reasoning can be applied to the acoustic intensity calibration.

Two in-vitro flow measurement experimentations, making use of two different setups, were carried on. The first one was based on videodensitometry using a TEE probe in fundamental harmonic while the second one was based on acoustic measurements using power modulation mode. Also the hydrodynamic setups were different. A complete description of the setups as well as the measurement results is provided below.



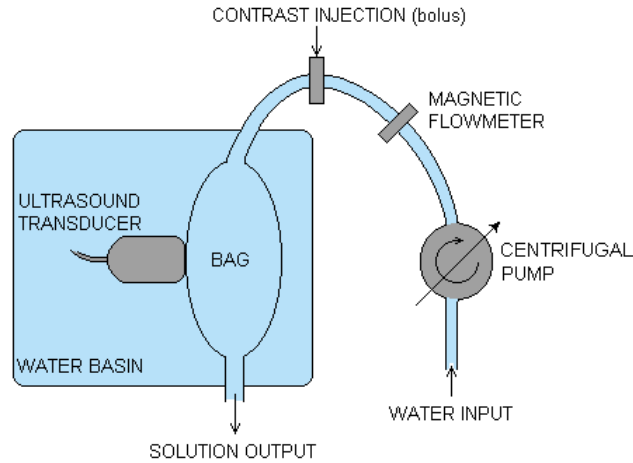


**Figure 5.6:** Experimental videodensitometric flow-measurement set-up.

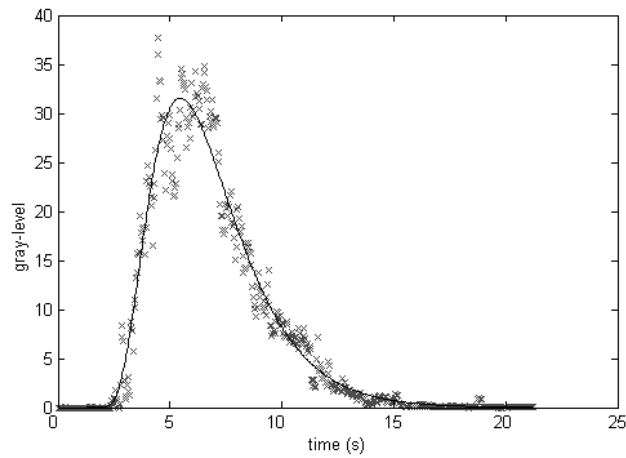


**Figure 5.7:** LDRW model fit of a noisy IDC.  $\rho^2 = 0.97$ .

Fig. (5.6) shows the first hydrodynamic in-vitro circuit that was built to test the videodensitometric method. A Medtronic 550 bio-console centrifugal pump with magnetic flowmeter (clinically used for extracorporeal circulation) generated and measured the flow. The flow measured by the magnetic flowmeter was the reference to validate the performance of the ultrasound method.

The contrast injector was positioned after the pump in order to avoid the collapse of the contrast micro-bubbles due to the turbulence of the pump. A TEE transducer was placed on a plastic bag, considered as a model for the cardiac chamber. The ultrasound transducer and the plastic bag were both submerged in a water-filled basin to obtain a good acoustic impedance matching. The adopted ultrasound scanner was a Sonos 4500 equipped with a TEE transducer (some measurements were also performed with a Sonos 2000 scanner). The centrifugal pump was covered by aluminium foils for magnetic isolation. Such a solution allowed avoiding the interference between scanner and pump.

Boluses of 10ml of SonoVue® diluted 1:100 (i.e., 50mg/L) in saline (0.9% NaCl) were injected for the flow measurements. As a result, the injected boluses contained 0.5mg of SonoVue® and a peak concentration of 5mg/L was barely reached in the perfusion bag. Therefore, the linear calibration hypothesis was applicable. The setting of the ultrasound scanner was the same as adopted for the fundamental harmonic calibration in Fig. (4.6).

A critical part of the set-up was the injector. A double injector system was developed in order to avoid the injection of air-bubbles. Several injections of degassed water were used in order to test the system. No air bubbles were detected.

The video output of the ultrasound scanner was grabbed by a 1407 PCI frame grabber (National Instruments) and processed in *real-time* to obtain the video intensity curves, i.e., the plots of the mean gray-level in the selected ROI versus time. The curve was then calibrated (linear calibration) and fitted by the LDRW model. The developed software integrates Labview® (National Instruments), and Matlab® (The Mathworks) implementations.

Since each ultrasound scanner is provided with a videorecorder (VCR), it is easy to generate analogical archives (S-VHS videotapes) and perform further off-line video analysis by playing the videotapes on a VCR.

The LDRW model fit of the measured IDCs gives always  $\rho^2 > 0.95$ . Fig. (5.7) shows the fit of a noisy IDC.

The MSE is not considered as a parameter to validate the LDRW model since it depends on the noise power. Instead, the MSE was used to compare the developed linear fitting algorithm to the standard Levenberg-Marquardt algorithm. The initial values of the Levenberg-Marquardt fitting were the parameters estimated by linear fitting. The results show that the Levenberg-Marquardt algorithm does not improve the MSE of the linear fit.

The flow estimates were validated by comparison with those measured by the magnetic flowmeter inserted in the experimental hydrodynamic circuit (see Fig. (5.6)). The results are shown in Fig. (5.8). The determination coefficient  $\rho^2$  between the flow measurements executed by UCA dilution and magnetic flowmeter is 0.997 and 0.982 using a Sonos 4500 and a Sonos 2000 ultrasound scanner respectively.

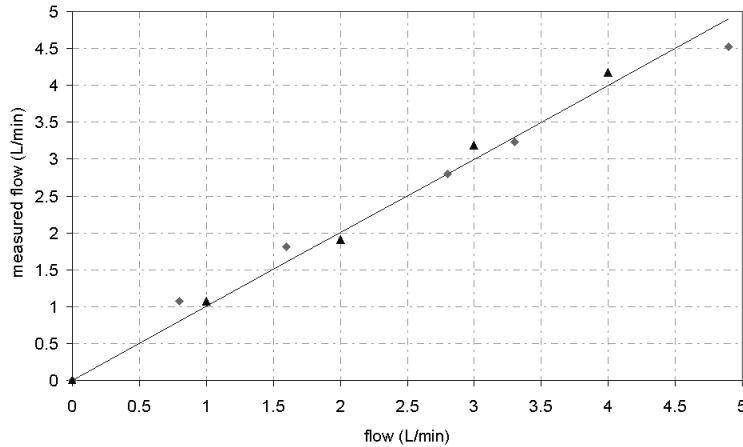


**Figure 5.8:** *Ultrasound videodensitometric flow measurements (Y axis) compared to magnetic flowmeter ones (X axis). The triangles and the rhombus are the results of the flow measurements made by a Sonos 2000 and a Sonos 4500 ultrasound scanner respectively. The determination coefficients are 0.999 and 0.994 respectively.*

A different set-up<sup>5</sup>, whose scheme is shown in Fig. (5.9), was used for acoustic intensity measurements. It consisted of an artificial ventricle, whose movements were driven by a piston pump that was fully controlled via PC. Two artificial valves simulated the mitral and the aortic valve (Fig. (5.10)) and a resistor<sup>6</sup> simulated the resistance of the circulatory system capillarity. The hydrodynamic circuit was open to avoid recirculation and permit repeated measurements. The input and output static pressures were stabilized.

The atrium was modelled as a water reservoir (290ml) on top of the ventricle, which also realized a ventricular pre-load (0.75mmHg). The contrast bolus (0.25mg SonoVue® in 5ml of saline) was injected in the tube leading to the ventricle pre-load. The use of power modulation allowed the reduction of the injected dose to half of the dose used with fundamental harmonic. This produced a further reduction of the attenuation effect and allowed a quicker injection, closer to the Dirac impulse injection that is assumed by the LDRW model.

A Sonos 5500 ultrasound scanner was used for the acoustic measurements. The scanner setting (power modulation mode) was identical with that used for the calibration in Fig. (4.2). The ultrasound transducer - an S3 probe - pointed to the ventricle

<sup>5</sup>The set-up was developed by prof.dr. van de Vosse and dr. Stijnen at the Biomedical Engineering Lab of the Eindhoven University of Technology and adapted to contrast-ultrasound measurements.

<sup>6</sup>The resistor, measured with flow equal to 3L/min, was  $32.4 \text{ MPa} \cdot \text{s} \cdot \text{m}^{-3}$ .

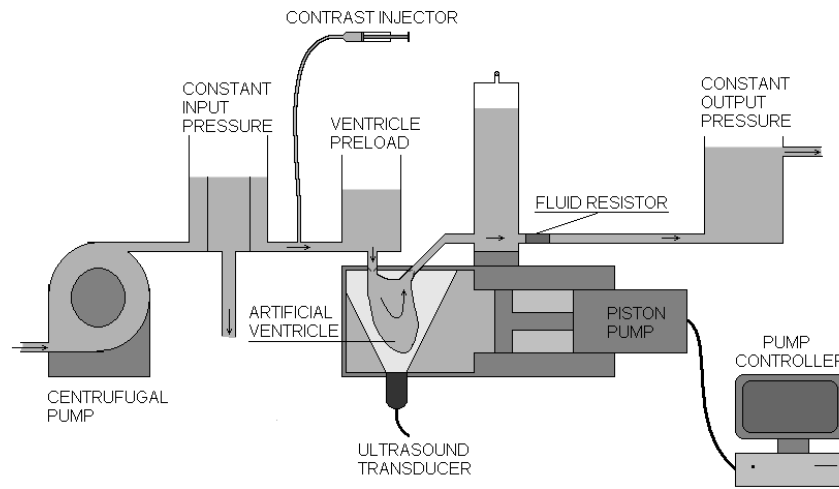


**Figure 5.9:** Scheme of the artificial ventricle used for acoustic flow measurements.



**Figure 5.10:** The prosthetic valve as used in the artificial ventricle set-up.

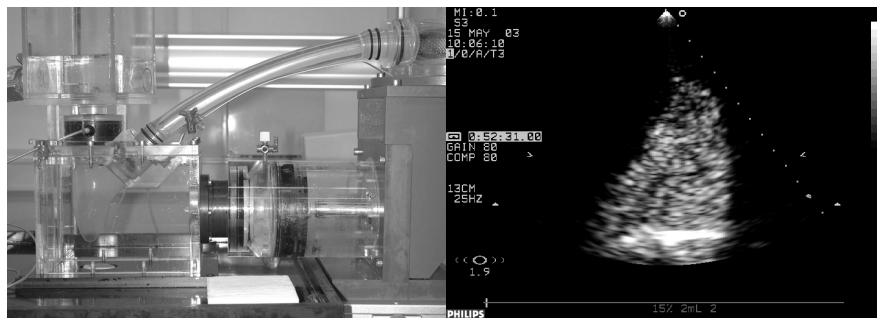


**Figure 5.11:** A picture of the artificial ventricle is shown together with a screen-shot of the B-mode video during a flow measurement. The ventricle is fully opacified by contrast.

apex through a window made of a thin polyurethane layer. The PR was fixed to 60 beats per minute and different flows from 0 to 3L/min were generated by adjusting the pump SV (piston excursion). Fig. (5.11) shows a picture of the system during a flow measurement together with the resulting B-mode video.

The results of two sets of measurements are shown in Fig. (5.12).  $\rho^2$  equals 0.909 and 0.995. The lower accuracy of the first set of measurements was due to the acoustic reverberation produced by the interface air-water in the ventricle pre-load during mitral valve opening. The problem was solved by submerging an acoustic absorber layer before the second set of measurements.

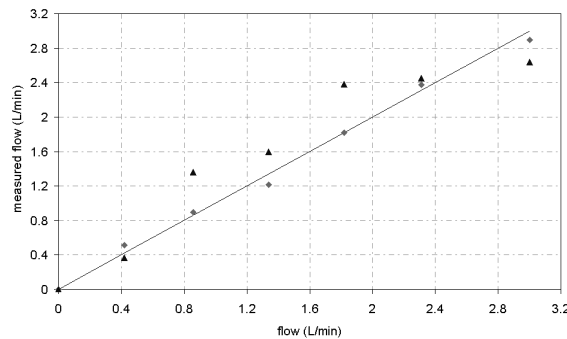


**Figure 5.12:** *Ultrasound flow measurements using the fluid-dynamic system in Fig. (5.9) and Fig. (5.11). The triangles and the rhombus are the results of two measurements sets. The determination coefficients are 0.909 and 0.995 respectively. The first measurements were affected by a large reverberation noise component coming from the mitral valve opening.*

The in-vivo measurement of CO is feasible once the calibration constant  $a_1$  is known. Due to the anatomic variability of patients, a unique value of  $a_1$  for TTE scanning cannot be defined. In fact, differences of gender, fat tissue, bone positions, end other factors influence significantly the calibration curve. However, based on in-vitro measurements, the CO could be measured by a TEE transducer. The TEE probe is placed behind the heart almost in touch with the left atrium, so that the same calibration and scanner setting as for the in-vitro calibration could be adopted. This approach has not been validated yet, since a reliable validation in patients requires a comparison with invasive thermo- or dye-dilution techniques. However, the promising in-vitro results, especially those obtained with a TEE probe, suggest pursuing it.

### 5.3 Pulmonary blood volume measurement

Based on the same principles, not only flow, but also volumes can be measured. The measurement is based on the contrast transit time estimate, which is multiplied by the flow for volume quantification. If different IDCs are measured in different sites, then the blood volume between the measurement sites can be assessed as the product of transit time times flow. Before presenting the measurement validation, the concepts of Mean Transit Time (MTT) and Mean Resident Time (MRT), already introduced in section 4.2.2, are investigated into details and related to the LDRW and FPT models for volume measurements. Moreover, the application of a deconvolution technique for the compensation of the injection function, which in reality is not a Dirac impulse as assumed by the LDRW and FPT models, is introduced. In fact, the injection function has effect on the estimation of the parameter  $\mu$  in the models (rather than on the estimation of the integral, see Remark in the end of section 5.3.2) and affects the volume assessment.

#### 5.3.1 Transit and resident time for volume measurements

The infinite tube model in Fig. (4.12), as for the derivation of the LDRW and the FPT models, is adopted to derive a formula for the volume measurement. A carrier fluid flows through the tube with a steady flow  $\Phi$ . An indicator bolus is injected (fast injection) at time  $t=0$  into the tube. The volume to measure is defined as the tube segment between the indicator injection and detection sections.

We define  $f(t)dt$  as the fraction of injected indicator that leaves the tube segment in the time interval  $[t, t+dt]$ . It is assumed that the indicator may not pass more than once through the detection section (FPT model hypothesis).

Due to the single passage hypothesis, the fraction of leaving bubbles corresponds to the fraction of bubbles that appear at the detection section. Therefore,  $f(t)$  equals the normalized indicator concentration that is measured at the detection site and is given as in Eq. (5.24).

$$f(t) = \frac{C(t)}{\int_0^{\infty} C(\tau) d\tau} \quad (5.24)$$

The fraction of indicator that has left the segment by time  $t$  is determined by  $F(t)$  as in Eq. (5.25).

$$F(t) = \int_0^t f(\tau) d\tau \quad (5.25)$$

The volume of fluid that enters the tube segment in the time interval  $[0, dt]$  is  $\Phi \cdot dt$  and the fraction that leaves the segment by time  $t$  is  $\Phi \cdot dt \cdot F(t)$ . Therefore, the volume of fluid that enters and leaves the tube segment in the time interval  $[0, t]$  is given as in Eq. (5.26).

$$\Phi \int_0^t F(\tau) d\tau \quad (5.26)$$

The difference between the entering and the leaving fluid volume in the time interval  $[0, t]$  is then given as in Eq. (5.27).

$$\Phi t - \Phi \int_0^t F(\tau) d\tau \quad (5.27)$$

Therefore, Eq. (5.27) expresses the volume of fluid that enters the segment in the time interval  $[0, t]$  and is still in the segment at time  $t$ . For time  $t \rightarrow \infty$  all the fluid in the segment is replaced by fluid that has entered for  $t \geq 0$ . Therefore, the total volume  $V$  of the segment is given as in Eq. (5.28).

$$V = \lim_{t \rightarrow \infty} \Phi \left( t - \int_0^t F(\tau) d\tau \right) \quad (5.28)$$

Eq. (5.28) can also be formulated<sup>7</sup> as given in Eq. (5.29).

$$V = \lim_{t \rightarrow \infty} \Phi \left[ t - [\tau F(\tau)]_0^t + \int_0^t \tau f(\tau) d\tau \right] = \Phi \int_0^{\infty} \tau f(\tau) d\tau \quad (5.29)$$

Due to the definition of  $f(t)$  and the FPT hypothesis, the right term of Eq. (5.29) represents the multiplication of the flow  $\Phi$  times the MTT of the indicator, i.e., the average time that the indicator takes to cover the distance between injection and detection section. Moreover, due to the FPT hypothesis and Eq. (5.24),  $f(t)$  may be represented by Eq. (4.28) (except for the coefficient  $m/\Phi$ ), which proves the convergence of the integral in Eq. (5.29).

---

<sup>7</sup>The integration per parts of  $\int_0^t \tau f(\tau) d\tau$  allows replacing  $\int_0^t F(\tau) d\tau$  in Eq. (5.28). In fact,

$$\int_0^t \tau f(\tau) d\tau = \int_0^t \tau dF(\tau) = [\tau F(\tau)]_0^t - \int_0^t F(\tau) d\tau .$$

In conclusion, the volume is given as in Eq. (5.30), where the MTT of the indicator, which equals the first moment of the IDC, is given as in Eq. (5.31).

$$V = \Phi \cdot MTT \quad (5.30)$$

$$MTT = \int_0^{\infty} \tau f(\tau) d\tau = \frac{\int_0^{\infty} \tau C(\tau) d\tau}{\int_0^{\infty} C(\tau) d\tau} \quad (5.31)$$

The definition of the indicator MTT as the first moment of the IDC is appropriate only under single passage hypothesis. In this case, the MTT corresponds to the MRT of the indicator in the defined segment and equals  $\mu$  in Eq. (4.28) [11]. In fact, the bubble appearance time at the detection section also corresponds to the disappearance time from the segment.

The LDRW model is more general and does not satisfy the hypothesis of single passage of the indicator. As a consequence, the first moment of the model, which still represents the MRT of the indicator in the tube segment [12, 16], differs from the MTT. The MTT, which is defined as the average time that the indicator takes to go from the injection to the detection site, is by definition equal to  $\mu$  in Eq. (4.25). In fact, in the LDRW model  $\mu$  equals the time that elapses to cover the distance between the injection and detection site at the carrier fluid velocity, i.e., the MTT of the indicator. Instead, the first moment of the model, which corresponds to the MRT and is derived in section 5.1.2, equals  $\mu(1 + 1/\lambda)$ . Therefore, the MRT exceeds the MTT by the term  $\mu/\lambda = 2D/u^2$ , i.e., twice the ratio between indicator diffusion constant  $D$  and squared velocity of the carrier fluid  $u^2$ . Large diffusion constants lead to increased numbers of bubble passages through the detection site and, therefore, to large differences between MRT and MTT.

In conclusion, when either the LDRW model or the FPT model is fitted to the IDC, Eq. (5.30) corresponds to Eq. (5.32).

$$V = \Phi \cdot \mu \quad (5.32)$$

Several techniques, as discussed in section 2.1 can be employed for the assessment of the flow  $\Phi$ .

### 5.3.2 Deconvolution and impulse response

The fluid-dynamic dilution system between contrast injection and detection is a linear system. In fact, if two boluses of mass equal to  $\alpha m$  and  $\beta m$  are injected ( $\alpha, \beta \in \mathbb{R}$ ), the detected IDC, as from Eq. (4.25) or Eq. (4.28), equals  $\alpha C(t) + \beta C(t)$ . As a consequence, the system can be described by an impulse response and both the



models given in Eq. (4.25) and Eq. (4.28) can be considered as the system impulse response.

Since both models assume an ideal bolus injection, which is modelled as a Dirac function and differs from a real injection, a deconvolution technique can be adopted to estimate the impulse response of the dilution system [191, 192]. Due to small SNR, direct deconvolution techniques fail. A more detailed discussion on deconvolution techniques is postponed to the next chapter (section 6.1), where the cardiac quantification is based on a linear system identification method based on a deconvolution algorithm.

A solution to overcome the low SNR problem is the employment of least square techniques, such as Wiener deconvolution filtering (see [193] pp. 337-348 and [194]). The Wiener filter  $W(\omega)$  is designed in the frequency domain with the hypothesis of uncorrelated noise as given in Eq. (5.33) (a derivation of Eq. (5.33) is shown in section 6.1).  $F^*$  is the complex conjugated Fourier transformation of a real injection function  $f(t)$ , which is represented by a normalized (integral equal to 1) 0.8s rectangular input, and  $S_{ff}(\omega)$ ,  $S_{hh}(\omega)$ , and  $S_{nn}(\omega)$  are the injection-function, the impulse-response, and the noise power spectrum respectively.

$$W(\omega) = \frac{F^*(\omega)}{S_{ff}(\omega) + \frac{S_{nn}(\omega)}{S_{hh}(\omega)}} \quad (5.33)$$

$S_{hh}(\omega)$  is estimated as the spectrum of the IDC model fit (without deconvolution) while  $S_{nn}(\omega)$  is estimated as the spectrum of the difference between the IDC and the fitted model. The measured IDC is filtered by the Wiener filter in Eq. (5.33) to obtain the impulse response of the system between injection and detection. The resulting impulse response estimate is fitted and interpreted by the models for the parameter assessment.

The Wiener filter was tested by a specific simulation. LDRW curves were generated and convoluted with a rectangular injection function of 0.8s. The SNR was then reduced by white noise addition as implemented in section 5.1.1 for the fitting simulation. The simulated IDCs were then filtered by the Wiener filter and fitted by the LDRW model. Due to the Wiener deconvolution, the noise characterization changes, so that the noise compensation in Eq. (5.6) is not valid and was not implemented anymore. For each integer value of  $\lambda \in [1..10]$ , a set of 1000 IDCs was generated with SNR=20dB (noise-to-signal amplitude ratio equal to 0.1), which is a typical ratio for real signals. The range of values for the parameter  $\lambda$  covers and exceeds the values encountered in clinical practice.

The fitting results in terms of average percentage MTT-estimate ( $\mu$ ) error are shown in Fig. (5.13). We may conclude that the use of deconvolution filtering leads to more accurate MTT estimates. The standard deviation of the estimates equals 0.38% with and without Wiener deconvolution. Fig. (5.14) shows a simulation example for SNR=20dB and injection function  $f(t)$  equal to a rectangle of 2s.

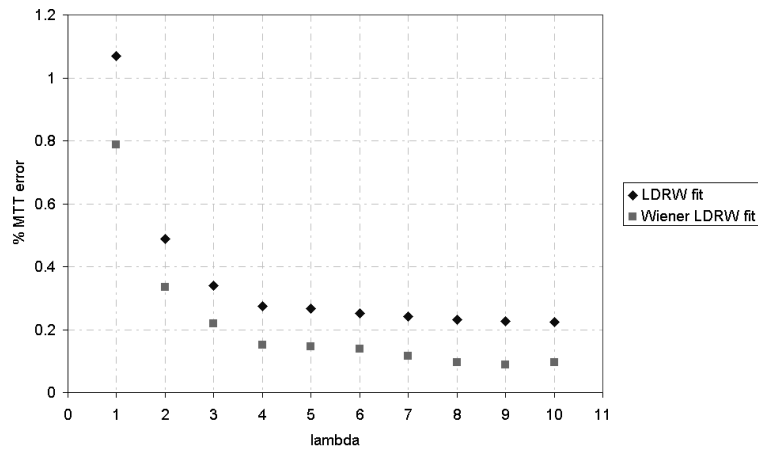


**Figure 5.13:** Wiener filter validation results. LDRW curves are generated and convoluted with a rectangle (injection function) of 0.8s. White noise is added to the curve and the SNR reduced to 20dB. 1000 different noise sequences are used and 1000 different IDCs generated for each integer value of  $\lambda \in [1, 10]$ . MTTs are estimated with and without Wiener filtering, and the average MTT-estimate percent error calculated.

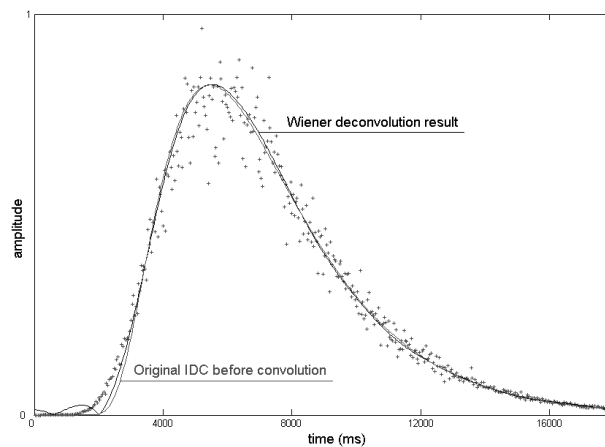


**Figure 5.14:** Example of IDC simulation for Wiener filter validation. The plus-points represent the convoluted noisy IDC, which is deconvoluted to estimate the original IDC.

**Remark**

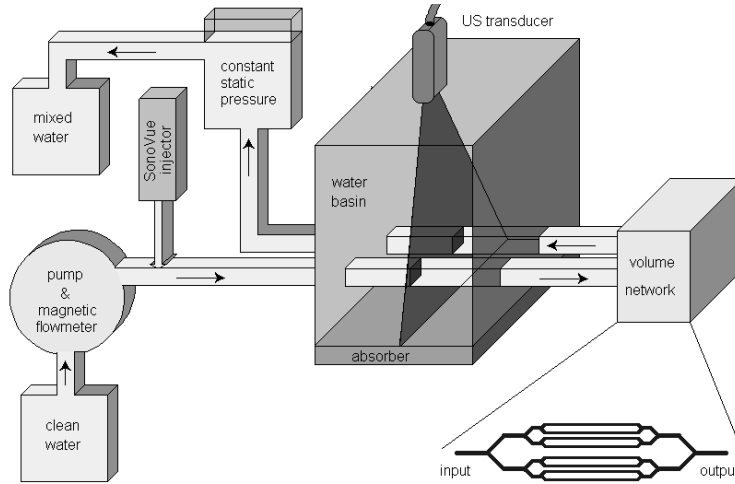
The convolution with a normalized rectangular function  $f(t)$  does not change the integral of the IDC. In fact, for a continuous signal

$$\int_t [f(t) * h(t)] dt = \int_t \int_\tau f(\tau) h(t - \tau) d\tau dt = \int_\tau \int_\xi f(\tau) h(\xi) d\tau d\xi = \int_\xi h(\xi) d\xi,$$

while for a discrete signal

$$\begin{aligned} \sum_{k=-\infty}^{+\infty} [f(k) * h(k)] &= \sum_{k=-\infty}^{+\infty} \sum_{i=-\infty}^{+\infty} f(i) h(k-i) = \\ &= \sum_{k=-\infty}^{+\infty} \frac{1}{L} \sum_{i=k-L}^k h(i) = \sum_{k=-\infty}^{+\infty} \frac{Lh(k)}{L} = \sum_{k=-\infty}^{+\infty} h(k). \end{aligned}$$

As a consequence, the injection function does not influence the flow measurement based on Eq. (2.6).

**5.3.3 In-vitro and in-vivo volume measurements**

**Figure 5.15:** In-vitro set-up for volume measurements.

The measurement of blood volumes by means of UCA dilution was tested and validated in-vitro. A specific hydrodynamic system was built to produce different water volumes as shown in Fig. (5.15). The system consisted of a flow generator (a

calibrated Medtronic 550 bio-console centrifugal pump), a measurement water-filled basin, a tube network that simulated the PBV, and a pressure stabilizer. The generated flow, which was controlled by an electromagnetic flowmeter, passed the water-filled basin through a very thin polyurethane tube. After the basin, the tube expanded into a network of eight tubes and converged again into a single tube that passed back through the basin. The hydrodynamic circuit was open in order to avoid UCA recirculation and the output static pressure was stabilized. The ultrasound measurements were performed in the basin (see Fig. (5.16)). An ultrasound transducer was mounted on the basin, so that both the tubes are simultaneously insonated.

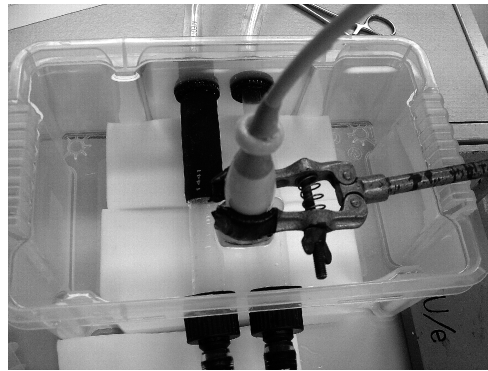


*Figure 5.16: Water-filled basin for ultrasonic measurements. Two thin polyurethane tubes are intercepted by the ultrasound beam for contrast quantification. The first tube (before the volume to measure) is partially reinforced (covered, except for the ultrasound measurement section) by a thick rubber tube in order to hold the pressure increase produced by high flows. The transducer is fixed on the basin in touch with water. It is isolated from water by a thin latex film filled with conductive gel. The bottom of the basin is covered by an ultrasound absorber layer to avoid reverberation.*

The transducer, a TTE Philips S3 probe, was fixed for stability and submerged to optimize acoustic impedance matching. It was covered by conductive gel and isolated from water by a thin plastic layer. The bottom of the basin was covered by an absorbing layer to reduce acoustic reverberation. A Sonos 5500 ultrasound scanner was used to generate B-mode videos. The scanner was set in power modulation with the same setting as for the acoustic calibration and flow measurements in sections 4.1 and 5.2.

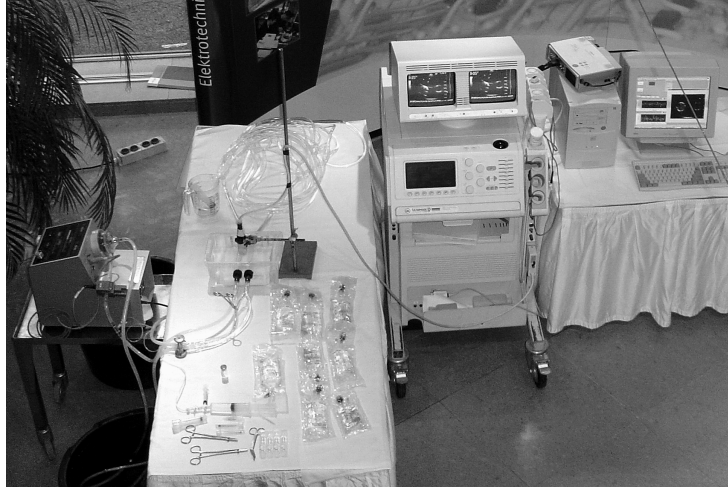


*Figure 5.17: In-vitro set-up for TTE volume measurements. Demonstration using an ATL Ultramark9<sup>®</sup> ultrasound system (Evoluon palace, Eindhoven, November 2003).*

A small bolus of UCA was injected right after the pump to minimize disruption of bubbles. The bolus consisted of 5ml of SonoVue<sup>®</sup> diluted 1:100 into saline (sodium chloride 0.9%), which corresponds to 0.25mg of SonoVue<sup>®</sup>. With this dose, the threshold of 12.5mg/L was never surpassed (see Fig. (4.2)). Therefore, as concluded in section 4.1, the attenuation effect was negligible and the relation between UCA concentration and backscattered acoustic intensity was linear. The passage of the contrast bolus through the first tube (before the network) and the second tube (after the network) was recorded by the ultrasound scanner. The B-mode digital records were analyzed by software Q-Lab<sup>®</sup> (Philips Medical Systems) for acoustic quantification.

A ROI was overlapped on each tube to quantify the acoustic intensity that was backscattered by the contrast passage (see Fig. (5.18)). Therefore, two IDCs (one for each tube) were generated. The IDCs were processed and fitted by the LDRW model and the FPT model in order to estimate the MTT of the contrast between the first and the second ROI.

The volume  $V$  between the two detection sites (before and after the tube network in Fig. (5.15)), was estimated as given in Eq. (5.34), where the MTT difference ( $\Delta\text{MTT}$ ) between the two measured IDCs is multiplied times the flow  $\Phi$ .

$$V = \Delta\text{MTT} \cdot \Phi = \Delta\mu \cdot \Phi \quad (5.34)$$



*Figure 5.18: Two B-mode frames showing the passage of the contrast bolus through the first tube (left frame) and the second tube (right frame). A ROI is placed on each tube for the acoustic intensity measurement.*

The IDC analysis system is implemented in Labview® and Matlab®, and runs on a personal computer. Apart from the off-line acoustic densitometry of digital records, also real-time video densitometry of analog video outputs of ultrasound scanners can be performed.

The hydrodynamic system described in Fig. (5.15) was used to measure different volumes and validate the method. The volume of the tube-network was changed by clamping the tubes in specific sites. Four different volumes were defined: 310ml, 412ml, 625ml, and 1080ml. The volumes were measured for five different flows, from 1L/min to 5L/min. Both the LDRW and the FPT models were used for the IDC fitting (see Eq. (4.25) and Eq. (4.28)). The flow was measured by the electromagnetic flowmeter that is combined with the pump (see Fig.(5.15)). The resulting volume estimates are plotted in Fig. (5.19) for both the LDRW and the FPT model fits.

The percent standard deviation of the measurements with respect to the average estimate (from the small to the large volume) is 2.1%, 3.2%, 0.8%, 0.7% for the LDRW fits, and 2.2%, 2.2%, 1.1%, 1% for the FPT model fits. Fig. (5.20) shows the average estimates over all the five flows using both models. The physiologic range for PBV measurements is highlighted<sup>8</sup> [82, 83]. The determination coefficient between the real and the estimated volumes is larger than 0.999 for both the LDRW and the FPT model fits. Both approaches produced very stable results in a wide range of flows. However, the FPT model volume estimates shows an average overestimation of 3.2% with respect to the LDRW model estimates, which are very accurate in the physiological PBV range. This is explained by the single passage hypothesis of the FPT model. In fact, since both models show excellent IDC fits (determination coefficient larger than 0.9), the estimates for the parameter  $\mu$  as derived from the FPT model are very close to the MRT estimates from the LDRW model (see Fig. (5.21)).

<sup>8</sup>The provided PBV values are non-indexed, i.e., they are not divided by the BSA index (see CI in section 2.1).

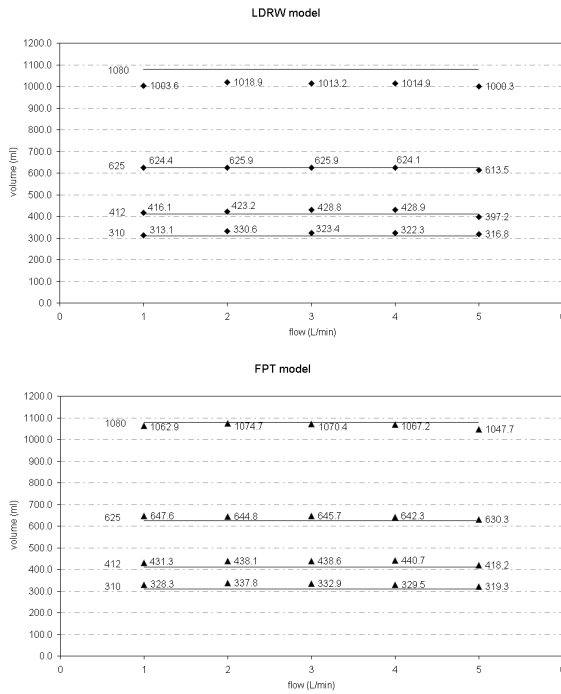


Figure 5.19: In-vitro flow measurements for different flows using the LDRW (upper) and the FPT (lower) model fits.

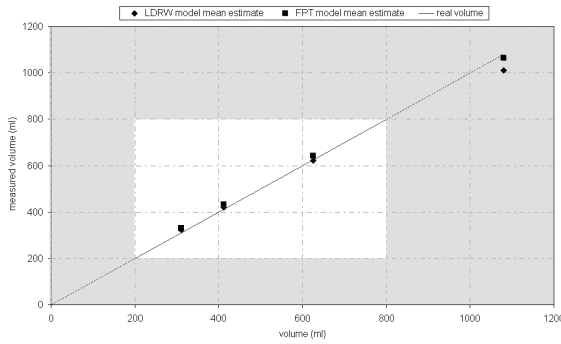
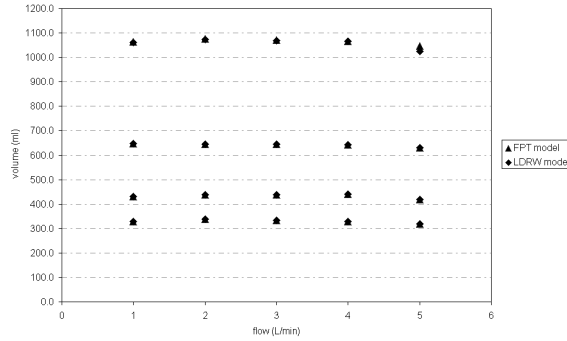


Figure 5.20: Average volume estimates over five different flows using both the LDRW and the FPT model fits. The line indicates the real volume. In the middle of the plot, the expected physiological PBV range is highlighted.



**Figure 5.21:** Volume measurements by FPT-model MTT estimates and LDRW-model MRT estimates.

As a consequence, the overestimation is quantified by the term  $\mu/\lambda$  from the LDRW model, which is related to the diffusion-to-convection ratio. When the diffusion component is larger, the difference between MTT and MRT is more pronounced.

The physical interpretation for the MTT-MRT difference in the UCA dilution context stands in the low MI insonation. The adopted 0.1 MI does not produce a significant bubble disruption rate. As a consequence, the FPT model hypothesis is not realistic.

Due to a problem in the volume network, the flow in the two main brunches of the largest volume (1080ml) was unbalanced. As a consequence, the resulting IDC is the sum of two different IDCs with different MTT. The fit of such a curve, as confirmed by specific simulation, provides with a MTT estimate that is close to the smallest MTT. This might be the reason for the underestimation of the largest volume with both models. However, a volume of 1080ml is beyond the physiological boundaries for the PBV.

A similar in-vitro experimentation was also performed using a TEE probe directly submerged into water together with the two polyurethane tubes as shown in Fig. (5.22). Two different volumes of 410ml and 700ml were realized by using one and two artificial lungs (COBE® oxygenators of 280ml) in parallel. The scanner was a Sonos 4500 and the setting was the same fundamental harmonic mode as for the calibration in Fig. (4.6). Since the injected dose was a SonoVue® bolus of 2.5mg (10 times larger than the usual dose), the effect of the video logarithmic compression was evident and the calibration formula in Eq. (4.4) had to be applied before the IDC interpolation.

**Remark** Referring to Eq. (4.4),  $a_1C(t) + a_2$  is equal to  $10^{\frac{G(t)}{a_0}}$ . Therefore, the only calibration parameter that influences the MTT estimate, which depends on the parameters  $\lambda$  and  $\mu$  of the LDRW and FPT models, is  $a_0$ .



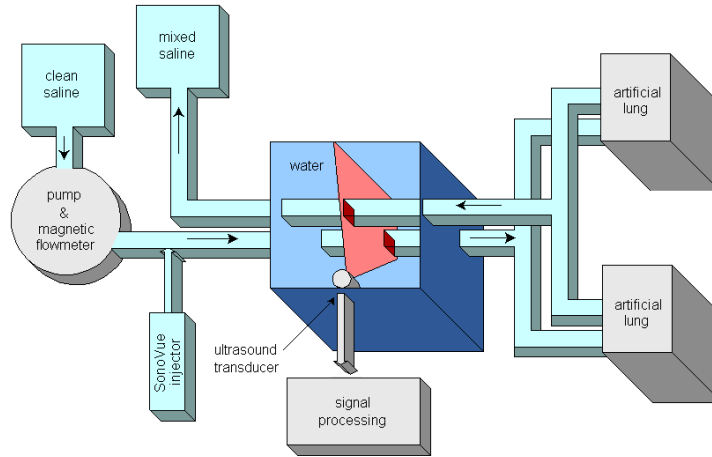


**Figure 5.22:** *In-vitro set-up for TEE volume measurements.*

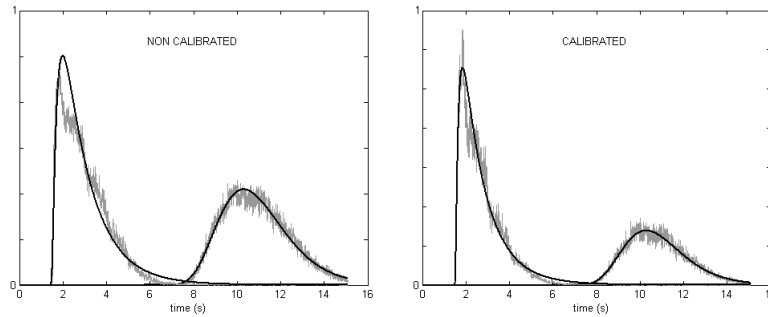


**Figure 5.23:** *LDRW model fits of video IDCs detected before and after the oxygenators. The left couple of IDCs is not calibrated while the right IDCs are calibrated by the model in Eq. (4.4) and, therefore, result in better LDRW fits.*

Fig. (5.23) shows the LDRW fits of a couple of experimental curves (before and after the artificial lungs) with and without calibration. As expected, the first IDC (before the oxygenators) shows a larger amplitude with respect to the second IDC (after the oxygenators). As a result, the first IDC was more affected by the log-compression, and the use of calibration improved the determination coefficient of the LDRW model fit from 0.97 to 0.98.

In general, the artificial lung traps part of the contrast micro-bubbles, which was the reason for the lower contrast concentrations of the second IDCs. Moreover, the larger micro-bubbles (about  $10\mu\text{m}$ ), which give the better response to ultrasounds [130], have a larger probability of being trapped in the oxygenator. However, for larger flows (beyond  $2\text{L}/\text{min}$ ), the second IDC showed a larger signal with respect to the first one. This was caused, according to the bubble dynamic models in section 3.2, by the pressure increase due to the resistance introduced by the oxygenator into the hydrodynamic system. In fact, a pressure  $P_0$  increase leads to an increase of elasticity constant ( $s$  in Eq. (3.26)) and resonance frequency (Eq. (3.28)) of the micro-bubbles [174]. The effects of this pressure increase were also recognizable from the stretching of the first polyurethane tube in the water-filled basin, which made this set-up limited to low flow measurements and eventually replaced by the tube-network set-up showed in Fig. (5.15). The acoustic backscatter dependency on pressure-flow variations makes the volume measurement set-up unsuitable for flow measurements, where the absolute relation between acoustic backscatter and contrast concentration must be determined.

The results based on the LDRW and FPT model fits showed a mean estimated value over six measurements flows (flows ranging from  $0.5\text{L}/\text{min}$  to  $3\text{L}/\text{min}$ ) equal to  $402.9\text{ml}$  and  $409.2\text{ml}$  for the single oxygenator and  $681.1\text{ml}$  and  $684.2\text{ml}$  for the double-oxygenator volume respectively. The standard deviations were  $2.1\%$  and  $1.6\%$  for the single volume and  $8.2\%$  and  $3.5\%$  for the double volume. The small negative bias of the mean value was caused by some air bubbles that were trapped in the oxygenator.

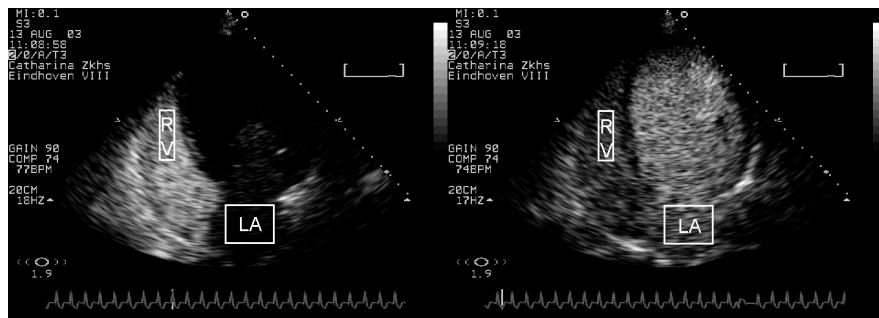


**Figure 5.24:** TTE four chamber view of the heart after a peripheral injection of a  $0.25\text{mg}$  bolus of SonoVue®. On the left, the opacification of the right side of the heart is shown, while later, on the right, the left side of the heart is opacified. Two ROI are placed in the right ventricle and the left atrium for the IDC measurements.

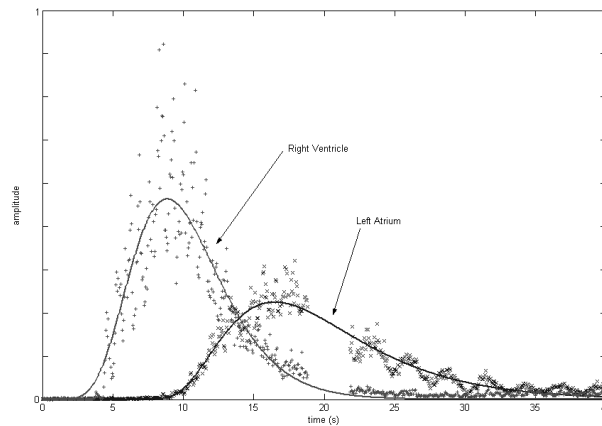


**Figure 5.25:** LDRW fits of two IDCs recorded from the right ventricle and the left atrium of a patient after an injection of 0.25mg of SonoVue® diluted in 5ml of saline.

The application of the system in humans requires the use of specific cardiac views where more IDCs can be measured simultaneously. A four chamber view, for instance, allows the measurement of four IDCs, one for each chamber, leading to an easy assessment of pulmonary, central, intra-thoracic, and systemic blood volumes (see section 2.3).

Fig. (5.24) shows the application of the system to a real patient. A TTE four-chamber view is used for the measurement. The PBV is assessed by placing two ROI in the RV and LA. The bolus (0.25mg of SonoVue® in 5ml of saline) is injected into a peripheral vein (arm). The CO is assessed by aortic Doppler time-integration technique (see section 2.1.4). The RV and LA IDCs are measured and fitted by the models (see Fig. (5.25)). The  $\Delta$ MTT is estimated from the IDCs and multiplied times the CO to obtain the PBV estimate. Fig. (5.26) shows the measured PBV in a group of 20 patients with different pathologies. The measurements were performed with a Sonos 5500 ultrasound scanner in power modulation.

Except for few patients (1, 12, 13, and 14), the difference between LDRW and FPT model estimates was minimal. In fact, the cardiac valves reduce the number of bubble passages through the detection sites (cardiac chambers) and the difference between MTT and MRT is minimal. In general, the worse the cardiac conditions, as diagnosed by cardiologists, the larger the PBV. In fact, all the patients with large PBV are heart failure patients (candidates for bi-ventricular pacing). This preliminary result corresponds to the expectations. In fact, a decrease of left ventricular efficiency could be compensated by a pulmonary blood volume (and pressure) increase.

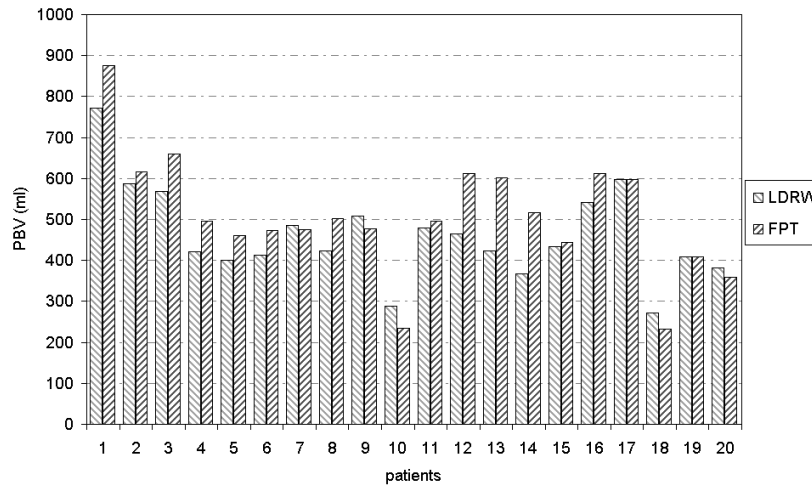


**Figure 5.26:** PBV measurements in patients. Both the LDRW and FPT model estimates are shown.

With respect to classic trans-pulmonary techniques (see section 2.3), we are able to exclude the right atrium, left ventricle, and aortic volume from the PBV measurement, resulting in a more accurate estimate.

In conclusion, the blood volume assessment by use of UCA dilution is feasible and accurate. The measurement can be performed with minimal invasiveness. As a consequence, this technique allows the measurement of some important diagnostic clinical parameters that cannot be measured without the use of very invasive techniques. Physiological processes can be studied more in detail resulting in increased knowledge, for instance, of the time course of chronic heart failure patients with minimal risk and discomfort for the patient and, possibly, new therapeutic strategies.

Moreover, this technique opens new possibilities for studying the relation between blood volumes and cardiac diseases. The characterization of this relation is already in progress and some preliminary results concerning the correlation between PBV decrease and EF increase during cardiac resynchronization are discussed in chapter 8.

Further research will also concern the use of the recirculation curve fit in order to assess the total circulating blood volume, which could be used to normalize the value of the other partial volumes. Fig. (5.27) shows the result of an automatic LDRW fit of the first and the second passage of the contrast. The interpolation of the recirculation is implemented as a standard LDRW fitting (as described in section 5.1.1) applied to the subtraction of the LDRW fit of the first passage curve to the complete IDC.

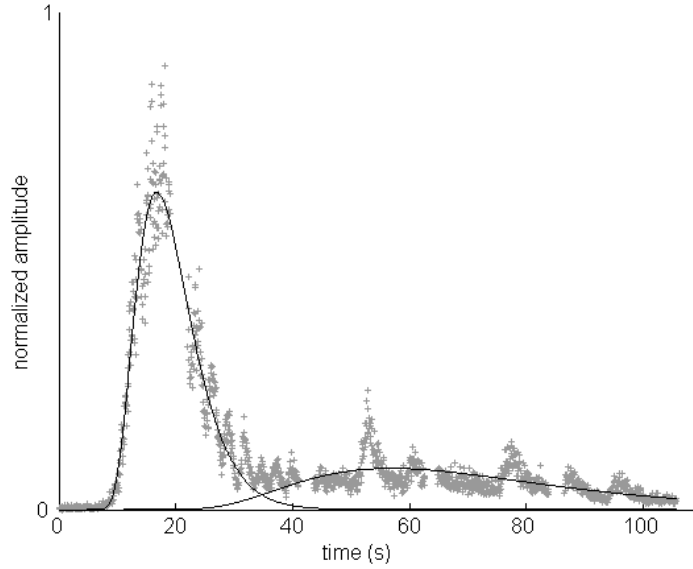


**Figure 5.27:** Example of right ventricle IDC with evident recirculation of the contrast. The LDRW-model curve fit of the first passage IDC is shown together with the LDRW fit of the second passage IDC, i.e., the recirculation.

## 5.4 Ejection fraction measurement

Based on the LDRW fit of the IDC and the concepts reported in section 2.2, a novel approach for the measurement of EF is developed. EF can be measured from the down-slope of the ventricular IDC if the injection is performed directly into the ventricle within a diastole, resulting in a very invasive practice. In fact, Eq. (2.19) and Eq. (2.21) are valid when the contrast is ejected from the ventricle with no incoming contrast.

However, we could still perform a minimally-invasive peripheral intra-venous injection and consider the limit of the LV IDC fit for  $t$  going to  $\infty$ . For large  $t$ , we might suppose that no contrast is present in the ventricular inflow, so that the hypothesis for Eq. (2.19) and Eq. (2.21) is fulfilled. Therefore, once the IDC is interpolated by the LDRW model, the EF can be calculated as the limit for  $t$  going to  $\infty$  of Eq. (2.19). The result is given as in Eq. (5.35), where  $\Delta t$  is the pulse period.

$$\text{EF} = \lim_{t \rightarrow \infty} \left[ 1 - \frac{C(t_{n+1})}{C(t_n)} \right] = \lim_{t \rightarrow \infty} \left[ 1 - \sqrt{\frac{t_n}{t_{n+1}}} e^{\frac{\lambda}{2} \left[ \left( \frac{t_n}{\mu} + \frac{\mu}{t_n} \right) - \left( \frac{t_{n+1}}{\mu} + \frac{\mu}{t_{n+1}} \right) \right]} \right] = 1 - e^{-\frac{\lambda \Delta t}{2\mu}} \quad (5.35)$$

Eq. (5.35) has the same structure as Eq. (2.21), where the time constant  $\tau$  is now given by the term  $2\mu/\lambda$ . With reference to the LDRW fitting parameters in Eq. (5.2), the EF, which in the IDC context is better referred to as FEF (see section 2.2), is given as in Eq. (5.36).

$$\text{FEF} = 1 - e^{P_2 \Delta t} \quad (5.36)$$

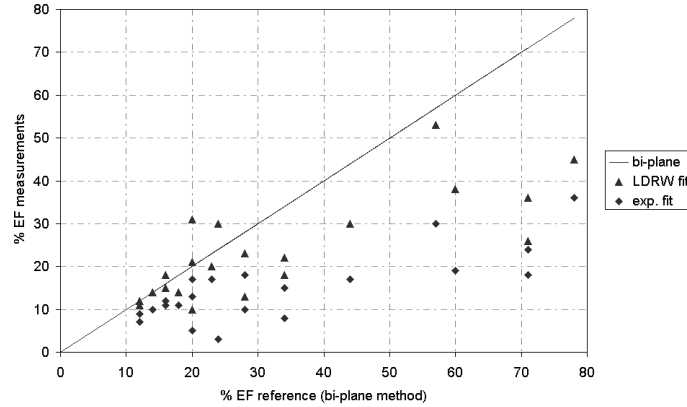


**Figure 5.28:** EF measurements by IDC exponential and LDRW fit compared to bi-plane echographic estimates.

The method was tested both in-vitro, using the set-up in Fig. (5.9) and Fig. (5.11), and in-vivo, comparing the measurements to bi-plane echographic measurements (see section 2.2) with contrast opacification. The in-vivo measurements were performed on the LV, since the RV EF cannot be quantified by geometric echocardiographic techniques. The mitral insufficiency was not significant, so that EF and FEF were approximately equal.

As shown in Fig. (5.28), the results were not satisfactory. The FEF assessment showed a significant underestimation for increasing EF. Probably, due to diffusion, the hypothesis of out-flowing contrast with no inflow is never fulfilled. However, the measurements made by direct exponential fitting on the IDC down-slope show an even more significant underestimation. The same conclusions are derived after in-vitro validation using the set-up in Fig. (5.9) and Fig. (5.11).

An alternative approach for the EF assessment based on a peripheral intravenous UCA bolus injection is proposed in the next chapter. It makes use of the estimation of the ventricular impulse response. This efficient technique results in more accurate measurements, which are independent on the injection site and function.



## Chapter 6

# Dilution system identification

*...nil sine magno vita labore dedit mortalibus (Horatius).*

This chapter proposes an alternative approach to that presented in the previous chapter for the measurement of EF and blood volumes. The dilution system is treated and interpreted as a linear system. The impulse response of the system between two indicator detection sites is estimated (system identification) by means of a deconvolution technique. The estimated impulse response is then interpolated by specific models for the measurement of EF and volumes. Section 6.1 introduces to the deconvolution theory for system identification while section 6.2 and section 6.3 apply the deconvolution approach to EF and blood volume measurements respectively.

### 6.1 Deconvolution techniques

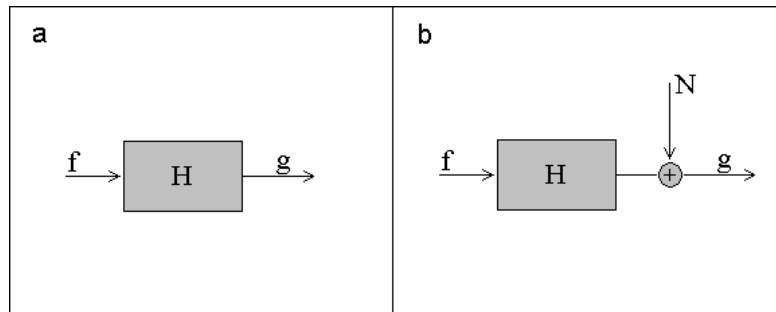


**Figure 6.1:** Scheme of a linear system characterized by its impulse response  $h(t)$  (or transfer function  $H(\omega)$ ). No noise is introduced in scheme **a** while the noise spectrum  $N(\omega)$  is added in **b**.

The fluid-dynamic dilution system between contrast injection and detection is a linear system. In fact, if two boluses of mass equal to  $\alpha M$  and  $\beta M$  are injected ( $\alpha, \beta \in \mathbb{R}$ ), the detected IDC, as from all the IDC models (see section 4.2), equals  $\alpha C(t) +$



$\beta C(t)$ . Therefore, once a couple ultrasound intensity curves (input and output of the dilution system) are transformed into IDCs by compensating for all the non-linear effects, they can be used as inputs of a deconvolution algorithm for the estimation of the impulse response of the dilution-system between the detection sites [192].

In general, if  $f(t)$  and  $g(t)$  are the input and output functions of a linear system as shown in Fig. (6.1a),  $g(t)$  is the result of a convolution operation between the input  $f(t)$  and the system impulse response  $h(t)$  ( $g(t) = h(t) * f(t)$ ). The impulse response  $h(t)$  characterizes the linear system. In fact, if  $f(t)$  is an impulse (Dirac function),  $h(t) = g(t)$ . However, when  $f(t)$  is not an impulse,  $h(t)$  can still be recovered from  $f(t)$  and  $g(t)$  by a deconvolution operation.  $g(t)$  can be expressed in discrete terms as given in Eq. (6.1).

$$g(n) = f(n) * h(n) = \sum_{i=-\infty}^{\infty} f(i) h(n-i) \quad (6.1)$$

The aim of a deconvolution operation is the determination of  $\tilde{f}(n)$  so that  $h(n)$  is given as in Eq. (6.2).

$$h(n) = \tilde{f}(n) * g(n) = \sum_{i=-\infty}^{\infty} \tilde{f}(i) g(n-i) \quad (6.2)$$

The deconvolution can be solved directly as an inversion of Eq. (6.1). If  $f(n)$  lasts  $L$  samples, the recursive solution is given as in Eq. (6.3), for  $n \in [-1..\infty)$ .

$$h(n+1) = \frac{g(n+1) - \sum_{i=1}^L f(i) h(n+1-i)}{f(0)} \quad (6.3)$$

When the impulse response  $h(n)$  represents a real system, it must be causal, i.e.,  $h(n) = 0$  for  $n < 0$ .

In frequency domain, a deconvolution is realized by a simple mathematical inversion. In fact, as a convolution becomes a multiplication, a deconvolution becomes a division by  $F(\omega)$  as given in Eq. (6.4), where  $\omega$  is the angular velocity in radians per second ( $\omega = 2\pi f$ ). The same can be expressed in the  $z$ -domain, with  $z = e^{j2\pi f T}$  ( $T$  sampling period).

$$\begin{aligned} g(t) &= f(t) * h(t) \xrightarrow{\mathfrak{F}} G(\omega) = F(\omega) H(\omega) \\ &\Downarrow \\ H(\omega) &= \frac{G(\omega)}{F(\omega)} \xrightarrow{\mathfrak{F}^{-1}} g(t) * \tilde{f}(t) = h(t), \quad \tilde{f} = \mathfrak{F}^{-1} \left( \frac{1}{F(\omega)} \right) \end{aligned} \quad (6.4)$$

UCA IDC measurements are influenced by several noise sources, such as bad mixing of the contrast, acoustic reverberation, backscatter oscillations due to pressure variations, bubble disruption due to ultrasound pressure, patient-movement and blood-acceleration artifacts, and contrast recirculation, resulting in very noisy IDCs. Due to the small SNR, direct deconvolution techniques based on either matrix inversion in time domain<sup>1</sup> or spectrum inversion in frequency domain fail [191, 192]. In fact, although these direct deconvolution techniques are rather simple, difficulties arise as soon as the SNR decreases.

In frequency domain, as shown in Fig. (6.1b), the signal to be deconvoluted is given as  $G(\omega) = F(\omega)(H(\omega) + N(\omega))$ . The result of a direct deconvolution in frequency domain, i.e., the input response estimate  $\hat{H}(\omega)$ , is given as in Eq. (6.5).

$$\hat{H}(\omega) = \frac{G(\omega)}{F(\omega)} = H(\omega) + \frac{N(\omega)}{F(\omega)} \quad (6.5)$$

The division of the noise spectrum  $N(\omega)$  by  $F(\omega)$  generates a high-frequency noise amplification, since the noise band is usually larger than the signal  $F(\omega)$  band. Especially for IDC applications,  $F(\omega)$  contains mainly low frequency components and  $N(\omega)$  is a broad-band noise. As a consequence, the high-pass filter  $F^{-1}(\omega)$  works as a noise amplifier and the deconvolution operation, as shown in Fig. (6.2), becomes very unstable.

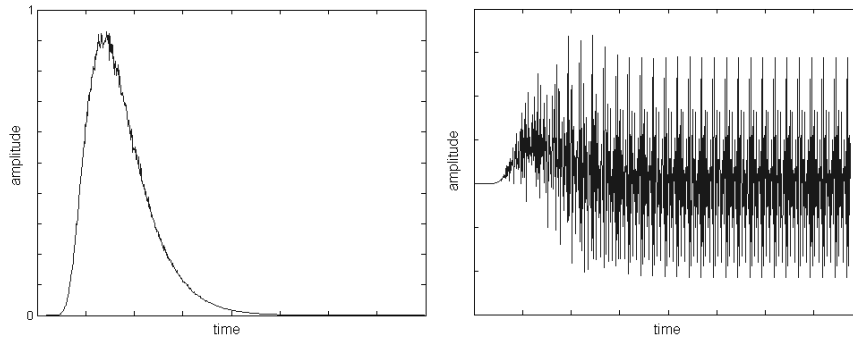


**Figure 6.2:** Simulation of an unstable direct deconvolution for a low noise IDC.  $f(t)$  is generated as a LDRW function, it is convoluted to a rectangular  $h(t)$ . After white noise addition (left plot), result is deconvoluted in order to estimate  $f(t)$  (right plot).

<sup>1</sup>A convolution can also be represented as the matrix product between the input vector  $\underline{f}$  and a circular matrix  $[H]$  whose lines contain the impulse response  $h(n)$ , i.e.,  $\underline{g} = [H]\underline{f}$ . In this context, the deconvolution in Eq. (6.3) can be expressed as a matrix inversion.

Apart from the direct deconvolution, many of the proposed deconvolution techniques are iterative ones. The first simple approach, studied by van Cittert in the early thirties, builds a correction term that is proportional to a defined error [195]. This error is given as the difference  $g(t) - h_i(t) * f(t)$ , where  $h_i(t)$  is the estimate of the impulse response made at the  $i^{\text{th}}$  cycle. Therefore, the final formula is given as in Eq. (6.3).

$$h_{i+1}(t) = h_i(t) + \alpha [g(t) - h_i(t) * f(t)] \quad (6.6)$$

$\alpha$  can be equal to one, but should be decreased for increasing noise power. However, the van Cittert's technique, which together with the previous techniques can be classified among the linear approaches, is not robust enough to treat the typical SNR of measured IDCs. Fig. (6.3) shows a van Cittert's deconvolution for an IDC with high SNR (40dB). The noise level, which is very low in the original IDC, is extremely amplified by the deconvolution operation.

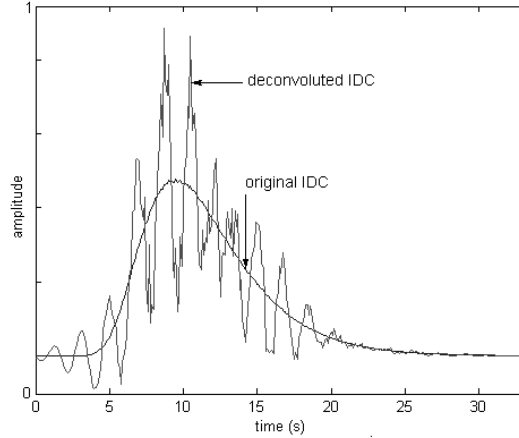


**Figure 6.3:** Simulation of an unstable van Cittert deconvolution for a low noise (SNR = 40dB) IDC.  $f(t)$  is generated as a LDRW function convoluted to a 1s rectangular  $h(t)$  with white noise addition. The result is deconvoluted in order to estimate  $f(t)$ .

Beyond the linear-deconvolution techniques, other non-linear recursive algorithms show very interesting results. In this context, we present two algorithms that give very accurate results even in case of low SNR. Based on the maximum likelihood, these techniques maximize the conditional probability defined by the Bayes formula as given in Eq. (6.7).

$$P(f * h | g) = \frac{P(g | f * h) P(f * h)}{P(g)} \quad (6.7)$$

If the statistics  $P(h)$  is assumed to be a Poisson statistics<sup>2</sup>, then  $P(f * h|g)$  is maximized by the Richardson-Lucy algorithm<sup>3</sup> (1972), while if  $P(h)$  is assumed to be a Gaussian statistics, then  $P(f * h|g)$  is maximized by the Muller algorithm (1997). Eq. (6.8) and Eq. (6.9) show the Richardson-Lucy and the Muller algorithm respectively.

$$h_{i+1}(t) = h_i(t) \left[ f(-t) * \frac{g(t)}{f(t) * h_i(t)} \right] \quad (6.8)$$

$$h_{i+1}(t) = h_i(t) \left[ \frac{g(t) * f(-t)}{f(t) * h_i(t) * f(-t)} \right] \quad (6.9)$$

Since the LDRW statistics includes a skewness parameter, it is closer to a Poisson distribution than to a Gaussian one.

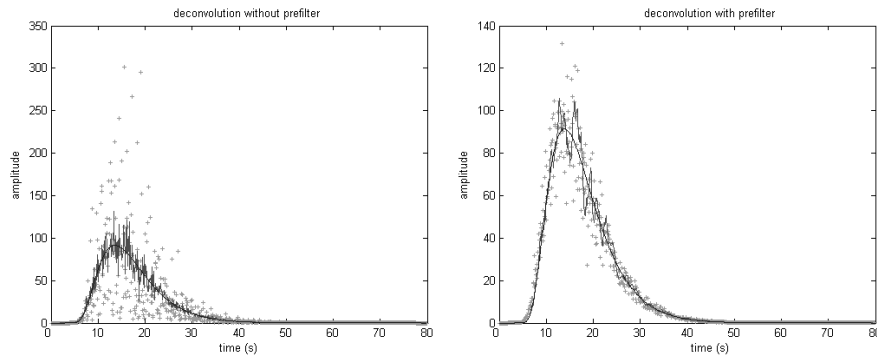


**Figure 6.4:** Simulation of an Richardson-Lucy deconvolution. The continuous smooth line is the result of a convolution between a 1s rectangle and a LDRW function. The overlapped noisy line is the result of the noise addition and the plus signal is the deconvolution result. The deconvolution result is shown without (left plot) and with (right plot) the employment of a pre-filter.

As clear from the inversion of  $F(\omega)$  in Eq. (6.4), the treatment of noisy signals becomes more unstable as the noise contains high frequency components. To overcome this problem, it is possible to apply a low-pass filter before the deconvolution. Pre-filtering the high frequencies of the signal leads to a significant improvement of the deconvolution stability. Fig. (6.4) shows the result of a Richardson-Lucy deconvolution with and without a pre-filter. As for the previous simulations, the deconvolution input  $g(t)$  is generated as LDRW function that is convoluted to a normalized

<sup>2</sup>Poisson distribution:  $P(t, \lambda) = \frac{e^{-\lambda} \lambda^t}{t!}$ .

<sup>3</sup>The Richardson-Lucy technique is also implemented in the Hubble Telescope to compensate the spread point function of the optical system.

rectangle of 1s and summed to white noise. The use of a low-pass pre-filter results in a significant improvement of the SNR.

An alternative solution to the deconvolution issue is the employment of a least square technique, such as a Wiener deconvolution filtering [41, 186, 191, 192, 194, 196, 197]. It is a least square estimation of the optimum deconvolution filter  $w(t)$ . This method aims to minimize the  $L^2$  distance  $d(g(t) * w(t), h(t))$ , which is defined as  $d(w) = \int (g(t) * w(t) - h(t))^2 dt$ .

The minimum distance is given by the zero crossing of the derivative of  $d$  with respect to  $w$ . It is a solution of the equation  $d'(w) = 0$ , which can be expressed as given in Eq. (6.10), where  $R_{hg}$  and  $R_{gg}$  represent the correlation between  $h(t)$  and  $g(t)$  and the autocorrelation of  $g(t)$  respectively [186, 194].

$$R_{hg}(t) = w(t) * R_{gg}(t) \quad (6.10)$$

Eq. (6.10) is referred to as *normal Wiener-Hopf equation*. For uncorrelated noise,  $R_{hg}(t) = R_{hn}(t) + R_{hh}(t) * f(-t) = R_{hh}(t) * f(-t)$  and  $R_{gg}(t) = 2R_{hn}(t) * f(-t) + R_{ff}(t) * R_{hh}(t) + R_{nn}(t) = R_{ff}(t) * R_{hh}(t) + R_{nn}(t)$ . Therefore, in frequency domain,  $W(\omega)$  is given as in Eq. (5.33) in section 5.3.2, where  $S_{ff}(\omega)$ ,  $S_{hh}(\omega)$ , and  $S_{nn}(\omega)$  are the input IDC, the system impulse response, and the noise power spectrum respectively.

Eq. (5.33) corresponds to a direct deconvolution filter in frequency domain except for the term  $S_{nn}(\omega)/S_{hh}(\omega)$ , which corresponds to the SNR spectrum. An application simulation of this filter is shown in Fig. (5.14), where the input function  $f(t)$  is a 0.8s normalized rectangle,  $S_{hh}(\omega)$  is approximated by the spectrum of the LDRW fit of  $g(t)$ , and  $S_{hh}(\omega)$  is approximated by the spectrum of the difference between  $g(t)$  and its LDRW fit.

In general, when the input function is known, such as for instance the rectangle that models the injection function, the performance of the Wiener and the Richardson-Lucy deconvolution are comparable. However, when the input function is also a measured noisy IDC, the Richardson-Lucy algorithm shows a significant convergence time increase as well as a limited robustness to small SNR. As a result, we decided to design a least square deconvolution algorithm based on a Wiener filter.

## 6.2 Ejection fraction measurement

As explained in sections 2.2 and 4.2.1, the EF can be measured by means of Eq. (2.21) from the LV IDC exponential fit after a fast bolus injection in the ventricle during diastole (Holt method [75]). In fact, the LV IDC after a fast bolus injection, which can be modelled as a Dirac impulse, corresponds to the LV dilution system impulse response, and is well modelled by a mono-compartment model.

Based on the presented theory, a new minimally-invasive indicator dilution technique for EF quantification is proposed. It is based on a peripheral injection of an ultrasound contrast agent bolus. The LA and LV acoustic intensities are recorded versus time by TTE. The measured curves are corrected for attenuation distortion and processed by an adaptive Wiener deconvolution algorithm for the estimation of the LV impulse response, which is interpolated by a mono-compartment exponential model for the EF assessment. This technique, as all the indicator dilution techniques, measures Forward Ejection Fraction (FEF), which excludes regurgitant volumes (see section 2.2).

Section 6.2.1 presents a solution to compensate for the attenuation between LV and LA. Although in the adopted concentration range the attenuation is usually negligible, EF measurements are strongly dependent on the IDC shape and, therefore, sensitive to any minimal non-linearity. Moreover, the presented deconvolution theory is based on the linear-system theory, which requires the linearity of the system by definition. After the system is linearized, a Wiener deconvolution scheme for EF measurements is proposed in section 6.2.2. Some validation results in patients are shown in section 6.2.3.

### 6.2.1 Attenuation compensation

After the LA and LV acoustic intensity curves are measured (see Fig. (6.5) and Fig. (6.6)), a deconvolution technique could estimate the impulse response of the system between the two sites (LV dilution system identification). However, a strict requirement is the linearity of the system. Although the contrast dilution system is linear, the relation between measured acoustic intensity and real contrast concentration is distorted by several non-linearities.

In order to ensure a linear relation between contrast concentration and acoustic backscatter, the injected dose of contrast is very small (0.5mg of SonoVue®). In fact, as discussed in section 3.2 and section 4.1, the integrated acoustic backscatter is linearly related to contrast concentration in the low-concentration range. However, also according to experimental measurements, a minimal attenuation effect is recognizable between LV and LA intensity curves [98, 140, 143, 145]. While the LV ROI is near the transducer, the LA ROI is beyond the LV and is detected by ultrasonic waves that pass twice through the contrast-filled LV (see Fig. (6.5)). Consequently, as shown in Fig. (6.6), the LA acoustic backscatter is attenuated and the LA intensity curve is lower than the LV curve.

The attenuation effect on the LV acoustic intensity curve is approximately constant (invariant with time), since it is mainly due to the tissue between the transthoracic transducer and the LV apex. Such an effect does not influence the linearity of the relation between contrast concentration and acoustic intensity. Non-linearities are introduced by the attenuation between LV and LA ROI. As a consequence, the

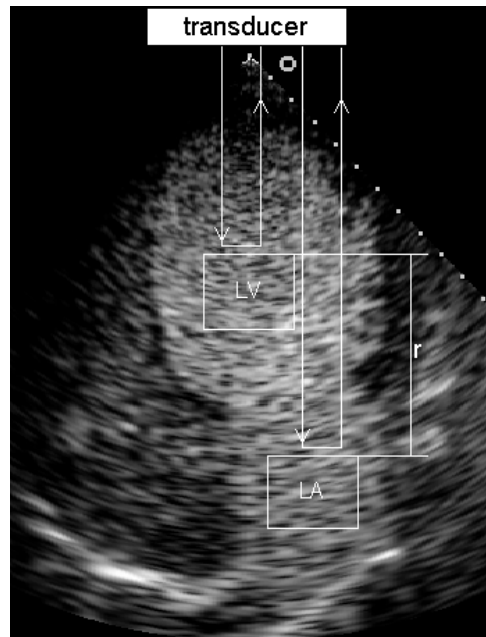


**Figure 6.5:** Trans-thoracic four-chamber view. Two ROIs are placed on the LV and LA for the IDC measurement. A simplified representation of the ultrasound wave paths to the LV and LA ROI is shown together with the distance difference  $r$  from the transducer.

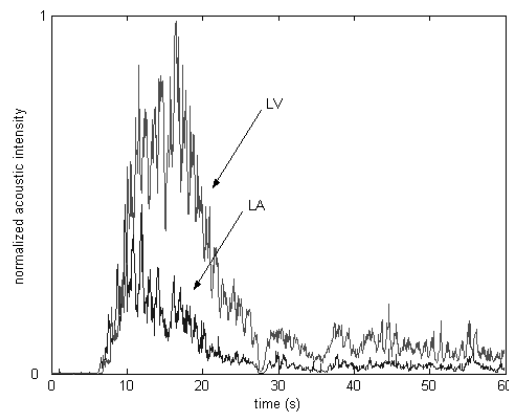


**Figure 6.6:** LA and LV acoustic intensity curves. The LA curve shows a lower intensity due to the LV attenuation effect.

attenuation of the LV acoustic intensity is neglected and the attenuation effect on the LA intensity curve can be compensated by exploiting the information derived from the LV acoustic intensity curve.

With reference to Eq. (4.2), the acoustic intensity decay between LV and LA due to attenuation is described by an exponential relation as given in Eq. (6.11), where  $\widehat{I}_{LA}$  and  $I_{LA}$  represent the acoustic intensity received from the LA with and without attenuation respectively ( $I_{LA} = I_0(\beta + \Delta\beta)$ ),  $a_t$  is the total attenuation coefficient, and  $r$  is the distance between the LA and LV ROI.

$$\widehat{I}_{LA} = I_{LA} \cdot e^{-4a_t r} \quad (6.11)$$

The attenuation coefficient  $a_t$  is the sum of two terms ( $a_t = a + \Delta a$ ): the stationary attenuation coefficient  $a$  due to physiological structures (tissue and blood) and the non-stationary attenuation coefficient  $\Delta a$  due to diluted contrast. The standard value for  $a$ , which is used to estimate *derated* pressure values in tissue, is equal to  $0.3\text{dB}\cdot\text{cm}^{-1}\cdot\text{MHz}^{-1}$  [96]. For small contrast concentrations, the attenuation coefficient  $\Delta a$  is linearly related to the contrast concentration (see section 3.2). Therefore,  $\Delta a$  is linearly related to the LV contrast concentration  $C_{LV}$  ( $\Delta a = k_1 C_{LV}$ ). Due to the constant attenuation of the LV acoustic intensity  $I_{LV}$ , the relation between  $C_{LV}$  and  $I_{LV}$  is linear ( $C_{LV} = k_2 I_{LV}$ ) and  $\Delta a$  can be represented as a linear function of  $I_{LV}$ . With  $k = 4k_1 k_2 r$ , Eq. (6.11) becomes as given in Eq. (6.12).

$$\widehat{I}_{LA}(t) = I_{LA}(t) \cdot e^{-(4ar + kI_{LV}(t))} \quad (6.12)$$

Since  $a$  and  $r$  are known, Eq. (6.12) contains only three unknowns, which are the constant coefficient  $k$  and the non-attenuated intensities  $I_{LA}$  and  $I_{LV}$ . In order to estimate  $I_{LA}$ , two conditions have to be added. The first condition concerns the ratio  $b$  between the peak concentration in the LV and LA. This condition can also be expressed as  $I_{LV_{max}} = bI_{LA_{max}}$ , where  $I_{LA_{max}}$  and  $I_{LV_{max}}$  represent the maxima of the LA and LV intensity curves without attenuation. The second condition is derived from the assumption of negligible attenuation of the LV acoustic intensity and is expressed as  $I_{LV} = \widehat{I}_{LV}$ . Combining these two conditions with Eq. (6.12),  $I_{LA}$  is derived from the measured (attenuated) intensities  $\widehat{I}_{LA}$  and  $\widehat{I}_{LV}$  as given in Eq. (6.13).

$$I_{LA}(t) = \widehat{I}_{LA}(t) e^{4ar} \cdot \left( \frac{\widehat{I}_{LV_{max}} e^{-4ar}}{b\widehat{I}_{LA_{max}}} \right)^{\left( \frac{\widehat{I}_{LV}(t)}{\widehat{I}_{LV_{max}}} \right)} \quad (6.13)$$

The distance  $r$  is usually fixed to 5cm and the ultrasound frequency is 1.9MHz. As a result,  $ar = 0.328$ . The ratio between peak concentrations in the LV and LA is difficult to determine. However, the final FEF measurements show reliable results when an equal peak concentration is considered. Therefore, the peak concentration ratio  $b$  is fixed to 1. Further research could include a specific experimentation for an



accurate assessment of the concentration ratio  $b$  and its dependency on physiological parameters<sup>4</sup>.

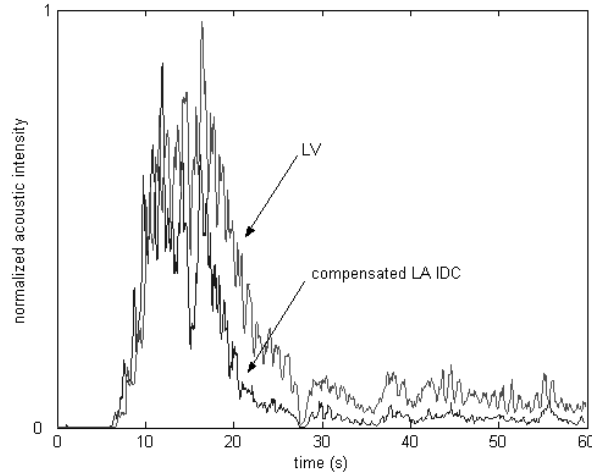


**Figure 6.7:** The LA and LV acoustic intensity curves in Fig. (6.6) after compensation for the LV attenuation effect.

Eq. (6.13) expresses the LA acoustic intensity curve without attenuation  $I_{LA}$  as a function of attenuated measurements, therefore, it allows compensating for the attenuation effect on the measured LA intensity curve  $\hat{I}_{LA}$  as shown in Fig. (6.7). After compensation, both the LA and LV intensity curves are linearly related to the contrast concentration and, therefore, they are referred to as IDCs. The resulting IDCs are suitable to be processed for the LV impulse response estimation.

## 6.2.2 Wiener deconvolution scheme

The LV impulse response power spectrum  $S_{hh}(\omega)$  can be derived from the exponential model in Eq. (4.6) and expressed as  $C_0^2 \tau^2 / (1 + \tau^2 \omega^2)$ . Due to the broad-band characteristic, the noise power spectrum  $S_{nn}(\omega)$  can be approximated by a constant  $N^2$  (white noise, see also section 5.1.1). As a result, Eq. (5.33) can be expressed as given in Eq. (6.14).

$$W(\omega) = \frac{F^*(\omega)}{S_{ff}(\omega) + \frac{N^2(1+\tau^2\omega^2)}{C_0^2\tau^2}} \quad (6.14)$$

<sup>4</sup>Interesting studies investigated, for instance, the relation between attenuation and hematocrit [198].

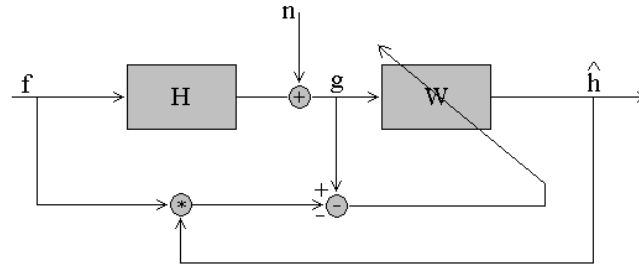


**Figure 6.8:** Scheme of the implemented adaptive Wiener deconvolution algorithm.

An adaptive version of the filter is realized as shown in Fig. (6.8). An iterative process minimizes the  $L^2$  distance  $d(g(t), f(t) * \hat{h}(t))$  by changing the parameters  $\tau^2$  and  $N^2/C_0^2$  of the Wiener filter in Eq. (6.14). The adopted minimization algorithm is the *Nelder-Mead Simplex Method* [199].

Especially for low SNR, the algorithm shows long convergence time. Therefore, a sub-optimal design of the Wiener filter is considered. The SNR is assumed to be constant [196, 197, 200], so that iterations only involve the optimization of one parameter. In addition, a FIR (Finite Impulse Response) low-pass pre-filter made of 5 taps (about 1/4 of the cardiac cycle for sampling frequency equal to 20Hz) is applied to both  $g(t)$  and  $f(t)$  in order to reduce the high frequency noise components before deconvolution. Several pre-filters have been tested, however, larger pre-filters do not lead to further improvements.

The adaptive Wiener filter is applied to the measured LV IDC to estimate the LV impulse response, which is fitted by the exponential mono-compartment model as shown in Fig. (6.9) and interpreted by Eq. (2.20) for the FEF estimate. In fact, the LV impulse response that is estimated after the attenuation compensation in Eq. (6.12) and the deconvolution filter in Fig. (6.8) fulfills the requirements for the application of Eq. (2.20). The exponential model is fitted to the impulse response down-slope by a multivariate linear regression in the logarithmic domain. It is fitted between 80% and 10% of the impulse response peak amplitude (see Fig. (6.9)).

The final design of the deconvolution filter was tested by specific simulations. As in section 5.1.1, we defined the SNR as  $20 \log(A/N)$ , where  $A$  is the amplitude of the signal (IDC) and  $N$  is the noise amplitude. The noise was assumed to be white, with an amplitude (standard deviation) that was linearly proportional to the signal amplitude (stationary SNR). The input IDC  $f(t)$  was generated according to the LDRW model. White noise was added to obtain SNRs equal to 10dB, 15dB, 20dB, and  $\infty$ .

An SNR smaller than 15dB is never measured in practice (see Fig. (6.10)).  $f(t)$  was then convoluted with a mono-compartment impulse response (exponential decay  $h(t)$ ) to obtain the output IDC  $g(t)$ . White noise was also added to  $g(t)$  and the same SNRs as for  $f(t)$  were generated.

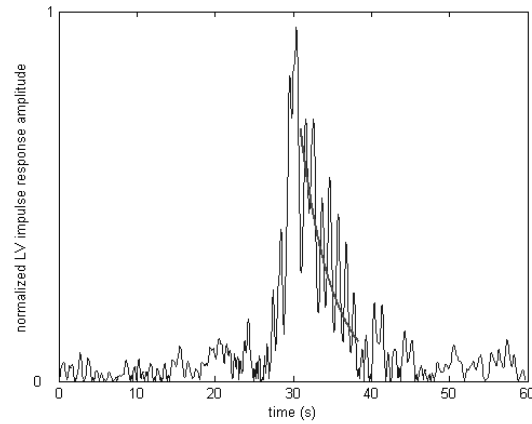


**Figure 6.9:** LV impulse response as derived by Wiener deconvolution applied to the IDCs in Fig. (6.7). The exponential model fits the curve along the down-slope between 80% and 10% of the peak amplitude.

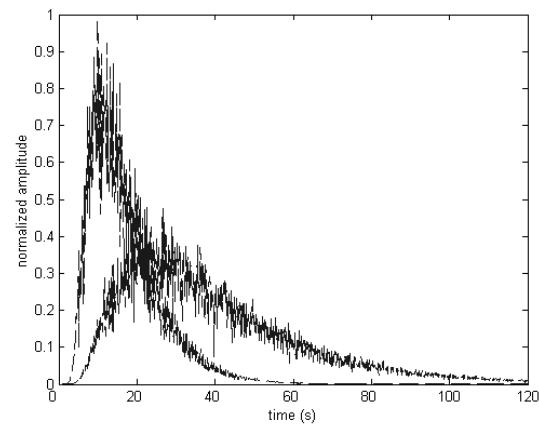


**Figure 6.10:** Example of simulated input-output IDCs for SNR=15dB and FEF=50%.

The time constant  $\tau$  of the mono-compartment impulse response was varied in order to generate FEFs going from 10% to 80%, which cover the real application range. Fig. (6.11) and Fig. (6.12) show the simulation results in terms of average values and standard deviations over 1000 different noise sequences for each SNR and FEF.

The algorithm shows robustness even in case of very low SNR. The correlation coefficients are 0.9964, 0.9993, 0.9999, and 1 for SNR going from 10dB to  $\infty$ . However, for large FEF, an average underestimation is recognizable for low SNR.

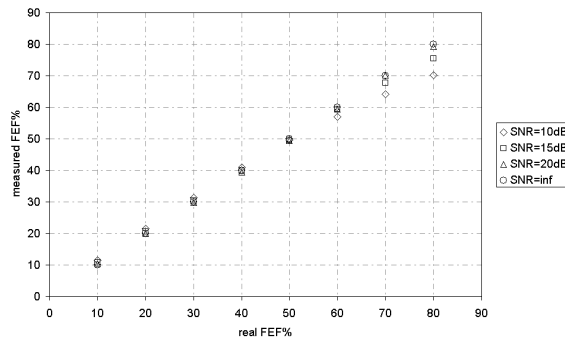


**Figure 6.11:** Simulation results. Percent FEF average estimates for different SNR and FEF% over 1000 different noise sequences.

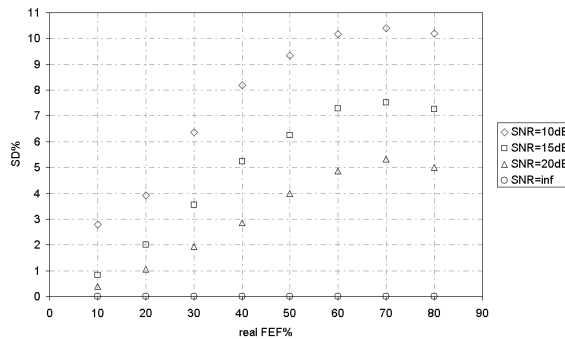


**Figure 6.12:** Simulation results. Percent standard deviations (SD%) for different SNR and FEF% over 1000 different noise sequences.

### 6.2.3 In-vivo measurements

The feasibility of the measurement was tested in patients. A 10ml bolus of SonoVue<sup>®</sup> contrast agent diluted 1:100 into saline (0.9% NaCl) was injected intravenously and detected in B-mode by an ultrasound scanner Sonos 5500 (Philips Medical Systems). A transthoracic S3 probe was positioned to show a four-chamber view. Software Q-Lab<sup>®</sup> (Philips Medical Systems) for acoustic quantification was used to measure the acoustic intensity curves. Two ROIs were placed on the LA and LV for the acoustic intensity curve measurements.

The scanner setting was the same power modulation mode as for the in-vivo blood volume measurements in section 5.3. The measured acoustic intensity curves were transformed into IDCs by attenuation compensation and analyzed off-line for the FEF assessment. The analysis was implemented on PC using both Labview<sup>®</sup> (National Instruments) and Matlab<sup>®</sup> (The MathWorks) software.

A group of 20 patients with EF going from 10% to 70% and no significant mitral insufficiency ( $EF \simeq FEF$ ) was selected. FEF estimates were compared to EF measurements obtained by echographic bi-plane method on two- and four-chamber views with contrast opacification. The average over three EF measurements was considered as the reference value to validate the FEF estimates.

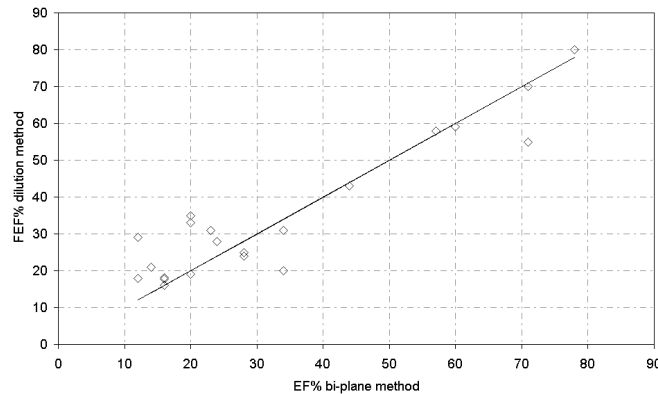


**Figure 6.13:** *In vivo results. FEF estimates compared to EF estimates by bi-plane echocardiographic method after contrast opacification.*

This preliminary study on 20 patients shows a correlation coefficient equal to 0.93 between FEF and EF estimates. The results are presented in Fig. (6.13).

Fig. (6.14) shows the Bland-Altman plot of the two compared techniques [17]. The bias equals 1.6% and the standard deviation (SD) equals 8%. Taking into account that comparisons between different EF measurement techniques always show

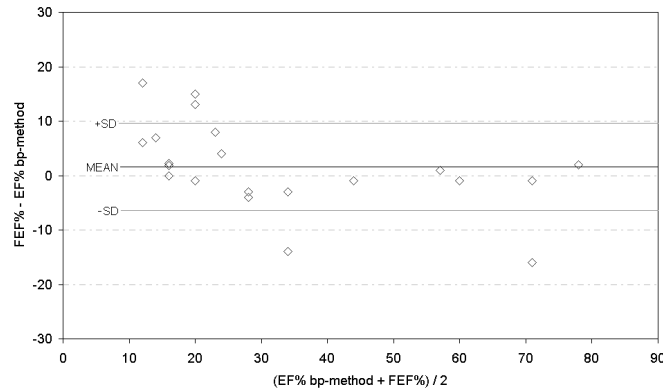


**Figure 6.14:** Bland-Altman plot of the EF and FEF estimates by dilution and bi-plane echographic methods.

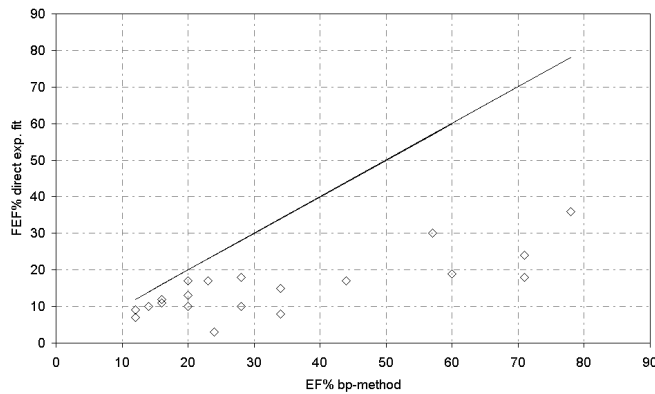


**Figure 6.15:** The same measurement as in Fig. (6.13) without use of deconvolution. The FEF is directly measured from the LV IDC exponential fit. The results show an evident underestimation.

significant standard deviations (usually larger than 15% [18, 67]), these preliminary results are promising and prove the feasibility of the method.

Fig. (6.15) shows the FEF estimates using the exponential fit of the measured LV IDC without deconvolution. As expected, there is a large FEF underestimation. In fact, since the contrast bolus is injected in an arm vein, the hypothesis of fast injection in the LV for the application of Eq. (2.20) is not fulfilled.

A very interesting use of the FEF estimation could aim to the quantification of Regurgitant EF (REF) (see section 2.2), i.e., the fraction of  $V_{ed}$  that is ejected back

in the atrium due to mitral valve insufficiency. Since geometrical EF measurements are the sum of FEF and REF, the difference between EF estimates, made by any accurate geometrical approach, and indicator dilution FEF estimates, made for instance by echo-contrast, provides with REF estimates. However, to be more specific, this technique does to allow distinguishing between mitral and aortic regurgitation.

Another advantage of using the contrast dilution approach for FEF assessments is represented by the simple and direct application of the method for RV FEF measurements, which, as discussed in section 2.2, are difficult to obtain by geometrical measurements.

### 6.3 Pulmonary blood volume measurement

The same dilution system identification approach can be used for volume measurements. In fact, the impulse response of the dilution system between two different measurement sites is the IDC that would be measured in the second site if the contrast injection were performed as a mathematical impulse in the first site. Therefore, once the system is linearized by compensating for the nonlinear distortions introduced by the measurement system (see section 6.2.1), the estimated impulse response can be analyzed for the measurement of the volume that is bounded between the two detection sites.

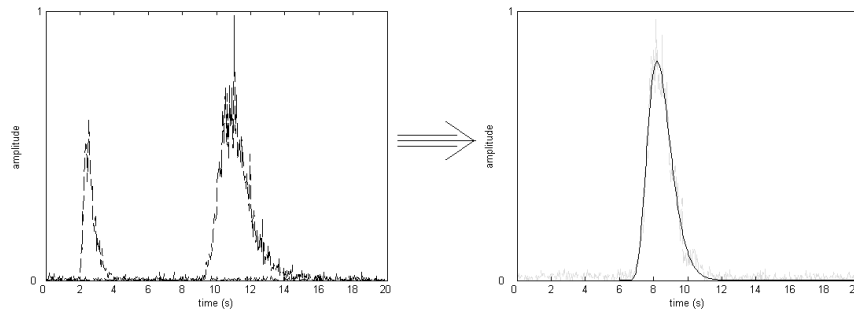


**Figure 6.16:** *In vitro* volume measurement application. The measured input and output IDCs (left plot) are shown together with the resulting impulse response and LDRW model fit (right plot).

The impulse response determines an IDC that can be interpolated and interpreted with the same means as discussed in section 5.3. If the impulse response is fitted by the LDRW model, then the MTT is determined by the parameter  $\mu$  of the model. Once the CO is known, then the volume is assessed as  $\text{CO} \cdot \text{MTT}$  as given in

Eq. (2.22)<sup>5</sup>. If the impulse response between the RV and the LA is estimated, then the LDRW model fit of the estimated curve leads to the measurement of the PBV.

A simulation test similar to that shown in the previous section was performed for different SNR. The exponential impulse response was substituted by a LDRW-model-like impulse response. For a SNR of 15dB (the worst encountered in practice), the standard deviation of the MTT estimates over 1000 different noise sequences ( $\lambda$  equal to 3 and MTT equal to 25s and 30s) is smaller than 1%.

Apart from the simulations, the system was tested both in vitro and in vivo. For the in vitro validation we used the same set of measurements (Sonos 5500 ultrasound scanner in power modulation mode) that was used for the in-vitro validation of volume assessments based on the interpolation of two curves (before and after the volume) in section 5.3.3. The measurement set-up is shown in Fig. (5.15) and Fig. (5.18) as well as the results based on double LDRW and FPT model interpolation are shown in Fig. (5.19) and Fig. (5.20). Fig. (6.16) shows the application of the system in vitro. As already discussed in section 5.3.3, the increase of pressure in the first tube (before the volume network) for higher flows, makes the amplitude of the first IDC smaller than the second one, despite the loss of bubbles between the detection sites.

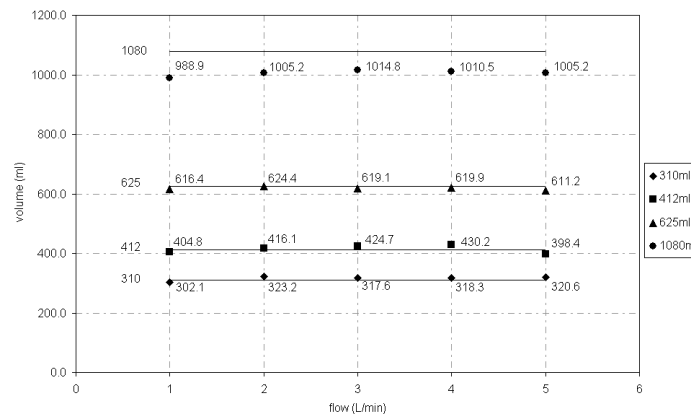


**Figure 6.17:** In vitro volume measurement results for different flows and volumes.

The estimates of the same four volumes as in Fig. (5.19) for five different flows going from 1L/min to 5L/min are shown in Fig. (6.17). The standard deviations with respect with the average estimate are 2.5%, 3.1%, 0.7%, and 0.8%. Fig. (6.18) shows the same estimates averaged over all the flows. The correlation coefficient with the real volumes is 0.999.

<sup>5</sup>Notice that Eq. (2.22) is only applicable for measurements in the central circulation. The IDCs must be measured where all the circulating blood is mixed together.



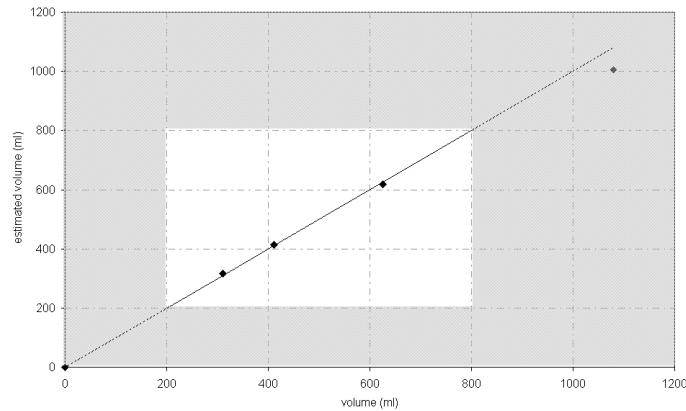


**Figure 6.18:** Average volume measurements over all the five flows.

For the in vivo application of the system, the IDCs were measured using the same procedure as shown in Fig. (5.24). Fig. (6.19) shows the LDRW fit of the impulse response that is estimated from the IDCs in Fig. (5.25). The IDCs were first linearized (see section 6.2.1) and then used as inputs of the deconvolution algorithm in Fig. (6.8) for the impulse response estimate. Since the linearization (attenuation compensation in Eq. (6.13)) concerns the LA IDC (there are no contrast opacified compartments between RV and transducer), the measurement of the LV IDC was also necessary.

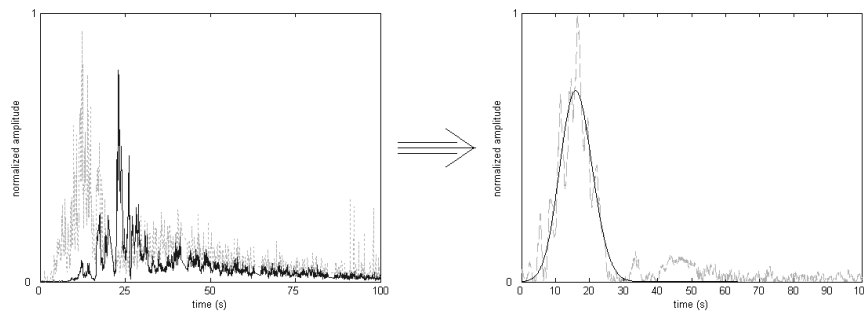


**Figure 6.19:** In vivo application of the system. The measured RV and LA IDCs (left plot) are shown after linearization together with the resulting impulse response and LDRW model fit (right plot).

Fig. (6.20) shows the results of the volume measurements performed on the same group of 20 patients as shown in Fig. (5.26). With respect to the double LDRW model fitting proposed in section 5.3, the use of the dilution system identification approach

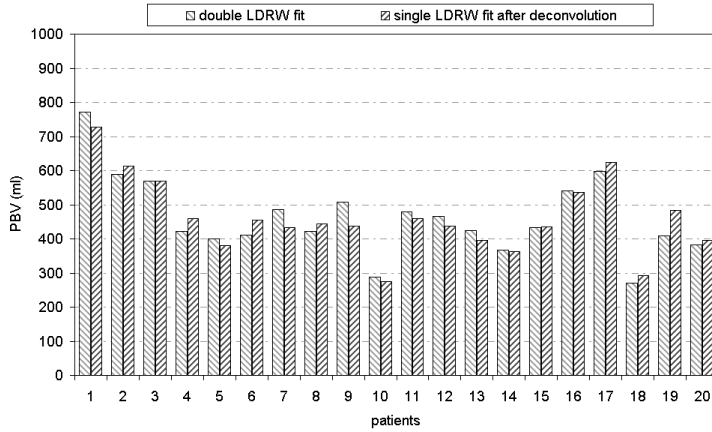


**Figure 6.20:** The same PBV measurements in patients as in Fig. (5.26) making use of the LDRW model fit of the estimated impulse response of the dilution system between the RV and the LA.

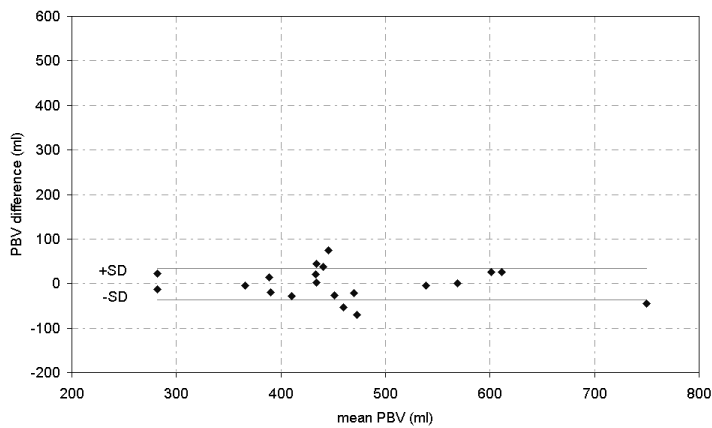


**Figure 6.21:** Bland-Altman plot for the comparison of the impulse response approach with the double LDRW model fitting approach. The agreement is very large, since the standard deviation is only 35ml and the mean value is -0.95ml.

requires the measurement of three IDCs from the RV, LA, and LV. The RV and LA IDCs represent the input and output of the dilution system and are the input of the deconvolution algorithm. The LV IDC is used to compensate the LA IDC for the attenuation introduced by the opacified LV, as described in section 6.2.1. The RV is

the first contrast-opacified target encountered by the ultrasound beam, therefore, the attenuation does not introduce significant nonlinearities. The CO was assessed by aortic echo-Doppler time-integration technique (see section 2.1.4).

The Bland-Altman plot in Fig. (6.21) shows the agreement of the PBV estimates made by use of deconvolution with those measured by double LDRW model fitting [17]. The standard deviation is 35ml (7.7%) and the mean value (impulse response measurements minus double LDRW fit measurements) is -0.95ml. Also the in vitro measurements in Fig. (6.17) are very close to those obtained by the double LDRW model fitting in section 5.3.3 and the standard deviation is only 1%. As always in this study, the shown results are not indexed (see section 2.3). A further in vivo investigation could compare the system with a different one. As widely accepted, the most accurate estimates are determined by double thermodilution catheterization (see section 2.3 and 2.4). Unfortunately, such a validation procedure is highly invasive.

In general, the advantage of using a deconvolution technique over a direct double IDC fitting stands in the independency of the resulting impulse response from the injection function, which does not need to be characterized and compensated as discussed in section 5.3.2. As in this chapter we propose two applications of the dilution system identification method, more opportunities, involving not only cardiac quantification, but also other applications, could be found and investigated in the future.

## Chapter 7

# Automatic region of interest detection for real-time applications

*Felix qui potuit cognoscere causas (Virgilius).*

Although all the studies make use of simple (usually rectangular) manually-defined ROIs for UCA IDC measurements [2, 5, 6, 8, 181, 201], a crucial issue in the video indicator dilution context for cardiac measurements is the automatic definition of one or more ROIs that stay inside the cardiac walls and maximize the covered surface. Therefore, this chapter concerns the automatic determination of multiple ROIs in real time for IDC measurements. An extremely accurate contour detection is not strictly necessary, but the segmentation must be robust to small SNR and ensure that no tissue is included into the ROI. Signal that is backscattered by the myocardium represents a disturb to the IDC measurement and should not be included in the ROI. A manual delineation of the ROI does not ensure to maximize the measurement area and slows down the operating room practice. The expansion of the ROI leads to larger average and IDC noise reduction. As a consequence, the interpretation of the IDC is more accurate.

Required features for a suitable image segmentation system also include a simple and efficient interface to the user in order to allow operating room applications. The adaptability to different echo-cardiographic probes (trans-esophageal and trans-thoracic), views, and contour shapes is necessary to use the system for different measurements (e.g., CO, LV and RV EF, PBV, etc.) and pathologies (e.g., an aneurysm). Moreover, the simultaneous detection of several contours in real time should be achieved without the employment of expensive hardware.

Several techniques are reported in literature for contour detection. However, it is difficult to determine a general solution that is optimal in terms of accuracy, reliability, and computation time. The most common approaches for cardiac-chamber contour detection can be divided into five main groups [41, 43, 202–206]: two-dimensional filters, morphologic segmentations, model based approaches, active contours, and level set methods.

*Two-dimensional filters* include all the linear and non-linear filters typically used for image processing [41, 43]. Different cascade of high-pass filters have been tested, but the robustness of this simple approach with echographic images is not sufficient. The detected edges are fragmented and difficult to interpret. Special algorithms can recombine the edge fragments [207], but they are slow and not applicable for real time processing. Furthermore, false edges due to *speckle* noise<sup>1</sup> [41, 47] should be distinguished.

*Morphologic segmentations* [41, 208] apply a threshold to gray-level images and transform them into binary ones, which are processed by binary filters. This approach seems to be not appropriate for contour detection in echographic images. The gray-levels that define the interface blood-myocardium is not a stable and reliable reference. As a consequence, the binary images can show several connections between different chambers or even segmentation of the chamber surface into separate particles. The selection of an appropriate threshold to generate the binary image is a critical point since it is difficult to define an algorithm that suits all the images [203]. A cascade of morphologic filters such as erosion and dilatation can solve some of the problems, but requires a large increase of computations.

*Model-based approaches*, such as *Active Appearance Models* [204–206, 209–211], first applied for face recognition, are based on *Principal Components Analysis* of a set of training images in order to build a *mean shape model*. An eigenvalue problem is solved to best adapt the model to the detected contours. When the mean shape model can represent the chamber contour, this method shows a reliable behavior. However, unless some extra-constraints are defined [212], the model fitting requires the optimization of a large set of parameters. One more disadvantage of model-based algorithms is their limitation to a specific contour shape. Different projections, such as *long and short axis views*<sup>2</sup>, require different models.

*Active-Contour-Model* or *Snake* techniques minimize an *energy function* associated to the contour curve (usually represented by a B-Spline) [43, 202, 213]. The total energy is defined as the sum of an internal energy and an external energy. The internal energy depends on the characteristic of the spline curve (elasticity and stiffness), while the external energy depends on the matching between the spline curve and the image features (gray level value, gradient, etc.). Since they are iterative techniques that locally deform the snake (spline), the user must define an initial contour (set of points). Each point of the initial contour is iteratively adjusted until the total energy of the spline, which interpolates all the points, reaches a minimum. The final result depends on the initial conditions and the weights associated to the inter-

---

<sup>1</sup>Speckle is the typical texture that characterizes echographic images. It is the result of echoes generated by small scatterers randomly distributed in tissues. Scattering effects that are generated outside the main lobe of the ultrasound beam also contribute to generate speckle noise (see section 3.1).

<sup>2</sup>The long and short axis views are the longitudinal and transverse plane projections of the ventricles respectively (see section 2.2).

nal and external energies. Unfortunately, the solution can easily converge into local minima. Moreover, especially with echographic images, the snake is easily attracted by features that are due to noise, ending with wrong results. A smoothing pre-filter can partially prevent from these errors, but reduces the gray-level gradient along the contours.

The *level set method* [214], which more in general can be considered as an optical-flow approach, is an emerging technique for tracking moving interfaces. The combination of segmentation and tracking allows exploiting the additive information that derives from motion. The algorithm uses a deformable contour that moves using gradient descent and seeks for local solutions. As a consequence, a powerful initialization technique is required (as for the snake technique). In fact, the final contour is strongly dependent on its initial position. The function that defines the deformable contour model allows the representation of any shape. The time differentiation of the contour function leads to a Hamilton-Jacobi type equation. The solution of this equation provides the contour segmentation. The final solution is a compromise between attraction to image features (e.g., the gradient) and contour smoothness. Computational cost, initialization, and noise sensitivity issues should be carefully considered.

For all the mentioned methods, the initialization is a critical issue and can be hardly automated. An initial manual definition of a few reference points or the entire contour is usually needed. The result is a difficult application of the system and a need for the employment of trained expertises. As a consequence, these algorithms do not suit the requirements for emergency routines and operating room applications. Moreover, the available algorithms are either insufficiently accurate, or constrained into a specific shape (or model), or computationally too expensive for multiple simultaneous contour detections in real time [206]. Therefore, in this specific context, none of the previously mentioned algorithms seems to fit the required characteristics.

This chapter presents a new automatic cardiac-wall tracking (contour-detection) algorithm dedicated to UCA IDC analysis. The IDCs are measured simultaneously in different cardiac cavities (ROIs), so that the measurement of various cardiac parameters, such as CO, EF (LV and RV), and PBV, is feasible by a single UCA bolus injection.

The computational cost of the implemented algorithm is limited, so that real-time detection of multiple ROIs does not require expensive hardware. Furthermore, the contour detection is projection-independent and allows the use of any cardiac view to the cardiologist.

The input of the system is the B-mode video output of the ultrasound scanner, which is processed in real time. Only a simple mouse click in the center of the cavities of interest is required by the user, resulting in a system that is also suitable for operating room applications. An off-line analysis of stored digital (AVIs) or analog (videotapes) movies is also integrated in the current set-up.

For IDC measurements the ultrasound scanner is set on fundamental mode to have a good view of the cardiac structures, which mainly behave like linear scatterers. The segmentation algorithm is based on a radial high-pass filter with an automatic outlier suppression. It is general enough to be also adopted for magnetic resonance imaging (MRI) analysis of gadolinium dilutions [31, 45].

The ROI is determined before the chamber opacification to avoid confusion between contrast and tissue. The contour tracking is performed for two cardiac cycles before the contrast injection. The minimum-area contour is automatically determined and used as the ROI for the following IDC measurement. The ROI is fixed inside the cardiac chamber while the contrast is flowing. The mean gray levels in the ROIs are processed in order to obtain the IDCs (videodensitometry). The use of the minimum-area contour over two cardiac cycles ensures that the cardiac walls, which introduce noise (high gray levels) into the measured IDC, are excluded from the ROI during the measurement.

## 7.1 The proposed algorithm

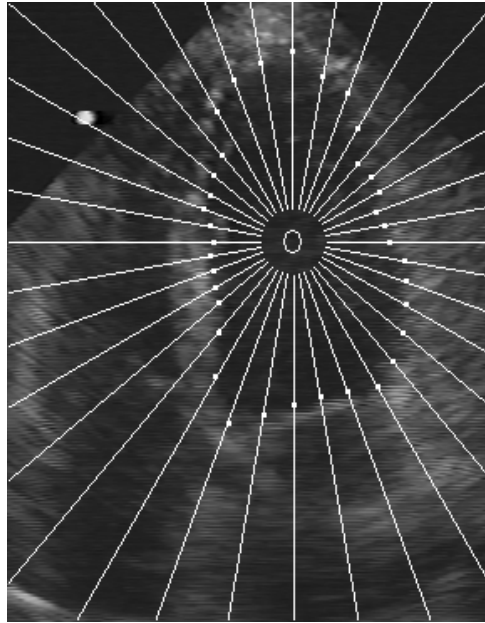


*Figure 7.1: Beam of rays from inside a left ventricle. The small squares represent the intersection between the rays and the endocardium.*

The proposed contour detection algorithm is initially designed for echographic images, which are the most difficult to treat due to their low SNR. However, once echographic images are successfully analyzed, the same algorithm is easily adapted to MRI, since the image contrast and the SNR are much larger.

The echographic B-mode view of a cardiac chamber consists of a dark region (the blood-filled inner of the chamber) surrounded by a bright structure due to the sound that is backscattered from the cardiac-wall-to-blood interface. A chamber can be interpreted as a two-dimensional convex object. A radial beam of rays that is originated at any point inside the chamber intercepts the border and defines the contour (see Fig. (7.1)). The presented contour detection approach is based on a radial edge-detection filter.

An edge produces spatial high frequency components and a high-pass filter can be used as an edge detector. Therefore, the basic principle of the proposed contour detection algorithm is the application of a mono-dimensional high-pass filter along a set of rays whose origin is determined by a simple mouse click, which makes the user interface simple and friendly. The origin point of the set of rays should be central, but not precisely in the chamber centroid. The transformation of a bi-dimensional problem into a mono-dimensional problem reduces the computational complexity and allows real-time applications of the system.

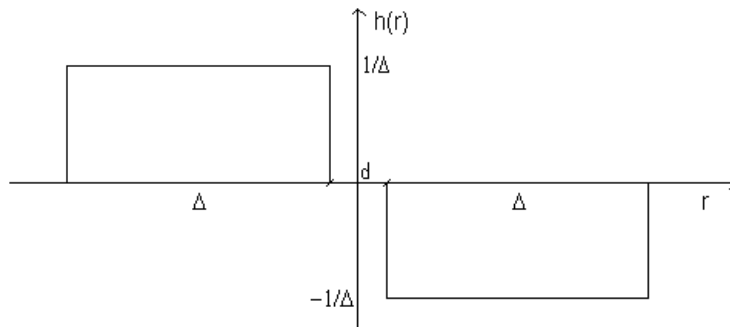


**Figure 7.2:** Impulse response of the radial filter. It is the function that is convoluted with the pixel intensities along each defined radial line. The distance from the radial line origin is represented by the variable  $r$ . The impulse response is made of two rectangular functions with the same length  $\Delta$  and amplitudes equal to  $1/\Delta$  and  $-1/\Delta$ . The distance between the rectangles is equal to  $d$ .



A linear high-pass filter is applied along each ray. The impulse response consists of two normalized rectangles. As shown in Fig. (7.2), the rectangle length and amplitude are equal to  $\Delta$  and  $\pm 1/\Delta$  respectively. One rectangle is positive while the other one is negative. The distance between the rectangles is determined by  $d$  ( $d \geq 0$ ). The filter is basically a modified radial-gradient operator. If  $I(x_k, y_k)$  represents the pixel intensity (gray level) along a radial line, then the discrete radial filter convolution is implemented as given in Eq. (7.1).

$$\begin{aligned} \xi_k = & \frac{1}{\Delta} \cdot \sum_{j=0}^{\Delta-1} I\left(x_{(k+j+\lceil \frac{d}{2} \rceil)}, y_{(k+j+\lceil \frac{d}{2} \rceil)}\right) + \\ & - \frac{1}{\Delta} \cdot \sum_{j=0}^{\Delta-1} I\left(x_{(k-j-1-\lfloor \frac{d}{2} \rfloor)}, y_{(k-j-1-\lfloor \frac{d}{2} \rfloor)}\right) \end{aligned} \quad (7.1)$$

The detected edge point along each ray corresponds to the first location  $(x_k, y_k)$  where the filter output  $\xi_k$  surpasses a pre-defined threshold.

A set of parameters controls the filter, so that the system is adaptable to different image features and imaging techniques. The parameters are the length  $\Delta$  and the mutual distance  $d$  of the impulse response rectangles, the number of rays, and the threshold. For echographic images we usually fix the number of rays and  $d$  to 360 and 2 (pixels) respectively. Typical ROI areas in echographic images (including all possible cardiac views and chambers) go from 5000 to 50000 pixels, therefore, 360 edge points are sufficient to reconstruct the contour. If the contour is very small (perimeter shorter than 500 pixels), then the number of edge points should be decreased. The choice for  $d$  is not critical. The length of the rectangle  $\Delta$  is fixed to 20 in order to detect the edges and filter out the speckle noise, which consists of spots that cover less than 50 pixels.

The threshold can be adjusted manually. Usually, for well equalized images, a contrast of 20 gray levels leads to the most accurate results. However, an automatic threshold estimation is implemented too. Based on the histogram of the image, the gray level standard deviation  $\sigma$  is calculated and the threshold  $S$  is determined as given in Eq. (7.2). The logarithm is used to compress the range of  $\sigma$ , which for echographic images covers a wide interval.

$$S = \lceil a \cdot \ln(\sigma + 1) \rceil \quad (7.2)$$

The value for the coefficient  $a$  is optimized over a set of 40 echographic images and fixed to 6.7. Also the use of the threshold proposed by Otsu has been investigated [203], however, the threshold defined in Eq. (7.2) suits better for this specific application and shows a more stable behavior. In fact, differently from typical morphologic applications, in this context the threshold problem regards the radial gradient rather than the absolute value of the video intensity.

A *median filter* [41, 43] is applied before the proposed radial filter to remove the spots due to speckle. The choice for a non-linear filter over a linear low-pass filter is due to the need for removing the speckle without blurring the image. A blurred image makes the subsequent edge detection less efficient. Instead, a median filter enhances the sharpness of continuous contours. The implemented filter is a 5x5 8<sup>th</sup> order median filter. The pixels covered by the 5x5 kernel are ordered from the minimum to the maximum gray-level. The pixel that corresponds to the center of the kernel is then substituted with the 9<sup>th</sup> pixel in the ordered list (8<sup>th</sup> order median filter). The size is chosen according to the typical size of the speckles.

A linear interpolation of the points that are detected by the radial filter (they should be 360, one for each degree, but along some rays the edge could be undetectable) defines the ROI. Unfortunately, due to the low quality of echographic images, the ROI contains several *outliers* (see Fig. (7.3) and Fig. (7.5)), and expands beyond the cardiac walls. In fact, very often, not all the cardiac wall-to-blood interface gives a good ultrasound reflection, and entire parts of the contour may be completely unrecognizable. Moreover, in long-axis projections the cardiac chamber is open through the valve (see Fig. (7.4)).

A routine is implemented to detect and correct the outliers (see Fig. (7.3)). It is based on the assumption of continuous and smooth edges. The Cartesian coordinates of the detected edge points are transformed into polar coordinates centered in the origin of the rays (see Fig. (7.6)). This mono-dimensional polar plot (distance from the origin versus angle) is processed to remove the outliers. The first derivative of the plot is calculated and the points whose amplitude surpass a pre-determined threshold removed. The hypothesis of bounded derivative is a consequence of the assumption of continuous and smooth edges. After an experimental optimization process, the threshold has been determined as to be equal to 7% of the standard deviation of the initial polar plot (before the outlier correction). For each removal the derivative function is updated. The process is repeated (clockwise and anticlockwise<sup>3</sup>) until all the points satisfy the threshold condition.

Once the outliers have been removed, a new ROI is defined as the linear interpolation of the remaining edge points (see Fig. (7.3)). Therefore, the removed edge points are replaced on the intersection between the interpolation line and the rays where they lay.

Usually the resulting ROI is too sharp (i.e., defined by many sharp angles), especially when several outliers are corrected. A more “anatomic” shape of the ROI is obtained by low-pass filtering (smoothing) the polar plot after the correction of the outliers. Before the contour smoothing, the ROI centroid is calculated and the polar coordinates referred to the new origin. This operation ensures a better independency of the smoothing filtering from the first origin-point choice.

---

<sup>3</sup>The derivative discontinuities may be asymmetric and must be detected in both directions.

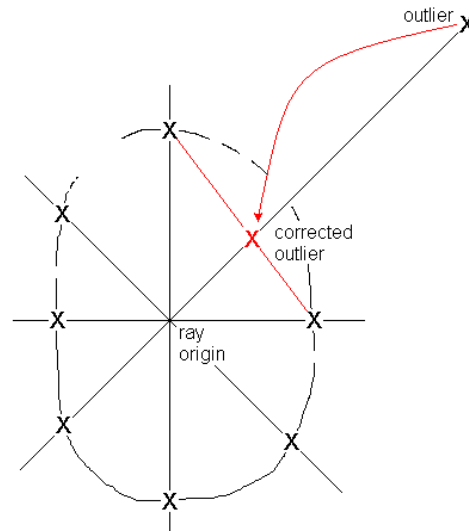


**Figure 7.3:** Schematic example of outlier correction. The outlier is replaced by the intersection between the ray where it lay and the linear-interpolation line of the detected edge points.

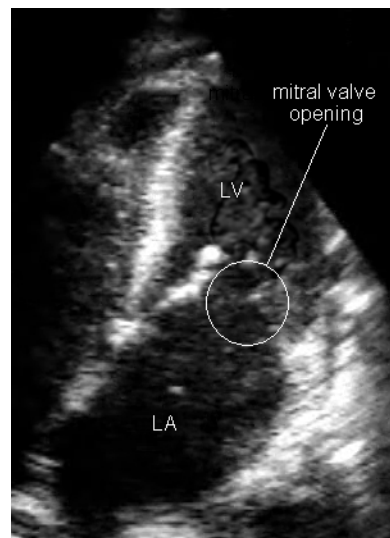


**Figure 7.4:** Two-chamber view with open mitral valve. No ultrasound waves are reflected through the open valve and the resulting echo-image shows the LA and LV as two connected cavities.

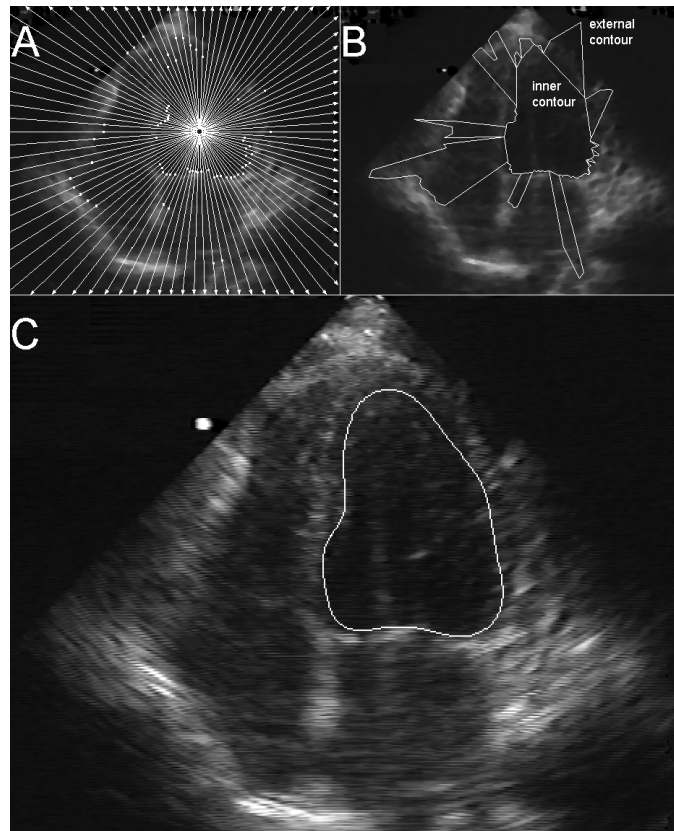


*Figure 7.5: The upper figures show the high-pass radial filter (A) and the outlier correction (B). The external contour includes the outliers while in the internal contour they are corrected by derivative filtering. Figure C shows the final smoothed contour.*

The adopted filter is a zero-phase low-pass filter, designed as a cascade of a causal FIR (Finite Impulse Response) low-pass filter and a phase shifter. The DC component of the filter impulse response is normalized to a value that is smaller than one, so that the ROI area is slightly decreased. This ensures the cardiac walls to be not included in the ROI. Fig. (7.5) and Fig. (7.6) show the contour detection process in Cartesian and polar coordinates respectively.

As presented in previous literature [215] and despite the accurate contour detection that is shown by the proposed method, the addition of an active contour (snake) optimization is tested. The initial contour is defined by the output of the previous algorithm. The algorithm developed by Amini et al. [216] has been modified and adapted to the radial structure of the system. The results for this implementation are

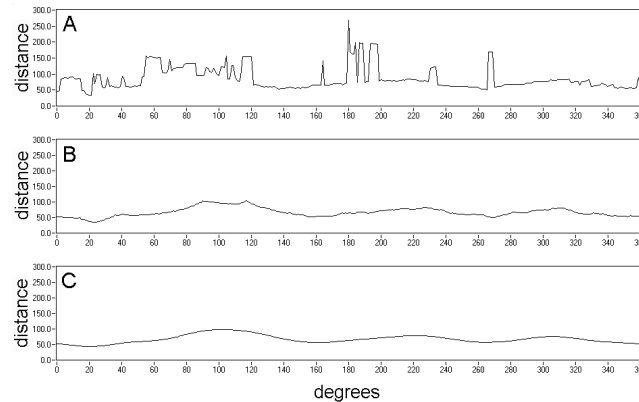


**Figure 7.6:** With reference to Fig. (7.5), plot A is the polar coordinate representation (distance from the radius origin versus angle) of the edges that are detected by the radial high-pass filter. Plot B and C show the effect of the outlier correction and smoothing processes respectively.

not encouraging. The snake optimization process requires a considerable increase in computations while the accuracy improvement is limited. Therefore, we have chosen not to implement the snake optimization into the IDC analysis system. Future research will consider alternative radial active contour optimizations.

Typically, the measurement of an IDC takes more than 20 seconds, and during this time the cardiac walls must stay outside the ROI. Because of the cardiac wall motion, a new ROI should be defined for each frame (wall tracking). Unfortunately, the ROI cannot be determined after the contrast appears in the chamber because the backscatter due to the cardiac tissue is confused with that due to the contrast (fundamental mode echo-analysis). Our solution is to determine the ROI before the contrast appearance and to keep it fixed during the IDC measurement. To ensure that the myocardium is never included, the minimum-area ROI is selected during two cardiac cycles before the chamber opacification.

In conclusion, the in-vivo IDC measurement is performed in the following three phases.

- A ROI is defined for each frame (wall tracking) during two cardiac cycles before the chamber opacification.
- The minimum-area ROI is automatically determined and fixed for the video-densitometry.
- The mean gray-level is calculated over the fixed ROI while the contrast bolus is flowing.

This algorithm is implemented in software and hardware to establish the performance of the algorithm in a realistic environment. The software implementation is made in Labview®, Imaq Vision®, and Matlab®. The developed software can process AVI files as well as it can be interfaced to the video output of either an ultrasound scanner or a videorecorder. The video interface is realized by a National Instruments 1407-PCI® frame grabber, which is controlled via Labview® and MAX® (Measurement and Automation Explorer). The video grabber can interface both European (CCIR) and American (RS-170) standards.

## 7.2 Results

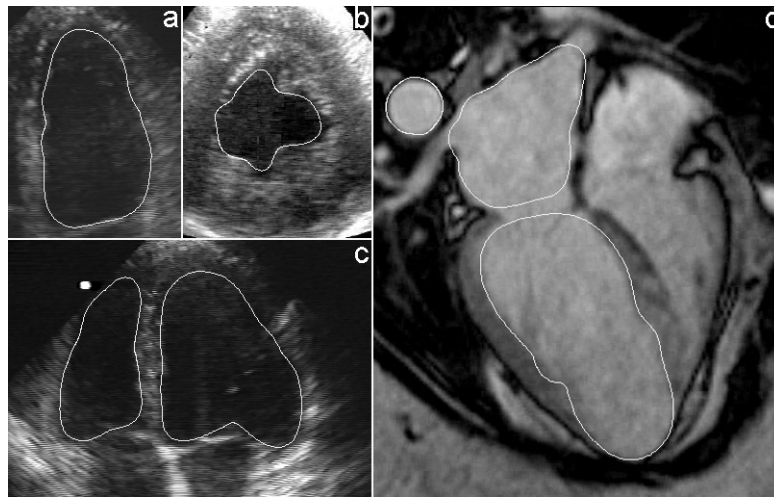


*Figure 7.7: Image a and b show the contour detection in a long-axis view and a short-axis view of the left ventricle. Image c shows a four-chamber view with the detection of the left and right ventricles. Image d shows the detection of different ROIs (LV, LA, and Ao) in a MRI frame.*

The proposed contour detection algorithm is applicable to different echographic and MRI cardiac projections as shown in Fig. (7.7). Since an absolute reference for the contour detection evaluation does not exist, medical image segmentation algorithms are usually compared to manual contour delineation, which is performed by expertises. A set of forty echographic images and twenty magnetic resonance (MR) images were randomly selected from clinical routine analysis of different patients

with various cardiac pathologies<sup>4</sup>. Both automatic and manual contour detection were used. The echographic contour detection was performed on four- and two-chamber views of twenty-six left ventricles and ten left atria as well as on short-axis views of four left ventricles. The MR contour detection was performed on ten four-chamber views and ten short-axis views of left ventricles. Only for this specific validation, the ROI area was not decreased as for indicator dilution applications.

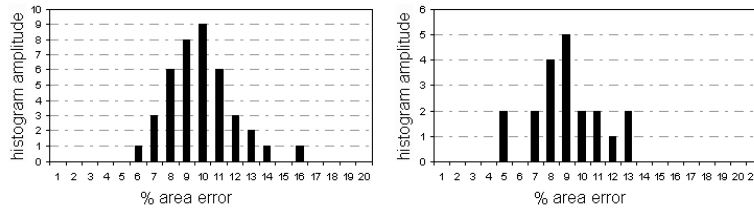


**Figure 7.8:** On the left, the histogram of the percent area error between automatic and manual measurements for the echographic images. On the right, the same histogram for the MR images.

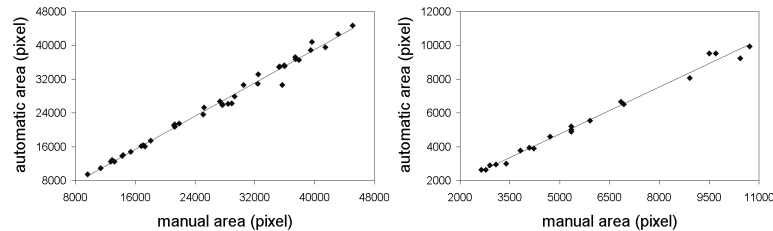


**Figure 7.9:** Automatic versus manual ROI areas (measured in image pixels) for the echographic (on the left) and the MR (on the right) images.

The error of the contour detection, which is referred to as *area error*, is estimated as the percent area difference between manual and automatic contours. The area is expressed in number of pixels. The error histograms for the echographic and the MR images are shown in Fig. (7.8). The average error for the echographic images is 10.0% with a standard deviation equal to 2.0%, while the average error for the MR images is 9.0% with a standard deviation of 2.2%. An error equal to 8.0% of the total area is shown in Fig. (7.11). Fig. (7.9) shows the correlation between the manual

<sup>4</sup>All the data are provided by the Departments of Cardiology and Radiology of the Catharina Hospital Eindhoven (The Netherlands).

and the automatic area for both the echographic and the MR images. The correlation coefficient is 0.995 and 0.998 respectively.

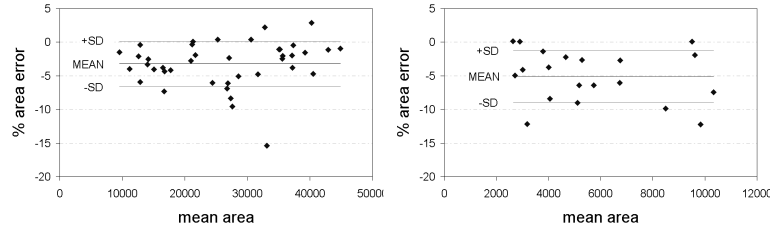


**Figure 7.10:** Bland-Altman plot of the area estimates by automatic and manual contour detection. On the left are the results on echographic images while on the right are the results on MR images. The percent area error is shown together with the mean value (MEAN) and the standard deviation (SD).

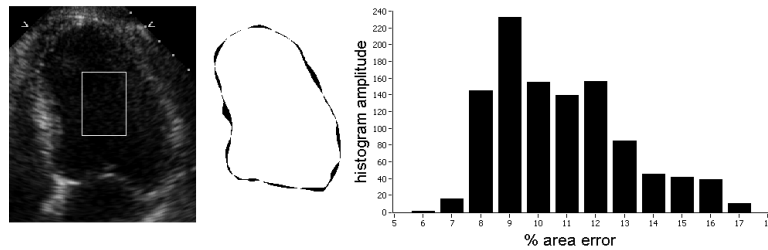
The comparison between manual and automatic contour detection is also shown by the Bland-Altman plot in Fig. (7.10) [17]. The average area error is  $-3.2\%$  (standard deviation equal to  $3.4\%$ ) and  $-5.1\%$  (standard deviation equal to  $3.9\%$ ) for echographic and MR images respectively. The standard deviation is small and the modest negative bias is a positive characteristic for IDC applications. These results show sufficient accuracy to fulfill the requirements for IDC applications.

All the echographic images were analyzed using the automatic threshold as in Eq. (7.2) except for five images, where the threshold was manually modified by few gray levels ( $\leq 5$ ). In fact, the automatic threshold in Eq. (7.2) depends on the region where the gray-level standard deviation  $\sigma$  is evaluated. Since  $\sigma$  is calculated over the complete image, white text or dark regions around echographic images influence the standard deviation. As a result, the automatic threshold may differ from the optimal value by few gray levels. Future implementations of the algorithm will include an automatic determination of the region for the evaluation of  $\sigma$ . The threshold for the analysis of all the MR images, where no text is included, was fixed to 60.

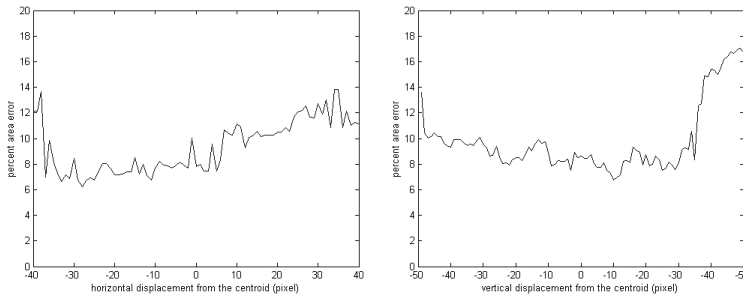
The sensitivity of the contour detection with respect to the origin of the radial filter was tested to evaluate the reproducibility of the results. The contour of the left ventricle in Fig. (7.11) was detected for the origin point position varying over the overlapped rectangle. The percent area error histogram is shown in Fig. (7.11). The error mean value is  $9.8\%$  with a standard deviation equal to  $2.3\%$ .

Referring to the same image, Fig. (7.12) shows the percent area error for vertical and horizontal displacements of the origin point with respect to the contour centroid. We may conclude that for reasonably-central positions the algorithm is robust to origin translations.





**Figure 7.11:** On the left, the original image with an overlapped rectangle indicating the region where the central point varies to generate the error histogram on the right. The error is represented by the percent area error for different central point positions. In the middle, in black, an 8% area error is shown.



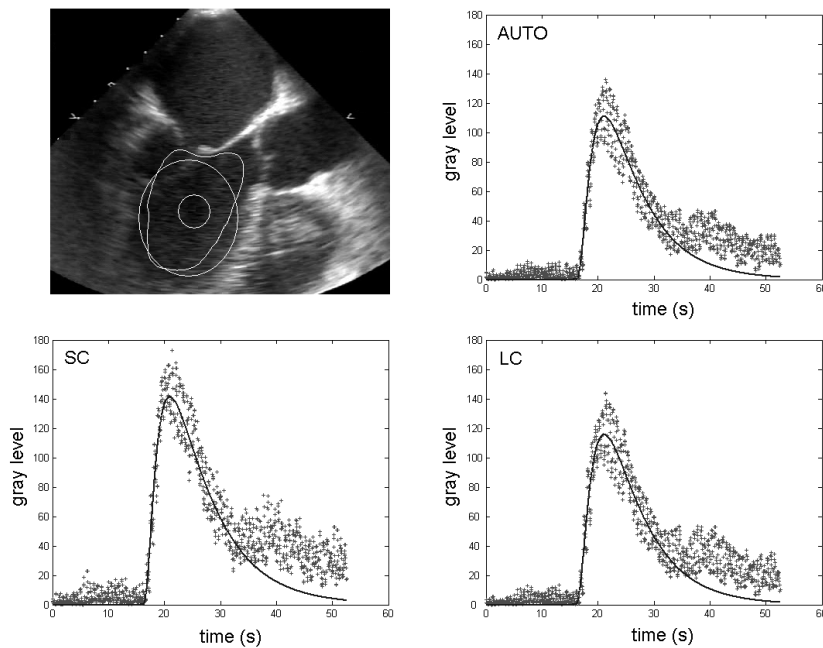
**Figure 7.12:** Percent area error between manual and automatic contours for central point displacements with respect to the manual ROI centroid. The horizontal (on the left) and the vertical (on the right) displacements are calculated along the horizontal and the vertical lines that intercept the contour centroid.

Fig. (7.13) shows an application of the algorithm for indicator dilution analysis in humans. A bolus of contrast agent (10ml diluted 1:100 of SonoVue®) is injected into a peripheral vein and detected by a TEE ultrasound transducer in the central circulation. In Fig. (7.13), a ROI is automatically determined and kept fixed in the LV while the contrast agent is flowing. The average video intensity in the ROI is calculated for each frame and used to build the IDC.

In order to validate the system, the use of the automatic ROI detection was compared to the use of simple manual ROI definitions. Two circular ROIs, a large and a small circle, were added for validation purpose (see Fig. (7.13)). The manual positioning of more complex ROIs is too slow and complex for real-time applications.

The resulting IDCs from the automatic ROI (AUTO), the large circular ROI (LC) and the small circular ROI (SC) were then fitted by a specific model as shown in Fig. (7.13). The second part of the IDC down-slope (end of the tail) shows the recirculation of the contrast (rise of the contrast concentration with respect of the model fit). Since the cardiac measurements are derived from the first passage IDC, the recirculation introduces an important noise component into the signal. As a consequence, as discussed in the previous chapters, the use of a model becomes necessary to fit the first part of the IDC and estimate the rest of the tail.

The Local Density Random Walk (LDRW) model described in section 4.2.2 is used to derive the cardiac parameters. Therefore, the interpolation accuracy is indeed the best parameter to evaluate the contour detection algorithm for IDC measurements. The LDRW fitting was performed by use of the fitting algorithm described in section 5.1.1.



**Figure 7.13:** On the upper left, a mid-esophageal three chamber view is shown together with three different ROIs in the left ventricle. A ROI is defined by automatic detection (AUTO) and two circular ROIs, a large (LC) and a small (SC) circle, are manually placed. The remaining three plots show the measured IDCs from each ROI together with the LDRW model fits.

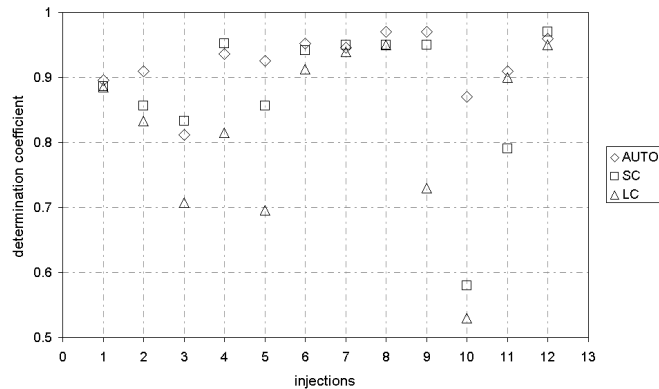


**Figure 7.14:** LDRW-fit determination coefficients for three sets of IDCs, which are measured by the automatic ROI (AUTO), a small circular ROI (SC), and a large circular ROI (LC).

The same validation as shown in Fig. (7.13) was performed for 12 trans-esophageal echographic inspections after the injection of a SonoVue® contrast agent bolus. Fig. (7.14) reports the determination coefficients ( $\rho^2$ , squared correlation coefficient) of the LDRW fits of the measured IDCs (video-intensity-versus-time curves) for the automatic and the two circular ROIs. The average determination coefficient is 0.922 for the automatic ROI, 0.876 for the small circular ROI, and 0.821 for the large circular ROI (standard deviations equal to 0.041, 0.110, and 0.131 respectively).

The IDC recorded by the automatic ROI detection shows a more stable behavior and the best average determination coefficient. When a large circle is used, the intrusion of cardiac tissue in the ROI adds large noise components to the IDC. This explains the smallest  $\rho^2$  for large circular ROIs. Sometimes, the use of a small ROI shows excellent results, slightly better than those obtained by use of automatic ROI detection. However, for low SNR images, the use of a small ROI results in very noisy IDCs (injections 5, 10, and 11 in Fig. (7.14)), and the LDRW-fit shows a much smaller  $\rho^2$  compared to the automatic ROI detection.

## Chapter 8

# Conclusion and perspectives

*Carpe diem, quam minimum credula postero (Horatius).*

The assessment of CO, PBV, and EF provides valuable information for both diagnosis and patient monitoring. Unfortunately, some of these measurements used to be difficult to assess and required the use of invasive techniques and hospitalization.

This thesis proposes an novel ambulatory technique for a minimally invasive quantification of CO, PBV, and EF (RV and LV). The invasiveness issue is overcome by using contrast echocardiography. The cardiac parameters of interest can be assessed by a single peripheral UCA bolus injection, resulting in a simple, quick (few minutes), and minimally invasive measurement.

A bolus of UCA is injected in a peripheral vein and detected by an ultrasound transducer for the simultaneous measurement of several IDCs from different sites in the central circulation. The use of small UCA doses allows a linear calibration of the system, i.e., the relation between UCA concentration and detected acoustic (or video) intensity is well approximated by a liner function.

The parameter estimation is performed by means of specific modelling and interpretation of the IDCs. In particular, random walk models are preferred over the others due to their accurate interpolation of the IDC and physical interpretation of the dilution process. The CO can be calculated either by the RV IDC or by aortic echo-Doppler time integration. Blood volumes are calculated as the product between the CO and the MTT that the contrast bolus takes to cover the distance between different detection sites. The MTT is derived from the LDRW model fits of the IDCs.

Two algorithms for the LDRW model interpolation of the IDC are proposed. They are based either on a multiple linear regression in the logarithmic domain or on the solution of the moment equations. Both of them show accurate fits ( $\rho^2 > 0.95$ ), however, the multiple liner regression is preferred when contrast recirculation is considerable.

A novel approach is proposed for EF measurements. It is based on the identification of the ventricular dilution system, which is treated as a linear system. A recursive Wiener deconvolution technique is adopted to estimate the impulse response that characterizes the system. The EF of both left and right ventricle can be measured

by the analysis of two IDCs from the atrium and the ventricle, which are considered as the input and output signals of the ventricular dilution system and processed by the Wiener deconvolution algorithm to estimate the ventricular dilution impulse response. The estimated impulse response can be fitted by a mono-compartment model for the EF assessment. An important achievement of this technique is the independency on the injection function and modality. As a result, a peripheral intravenous injection can substitute the ventricular fast injection that was required by previous techniques.

A similar approach also allows assessing the PBV by the identification of the dilution system between RV and LA. The MTT is derived from the parameters of the LDRW model fit of the estimated impulse response.

CO measurements were validated in-vitro and show accurate results ( $\rho^2 > 0.9$ ). However, due to the complicated calibration, the in-vivo application requires the employment of a trans-esophageal probe. A reliable set-up for an in-vivo validation requires a comparison with thermodilution. Such a study, due to the invasiveness of thermodilution, is complicated to arrange and is not included in this thesis.

Also the PBV measurement method was validated in-vitro. The calibration is simpler (only the linearity of the relation between contrast concentration and measured intensity is required) and a trans-thoracic transducer is sufficient for the measurement. The results show stable and reproducible volume estimates for a wide range of flows ( $\rho^2 > 0.99$ ). The results obtained by using the LDRW model fit of two IDCs (from the two measurement sites) or the LDRW model fit of the estimated impulse response are similar. Both the LDRW and the FPT model were tested for the measurement and show accurate results. However, a preference is given to the LDRW model due to the MTT overestimation of the FPT model for diffused curves. The PBV measurement was also tested in humans with promising results. However, for a reliable validation in patients, comparison with trans-pulmonary thermodilution, which requires a double catheterization, should be considered in the future.

The EF measurement was tested on a group of twenty patients by both the proposed dilution method (using TTE) and the echographic bi-plane method with contrast opacification ( $\rho^2 = 0.87$ ). This preliminary validation proves the feasibility and reliability of the dilution method. However, for a more accurate validation, comparison with MRI could be considered in the future.

This study proves that the simultaneous assessment of CO, EF (LV and RV), and PBV by use of UCA dilution is feasible and accurate. The measurement can be performed with minimal invasiveness. As a consequence, the proposed techniques may represent a useful tool in cardiology, anaesthesiology, and intensive-care, for the simultaneous measurement of important diagnostic parameters, some of which cannot be measured without the employment of very invasive techniques. Apart from the assessment of the mentioned cardiac parameters, the proposed techniques open a wide

range of possible applications, which involve both assessments of more cardiovascular parameters and clinical studies on the relations between the measured parameters.

The total circulating blood volume, for instance, could be assessed by means of the recirculation curve fit. The idea was tested successfully in a few patients (see Fig. (5.27)). This measurement can be used, for instance, to normalize blood volumes and replace the indexed values (division by BSA).

Another important application of the presented techniques could aim to the assessment of Regurgitant EF (REF). In fact, as the proposed UCA dilution approach allows an easy assessment of FEF, this value could be compared to the geometric EF assessment performed by any medical imaging technique (echography, MRI, CAT, etc.). The difference  $EF - FEF$  represents the fraction of EF that does not contribute to the forward flow, i.e., the REF. This parameter could be used as an indicator of the cardiac valve condition, although it does not distinguish between mitral and aortic valve insufficiency.

Also the regurgitant volume could be assessed. In fact,  $FEF = SV/V_{ed}$ , where the SV is the blood volume that is ejected forward during one cardiac cycle.  $V_{ed}$  and  $V_{es}$  can be measured by several geometric image analysis techniques. Therefore, the regurgitant volume can be quantified as  $V_{ed} - V_{es} - SV = V_{ed}(1 - FEF) - V_{es}$ .

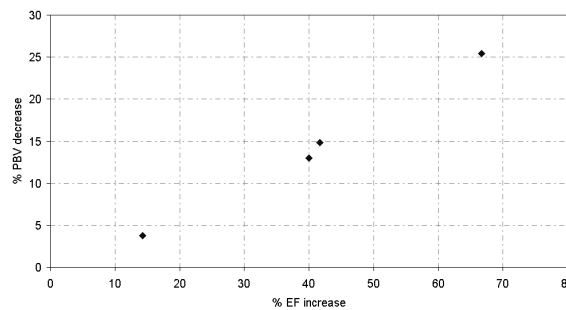


**Figure 8.1:** Results of a preliminary study to investigate the correlation between percent EF increase and percent PBV decrease during resynchronization therapy. The determination coefficient is 0.99.

Possible clinical studies could involve the establishment of a relation between blood volumes and cardiac condition. A preliminary study on the relation between EF improvement and PBV decrease during resynchronization therapy already shows promising results. The echographic bi-plane LV EF and the PBV were measured in four patients before bi-ventricular pacing and three months later. The results, as reported in Fig. (8.1), show a clear correlation ( $\rho^2 = 0.99$ ) between the EF increase (improved LV functionality) and the PBV decrease. In fact, when the LV contraction is less efficient than that of the RV, the blood pressure in the pulmonary circulation in-

creases until the LV and RV blood flows are balanced. The PBV expansion is a direct consequence of the pulmonary blood pressure increase. Therefore, after ventricular resynchronization, the improvement of the LV efficiency (EF) can be correlated to the decrease of PBV. This is an example of the opportunities that this technique opens for new clinical studies.

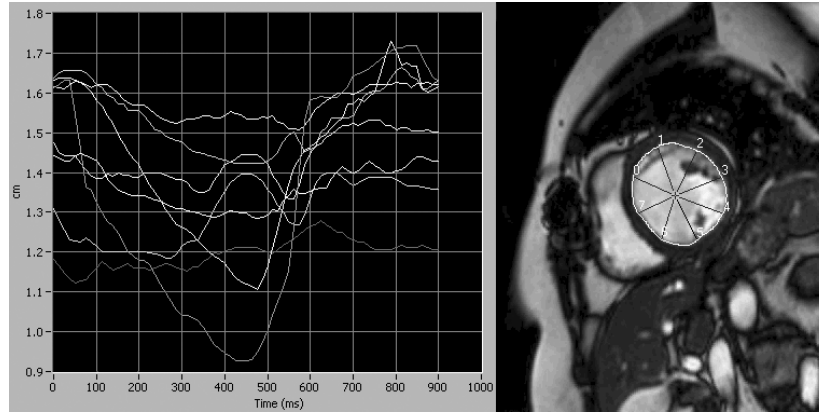


**Figure 8.2:** Application of the image segmentation algorithm for ventricular synchronicity evaluation. Eight rays are selected in a short axis MRI slice for the wall displacement measurement and the resulting time plots are shown on the left.

Also the segmentation algorithm presented in chapter 7 can be used for interesting clinical studies. A first application, already in progress, concerns the measurement of the LV contraction synchronicity. As shown in Fig. (8.2), the system is applied to a short axis view. Short axis MRI is used to obtain the highest image quality (high contrast) for a more accurate contour detection. The time resolution is 11ms. Eight of the radial filter rays (it can be any number of rays) are selected and the distance between the intersection ray-endocardium and the ray origin is plotted versus time during one cardiac cycle. Different plots are recorded from different segments (rays) and compared by a cross-correlation in order to determine the mutual delay of the ventricular contraction. The aim of this study is to determine the temporal-spatial distribution of the ventricular contraction, which might be used for more accurate positioning of the pacing electrodes.

Apart from several applications for new measurements and studies, also a different use of the same principles could be investigated. Inspired by the release-burst imaging techniques described in section 3.3, all the theory described in this thesis could be applied to *negative* (vertically flipped) IDCs. Using a continuous infusion of contrast, an homogeneous opacification of the circulatory system could be obtained. Therefore, if a destructive ultrasound burst with a high MI ( $MI > 1$ ) is transmitted, a

fraction of bubbles is destroyed and a negative IDC could be obtained from acoustic or video intensity measurements in specific ROIs.

In order to test the idea, the same fluid-dynamic system that is shown in Fig. (5.15) was closed to allow recirculation and filled with contrast (one vial of SonoVue®). Then an ultrasound burst was transmitted to the tubes. As a result, a negative IDC could be measured from the ROI in the second tube after the passage of the *negative bolus* through the network. Fig. (8.3) shows the LDRW fit of an inverted IDC. Several problems concerning this approach arose. First of all, the dose should be quantified in terms of energy of the ultrasound burst and related to the amount of destroyed bubbles. This procedure seems to be complicated, resulting in an extremely difficult calibration of the system.

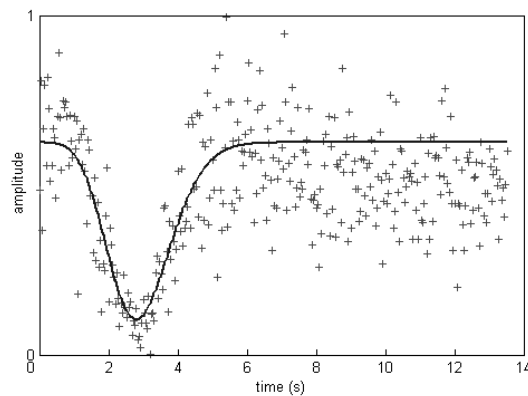


**Figure 8.3:** *LDRW model fit of a negative IDC.*

Moreover, the continuous imaging, despite the low MI, produces bubble disruption, as evident from the IDC baseline decay that is shown in Fig. (8.4). It is a monotonic decrease of the backscattered signal due to bubble clearance, which seems likely to be related to the insonation at 25 frames per second. A significant problem is also represented by the SNR, which is lower than that obtained by UCA bolus injections. In fact, while destructive bursts are very efficient in the myocardium and are exploited by replenishment techniques for flow quantification, the same does not apply to the ventricle, where only a small fraction of bubbles is destroyed.

As for the cardiac image segmentation algorithm, also the proposed indicator dilution techniques are not limited to echographic applications. In fact, apart from the calibration issues, which are strictly related to contrast echocardiography, the same indicator dilution principles can be applied to any contrast imaging techniques, such as PET or MRI (gadolinium dilution).



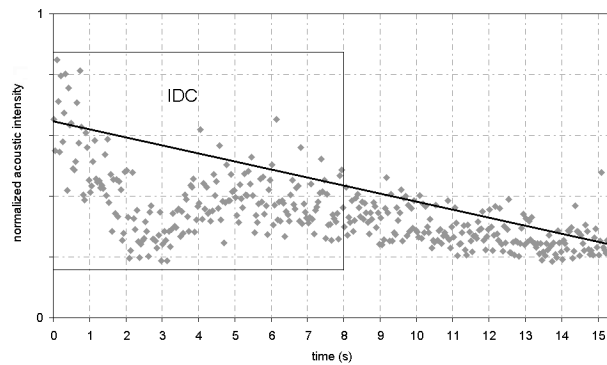


**Figure 8.4:** *Negative IDC. A monotone decrease of the ultrasound backscattered intensity is evident.*

In conclusion, new contrast imaging technologies can be exploited with specific signal processing and modelling for the measurement of several clinical diagnostic parameters. In this context, the contribution of this thesis consists in the development and validation of several techniques for cardiac and cardiovascular measurements based on contrast echocardiography. Consequently, this thesis also opens the way to a large number of clinical applications and studies based on the same principles. The ultimate goal, which is the major motivation of any biomedical research, is the realization of efficient instruments for a better understanding and treatment of human diseases.

## Appendix A

# Multiple linear regression

The multiple (or multivariate) linear regression is used in order to solve with a Least Square Estimation (LSE) the linear system given in Eq. (A.1), where  $\underline{Y}$  is the vector of the measured values,  $\underline{X}_1 \dots \underline{X}_p$  are the vectors of the stochastic variables that can influence the process, and  $p_0 \dots p_p$  are the parameters to optimize.

$$\underline{Y} = p_0 + p_1 \underline{X}_1 + p_2 \underline{X}_2 + \dots + p_p \underline{X}_p \quad (\text{A.1})$$

The LSE is the search of the absolute minimum of the squared error  $\varepsilon^2$ , which is defined as in Eq. (A.2).

$$\begin{aligned} \varepsilon^2(\underline{P}) &= \|\underline{Y} - (p_0 + p_1 \underline{X}_1 + p_2 \underline{X}_2 + \dots + p_p \underline{X}_p)\|_2 = \\ &= \sum_{i=1}^n (y_i - (p_0 + p_1 x_{i1} + p_2 x_{i2} + \dots + p_p x_{ip}))^2 \end{aligned} \quad (\text{A.2})$$

By defining the matrix  $[X] = \begin{bmatrix} 1 & x_{11} & x_{12} & \dots & x_{1p} \\ 1 & x_{21} & x_{22} & \dots & x_{2p} \\ \vdots & \vdots & \vdots & \ddots & \vdots \\ 1 & x_{n1} & x_{n1} & \dots & x_{np} \end{bmatrix}$ ,

$\varepsilon^2(\underline{P})$  can be expressed as given in Eq. (A.3).

$$\varepsilon^2(\underline{P}) = (\underline{Y} - [X]\underline{P})^t (\underline{Y} - [X]\underline{P}) = \underline{Y}^t \underline{Y} - 2\underline{P}^t [X]^t \underline{Y} + \underline{P}^t [X]^t [X] \underline{P} \quad (\text{A.3})$$

The usual way of proceeding is by differentiating  $\varepsilon^2(\underline{P})$  with respect to  $\underline{P}$  and imposing the resulting derivative to be equal to zero [217]. An alternative way [190], not involving calculus, is to notice that if  $\underline{P}'$  is any value of  $\underline{P}$  satisfying  $[X]^t [X] \underline{P}' = [X]^t \underline{Y}$ , then<sup>1</sup>  $\varepsilon^2(\underline{P}) \leq \varepsilon^2(\underline{P}')$  for all  $\underline{P}$ . If there were two different solutions  $\underline{P}'_{(1)}$  and  $\underline{P}'_{(2)}$ , then we would have  $[X]^t [X] (\underline{P}'_{(1)} - \underline{P}'_{(2)}) = 0$ , which implies

<sup>1</sup>This result can be established in the following steps. First, from the definition of  $\varepsilon^2$  we have  $\varepsilon^2(\underline{P}) - \varepsilon^2(\underline{P}') = \underline{P}'^t [X]^t [X] \underline{P} - 2\underline{P}'^t [X]^t \underline{Y} + 2(\underline{P}')^t [X]^t \underline{Y} - (\underline{P}')^t [X]^t [X] \underline{P}'$ .

Then, substituting  $[X]^t \underline{Y}$  with  $[X]^t [X] \underline{P}'$  we obtain  $\varepsilon^2(\underline{P}) - \varepsilon^2(\underline{P}') = \underline{P}'^t [X]^t [X] \underline{P} - 2\underline{P}'^t [X]^t [X] \underline{P}' + 2(\underline{P}')^t [X]^t [X] \underline{P}' = ([X] (\underline{P} - \underline{P}'))^t ([X] (\underline{P} - \underline{P}')) \geq 0$ , since it is a sum of squares. This establishes the result.

---

that the determinant of  $([X]'[X])$  is equal to zero. Thus, if  $[X]'[X]$  is non-singular ( $\det([X]'[X]) \neq 0$ ), then  $\underline{P}' = ([X]'[X])^{-1} [X]'\underline{Y}$  is the unique least squares estimator of  $\underline{P}$ .

## Appendix B

# Derivation of the LDRW model from a binomial step distribution

Referring to Fig. (4.12), we focus on one particle that is assumed to move stepwise (discrete motion). It is considered able to make a step ahead with probability  $p$  and a step backwards with probability  $q$ . The length of the step is fixed and equal to  $s$ , and it is executed with time period  $T$ .

Therefore, after  $n$  steps ( $k$  ahead and  $n - k$  backwards) the position  $X(nT)$  (with  $X$  random variable) is given as in Eq. (B-1).

$$\begin{aligned} X(nT) &= ks - (n - k)s = ms \\ m &= 2k - n \end{aligned} \quad (\text{B-1})$$

Therefore, the probability of finding the particle at position  $x = ms$  is given by the binomial model as in Eq. (B-2).

$$P\{X(nT) = ms\} = \binom{n}{k} p^k q^{n-k} \quad (\text{B-2})$$

The expected value  $E\{X(nT)\} = 0$  and the variance  $Var\{X(nT)\}$  is equal to  $E\{X^2(nT)\} = ns^2$ .

The simplest case is  $p = q = 1/2$ . Notice that this assumption implies a diffusion without drift, i.e., no flow is present.

**Theorem B-1 (Central Limit Theorem (CLT))** *Given a set  $X_1, X_2, \dots, X_n$  of independent, identically-distributed stochastic variables, suppose each  $X_i$  has mean  $\mu$  and variance  $\sigma^2 < \infty$ .*

*Defined  $Y_n = \sum_{i=1}^n X_i$ , then  $\lim_{n \rightarrow \infty} \frac{Y_n - n\mu}{\sigma\sqrt{n}}$  has a Gaussian distribution with  $\mu = 0$  and  $\sigma^2 = 1$ .*

□

For a number of steps  $n$  that is large enough, we can express the binomial model by means of the Central Limit Theorem (CLT, see Theorem B-1), since the steps are independent from each other and identically distributed ( $X(nT)$  is a *Markov process*). For a single step  $X_i$  the expected value  $E\{X_i\} = 0$  and the variance  $Var\{X_i\} = E\{X_i^2\} = s^2(1/2) + (-s)^2(1/2) = s^2$ . Hence, from the CLT it derives that  $P\{X(nT) = ms\}$ , referred to as the discrete process  $X(ms, nT)$ , is given as in Eq. (B-3).

$$P\{X(nT) = ms\} \triangleq X(ms, nT) = \frac{1}{\sqrt{2\pi ns^2}} e^{-\frac{(ms)^2}{2ns^2}} \quad (\text{B-3})$$

In order to transform the discrete process given in Eq. (B-3) into a continuous one, we can apply a limit operation for  $n \rightarrow \infty$ , which justifies the previous application of the CLT or, equivalently, we can consider the continuous time domain  $t = \lim_{T \rightarrow 0} nT$ .

With  $x = ms$  and assuming  $\lim_{T \rightarrow 0} (s^2/T) = \alpha$ , we obtain the Wiener process  $W(x, t)$  as given in Eq. (B-4)<sup>1</sup>.

$$W(x, t) = \frac{1}{\sqrt{2\pi\alpha t}} e^{-\frac{x^2}{2\alpha t}} \quad (\text{B-4})$$

It is interesting to notice that the Wiener process in Eq. (B-4) is solution of the mono-dimensional diffusion equation without drift (diffusion without convection) for a unit mass injected and unitary section of the tube (see Eq. (C-8)). Therefore,  $\alpha$  equals the diffusion coefficient  $D$  multiplied by two (see section 4.2.2).

This result is obtained with the hypothesis  $p = q = 1/2$ , i.e., when flow is absent. To introduce a carrier flow, we can assume  $p > q$  (probability of a step ahead larger than the probability of a step backwards).

The Random Walk process with  $p \neq q$  is known as *Generalized Random Walk*. For one step  $E\{X_i\} = s(p - q)$  and  $Var\{X_i\} = E\{X_i^2\} - E^2\{X_i\} = s^2 - (s(p - q))^2 = 4pqs^2$ . Therefore, if we apply the CLT, after  $n$  steps we have that the process  $X(ms, nT)$  can be approximated by a Gaussian distribution with expected value  $E\{X(nT)\} = ns(p - q)$  and variance  $Var\{X(nT)\} = 4npqs^2$  as given in Eq. (B-5).

$$P\{X(nT) = ms\} \triangleq X(ms, nT) = \frac{1}{\sqrt{8\pi npqs^2}} e^{-\frac{[ms - n(p - q)s]^2}{8npqs^2}} \quad (\text{B-5})$$

---

<sup>1</sup>The limit operation that defines  $\alpha$  must be interpreted as a statistical condition to keep the same description of the process (finite variance) when  $T$  and  $s$  become very small [185]. Analytical and physical interpretations in the continuous domain are meaningless.

Therefore, for  $T \rightarrow 0$  (or equivalently  $n \rightarrow \infty$ ) and with the substitutions given in Eq. (B-6), we obtain the same process  $X(x, t)$  as given in Eq. (4.21).

$$\begin{aligned}t &= nT \\ \alpha &= \frac{4pqs^2}{T} \\ x &= ms \\ u &= \frac{(p-q)s}{T}\end{aligned}\tag{B-6}$$

Eq. (4.25) is derived from Eq. (4.21) as explained in section 4.2.2. From Eq. (4.21) it results that  $\alpha$  is again equal to  $2D$ . The linear velocity of the carrier is now defined as  $u = (p - q)s/T$ .



## Appendix C

### LDRW model and diffusion equation

The transport of a tracer by means of a carrier is due to two contributions: the *diffusion process* and the *convection process*.

The the diffusion process represents the diffusion of a tracer in a carrier due to different concentrations of the tracer itself. We are considering a random walk of particles whose result is an average movement from regions of higher concentration to regions of lower concentration. The mathematical formulation is given by the *First Fick Equation* as in Eq. (C-1).

$$\begin{aligned}\vec{J}_{diff} &= -D\nabla C & (C-1) \\ C &= \text{concentration of the tracer} \\ D &= \text{diffusion coefficient} \\ \vec{J}_{diff} &= \text{diffusion flux}\end{aligned}$$

The convection process is the contribution to the transportation given by the motion of the tracer. It is modelled as given in Eq. (C-2).

$$\begin{aligned}\vec{J}_{conv} &= C\vec{u} & (C-2) \\ C &= \text{concentration of the tracer} \\ \vec{u} &= \text{carrier velocity} \\ \vec{J}_{conv} &= \text{convection flux}\end{aligned}$$

Eq. (C-2) is nothing else than a mathematical expression for the translation of the Gaussian distribution as shown in Fig. (4.12). Combining Eq. (C-1) and Eq. (C-2) we obtain the total tracer flux  $\vec{J}_{tot}$  as given in Eq. (C-3), where  $\vec{v}$  is the tracer velocity.

$$\vec{J}_{tot} \triangleq C\vec{v} = C\vec{u} - D\nabla C \quad (C-3)$$



The *diffusion coefficient*  $D$  (usually expressed in  $\text{cm}^2 \cdot \text{s}^{-1}$ ) depends on the concentration of the tracer as well as on the specific flow. For instance, the blood flow through large vessels during the main part of the cardiac cycle is a *laminar flow* with *Taylor diffusion*<sup>1</sup> and longitudinal diffusion coefficient  $D_L = (r^2 u^2)/(192 D_m)$  ( $u$  is the linear velocity in the center of the vessel,  $r$  is the radius of the vessel, and  $D_m$  is the molecular diffusion coefficient), while in the remaining part of the cardiac cycle it is a turbulent flow and  $D_L$  is linearly related to the *Reynolds number*<sup>2</sup> [11].

The measure of the relative contribution of convection and diffusion with respect to the tracer transport is known as *Peclet number* and it is related to the parameters of the LDRW model [11, 16]. In fact, as explained in section 4.2.2, the parameter  $\lambda$  not only defines the skewness of the curve, but also is directly related to the Peclet number.

Another equation of the hydrodynamics that is related to the dispersion process is the *continuity equation*, which states the *conservation of the mass*. Eq. (C-4) represents its formulation as given by Menzel.

$$\begin{aligned} \frac{\partial C}{\partial t} &= -\nabla \cdot C \vec{v} + R_{a,v} - R_{d,v} & \text{(C-4)} \\ C &= \text{concentration of the tracer} \\ \vec{v} &= \text{tracer velocity} \\ R_{a,v} &= \text{rate of appearance} \\ R_{d,v} &= \text{rate of disappearance} \end{aligned}$$

The terms  $R_{a,v}$  and  $R_{d,v}$  represent respectively the sources ( $\partial C/\partial t$ ) and sinks ( $-\partial C/\partial t$ ) of the tracer. In practice, Eq. (C-4) states that the rate of change of concentration at any point is equal to the sum of changes inducted by physical and chemical means. Physically, the concentration is regulated by the tracer transport (i.e., by convection and diffusion), which is represented by the term  $\nabla \cdot C \vec{v}$ . Chemically, the concentration is regulated by the difference between the rates of production and degradation of tracer, which is represented by the term  $(R_{a,v} - R_{d,v})$ .

Substituting  $C \vec{v}$  given by Eq. (C-3) into Eq. (C-4) and excluding the presence of sinks and sources we obtain Eq. (C-5).

$$\frac{\partial C}{\partial t} = -\nabla \cdot (C \vec{u} - D \nabla C) = D \nabla^2 C - \nabla \cdot C \vec{u} = D \nabla^2 C - (\vec{u} \cdot \nabla C + C \nabla \cdot \vec{u}) \quad \text{(C-5)}$$

<sup>1</sup>Taylor diffusion is the diffusion process under laminar flow conditions.

<sup>2</sup>The Reynolds number [47,218] is a non-dimensional parameter adopted to define the transition of a fluid from *laminar-* to *turbulent-flow* condition. Reynolds (1883) introduced this parameter by a specific experiment. A fluid with viscosity  $\mu_f$  and density  $\rho$  is made flow with linear velocity  $u$  into a circular pipe having radius  $r$  (*circular Poiseuille flow*). The Reynolds number is given as  $\text{Re} = 2\mu r \rho / \mu_f$ . The critical value 2000 determines the transition from laminar to turbulent flow.

Assuming the fluid to be incompressible, we have that  $\nabla \cdot \vec{u} = 0$  [16]. Therefore, Eq. (C-5) can be written as given in Eq. (C-6).

$$\frac{\partial C}{\partial t} = D \nabla^2 C - \vec{u} \cdot \nabla C \quad (\text{C-6})$$

To consider sources and sinks, the additional term  $R_{a,v} - R_{d,v}$  must be included. Eq. (C-6) is the formulation of the *diffusion with drift equation* or *equation of convective diffusion* [16].

For a mono-dimensional model (along the  $X$  axis) the diffusion equation can be written as given in Eq. (C-7) [10, 11], which is the mono-dimensional version of Eq. (C-6).

$$\frac{\partial C(x, t)}{\partial t} = D \frac{\partial^2 C(x, t)}{\partial x^2} - u \frac{\partial C(x, t)}{\partial x} \quad (\text{C-7})$$

This equation describes the process that is modelled in Fig. (4.12). It is based on the same assumption previously stated of Brownian motion of the particles that follow a random walk motion. The presence of the term  $-u(\partial C(x, t)/\partial x)$  is due to the convection transport and, therefore, to the flow of the carrier. Eq. (C-7) can be simplified by means of a change of reference coordinates in order to observe the system moving at the same velocity  $u$  of the carrier fluid. Therefore, after the substitution  $x' = x - ut$ , Eq. (C-7) becomes the classical mono-dimensional diffusion equation as given in Eq. (C-8).

$$\frac{\partial C(x', t)}{\partial t} = D \frac{\partial^2 C(x', t)}{\partial x'^2} \quad (\text{C-8})$$

With the initial conditions as given in Eq. (C-9) and Eq. (C-10)<sup>3</sup>, where  $A$  is the mean sectional area of the tube and  $u_0(x)$  is a Dirac impulse that represents the fast injection of the tracer bolus (see also Fig. (4.12)), the solution of Eq. (C-8) is given as in Eq. (C-11) [16], which is a Gaussian (normal) distribution whose variance is equal to  $2Dt$ .

$$C(x, 0) = \left(\frac{m}{A}\right) u_0(x) \quad (\text{C-9})$$

$$m = A \int_{-\infty}^{\infty} C(x, t) dx \quad (\text{C-10})$$

$$C(x', t) = \frac{m}{A\sqrt{4\pi Dt}} e^{-\frac{x'^2}{4Dt}} \quad (\text{C-11})$$

In the original fixed reference coordinates (i.e.,  $x$  instead of  $x'$ ), Eq. (C-11) is given as in Eq. (C-12), which is a solution of Eq. (C-7).

$$C(x, t) = \frac{m}{A\sqrt{4\pi Dt}} e^{-\frac{(x-ut)^2}{4Dt}} \quad (\text{C-12})$$

<sup>3</sup>Notice that the defined initial conditions remain valid for both  $x$  and  $x'$ .

With the substitution  $2D = \alpha$ , Eq. (C-12) is equal to  $(m/A)W(x, t)$  as from Eq. (4.21), therefore, Eq. (4.25) can be obtained with the same procedure as shown for Eq. (4.21) in section 4.2.2.

## Appendix D

### LDRW model time integration

As from Eq. (5.11) and neglecting the coefficient  $A$ , the LDRW model can be expressed as given in Eq. (D-1).

$$C(t) = \frac{1}{\sqrt{2\pi K^2 t}} e^{-\frac{(\mu-t)^2}{2K^2 t}} \quad (\text{D-1})$$

In fact, for  $K^2 = 2D/v^2$  and  $\mu = x_0/v$  Eq. (D-1) becomes the Wiener process as given in Eq. (4.21), which, as discussed in section 4.2.2, is equal to Eq. (4.25) (previa a few substitutions). In this appendix, the integral of  $C(t)$  (refer to Eq. (D-1)) in the interval  $(0, \infty)$  is proven to be equal to 1. The proof is divided in five steps, which prove the following five equations ( $i = \sqrt{-1}$  and  $x, y$ , and  $\xi \in \mathbb{R}$ ).

#### Step 1

$$\int_{-\infty}^{+\infty} e^{-y^2} \cdot e^{ixy} dy = \sqrt{\pi} e^{-\frac{x^2}{4}} \quad (\text{D-2})$$

#### Step 2

$$\int_{-\infty}^{+\infty} e^{-ty^2} \cdot e^{ixy} dy = \sqrt{\frac{\pi}{t}} e^{-\frac{x^2}{4t}}, \quad \forall t > 0 \quad (\text{D-3})$$

#### Step 3

$$\int_{-\infty}^{+\infty} \frac{1}{\xi^2 + b^2} e^{ix\xi} d\xi = \frac{\pi}{b} e^{-bx}, \quad \forall b > 0 \quad (\text{D-4})$$

#### Step 4

$$\frac{b}{\pi} \int_0^{+\infty} \frac{1}{\sqrt{t}} e^{\frac{b^2}{t} (\frac{x}{2b} - t)^2} dt = 1, \quad b, t \in \mathbb{R}^+ \quad (\text{D-5})$$

**Step 5**

$$\int_{-\infty}^{+\infty} \frac{1}{\sqrt{2\pi K^2 t}} e^{-\frac{(\mu-t)^2}{2K^2 t}} dt = 1, \quad K, \mu \in \mathbb{R}^+ \quad (\text{D-6})$$

In the following, each step is proven.

**Proof of step 1.** We define

$$f(x) = \int_{-\infty}^{+\infty} e^{-y^2} \cdot e^{ixy} dy.$$

In order to calculate the derivative  $f'(t)$ , we notice that

$$\frac{d}{dx} \left( e^{-y^2} \cdot e^{ixy} \right) = iy e^{-y^2} e^{ixy}$$

and

$$\left| \frac{d}{dx} \left( e^{-y^2} \cdot e^{ixy} \right) \right| = |y| e^{-y^2}.$$

Therefore, the integral of the absolute value converges and the derivation can be performed under the integration operator.

$$f'(x) = \int_{-\infty}^{+\infty} \frac{d}{dx} \left( e^{-y^2} \cdot e^{ixy} \right) dy = i \int_{-\infty}^{+\infty} y e^{-y^2} \cdot e^{ixy} dy.$$

$f'(x)$  can be integrated per parts as follows.

$$\begin{aligned} f'(x) &= -\frac{i}{2} \int_{-\infty}^{+\infty} e^{ixy} d e^{-y^2} = \left[ -\frac{i}{2} e^{ixy} \cdot e^{-y^2} \right]_{-\infty}^{+\infty} + \frac{i}{2} \int_{-\infty}^{+\infty} e^{-y^2} d e^{ixy} = \\ &= -\frac{x}{2} \int_{-\infty}^{+\infty} e^{-y^2} \cdot e^{ixy} dy = -\frac{x}{2} f(x). \end{aligned}$$

As a result,  $f(x)$  is solution of the differential equation  $f'(x) = -\frac{x}{2} f(x)$  and can be expressed as

$$f(x) = f(0) e^{-\int_{-\infty}^x \frac{\xi}{2} d\xi} = f(0) e^{-\frac{x^2}{4}}.$$

$f(0)$  is equal to the well known integral<sup>1</sup>

$$f(0) = \int_{-\infty}^{+\infty} e^{-y^2} dy = \sqrt{\pi}.$$

As a result,  $f(x) = \sqrt{\pi} e^{-\frac{x^2}{4}}$ , which proves Eq. (D-2).

**Proof of step 2.** Eq. (D-3) can be proven by the variable substitution  $\sqrt{t}y = \xi$  (so that  $dy = d\xi/\sqrt{t}$ ) and the application of Eq. (D-2) as follows.

$$\int_{-\infty}^{+\infty} e^{-ty^2} \cdot e^{ixy} dy = \int_{-\infty}^{+\infty} e^{-\xi^2} \cdot e^{\frac{ix\xi}{\sqrt{t}}} \frac{1}{\sqrt{t}} d\xi = \sqrt{\frac{\pi}{t}} e^{\frac{-x^2}{4t}}.$$

**Proof of step 3.** Eq. (D-4) can be proven by use of the *residual integration theory* [219]. According to this theory, if  $g(z)$  is a rational function of  $z$  ( $z \in \mathbb{C}$ ), which is real and with no poles on the real axis, and such that  $|g(z)| = O(1/|z|)$  for  $|z| \rightarrow \infty$ , then, if  $z_j$  (with  $j = [1..n]$ ) are the poles of  $g(z)$  for  $\Im[z] > 0$ ,

$$\int_{-\infty}^{+\infty} g(\xi) e^{ix\xi} d\xi = 2\pi i \sum_{j=1}^n \text{Res} [g(z) e^{ixz}]_{z=z_j}, \quad x > 0.$$

---

<sup>1</sup>A solution of this integral is shown.  $f(0)$  is equal to the integral of  $2 e^{-y^2}$  between  $y = 0$  and  $y = +\infty$ . We can notice that ( $x, y$ , and  $\xi \in \mathbb{R}$ )

$$\iint_{\mathbb{R}_+^2} e^{-(x^2+y^2)} dx dy = \int_0^{+\infty} e^{-x^2} dx \int_0^{+\infty} e^{-y^2} dy = \left( \int_0^{+\infty} e^{-\xi^2} d\xi \right)^2.$$

Moreover, passing into polar coordinate ( $r, \theta$ ), we have

$$\iint_{\mathbb{R}_+^2} e^{-(x^2+y^2)} dx dy = \int_0^{\frac{\pi}{2}} d\theta \int_0^{+\infty} e^{-r^2} r dr = \frac{\pi}{4}.$$

Therefore,

$$\int_{-\infty}^{+\infty} e^{-y^2} dy = 2 \int_0^{+\infty} e^{-y^2} dy = 2\sqrt{\frac{\pi}{4}} = \sqrt{\pi}.$$

We define  $g(z) = 1/[(z - ib)(z + ib)]$ . If  $b > 0$ , the only pole for  $\Im[z] > 0$  is a first order pole in  $z = ib$ . The related residual is equal to  $\lim_{z \rightarrow ib} [g(z)(z - ib)] = (-ie^{-bx})/(2b)$ . As a consequence,

$$\int_{-\infty}^{+\infty} \frac{1}{\xi^2 + b^2} e^{ix\xi} d\xi = 2\pi i \left( \frac{-ie^{-bx}}{2b} \right) = \frac{\pi}{b} e^{-bx} \quad b > 0,$$

and Eq. (D-4) is proven.

**Proof of step 4.** We notice that

$$\frac{1}{\xi^2 + b^2} = \int_0^{+\infty} e^{-t(\xi^2 + b^2)} dt = \left[ \frac{-1}{\xi^2 + b^2} e^{-t(\xi^2 + b^2)} \right]_{t=0}^{t=+\infty}.$$

Therefore, Eq. (D-4) can be written as follows.

$$\int_{-\infty}^{+\infty} \left( \int_0^{+\infty} e^{-t(\xi^2 + b^2)} dt \right) e^{ix\xi} d\xi = \frac{\pi}{b} e^{-bx}.$$

We introduce a theorem.

**Theorem D-1 (Fubini's theorem)** *Let  $g(x, y)$  be a continuous function on the rectangular region  $R$ :  $a \leq x \leq b$  and  $c \leq y \leq d$ . Then*

$$\iint_R g(x, y) dx dy = \int_c^d \left( \int_a^b g(x, y) dx \right) dy = \int_a^b \left( \int_c^d g(x, y) dy \right) dx.$$

□

According to Theorem D-1, we can invert the order of integration. Therefore, applying Eq. (D-3), we obtain

$$\int_0^{+\infty} e^{-tb^2} \int_{-\infty}^{+\infty} e^{-t\xi^2} e^{ix\xi} d\xi dt = \int_0^{+\infty} \sqrt{\frac{\pi}{t}} e^{-\frac{x^2}{4t}} e^{-tb^2} dt = \frac{\pi}{b} e^{-bx}.$$

After rearranging the terms, Eq. (D-5) is derived as follows.

$$1 = \frac{b}{\pi} \int_0^{+\infty} \frac{1}{\sqrt{t}} e^{(bx - tb^2 - \frac{x^2}{4t})} dt = \frac{b}{\pi} \int_0^{+\infty} \frac{1}{\sqrt{t}} e^{\frac{b^2}{t} (\frac{x}{2b} - t)^2} dt.$$

**Proof of step 5.** Eq. (D-5) is directly derived from Eq. (D-5) with the substitutions  $x/(2b) = \mu$  and  $1/b^2 = 2K^2$ .

---

## Bibliography

- [1] P. A. Heidenreich, J. G. Wiencek, J. G. Zaroff, S. Aroson, L. J. Segil, P. V. Haper, and S. B. Feinsten, "In vitro calculation of flow by use of contrast ultrasonography," *J Am. Soc. Echocardiography*, vol. 6, no. 1, pp. 51–61, 1993.
- [2] D. Rovai, M. Lombardi, L. Taddei, A. Mazzarisi, L. Landini, G. Ghelardini, A. Distane, A. Benassi, and A. L' Abbate, "Flow quantitation by contrast echocardiography," *The International Journal of Cardiac Imaging*, vol. 9, pp. 21–27, 1993.
- [3] K. Mizushige, A. N. DeMaria, Y. Toyama, H. Morita, S. Senda, and H. Matsuo, "Contrast echocardiography for evaluation of left ventricular flow dynamics using densitometric analysis," *Circulation*, vol. 88, pp. 588–595, 1993.
- [4] A. N. Dearia, W. Bommer, L. Kwan, K. Riggs, M. Smith, and J. Waters, "In vivo correlation of thermodilution cardiac output and videodensitometric indicator-dilution curves obtained from contrast two-dimensional echocardiograms," *J. of Am. College of Cardiology*, vol. 3, no. 4, pp. 999–1004, 1984.
- [5] H. Bleeker, K. Shung, and J. Barnhart, "On the application of ultrasonic contrast agents for blood flowmetry and assesment of cardiac perfusion," *Ultrasound in Med. and Biol.*, vol. 9, pp. 461–471, 1990.
- [6] L. Gerfault, E. Helms, V. Bailleau, N. Rognin, G. Finet, M. Janier, and C. Cachard, "Assessing blood flow in isolated pig heart with usca," in *IEEE International Ultrasonics Symposium*. IEEE UFFC Society, October 1999, vol. 2, pp. 1725–1728.
- [7] B. Herman, S. Einav, and Z. Vered, "Feasibility of mitral flow assessment by echo-contrast ultrasound, part ii: experimental study on a mechanical model of the left heart," *Ultrasound in Med. and Biol.*, vol. 26, no. 5, pp. 797–806, 2000.
- [8] D. Rovani, S. E. Nissen, E. Jonathan, M. Smith, A. L'Abbate, Oi Ling Kuan, and A. N. De Maria, "Contrast echo washout curves from left ventricle: application of basic principles of indicator-dilution theory and calculation of ejection fraction," *J. Am. Coll. Cardiol.*, vol. 10, pp. 125–134, 1987.



- [9] J. M. Bogaard, J. R. C. Jansen, E. A. von Reth, A. Versprille, and M. E. Wise, "Random walk type models for indicator-dilution studies: comparison of a local density random walk and a first passage times distribution," *Cardiovascular Research*, vol. 20, no. 11, pp. 789–796, 1986.
- [10] E. A. von Reth and J. M. Bogaard, "Comparison of a two-compartment model and distributed models for indicator dilution studies," *Med. & Biol. Eng. & Comput.*, vol. 21, pp. 453–459, 1983.
- [11] J. M. Bogaard, S. J. Smith, A. Versprille, M. E. Wise, and F. Hagemeyer, "Physiological interpretation of skewness of indicator-dilution curves; theoretical considerations and practical application," *Basic Res. Cardiol.*, vol. 79, pp. 479–493, 1984.
- [12] M. E. Wise, "Tracer dilution curves in cardiology and random walk and log-normal distributions," *Acta Physiol. Pharmacol. Neerl.*, vol. 14, pp. 175–204, 1966.
- [13] R. K. Millard, "Indicator-dilution dispersion models and cardiac output computing methods," *The American Physiological Society*, vol. 272, no. 4, pp. H2004–H2012, 1997.
- [14] E. A. von Reth, "Assesment of the indicator-dilution technique in non-stazionary flow," Ph.D. thesis, Eindhoven University of Technology, Eindhoven, The Netherlands, 1984.
- [15] C. W. Sheppard, *Basic principles of tracer methods: introduction to mathematical tracer kinetics*, Wiley, New York, 1962.
- [16] K. H. Norwich, *Molecular dynamics in biosystems*, Pergamon Press, 1977.
- [17] J. M. Bland and D. G. Altman, "Statistical methods for assessing agreement between two methods of clinical measurement," *Lancet*, vol. 1, pp. 307–310, 1986.
- [18] N. G. Bellenger, M. I. Burgess, S. G. Ray, A. Lahiri, A. J. Coats, J. G. Cleland, and D. J. Pennell, "Comparison of left ventricular ejection fraction and volumes in heart failure by echocardiography, radionuclides, ventriculography and cardiovascular magnetic resonance; are they interchangeable?," *Eur. Heart*, vol. 21, no. 16, pp. 1387–1396, 2000.
- [19] J. G. Webster, Ed., *Medical Instrumentation : Application and Design*, CRC Press, Boca Raton, third edition, 1997.

- 
- [20] Joseph D. Bronzino, Ed., *The biomedical engineering handbook*, CRC Press, Boca Raton, second edition, 2000.
- [21] J. G. Webster, Ed., *Measurement, instrumentation and sensors handbook*, CRC Press, Boca Raton, 2000.
- [22] J. R. C. Jansen, “The thermodilution method for clinical assesment of cardiac output,” *Intensive Care Med.*, vol. 21, pp. 691–697, 1995.
- [23] M. Yelderman, “Continuous measurement of cardiac output with the use of stochastic system identification techniques,” *J. Clin. Monit.*, vol. 6, pp. 322–332, 1990.
- [24] F. P. Branca, *Fondamenti di ingegneria clinica*, Springer, Milan, 2000.
- [25] F. P. Branca, *Misure meccaniche*, Masson, 1988.
- [26] H. J. C. Swan, W. Ganz, J. Forrester, H. Marcus, G. Diamond, and D. Chonette, “Catheterization of the heart in man with use of a flow-directed, balloon-tipped catheter,” *N. Engl. J. Med.*, vol. 283, pp. 447–451, 1971.
- [27] G. Williams, M. Grounds, and A. Rhodes, “Pulmonary artery catheter,” *Current Opinion in Critical Care*, vol. 8, pp. 251–256, 2002.
- [28] A. F. Connors, T. Speroff, N. V. Dawson, and al., “The effectiveness of right heartcatheterization in the initial care of critically ill patients,” *Journal of the American Medical Association*, vol. 287, no. 11, pp. 889–897, 1996.
- [29] R. A. F. Linton, N. W. F. Linton, and D. M. Band, “A new method of analysing indicator dilution curves,” *Cardiovascular Research*, vol. 30, pp. 930–938, 1995.
- [30] Xucai Chen, K. Q. Schwarz, D. Phillips, S. D. Steinmetz, and R. Schlief, “A mathematical model for the assessment of hemodynamic parameters using quantitative contrast echocardiography,” *IEEE Trans. on Biomedical Engineering*, vol. 45, no. 6, pp. 754–765, 1998.
- [31] F. Wittlich, K. Koho, G. Mies, D. Norris, and M. Hoehn-Berlage, “Quantitative measurement of regional blood flow with gadiolinium diethylenetriaminepentaacetate bolus track nmr imaging in cerebral infarcts in rats: validation with the iodio<sup>[14c]</sup>antipyrene technique,” in *Proc. Natl. Acad. Sci. USA*. Natl. Acad. Sci. USA, 1995, vol. 92, pp. 1846–1850.
- [32] K. Zierler, “Indicator dilution methods for measuring blood flow, volume, and other properties of biological systems: a brief history and memoir,” *Annals of Biomedical Engineering*, vol. 28, pp. 836–848, 2000.

- [33] G. N. Stewart, "Researches on the circulation time and on the influences which affect it," *J. Physiology*, vol. 22, pp. 159–183, 1897.
- [34] W. F. Hamilton, J. W. Moore, J. M. Kinsman, and R. G. Spurling, "Simultaneous determination of the pulmonary and systemic circulation times in man and of a figure related to cardiac output," *Am. J. of Physiology*, vol. 84, pp. 338–334, 1928.
- [35] N. Gefen, O. Barnea, A. Abramovich, and W. P. Santamore, "Experimental assesment of error sources in thermodilution mesurements of cardiac output and ejection fraction," in *IEEE Proceedings of the First Joint BMES/EMBS Conference Serving Humanity, Advancing Technology*, Atlanta, 1999, IEEE EMBS Society, p. 796.
- [36] G. Fegler, "Measurement of cardiac output in anaesthetised animals by a thermodilution method," *Q. J. Exp. Physiol.*, vol. 39, pp. 153–164, 1954.
- [37] M. Jonas, D. Hett, and J. Morgan, "Real time, continuous monitoring of cardiac output and oxygen delivery," *Int. J. of Intesive Care*, vol. 9, no. 1, 2002.
- [38] T. Kurita, K. Morita, S. Kato, H. Kawasaki, M. Kikura, T. Kazama, and K. Ikeda, "Lithium dilution cardiac output measurements using a peripheral injection site: comparison with central injection technique and thermodilution," *J. of Clinical Monitoring and Computing*, vol. 15, pp. 279–285, 1999.
- [39] T. T. Hamilton, L. M. Huber, and M. E. Jessen, "Pulseco: a less-invasive method to monitor cardiac output from arterial pressure after cardiac surgery," *A. Thoracic Surgery*, vol. 74, pp. S1408–1412, 2002.
- [40] M. M. onas and S. J. Tanzer, "Lithium dilution measurements of cardiac output and arterial pulse waveform analysis: an indicator dilution calibrated beat-by-beat system for continuous estimation of cardiac output," *Current Opinion in Critical Care*, vol. 8, pp. 257–261, 2002.
- [41] A. P. Dhawan, *Medical Image Analysis*, John Wiley and Sons, New Jersey, 2003.
- [42] A. Gilardoni, M. T. Gilardoni, A. A. Orsini, and L. Orsini, *Radiology - Electromedicine*, Ed. Gilardoni Spa, Madello Lario, Italy, 1987.
- [43] A. K. Jain, *Fundamentals of digital image processing*, Prentice Hall, 1989.
- [44] Klaus Roth, *NMR Tomography and Spectroscopy in Medicine: an introduction*, Springer-Verlag, 1984.

- 
- [45] J. Morkenborg, M. Pedersen, F. T. Jensen, H. Stodkilde-Jorgensen, J. C. Djurhuus, and J. Frokiaer, "Quantitative assessment of gd-dtpa contrast agent from signal enhancement: an in-vitro study," *Magnetic Resonance Imaging*, vol. 21, pp. 637–643, 2003.
- [46] Harvey Feigenbaum, *Echocardiography*, Lippincott Williams & Wilkins, fifth edition, 1994.
- [47] W. R. Hedrick, D. L. Hykes, and D. E. Starchman, *Ultrasound physics and instrumentation*, Mosby, Naples, third edition, 1995.
- [48] S. K. Samijo, "Wall shear stress in human arteries," Ph.D. thesis, Maastricht University, Maastricht, The Netherlands, 2001.
- [49] L. A. F. Ledoux, "A modelled approach to absolute velocity detection with ultrasound," Ph.D. thesis, Maastricht University, Maastricht, The Netherlands, 1999.
- [50] A. C. Perrino, "Cardiac output monitoring by echocardiography: should we pass on swan-ganz catheters?," *Yale Journal of Biology and Medicine*, vol. 66, pp. 397–413, 1994.
- [51] B. Valtier, B. P. Cholley, J. P. Belot, J. E. de la Coussaye, J. Mateo, and D. M. Payen, "Noninvasive monitoring of cardiac output in critically ill patients using transesophageal doppler," *Am. J. Respir. Crit. Care Med.*, vol. 158, no. 1, pp. 77–83, 1998.
- [52] D. Leone, G. Servillo, E. Robertis, F. Rossano, and R. Tufano, "Monitoring cardiac output: esophageal doppler vs thermodilution," *Minerva Anestesiol.*, vol. 64, no. 7.
- [53] A. Cariou, M. Monchi, L. M. Joly, F. Bellefant, Y.E. Claessens, D. Thebert, F. Brunet, and J. F. Dhainaut, "Noninvasive cardiac output monitoring by aortic blood flow determination: evaluation of the sometec dynemo-3000 system," *Crit. Care Med.*, vol. 26, no. 12, pp. 2066–2072, 1998.
- [54] G. Bernardin, F. Tiger, R. Fouche, and M. Mattei, "Continuous noninvasive measurement of aortic blood flow in critically ill patients with a new esophageal echo-doppler system," *J. Crit. Care*, vol. 13, no. 4, pp. 177–183, 1998.
- [55] R. Dummler, M. Emmerich, G. Klein, and G. Wagner, "Semi-invasive cardiac output measurement using combined transesophageal ultrasound device.early experiences," *Anaesthetist*, vol. 49, no. 3, pp. 207–210, 2000.

- [56] J. Poelaert, C. Schmidt, H. Van Aken, F. Hindler, and H. M. Loick T. Mollhoff, "A comparison of transoesophageal echographic doppler across the aortic valve and the thermodilution technique for estimating cardiac output," *Anaesthetist*, vol. 54, no. 2, pp. 128–136, 1999.
- [57] A. Derscorps-Declere, N. Smail, B. Vigue, J. Duranteau, O. Mimos, A. Edouard, and K. Smaii, "Transgastric, pulsed doppler echocardiographic determination of cardiac output," *Intensive Care Med.*, vol. 22, no. 1, pp. 34–38, 1996.
- [58] B. Lavandier, D. Cathignol, R. Muchada, B. B. Xuan, and J. Motin, "Noninvasive aortic blood flow measurement using an intraesophageal probe," *Ultrasound in Med. and Biol.*, vol. 11, no. 3, pp. 451–460, 1985.
- [59] A. N. Owen, P. Simon, R. Moidl, M. Hiesmayr, A. Moritz, E. Wolner, and W. Mohl, "Measurement of aortic flow velocity during transesophageal echography in the transgastric five-chamber view," *Am. J. of Echicardiography*, vol. 8, no. 6, pp. 874–878, 1995.
- [60] B. Lynn J. Shakhanbeh B. Cotsell, J. Foreman, "The use of an infra-red laser-doppler flow meter to measure changes in skin blood flow in man and in experimental animals," *Perfusion*, vol. 7, pp. 283–290, 1992.
- [61] C. Mencuccini and V. Silvestrini, *Fisica 1*, Liguori Ed., Naples, second edition, 1987.
- [62] J. Malmivuo and R. Plonsey, *Bioelectromagnetism*, Springer-Verlag, New York, second edition, 1982.
- [63] A. L. H. Deng, S. H. Karagiannoglou, W. I. Sakkas, G. D. O. Lowe, and J. C. Barbenel, "The impedance measurement of human blood in relations to the hemorheological determinants," *Int. J. of Bioelectromagnetism*, vol. 4, no. 2, pp. 167–168, 2002.
- [64] P. Brigger, P. Bacharach, A. Aldroubi, and M. Unser, "Segmentation of gated spect images for automatic computation of myocardial volume and ejection fraction," in *IEEE Proc. of Int. Conf. on Image Processing*. IEEE, Oct. 1997, pp. 113–116.
- [65] A. Khorsand, S. Graf, C. Pirich, G. Wagner, D. Moertl, and al., "Image analysis of gated cardiac pet to assess left ventricular volumes and contractile function," in *IEEE Proc. on Computers in Cardiology*. IEEE, Sept. 2000, pp. 311–314.

- 
- [66] R. J. van der Geest, E. Jansen, V. G. M. Buller, and J. H. C. Reiber, "Automated detection of left ventricular epi- and endocardial contours in short-axis mr images," in *IEEE Proc. on Computers in Cardiology*. IEEE, Sept. 1994, pp. 33–26.
- [67] S. Schalla, E. Nagel, H. Lehmkuhl, A. Bornstedt C. Klein, B. Schnackenburg, U. Schneider, and E. Fleck, "omparison of magnetic resonance real-time imaging of left ventricular function with conventional magnetic resonance imaging and echocardiography," *Am. J. of Cardiology*, vol. 87, pp. 95–99, 2001.
- [68] W. C. Brogan, B. Glamann, and L. D. Hillis, "Comparison of single and bi-plane ventriculography for determination of left ventricular volume and ejection fraction," *Am. J. of Cardiology*, vol. 69, no. 12, pp. 1079–1082, 1992.
- [69] T. Shiota, P. M. McCarthy, R. D. White, Jian Xin Quin, N. L. Greenberg, S. D. Flamm, J. Wong, and J. D. Thomas, "Initial clinical experience of real-time three-dimensional echocardiography in patients with ischemic and idiopathic dialated cardiomyopathy," *Am. J. of Cardiology*, vol. 84, pp. 1068–1073, 1999.
- [70] W. A. Helbing, H. G. Bosch, C. Maliepaard, and al., "Comparison of echocardiographic methods with magnetic resonance imaging for assessment of right ventricular function in children," *Am. J. of Cardiology*, vol. 76, pp. 589–594, 1995.
- [71] M. B. Rominger, G. F. Bachmann, W. Pabst, W. W. Ricken, H. P. Dinkel, and W. S. Rau, "Left ventricular heart volume determination with fast mri in breath holding technique: how different are quantitative heart catheter, quantitative mri and visual echocardiography," *Rofo Fortschr Geb Rontgenstr Neuen Bildgeb Verfah*, vol. 172, no. 1, pp. 23–32, 2000.
- [72] S. Fujimoto, R. Mizuno, Y. Nakagawa, K. Dohi, and H. Nakano, "Estimation for right ventricular volume and ejection fraction by transthoracic three-dimensional echocardiography. a validation study using magnetic resonance imaging," *Int. J. Card. Imaging*, vol. 14, no. 6, pp. 385–390, 1998.
- [73] L. E. Teichholz, T. Kreulen, M. V. Herman, and R. Gorlin, "Problems in echocardiographic volume determinations: echocardiographic-angiographic correlations in the presence or absence of asynergy," *Yale Journal of Biology and Medicine*, vol. 66, pp. 397–413, 1994.
- [74] G. de Simone, R. B. Devereux, A. Ganau, R. T. Hahn, P. S. Saba, G. F. Mureddu, M. J. Roman, and B. V. Howard, "Estimation of left ventricular

- chamber and stroke volume by limited m-mode echocardiography and validation by two-dimensional and doppler echocardiography," *Am. J. Cardiology*, vol. 78, pp. 801–807, 1996.
- [75] J. P. Holt, "Estimation of residual volume of the ventricle of the dog by two indicator dilution techniques," *Circ. Res.*, pp. 4–181, 1956.
- [76] Sunyoung Jang, R. J. Jaszczak, Jianying Li, J. F. Debatin, S. N. Nadel, A. J. Evans, K. L. Greer, and R. E. Coleman, "Cardiac ejection fraction and volume measurements using dynamic cardiac phantoms and radionuclide imaging," *IEEE Transactions on Nuclear Science*, vol. 41, no. 6, pp. 2845–2849, 1994.
- [77] H. Lehmkuhl, T. Machnig, B. Eicker, K. Barth, K. Reynen, and K. Bachmann, "Digital subtraction angiography: feasibility of densitometric evaluation of left ventricular volumes and comparison to measurements obtained by the mono-plane area-length-method," in *IEEE Proc. on Computers in Cardiology*. IEEE, Sept. 1993, pp. 29–32.
- [78] T. Machnig, B. Eicker, K. Barth, H. Lehmkuhl, and K. Bachmann, "Measurement of left ventricular ejection fraction (ef) by densitometry from digital subtraction angiography," in *IEEE Proc. on Computers in Cardiology*. IEEE, Sept. 1990, pp. 589–592.
- [79] A. J. G. H. Bindels, J. G. van der Hoeven, A. D. Graafland, J. de Koning, and A. E. Meinders, "Relationships between volume and pressure measurements and stroke volume in critically ill patients," *Crit. Care*, vol. 4, pp. 193–199, 2000.
- [80] A. Hoeft, B. Schorn, A. Weyland, and al., "Bedside assessment of intravascular volume status in patients undergoing coronary bypass surgery," *Anesthesiology*, vol. 81, pp. 76–86, 1994.
- [81] S. G. Sakka, C. C. Ruhl, U. J. Pfeiffer, R. Beale, A. McLuckie, K. Reinhart, and A. Meier-Hellmann, "Assessment of cardiac preload and extravascular lung water by single transpulmonary thermodilution," *Intensive Care Med.*, vol. 26, pp. 180–187, 2000.
- [82] W. Buhre, S. Kazmaier, H. Sonntag, and A. Weiland, "Changes in cardiac output and intrathoracic blood volume: a mathematical coupling of data?," *Acta Anaesthesiol Scand*, vol. 45, pp. 863–867, 2001.
- [83] W. Buhre, A. Weyland, K. Buhre, S. Kazmaier, K. Mursch, M. Schmidt, M. Sydow, and H. Sonntag, "Effects of the sitting position on the distribution of blood volume in patients undergoing neurosurgical procedures," *British Journal of Anaesthesia*, vol. 84, no. 3, pp. 354–357, 2000.

- 
- [84] O. Picker, G. Weitasch, T. W. L. Sceeren, and J. O. Arnd, "Determination of total blood volume by indicator dilution: a comparison of mean transit time and mass conservation principle," *Intensive Care Med.*, vol. 27, no. 3, pp. 767–774, 2001.
- [85] Kevin Wei, A. R. Jayaweera, S. Firoozan, A. L., D. M. Skyba, and S. Kaul, "Quantification of myocardial blood flow with ultrasound-induced destruction of microbubbles administered as a constant venous infusion," *Circulation*, vol. 97, no. 5, pp. 473–483, 1998.
- [86] C. K. Yeh, D. E. Kruse, M. C. Lim, D. E. Redline, and K. W. Ferrara, "A new high frequency destruction/reperfusion system," in *IEEE International Ultrasonics Symposium*, 2003, pp. 433–436.
- [87] P. N. T. Wells, *Biomedical ultrasonics*, Academic Press, New York, 1977.
- [88] A. P. Dowling and J. E. F. Williams, *Sound and sources of sound*, John Wiley and Sons, New York, 1983.
- [89] B. H. Mahan and R. J. Myers, *Chimica*, Casa Editrice (A.
- [90] V. A. Shutilov and M. E. Alferieff, *Fundamentals physics of ultrasound*, Gordon and Breach Science Publishers, London, second edition, 1988.
- [91] F. Scudieri, *Appunti di Fisica 1*, Unitor, Rome, first edition, 1990.
- [92] Advanced Technology Laboratories, Bothell, WA, *Ultramark9 ultrasoud system operation manual*, 1993.
- [93] R. Krimholtz, D.A. Leedom, and G.L. Matthaei, "New equivalent circuit for elementary piezoelectric transducers," *Electron Letters*, vol. 6, pp. 398–399, 1970.
- [94] G. S. Kino, *Acoustic waves: devices, imaging, and analog signal processing*, Prentice-Hall, 1987.
- [95] J. M. Cannata, J. Z. Zhao, S. Ayyappan, T. A. Ritter, W. Chen, and K. K. Shung, "Fabrication of high frequency (25-75 mhz) single elment ultrasonic transducers," in *IEEE International Ultrasonics Symposium*, October 1999, vol. 2, pp. 1199–1003.
- [96] "Information for manufactures seeking marketing and clearance of diagnostic ultrasound systems and transducers," Report, U.S. Departeme of Health and Human Serices, Food and Drug Administration, Center for Devices and Radiological Healt, November 1997.



- [97] J. A. Zagzebski, *Essentials of ultrasound physics*, Mosby, London, 1996.
- [98] B. Herman, S. Einav, and Z. Vered, "Feasibility of mitral flow assessment by echo-contrast ultrasound, part I: determination of the properties of echo-contrast agents," *Ultrasound in Med. and Biol.*, vol. 26, no. 5, pp. 785–795, 2000.
- [99] S. Stergiopoulos, *Advanced Signal Processing Handbook*, CRC Press, Boca Raton, 2001.
- [100] A. Trucco and F. Bertora, "Harmonic beamforming: a new approach to remove the linear contributions in harmonic imaging," in *IEEE International Ultrasonics Symposium*, Honolulu, Hawaii, October 2003, IEEE UFFC Society, pp. 457–460.
- [101] K. K. Djoa, N. de Jong, F. C. van Egmond, J. D. Kasprzak, W. B. Vletter, C. T. Lancee, A. F. W. van der Steen, N. Bom, and J. R. T. C. Roelandt, "A fast rotating scanning unit for real-time threedimensional echo data acquisition," *Ultrasound in Med. and Biol.*, vol. 26, no. 5, pp. 863–869, 2000.
- [102] P. Arbeille, V. Eder, D. Casset, L. Quillet, C. Hudelo, and S. Herault, "Real-time 3-d ultrasound acquisition and display for cardiac volume and ejection fraction evaluation," *Ultrasound in Med. and Biol.*, vol. 26, no. 2, pp. 201–208, 2000.
- [103] Y. F. M. Nosir, P. M. Fioretti, W. B. Vletter, E. Boersma, A. Salustri, J. Tjoa Postma, A. E. M. Reijs, F. J. Ten Cate, and J. R. T. C. Roelandt, "Accurate measurement of left ventricular ejection fraction by three-dimensional echocardiography, a comparison with radionuclide angiography," *Circulation*, vol. 94, pp. 460–466, 1996.
- [104] P. J. A. Frinking and N. de Jong, "Acoustic modeling of shell encapsuled gas bubbles," *Ultrasound in Med. and Biol.*, vol. 24, no. 4, pp. 523–533, 1998.
- [105] S. Mayer and P. A. Grayburn, "Myocardial contrast agents: recent advances and future directions," *Progress in Cardiovascular Diseases*, vol. 44, no. 1, pp. 33–44, 2001.
- [106] S. B. Feinstein, "The powerful microbubble: from bench to bedside, from intravascular tracer to therapeutic delivery system, and beyond," *Editorial of Am. J. of Physiology*, 2004.
- [107] P. J. A. Frinking, A. Bouakaz, J. Kirkhorn, F. J. Ten Cate, and N. de Jong, "Ultrasound contrast imaging, current and new potential methods," *Ultrasound in Med. and Biol.*, vol. 26, no. 6, pp. 965–975, 2000.

- 
- [108] S. Kaul, "Myocardial contrast echocardiography: basic principles," *Progress in Cardiovascular Diseases*, vol. 44, no. 1, pp. 1–11, 2001.
- [109] T. G. Leighton, *The acoustic bubble*, Oxford University Press, New York, 1995.
- [110] N. de Jong, "Acoustic properties of ultrasound contrast agents," Ph.D. thesis, Erasmus University, Rotterdam, The Netherlands, June 1993.
- [111] G. K. Batchelor, *An introduction to fluid dynamics*, Cambridge University Press, 1967.
- [112] F. N. van de Vosse and M. E. H. van Dongen, *Cardiovascular fluid mechanics*, Eindhoven University of Technology, Eindhoven (NL), 1998.
- [113] S. Hilgenfeldt, M. P. Brenner, S. Grossman, and D. Lohse, "Analysis of rayleighplessert dynamics for sonoluminescing bubbles," *J. Fluid Mech.*, vol. 365, pp. 171–204, 1998.
- [114] L. Hoff, *Acoustic caracterization of contrast agents for medical ultrasound imaging*, Kluwer Academica Publishers, Dordrecht, first edition, 2001.
- [115] E. A. Neppiras and B. E. Noltingk, "Cavitation produced by ultrasonics: theoretical conditions for the onset of cavitation," *Proc. Phys Soc.*, vol. B63, pp. 1032–1038, 1951.
- [116] H. Poritsky, "The collapse or growth of a spherical bubble or cavity in a viscous fluid," *Proc. 1st US Nat. Cong. on Apllied Mechanics*, pp. 813–821, 1952.
- [117] C. C. Church, "Prediction of rectified diffusion during nonlinear bubble pulsations at biomedical frequencies," *J. of Acoustic Society of America*, vol. 83, no. 6, pp. 2210–2217, 1988.
- [118] C. C. Church, "A method to account for acoustic microstreaming when predicting bubble growth rates produced by rectified diffusion," *J. of Acoustic Society of America*, vol. 84, no. 5, pp. 1758–1764, 1988.
- [119] N. de Jong, L. Hoff, T. Skotland, and N. Bom, "Absorption and scatter of encapsulated gas filled microspheres: theoretical considerations and some measurements," *Ultrasonics*, vol. 30, no. 2, pp. 95–103, 1992.
- [120] L. Hoff, "Acoustic properties of ultrasound contrast agents," *Ultrasonics*, vol. 34, pp. 591–593, 1996.

- [121] F. R. Gilmore, "The collapse and growth of a spherical bubble in a viscous compressible liquid," Report 26-4, Calif. Inst. of Tech. Hydrodynamics Lab., 1952.
- [122] C. Herring, "Theory of pulsations of the gas bubble produced by an underwater explosion," Report 236, O.S.R.D., 1941.
- [123] Z. C. Feng and L. G. Leal, "Nonlinear bubble dynamics," *Annu. Rev. Fluid Mech.*, vol. 29, pp. 201–243, 1997.
- [124] V. Sboros, C. A. MacDonald, S. D. Pye, C. M. Mran, J. Gomatam, and W. N. McDicken, "The dependence of ultrasound contrast agents backscatter on acoustic pressure: theory versus experiment," *Ultrasonics*, vol. 40, pp. 579–583, 2002.
- [125] H. G. Flynn, "Cavitation dynamics I: A mathematical formulation," *J. of Acoustic Society of America*, vol. 57, pp. 1379–1396, 1975.
- [126] C. T. Chin and P. Burns, "Predicting the acoustic response of a microbubble population for contrast imaging in medical ultrasound," *Ultrasound in Med. and Biol.*, vol. 26, no. 8, pp. 1293–1300, 2000.
- [127] J. B. Keller and M. Miksis, "Bubble oscillations of large amplitude," *J. of Acoustic Society of America*, vol. 68, pp. 628–633, 1980.
- [128] A. Prosperetti, L. A. Crum, and K. W. Commander, "Nonlinear bubble dynamics," *J. of Acoustic Society of America*, vol. 83, pp. 502–514, 1988.
- [129] K. E. Morgan, J. S. Allen, P. A. Dayton, A. L. Klibanov, J. E. Chomas, K. W. Ferrara, and H. Medwin, "Experimental and theoretical evaluation of microbubbles behavior: effect of transmitted phase and bubble size," *IEEE Trans. on Ultrasonics, Ferroelectrics, and Frequency Control*, vol. 47, no. 6, pp. 1494–1509, 2000.
- [130] J. M. Gorce, M. Arditi, and M. Schneider, "Bubble oscillations of large amplitude," *Invest. Radiol.*, vol. 35, no. 11, pp. 661–671, 2000.
- [131] P. S. Pawlik H. Reismann, *Elasticity: theory and applications*, John Wiley and Sons, New York, 1980.
- [132] H. Medwin and C.S. Clay, *Fundamentals of Oceanography*, Academic Press, San Diego, 1998.
- [133] A. L. Anderson and L. D. Hampton, "Acoustics of gas-bearing sediments: background," *J. of Acoustic Society of America*, vol. 67, no. 6, pp. 1865–1889, 1980.

- 
- [134] H. Medwin, "Counting bubbles acoustically: a review," *Ultrasonics*, vol. 15, no. 1, pp. 7–13, 1977.
- [135] C. T. Chi, M. Versluis, C. Lancee, and N. de Jong, "Free oscillations of microbubbles as observed using a new 25 million frames per second camera," in *IEEE International Ultrasonics Symposium*, Honolulu, Hawaii, October 2003, IEEE UFFC Society.
- [136] N. de Jong, P. J. A. Frinking, A. Bouakaz, M. Goorden, T. Schourmans, Xu Jingping, and F. Mastik, "Optical imaging of contrast agent microbubbles in an ultrasound field with a 100-mhz camera," *Ultrasound in Med. and Biol.*, vol. 26, no. 3, pp. 487–492, 2000.
- [137] M. Postema, A. Bouakaz, and C. T. Chin, "Simulations and measurements of optical images of insonified ultrasound contrast microbubbles," *IEEE Trans. on Ultrasonics, Ferroelectrics, and Frequency Control*, vol. 50, pp. 523–536, 2003.
- [138] P. J. A. Frinking and N. de Jong, "Modeling of ultrasound contrast agents," in *IEEE International Ultrasonics Symposium*. IEEE UFFC Society, October 1997, pp. 1601–1604.
- [139] N. de Jong, P. J. A. Frinking, F. ten Cate, and P. van der Wouw, "Characteristics of contrast agents and 2d imaging," in *IEEE International Ultrasonics Symposium*. IEEE UFFC Society, October 1996, pp. 1449–1558.
- [140] C. S. Sehgal and P. H. Arger, "Mathematical modeling of dilution curves for ultrasonographic contrast," *J. Ultrasound in Medicine*, vol. 16, pp. 471–479, 1997.
- [141] M. Shneider, "Influence of bubble size distribution on echogenicity of ultrasound contrast agents: a study of sonovue," *Echocardiography*, vol. 16, no. 7, pp. 743–746, 1999.
- [142] R. A. Thuraisingham, "New expressions of acoustic cross-sections of a single bubble in the monopole bubbly theory," *Ultrasonics*, vol. 35, pp. 407–409, 1997.
- [143] A. Bouakaz, N. de Jong, L. Gerfault, and C. Cachard, "In vitro standard acoustic parameters of ultrasound contrast agents: definitions and calculations," in *IEEE International Ultrasonics Symposium*, October 1996, vol. 2, pp. 1445–1448.

- [144] A. Bouakaz, N. de Jong, and C. Cachard, "Standard properties of ultrasound contrast agents," *Ultrasound in Med. and Biol.*, vol. 24, no. 3, pp. 469–472, 1996.
- [145] V. Uhlendorf, "Physics of ultrasound contrast imaging: scattering in the linear range," *IEEE Trans. on Ultrasonics, Ferroelectrics, and Frequency Control*, vol. 41, no. 1, pp. 70–79, 1994.
- [146] M. O'Donnell, D. Bauwens, J. W. Mimbs, and J. G. Miller, "Broadband integrated backscatter: an approach to spatially localized tissue characterization in vivo," in *Ultrasonic Symposium*, 1979, pp. 175–178.
- [147] N. Sponheim, L. Hoff, A. Waaler, B. Muan, H. Morris, S. Holm, M. Myrum, N. de Jong, and T. Skotland, "Albunex - a new ultrasound contrast agent," in *IEE conference Acoustinc Sensing and Imaging*. IEEE, March 1993, pp. 103–107.
- [148] H. Becher and P. N. Burns, *Handbook of contrast Echography*, Springer Verlag, New York, 2000.
- [149] D. Bokor, "Diagnostic efficacy of SonoVue," *Am. J. of Cardiology*, vol. 86, pp. 19G–24G, 2000.
- [150] R. J. Erckersley, C. A. Sennoga, R. C. Campbell, and M. J. K. Blomely, "Characterization of novel microbubble contrast agents," in *IEEE International Ultrasonics Symposium*, Honolulu, Hawaii, October 2003, IEEE UFFC Society, pp. 1499–1502.
- [151] S. L. Bridal, O. Lucidarme, J. M. Correas, P. N. Burbs, J. F. Morreau, and G. Berger, "Quantification of ultrasound contrast aent in an in vitro perfusion phantom," in *IEEE International Ultrasonics Symposium*. IEEE UFFC Society, October 1999, pp. 1759–1762.
- [152] P. J. A. Frinking, A. Bouakaz, N. de Jong, F. ten Cate, and S. Keating, "Effect of ultrasound on release of micro-encapsuled drugs," *Ultrasonics*, vol. 36, pp. 709–712, 1998.
- [153] J. D. Lathia, L. Leodore, and M. A. Wheatley, "Polymeric contrast agent with targeting potential," *Ultrasonics*, vol. 42, pp. 763–768, 2004.
- [154] A. van Wamel, A. Bouakaz, B. Bernard, F. ten Cate, and N. de Jong, "Radionuclide tumour therapy with ultrasound contrast microbubbles," *Ultrasonics*, vol. 42, pp. 903–906, 2004.

- 
- [155] J. E. Chomas, P. Dayton, J. Allen, K. Morgan, and K. W. Ferrara, "Detection procedures of ultrasound contrast agents," *IEEE Trans. on Ultrasonics, Ferroelectrics, and Frequency Control*, vol. 48, no. 1, pp. 232–248, 2001.
- [156] G. T. Sieswerda, O. Kamp, R. van den Ende, and C. A. Visser, "Intermittent harmonic imaging and videodensitometry significantly enhance ability of intravenous air-filled ultrasonographic contrast agent to produce ventricular and myocardial opacification," *J. Am. Soc. Echocardiography*, vol. 14, no. 1, pp. 20–28, 2001.
- [157] J. Hancock, H. Dittrich, D. E. Jewitt, and M. J. Monaghan, "Evaluation of myocardial, hepatic, and renal perfusion in a variety of clinical conditions using an intravenous ultrasound contrast agent (Optison) and second harmonic imaging," *Heart*, vol. 81, pp. 636–641, 1999.
- [158] N. de Jong, P. J. A. Frinking, A. Bouakaz, and F. J. Ten Cate, "Detection procedures of ultrasound contrast agents," *Ultrasonics*, vol. 38, pp. 93–98, 2000.
- [159] A. Bouakaz, S. Frigstad, F. J. Ten Cate, and N. de Jong, "Improved contrast to tissue ratio at higher harmonics," *Ultrasonics*, vol. 40, pp. 575–578, 2002.
- [160] N. de Jong, A. Bouakaz, and F. J. Ten Cate, "Contrast harmonic imaging," *Ultrasonics*, vol. 40, no. 1, pp. 567–573, 2002.
- [161] N. de Jong, A. Bouakaz, and P. Frinking, "Harmonic imaging for ultrasound contrast agents," in *IEEE International Ultrasonics Symposium*. IEEE UFFC Society, October 2000, pp. 1869–1876.
- [162] A. Bouakaz, S. Frigstad, N. de Jong, and F. J. Ten Cate, "Super harmonic imaging: a new imaging technique for improved contrast detection," *Ultrasound in Med. and Biol.*, vol. 28, no. 1, pp. 59–68, 2002.
- [163] F. Forsberg, W. T. Shi, and B. B. Goldberg, "Subharmonic imaging of contrast agents," *Ultrasonics*, vol. 38, pp. 87–92, 2000.
- [164] J. Borsboom, C. T. Chin, and N. de Jong, "Experimental evaluation of non-linear coded excitation method for contrast imaging," *Ultrasonics*, vol. 42, pp. 671–675, 2002.
- [165] P. P. Chang, Wen-Shiang Chen, P. D. Mourad, S. L. Poliachik, and L. A. Crum, "Thresholds for inertial cavitation in albumin suspensions under pulsed ultrasound conditions," *IEEE Trans. on Ultrasonics Ferroelectrics, and Frequency Control*, vol. 48, no. 1, pp. 161–170, 2001.

- [166] J. Kirkhorn, P. J. A. Frinking, N. de Jong, and H. Torp, "Three-stage approach to ultrasound contrast detection," *IEEE Trans. on Ultrasonics, Ferroelectrics, and Frequency Control*, vol. 48, no. 4, pp. 1013–1021, 2001.
- [167] P. J. A. Frinking, E. I. Cespedes, J. Kirkhorn, H. G. Torp, and N. de Jong, "A new ultrasound contrast imaging approach based on the combination of multiple imaging pulses and a separate release burst," *IEEE Trans. on Ultrasonics, Ferroelectrics, and Frequency Control*, vol. 48, no. 3, pp. 643–651, 2001.
- [168] K. Peels and E. Korsten, *Practical Echocardiography*, [www.vesalius.org](http://www.vesalius.org), 2000.
- [169] P. Voci, F. Bilotta, P. Merialdo, and L. Agati, "Myocardial contrast enhancement after intravenous injection of sonicated albumin microbubbles: a transesophageal echocardiography dipyridamole study," *American Society of Echocardiography*, vol. 7, pp. 337–346, 1994.
- [170] L. J. Bos, J. J. Piek, and J. A. E. Spaan, "Effects of shadowing on the time-intensity curves in contrast echocardiography: a phantom study," *Ultrasound in Med. and Biol.*, vol. 22, no. 2, pp. 217–227, 1996.
- [171] C. K. Yeh, M. I. Yang, and P. C. Li, "Contrast-specific ultrasonic flow measurements based on both input and output time intensities," *Ultrasound in Med. and Biol.*, vol. 29, no. 5, pp. 671–678, 2003.
- [172] V. Uhlendorf, F.-D. Scholle, and M. Reinhardt, "Acoustic behaviour of current ultrasound contrast agents," *Ultrasonics*, vol. 38, pp. 81–86, 2000.
- [173] J. M. Correas, P. N. Burns, X. Lai, and X. Qi, "Infusion versus bolus of an ultrasound contrast agent," *Investigative Radiology*, vol. 35, no. 1, pp. 72–79, 2000.
- [174] A. Bouakaz, N. de Jong, C. Cachard, and K. Jouini, "On the effect of lung filtering and cardiac pressure on the standard properties of ultrasound contrast agents," *Ultrasonics*, vol. 36, pp. 703–708, 1998.
- [175] D. Adam and E. Burla, "Study of pressure dependence of signals from ultrasound contrast agents," in *IEEE EMBS International Conference*, Istanbul, Turkey, October 2001, IEEE EMB Society, pp. 3370–3373.
- [176] F. D. Scholle, V. Uhlendorf, and T. Fritsch, "Physical mechanism of inhomogeneous left ventricular echocontrast," in *IEEE International Ultrasonics Symposium*. IEEE UFFC Society, 1994, pp. 1563–1566.

- 
- [177] J. M. Bogaard, W. A. van Duyl, A. Vesprille, and M. E. Wise, "Influence of random noise on the accuracy of the indicator-dilution method," *Clin. Phys. Physiol. Meas.*, vol. 6, no. 1, pp. 59–64, 1985.
- [178] P. S. Hamilton, M. G. Curely, and R. M. Aimi, "Levenberg-marquardt estimation for accurate end efficient continuous measurement of cardiac output," in *IEEE EMBS International Conference*, Chicago, July 2000, IEEE EMB Society, pp. 1954–1957.
- [179] D. M. Band R. A. F. Linton, N. W. F. Linton, "A new method for analysing indicator dilution curves," *Cardiovascular Res.*, vol. 30, pp. 930–938, 1995.
- [180] A. Lopatzidis and R. K. Millard, "Empirical estimators of gamma fits to tracer dilution curves and their technical basis and practical scope," *Physiological Measurements*, vol. 22, pp. N1–N5, 2001.
- [181] T. Gustavsson and M. Beckman-Suurkula, "Videodensitometric measurements in contrast-echocardiology," *Computers in Cardiology*, vol. B63, pp. 709–712, 1996.
- [182] J. L. M. Marinus, C. H. Massen, E. A. von Reth, J. M. Bogaard, J. R. C. Jansen, and A. Versprille, "Interpretation of circulatory shunt-dilution curves as bimodal distribution functions," *Med. & Biol. Eng. & Comp.*, vol. 22, pp. 326–332, 1984.
- [183] C. W. Sheppard and L. J. Savage, "The random walk problem in relation to the physiology of circulatory mixing," *Phys. Rev.*, vol. 83, pp. 489–490, 1951.
- [184] G. J. M. Uffink, "Analysis of dispersion by the random walk method," Ph.D. thesis, Technische Universiteit Delft, Delft, The Netherlands, 1990.
- [185] A. B. de Finetti, *Teoria delle probabilita'*, vol. 2, Giulio Einaudi Ed., 1970.
- [186] A. Papoulis, *Probability, Random Variables, and Stochastic Processes*, McGraw-Hill, New York, third edition, 1991.
- [187] J. W. Delleur, *The handbook of groundwater engineering*, CRC Press, Boca Raton, 1999.
- [188] G. A. F. Seber and C. J. Wild, *Nonlinear regression*, Wiley, 1989.
- [189] T. Coleman, M. A. Branch, and A. Grace, *Optimization Toolbox for use with MATLAB*, The MATH WORKS Inc., second edition, 1999.
- [190] W. J. Krzanowsky, *An introduction to statistical modelling*, Arnold, New York, 1998.



- [191] P. A. Jansson, *Deconvolution with applications in spectroscopy*, Academic Press, 1984.
- [192] P. A. Jansson, *Deconvolution of images and spectra*, Academic Press, 1997.
- [193] A. Papoulis, *Signal Analysis*, McGRAW-HILL, 1984.
- [194] P. Z. Peebles, *Probability, random variables, and random signal principles*, McGRAW-HILL, third edition, 1993.
- [195] A. Bennis and S. M. Riad, "Filtering capabilities and convergence of the van-cittert deconvolution technique," *IEEE Transactions on Instrumentation and Measurement*, vol. 41, no. 2, pp. 246–250, 1992.
- [196] A. Monti Guarnieri, F. Rocca, P. Guccione, and C. Cafforio, "Optimal interferometric scansar focusing," in *IEEE Geoscience and Remote Sensing Symposium*. IEEE, June 1999, vol. 3, pp. 1718–1720.
- [197] Yangseok Jeong, Heugryeol Ryou, and Chungyong Lee, "A high resolution delay estimation technique in frequency domain for positioning systems," in *IEEE Vehicular Technology Conference*. IEEE, Sept. 2002, vol. 2, pp. 2318–2321.
- [198] S. H. Wang and K. K. Shung, "In vivo measurements of ultrasonic backscattering in blood," *IEEE Transactions on Ultrasonics, Ferroelectrics and Frequency Control*, vol. 48, no. 2, pp. 425–431, 2001.
- [199] J. C. Lagarias, J. A. Reeds, M. H. Wright, and P. E. Wright, "Convergence properties of the nelder-mead simplex method in low dimensions," *SIAM Journal of Optimization*, vol. 9, no. 1, pp. 112–147, 1998.
- [200] T. Taxt and G. V. Frolova, "Noise robust one-dimensional blind deconvolution of medical ultrasound images," *IEEE Transactions on Ultrasonics, Ferroelectrics, and Frequency Control*, vol. 46, no. 2, pp. 291–299, 1999.
- [201] D. Rovai, M. Lombardi, A. Mazzarisi, L. Landini, Taddei, A. Distane, A. Benassi, and A. L' Abbate, "Flow quantitation by radio frequency analysis of contrast echocardiography," *The International Journal of Cardiac Imaging*, vol. 9, pp. 7–19, 1993.
- [202] M. Kass, A. Witkin, and D. Terzopoulos, "Snakes: Active contour models," *International Journal of Computer Vision*, vol. 1, no. 4, pp. 321–331, 1987.
- [203] N. Otsu, "A threshold selection method from gray-level histograms," *IEEE Transactions Systems, Man, and Cybernetics*, vol. 9, no. 1, pp. 62–66, 1979.

- 
- [204] A. D. Parker, A. Hill, C. J. Taylor, T. F. Cootes, X. Y. Jin, and D. G. Gibson, "Application of point distribution models to automated analysis of echocardiograms," *Computers in Cardiology*, pp. 25–28, 1994.
- [205] A. Lantis, C. J. Taylor, and T. F. Cootes, "Automatic interpretation and coding of face images using flexible models," *IEEE Transactions on Pattern Analysis and Machine Intelligence*, vol. 19, no. 7, pp. 743–756, 1997.
- [206] B. van Ginneken, A. F. Frangi, J. J. Staal, B. M. ter Haar Romeny, and M. A. Viergever, "Active shape model segmentation with optimal features," *IEEE Transactions on Medical Imaging*, vol. 21, no. 8, pp. 924–933, 2002.
- [207] R. G. Aarnink, "Automated contour detection, design and clinical applications in urology," Ph.D. thesis, Catholic University Nijmegen, Nijmegen, The Netherlands, 1996.
- [208] Takashi Fujino et al., "New method of on-line quantification of regional wall motion with automated segmental motion analysis," *Journal of the American Society of Echocardiography*, vol. 14, no. 9, pp. 892–901, 2001.
- [209] H. G. Bosch, S. C. Mitchell, B. P. F. Lelieveldt, F. Nijland, O. Kamp, M. Sonka, and J. H. C. Reiber, "Active appearance-motion models for fully automated endocardial contour detection in time sequences of echocardiograms," in *CARS-CVI*, Berlin, June 2001, IEEE, vol. 1, pp. 27–30.
- [210] I. Craw, N. Costen, T. Kato, and S. Akamatsu, "How should we represent faces for automatic recognition?," *IEEE Trans. on Pattern Analysis and Machine Intelligence*, vol. 21, no. 8, pp. 725–736, 2001.
- [211] T. F. Cootes, G. J. Gareth, and C. J. Taylor, "Active appearance models," *IEEE Trans. on Pattern Analysis and Machine Intelligence*, vol. 23, no. 6, pp. 681–685, 2001.
- [212] T. F. Cootes and C. J. Taylor, "Constrained active appearance models," in *IEEE Proc. Eighth International Conference on Computer Vision*, Vancouver, Canada, July 2000, IEEE, vol. 1, pp. 748–754.
- [213] K. Althoff, G. Hamarneh, M. Beckman Suurkula, and T. Gustavsson, "Tracking contrast in echography by a combined snake and optical flow technique," *Computers in Cardiology*, vol. 27, pp. 29–32, 2000.
- [214] S. Osher and J. Sethian, "Fronts propagating with curvature-dependent speed: algorithms based on hamilton-jacobi formulation," *Journal of Computational Physics*, vol. 79, pp. 12–49, 1988.

- 
- [215] N. Frieland and D. Adam, "Automatic ventricular cavity boundary detection from sequential ultrasound images using simulated annealing," *IEEE Transactions on Medical Imaging*, vol. 8, no. 4, pp. 344–353, 1989.
- [216] A. A. Amini, T. E. Weymouth, and R. C. Jain, "Using dynamic programming for solving variational problems in vision," *IEEE Transactions on Pattern analysis and machine intelligence*, vol. 12, no. 9, pp. 855–867, 1990.
- [217] K. W. Smillie, *An introduction to regression and correlation*, Accademic Press, 1966.
- [218] M. Lesieur, *Turbulence in Fluids*, Kluwer Academic Publishers, 1997.
- [219] P. de Mottoni, Ed., *Complementi di matematica*, ARACNE, Rome, first edition, 1992.

## List of publications

### Journal papers

- [JP-1] M. Mischi, A.H.M. Jansen, A.A.C.M. Kalker, H.H.M. Korsten, "Identification of Ultrasound-Contrast-Agent Dilution Systems for Ejection Fraction Measurements," Accepted for publication in *IEEE Transactions on Ultrasonics, Ferroelectrics, and Frequency Control*, 2004.
- [JP-2] M. Mischi, A.A.C.M. Kalker, H.H.M. Korsten, "Cardiac Image Segmentation for Contrast Agent Videodensitometry," Accepted for publication in *IEEE Transactions on Biomedical Engineering*, 2004.
- [JP-3] M. Mischi, A.A.C.M. Kalker, H.H.M. Korsten, "Contrast Echocardiography for Pulmonary Blood Volume Quantification," Accepted for publication in *IEEE Transactions on Ultrasonics, Ferroelectrics, and Frequency Control*, 2004.
- [JP-4] M. Mischi, A.C.C.M. Kalker, H.H.M. Korsten, "Videodensitometric Methods for Cardiac Output measurements," *EURASIP Journal on Applied Signal Processing*, vol. 2003, no. 5, pp. 479-489, 2003.

### Published reports

- [PR-1] M. Mischi, *Videodensitometric Cardiac Output Measurements by Dilution of Ultrasound Contrast Agents: Modeling and In-vitro Experimentation*, Final Report M.T.D., Stan Ackermans Institute, Reference ISBN 90-444-0188-2, Apr. 2002.

### International conferences

- [IC-1] M. Mischi, A.A.C.M. Kalker, H.H.M. Korsten, "Identification of Ultrasound-Contrast-Agent Dilution Systems for Cardiac Quantification," *2004 IEEE International Ultrasonics, Ferroelectrics, and Frequency Control 50th Anniversary Joint Conference*, Montreal (Canada), Aug. 24-27, 2004 .

- [IC-2] M. Mischi, A.H.M. Jansen, A.A.C.M. Kalker, H.H.M. Korsten, "A New Ultrasound Dilution Method for EF Quantification," *15th Annual Scientific Sessions of the American Society of Echocardiography*, San Diego (CA), 26-30 June 2004.
- [IC-3] M. Mischi, A.A.C.M. Kalker, H.H.M. Korsten, "Moment Method for the Local Density Random Walk Model Interpolation of Ultrasound Contrast Agent Dilution Curves," *Proceedings on the 17th International EURASIP Conference BIOSIGNAL 2004*, Brno (Chzec Rep.), pp. 33-35, June 23-25, 2004.
- [IC-4] M. Mischi, A.H.M. Jansen, A.A.C.M. Kalker, H.H.M. Korsten, "Impulse Response Estimation of Ultrasound-Contrast-Agent Dilution Systems for Cardiac Parameter Measurements", *The Ninth European Symposium on Ultrasound Contrast Imaging*, Rotterdam (NL), pp. 61-62, Jan. 22-23, 2004 - **Poster Award Winner**.
- [IC-5] M. Mischi, A.H.M. Jansen, A.A.C.M. Kalker, H.H.M. Korsten, "Contrast Ultrasound Quantification of Ejection Fraction and Pulmonary Blood Volume," *The Ninth European Symposium on Ultrasound Contrast Imaging*, Rotterdam (NL), pp. 6-8, Jan. 22-23, 2004.
- [IC-6] M. Mischi, A.H.M. Jansen, A.A.C.M. Kalker, H.H.M. Korsten, "Sparkling waves and echocardiographic quantification," *18th Annual Advances in Contrast Ultrasound*, Chicago (IL), Oct. 30-31, 2003 - **Poster Award Winner**.
- [IC-7] M. Mischi, A.H.M. Jansen, A.A.C.M. Kalker, H.H.M. Korsten, "Intra-Thoracic Blood Volume Assessment by Dilution of Ultrasound Contrast Agents," *IEEE-UFFC Proceedings on the IEEE International Ultrasonics Symposium*, Honolulu (Hawaii), pp. 1179-1182, 5-8 Oct. 2003.
- [IC-8] M. Mischi, A.A.C.M. Kalker, H.H.M. Korsten, "Blood Volume Measurements by Videodensitometric Analysis of Ultrasound-Contrast-Agent Dilution Curves," *IEEE-EMBS Proceedings on the 25th Annual International Conference of the IEEE Engineering in Medicine and Biology Society*, pp. 791-794, Cancun (Mexico), 17-21 Sept. 2003.
- [IC-9] M. Mischi, A.A.C.M. Kalker, H.H.M. Korsten, "Assessment of Cardiac Parameters by Ultrasound Contrast Agent Dilution," *The Eighth European Symposium on Ultrasound Contrast Imaging*, pp. 54-55, Rotterdam (NL), Jan. 22-24, 2003.
- [IC-10] M. Mischi, A.A.C.M. Kalker, H.H.M. Korsten, "Bubbles and Indicator Dilution Principles in Echocardiography," *17th Annual Advances in Contrast Ultrasound*, Chicago (IL), Oct. 31, 2002.

- [IC-11] M. Mischi, T. Kalker, C.H. Peels, R.J.E. Grouls, H.H.M. Korsten, "Cardiac Output Measurements by Dilution of Ultrasound Contrast Agents: Modeling and In-vitro Experimentation," *The Seventh European Symposium on Ultrasound Contrast Imaging*, Rotterdam (NL), p. 40, Jan. 24-25, 2002.

### **Regional conferences**

- [RC-1] M. Mischi, H.H.C.M. Kalker, H.H.M. Korsten, "Contrast Echocardiographic Quantification," *Proceedings of the Signal Processing Systems Research Symposium*, pp. 91-99, Eindhoven (NL), March 25, 2004.
- [RC-2] M. Mischi, H.H.C.M. Kalker, H.H.M. Korsten, "Videodensitometric Cardiac Output Measurements by Dilution of Ultrasound Contrast Agents: Modeling and In-vitro Experimentation," *Dutch Spring Meeting on Ultrasounds*, Leiden (NL), 2002.



---

## List of abbreviations

A-mode	Amplitude mode
Ao	Aorta
AV	Aortic Valve
B-mode	Brightness mode
BSA	Body Surface Area
CAT	Computerized Axial Tomography
CBV	Central Blood Volume
CI	Cardiac Index
CLT	Central Limit Theorem
CO	Cardiac Output
CTR	Contrast to Tissue Ratio
CW	Continuous Wave
EF	Ejection Fraction
EMF	Electro-Motive Force
FEF	Forward Ejection Fraction
FIR	Finite Impulse Response
FPT	First Passage Time
IHI	Intermittent Harmonic Imaging
IDC	Indicator Dilution Curve
ITBV	Intra-Thoracic Blood Volume
LA	Left Atrium
LDRW	Local Density Random Walk
LSE	Least Square Estimation
LV	Left Ventricle
MI	Mechanical Index
M-mode	Motion mode
MR	Magnetic Resonance
MRI	Magnetic Resonance Imaging
MRT	Mean Residence Time
MSE	Mean Square Error
MTT	Mean Transit Time
MV	Mitral Valve
PA	Pulmonary Artery
PBV	Pulmonary Blood Volume



---

PET	Positron Emission Tomography
PMPI	Power Modulation Pulse Inversion
PR	Pulse Rate
PRF	Pulse Repetition Frequency
PV	Pulmonary Valve
PW	Pulsed Wave
RA	Right Atrium
REF	Regurgitant Ejection Fraction
RF	Radio Frequency
ROI	Region Of Interest
RV	Right Ventricle
SC	Systemic Circulation
SD	Standard Deviation
SNR	Signal-to-Noise Ratio
SPECT	Single Positron Emission Tomography
STAR	Scattering to Attenuation Ratio
SV	Stroke Volume
TEE	Trans-Esophageal Echocardiography
TTE	Trans-Thoracic Echocardiography
TV	Tricuspid Valve
UCA	Ultrasound Contrast Agent

## Acknowledgment

First of all, it is with my greatest pleasure that I thank my supervisors: prof.dr. Erik Korsten for his ideas, enthusiasm, and fundamental support to both this research and my life abroad, and prof.dr. Ton Kalker for his scientific and technical guide as well as for his willingness to give me advices regarding any sort of issue, also when not really related to any technical content.

Then I like to thank the Dept. of Cardiology of the Catharina Hospital in Eindhoven, represented for me by dr. Katinka Peels and dr. Jan Melle van Dantzig. In particular, my biggest thanks go to Annemieke Jansen for her tight cooperation with this research and for providing it with most of the measurements in patients. Also some MRI segmentation results are presented in this research. I like to thank Harrie van den Bosch (Dept. of Radiology of the Catharina Hospital in Eindhoven) for supplying me with all the MR analysis.

A lot of thanks to the operating room staff of the Catharina Hospital and in particular to Susan van den Elzen for her important support with the in-vitro experimentation. Also many thanks to the perfusionists, especially Monique van den Yssel-Hessels and Henk Box, who were always willing to build new experimental systems and provide me with all the necessary equipment. I was used to walk in the operating rooms carrying strange devices. Everybody looked at me like I was an alien... an engineer among doctors. However, I could always find help and support at any time.

Thanks to dr. René Grouls (Dept. of Pharmacology of the Catharina Hospital) for preparing and assisting the calibration experimentation. I was always very concerned and concentrated, so that I could not really enjoy those late experiments that we made together with Erik. Now, looking back, I realize that it was a lot of fun.

I am very grateful to prof. Steven Feinstein (Rush University Medical center, Chicago). He encouraged me and this research since the first moment. He gave me the chance to cross the ocean for my first time and visit a really “marvellous” city, Chicago.

I also like to address an important acknowledgment to dr. Marcel Arditi (Bracco research group in Geneva). After a skeptical start, he believed that this research was going to be successful and he supported us not only with the ultrasound contrast for all the in-vitro experimentation, but also with really valuable suggestions.

Many thanks also to prof.dr. Antonio Avantaggiati (La Sapienza University of Rome) for the analytical solution of the LDRW model time integral.

A lot of thanks to dr. Terence O'Brien for providing us with the LiDCO system for the calibration experimentation and to Wout van Nierop for his assistance and help with the lithium dilution experimentation. I remember that the final set-up was so complicated that each of us would have needed four hands to control it.

Many thanks to Wim van de Vooren (Philips Medical Systems) for the use of the Sonos 5500 ultrasound system and to prof.dr. Frans van de Vosse and dr. Marco Stijnen (Eindhoven University of Technology) for the use of the artificial ventricle set-up during the experimentation at the Biomedical Engineering Lab of the Eindhoven University of Technology.

Huge thanks to the Signal Processing Systems Group of the Eindhoven University of Technology, starting from the director prof.dr. Jan Bergmans, to all the professors, the technical staff, and the students, for their continuous support and help at any time I needed. In particular, I like to thank those who have been closer to me during these years. I am referring to my room mates Paul de Clercq, Harald van den Meerendonk, Peiyu He, Andrei Sazonov, and Susanne Kentgens.

I could never forget to thank Rian van Gaalen (Eindhoven University of Technology), whose door has always been open to answer questions and help me with any problem I might had. The most generous and kind person I have ever met.

For many reasons the luckiest coincidence in these years has been meeting a real friend. When they say "who finds a friend finds a treasure", I feel like this is really what I have experienced. Therefore, I like to address a special thank you to my friend Genia for having represented my major support through all the difficulties. Obviously, I have not encountered only difficulties in Holland. I had a lot of fun and enjoyable time. For this time, I like to thank all my friends, and in particular Antonio Martino, Barbara Vicari, and Francesca Altavilla, my very favorite company. I also like to mention and thank my friends at university Massimo Ciacci and Francesca Scaltro.

Last, but certainly not least, I like to thank Occhiolina and her beautiful mother... who despite everything, has always believed in me and has always been my reference point and strength source. Thank you so much.



*Learning process ...*



## Curriculum Vitae

Massimo Mischi was born in Rome (Italy) in 1973. In 1991 he obtained his high school (Liceo Classico) leaving certificate at the Liceo Orazio in Rome.

In 1999 he received his M.S. degree in electronic engineering at La Sapienza University of Rome. In his final thesis he designed and validated a new device for optical-performance measurements of clinical fibre-optic endoscopes. This research was developed at the Mechanical and Thermal Measurements laboratory of La Sapienza University and the Clinical Engineering Department of the Bambin Gesù Hospital (Vatican City).

In 2002 he obtained his PDEng-degree (Professional Doctorate in Engineering) after completing successfully the two-year Post-Master's program in Technological Design at the Eindhoven University of Technology (The Netherlands) in the field of Information and Communication Technology. His final thesis was focused on the use of indicator dilution theory and ultrasound contrast agents for cardiac output measurements.

This study was then extended to the quantification of several cardiac parameters by means of contrast echocardiography and is reported in this Ph.D. thesis, which has been developed at the Signal Processing Group of the Eindhoven University of Technology and the Catharina Hospital in Eindhoven (The Netherlands).

Massimo Mischi is a member of the Institute of Electric and Electronics Engineers (IEEE). He is also registered in the Italian Register of Engineers (Ordine degli Ingegneri) and in the Dutch Royal Institute of Engineers.

